Scaling of Overall Cooling Effectiveness of HPT NGVs from Conventional Laboratory Conditions to Engine Conditions

James Andrew Cartlidge

University College

University of Oxford

A thesis submitted for the degree of

Doctor of Philosophy

Trinity 2024

Abstract

The increased use of engine-realistic test vehicles in turbomachinery research has contributed to practical and academic interest in a robust validated theory for the scaling of overall cooling effectiveness (θ) from conventional laboratory conditions to engine conditions. The purpose of this thesis is to quantify and explain the effect of moving from conventional laboratory conditions to engine conditions on θ, via theoretical considerations and experimental validation.

In chapter 2, the impact of temperature ratio on overall cooling effectiveness is quantified using a bespoke conjugate low-order solver. The network model consists of a single row of film cooling holes; a near-wall mixing region; internal cooling channels in both the leading circuit and trailing-edge (TE) circuit; a diabatic external wall; and an adiabatic internal wall. The geometry of the model is representative of real-engine high-pressure turbine (HPT) nozzle guide vanes (NGVs). For the near-wall mixing region, the film effectiveness distribution at the reference temperature ratio (TR) is modelled using a conventional correlation from literature and scaled to non-reference TR by using an entrainment-based mixing model (assumption of fully-mixed flow). Conventional correlations from literature are used to model external and internal heat transfer coefficients, and coolant pressure loss in the internal cooling channels. The streamwise distributions of these parameters may deviate—slightly—from those of real-engine HPT NGVs, however using representative correlations from literature ensures that the model captures the relevant physics for accurately predicting *changes* in θ with TR for real-engine HPT NGVs. When subject to specific boundary conditions (BCs), the system is solved by considering energy and mass conservation arguments, and geometrical constraints on the system. Three different internal cooling system networks and two domain-global BCs (the macro BCs on the implied NGV row) are considered. It is shown that θ decreases with reducing TR and that the magnitude of the change is insensitive to the internal cooling system architecture; the type of domain-global BC imposed; and the surface-averaged value of overall cooling effectiveness at the reference TR. It is shown that there are significant scaling effects associated with absolute temperature and mainstream gas

properties and that the result is highly sensitive to the particular definition of θ. The work presented in this chapter is the subject of a published journal paper [1].

In chapter 3, the theory for scaling of overall cooling effectiveness with temperature ratio (discussed in chapter 2) is independently applied to a fourth cooling system. This system consists of three rows of film cooling holes; diabatic external and internal walls; and conducting webs connecting the external and internal wall. Low-order-model predictions show that θ decreases with reducing TR, however the magnitude of the change is significantly smaller than that predicted for the three systems above. It is shown that this is due to the presence of the conducting webs. The low-order-model-predicted results are experimentally validated by conducting experiments in a high-temperature flat-plate test facility. The work presented in this chapter is the subject of an upcoming journal paper, which is currently under review [2].

In chapter 4, the theory for scaling of overall cooling effectiveness with TR is experimentally validated by conducting experiments in the ECAT+ facility using real-engine HPT NGVs. ECAT+ is a new second-generation engine-realistic test vehicle at the University of Oxford that allows testing at engine-realistic conditions of Reynolds number (Re), Mach number (M), coolant-to-mainstream pressure ratio (CMPR), turbulence intensity (Tu) and TR. The general experimental results are broadly in agreement with the low-order-model predictions for the four NGV-representative cooling systems discussed in chapters 2 and 3. The work presented in this chapter is the subject of a complete draft of an upcoming journal paper [3].

It is hoped that the theoretical and experimental results reported in this thesis will be useful to other researchers when scaling their experimental results to engine conditions.

Acknowledgements

First of all, I would like to thank my supervisor Prof. Thomas Povey for giving me the opportunity to study at the University of Oxford at both undergraduate and postgraduate level. Tom first interviewed me for undergraduate admission in 2014, he was one of my undergraduate tutors, and he supervised me for both the fourth year project and DPhil. I will always be immensely grateful to Tom for the knowledge and expertise that he has passed on to me over the years, and for training me to be a scientist. Some of my favourite memories of the DPhil are the times spent collaborating with Tom on the various papers that we have worked on over the last five years.

I would like to thank Andrew Messenger for his support with instrumentation design and running the ECAT+ rig. His technical expertise was a major factor in obtaining such a high-quality and extensive data set during the ECAT+ commissioning campaign. I am also grateful to Nafiz Chowdhury for his support with running the ECAT+ rig.

I appreciate the support of all technicians and staff at the Osney lab. In particular, I would like to thank Liam Boland, Andreea Dabija, Dominic Harris, Leo Verling, Leon Blake and Craig Parsons. I would also like to thank all of my Osney mates for their moral support and the many technical discussions over the years!

I am indebted to Mkrtich Harutyunyan of National Instruments Corporation for his technical support with implementing the ECAT+ data acquisition system.

I extend my deepest gratitude to my family for their unwavering support. In particular, I am forever indebted to Dad for his technical support with extracting infrared (IR) temperatures from RAVI files. Had we not learned how to do this, it would have been impossible to process much of the data presented in this thesis. I am extremely grateful to Mum for the endless cups of tea; meals; and moral support!

Finally, I would like to thank Rolls-Royce Plc, Innovate UK, United Kingdom Aerospace Technology Institute (ATI), and EPSRC for each funding various aspects of the project.

Contents

Nomenclature

Romans

a	best-fit coefficient, –
A	cross-sectional area, m^2
b	best-fit coefficient, –
Bi	Biot number, –
c	recovery ratio, –
	best-fit coefficient, –
c_c	recovery ratio of a hypothetical unmixed coolant stream with adiabatic wall condition, –
c_{p0}	specific heat capacity at constant pressure evaluated at T_0, J kg^{-1} K^{-1}
c_v	specific heat capacity, constant volume, J kg^{-1} K^{-1}
C_x	(chapter 2) plate surface length, m
	(chapter 4) axial chord, m
d	(chapter 2) film cooling hole diameter, m
	best-fit coefficient, –
D	hydraulic diameter, m
	(chapter 3) film cooling hole diameter, mm
D_c	hydraulic diameter of internal cooling channel, mm
D_{plen}	hydraulic diameter of cooling plenum, mm
$d\dot{m}$	incremental change in mass flow rate, kg s^{-1}
dq_m	incremental heat loss to the wall, W
dx	incremental change in streamwise position, mm
C_1–C_6	calibration multipliers for transient thermal model, –
C_x	surface arc length, mm
f_c	friction factor of the internal cooling channel, –
h	heat transfer coefficient, W m^{-2} K^{-1}
H	(chapter 2) internal cooling channel height, m
	(chapter 3) module height, m
h_c	internal heat transfer coefficient, W m^{-2} K^{-1}
h_m	external heat transfer coefficient, W m^{-2} K^{-1}
k	thermal conductivity, W m^{-1} K^{-1}
$\bar{k}_w$	local through-wall average wall thermal conductivity, W m^{-1} K^{-1}
k_1	multiplication factor used in modified mixing layer effectiveness correlation, –
k_2	multiplication factor used in modified external Nusselt number correlation, –
k_3	multiplication factor used in modified internal Nusselt number correlation, –
K	multiplication factor used in Nusselt number correlation for system 2, –

	multiplier used in Nusselt number correlation in the test section in the 2D transient thermal facility model, –
K_1	multiplication factor used in correlation for internal friction factor, –
K_2	multiplication factor used in correlation for internal Nusselt number, –
K_{web}	multiplication factor for effective width of webs separating modules in the lateral direction, –
l	turbulence length scale, mm
L	(chapter 3) flat-plate length, mm
M	Mach number, –
$\dot{m}$	mass flow rate, kg s^{-1}
$\dot{m}_{\text{e}}$	integrated entrainment mass flow rate distribution, kg s^{-1}
$\dot{m}_{\text{h}}$	mainstream mass flow rate, kg s^{-1}
$\dot{m}_{\text{m}}$	integrated mixing layer mass flow rate, kg s^{-1}
Nu	Nusselt number, –
Nu'_{c}	modified cooling-channel Nusselt number, –
Nu'_{m}	modified external Nusselt number, –
Pr	Prandtl number, –
p	static pressure, Pa
p_0	total pressure, Pa
P1–P4	planes 1–4
q_{m}	external convective heat flux, W m^{-2}
q^*	total surrounding radiant flux, W m^{-2}
Q_{A}	heat transfer rate from external wall to webs, W
Q'_{A}	heat transfer rate from external wall to webs, assuming no variation in wall temperature in lateral direction, W
Q_{B}	heat transfer rate from webs to internal wall, W
Q'_{B}	heat transfer rate from webs to internal wall, assuming no variation in wall temperature in lateral direction, W
r	recovery factor, –
s	(chapter 4) streamwise co-ordinate, –
R	specific gas constant, J kg^{-1} K^{-1}
	raw image value, –
$\Re$	recovery and redistribution parameter, –
Re	Reynolds number, –
Re_D	mainstream outlet-Re based on hole diameter, –
S	span fraction, %
t	time, s
t_{w}	wall thickness, m
t_{w1}	external wall thickness, mm
t_{w2}	internal wall thickness, mm
T	temperature, K

$\bar{T}$	average temperature, K
T_0	total temperature, K
T'	temperature, corrected for transient effects, K
Tu	turbulence intensity, %
T_{aw}	adiabatic wall temperature, K
$T_{\Re}$	recovery and redistribution temperature, K
u	velocity, m s^{-1}
u'_{1c}	coolant velocity at film cooling hole exit, m s^{-1}
$U_{\Delta T}$	uncertainty in ΔT, K
U_T	uncertainty in T, K
$U_{\Delta\theta}$	uncertainty in $\Delta\theta$, –
U_θ	uncertainty in θ, –
w	(chapter 2) plate width, m
	(chapter 3) width of webs separating modules in the lateral direction, mm
W	module width, mm
x	(chapters 2 and 3) streamwise co-ordinate, mm
x'	local streamwise co-ordinate based on stream-wise distance from the channel inlet, m
y	(chapter 2) surface-normal co-ordinate, m
	(chapters 3 and 4) lateral co-ordinate, mm
z	(chapters 3 and 4) surface-normal co-ordinate, mm

Greek letters

α	angle of film cooling hole, degrees
β	IR camera viewing angle, degrees
β_1	multiplication factor in equation for θ', –
β_2	multiplication factor in equation for θ'', –
β_1–β_6	multipliers used in steady thermal model, –
γ	ratio of specific heat capacities (c_p/c_v), –
Δ	change in quantity, –
ΔT_{CP}	temperature offset used for Calibration Method 3, K
$\Delta\theta$	change in overall cooling effectiveness as TR is varied, –
$\Delta\theta_{ABS}$	change in overall cooling effectiveness as temperature is varied from high absolute temperature to low absolute temperature at fixed TR, –
$\Delta\theta_{E\text{-}R}$	overall engine-to-rig correction, –
$\Delta\theta_{E-R}^{M1}$	overall engine-to-rig correction (method 1), –
$\Delta\theta_{E-R}^{M2}$	overall engine-to-rig correction (method 2), –
$\Delta\theta_{GP}$	change in overall cooling effectiveness as fluid properties of mainstream are varied from combustion products to air at fixed TR, –
ε	total non-dimensional external-side heat flux between any location and the cooling channel inlet, –

	flat-plate surface emissivity, –
	emissivity of the vane surface, –
ε'	modified emissivity of the vane surface, –
ε_{CP}	emissivity of the calibration patch, –
ε'_{CP}	modified emissivity of the calibration patch, –
η	adiabatic film effectiveness, –
η_{aw}	adiabatic film effectiveness, –
η_{fl}–η_{f3}	contribution by mass fraction of each cooling film 1–3 to adiabatic film effectiveness, –
η_{ML}	film effectiveness of the mixing layer, –
η'_{ML}	modified effectiveness of the mixing layer, –
θ	overall cooling effectiveness, –
$\bar{\theta}$	average overall cooling effectiveness, –
θ_0	value of θ at design conditions of Re_D, M and CMPR, –
θ_{Air}	overall cooling effectiveness for air, –
θ_{CP}	overall cooling effectiveness for combustion products, –
θ_{LT}	overall cooling effectiveness at low absolute temperature, –
θ_{HT}	overall cooling effectiveness at high absolute temperature, –
θ^*	θ, for IR temperature measurements corrected with Calibration Method 2, –
θ^{**}	θ, for IR temperature measurements corrected with Calibration Method 3, –
θ^{***}	θ, for IR temperature measurements corrected with Calibration Method 4, –
θ'	overall cooling effectiveness, corrected for transient effects, –
$\theta^{*\prime}$	θ', for IR temperature measurements corrected with Calibration Method 2, –
$\theta^{**\prime}$	θ', for IR temperature measurements corrected with Calibration Method 3, –
$\theta^{***\prime}$	θ', for IR temperature measurements corrected with Calibration Method 4, –
θ''	overall cooling effectiveness, corrected for both transient effects and off-design conditions of Re_D, M and CMPR, –
$\theta^{*\prime\prime}$	θ'', for IR temperature measurements corrected with Calibration Method 2, –
$\theta^{**\prime\prime}$	θ'', for IR temperature measurements corrected with Calibration Method 3, –
$\theta^{***\prime\prime}$	θ'', for IR temperature measurements corrected with Calibration Method 4, –
λ	internal cooling effectiveness, –
μ	dynamic viscosity, Pa s
ρ	density, kg m^{-3}
ρ'_{1c}	coolant density at film cooling hole exit, kg m^{-3}
σ	Stefan-Boltzmann constant, W m^{-2} K^{-4}
τ	transmittance of the IR window, –
τ'	modified transmittance of the IR window, –
τ_{flow}	time constant of the mainstream flow, s
τ_{model}	time constant of the test article, s
φ	internal surface effectiveness, –

Subscripts

1 to 4	plane numbers
1c	leading-circuit exit conditions
1h	mainstream inlet conditions
2c	cooling system inlet conditions
3c	coolant exit conditions
3h	mainstream exit conditions
3m	mixing layer exit conditions
a	system a
aw	adiabatic wall
A–C	averaging regions on Surface 1
bb	black body
c	internal coolant conditions
c2–c5	cooling channel Surfaces 2–5 (for identification of local surface boundary conditions)
case	case coolant plenum conditions
CP	calibration patch
c,in	cooling channel inlet conditions
D–F	averaging regions on Surface 5
e	entrained hot-gas conditions
E1 to E8	effects 1–8
h	mainstream conditions
hub	hub coolant plenum conditions
i	surface index
in	cooling system inlet conditions
j	effect index
	cooling film index
m	mixing layer conditions
max	maximum value
opt	IR window
PS	pressure surface
SS	suction surface
R	surrounding enclosure
ref	reference conditions
S	Surface
S1–S5	Surface 1–5
w	Wall
w1	(chapter 2) wall external surface conditions
	(chapter 3) external wall

w2	(chapter 2) wall internal surface conditions
	(chapter 3) internal wall
web	web separating modules in the lateral direction
WS	working section

Abbreviations

BC	boundary condition
CFD	computational fluid dynamics
CFVN	critical-flow venturi nozzle
CMPR	coolant-to-mainstream pressure ratio, –
ECAT	Engine Component Aerothermal
ECAT+	Second-Generation High-Temperature Engine Component Aerothermal
FOV	field of view
FSO	full-scale output
HPT NGV	high-pressure turbine nozzle guide vane
IISS	inferred instantaneously steady state
IR	Infrared
LE	leading edge
LES	large eddy simulation
LV	leading vane
NI	National Instruments
PID	proportional-integral-derivative
PLC	programmable logic computer
PR	domain inlet-to-exit total-to-static pressure ratio, –
PS	pressure surface
RANS	Reynolds Averaged Navier Stokes
RMS	root-mean-square
SS	suction surface
TE	trailing edge
TR	mainstream-to-coolant temperature ratio, –
TV	trailing vane

1. Introduction

In this section, the problem of scaling overall cooling effectiveness from conventional laboratory conditions to engine conditions is introduced. Gaps in existing literature and the research contribution provided in this thesis are outlined and guidance on scaling laboratory overall cooling effectiveness measurements is provided for turbine vane designers.

1.1 Previous literature

In modern gas turbine engines, combustor outlet temperature can be as high as 2000 K. High-pressure turbine (HPT) nozzle guide vanes (NGVs) are typically cooled with a combination of internal cooling and film cooling. In HPT NGV experiments, the measured surface temperatures are commonly expressed in non-dimensional form either as adiabatic film effectiveness, η_{aw} (typically when only film cooling is considered), or overall cooling effectiveness, θ (typically when both internal cooling and film cooling is considered). These parameters are commonly defined by

$$\eta_{\mathrm{aw}}(x) = \frac{T_{01\mathrm{h}} - T_{\mathrm{aw}}(x)}{T_{01\mathrm{h}} - T_{01\mathrm{c}}} \tag{1}$$

and,

$$\theta(x) = \frac{c_{\mathrm{h}}(x)T_{01\mathrm{h}} - T_{\mathrm{w1}}(x)}{c_{\mathrm{h}}(x)T_{01\mathrm{h}} - c_{\mathrm{c}}(x)T_{02\mathrm{c}}} \tag{2}$$

where $T_{01\mathrm{h}}$ is mainstream total temperature, $T_{\mathrm{aw}}(x)$ is adiabatic wall temperature, $T_{01\mathrm{c}}$ is coolant temperature at the cooling hole outlet, $c_{\mathrm{h}}(x)$ is mainstream recovery ratio, $T_{\mathrm{w1}}(x)$ is wall external surface temperature, $c_{\mathrm{c}}(x)$ is the local recovery ratio of a *hypothetical unmixed coolant stream with adiabatic wall condition* and total pressure and temperature equal to those of the coolant at plane 1, and $T_{02\mathrm{c}}$ is total temperature at the cooling system inlet.

Sets of non-dimensional groups for *adiabatic film effectinvess*, $\eta_{\mathrm{aw}}(x)$, have been developed by Ornano and Povey [4], Eckert [5], Baldauf and Scheurlen [6] and Greiner et al. [7]. Ornano

and Povey [4] emphasise the inclusion of temperature ratio (TR = T_{01h}/T_{02c}) as a non-dimensional group because of its significnace in determining adiabatic film effectivness. This point is returned to later.

There have been fewer studies of the scaling of the overall cooling effectiveness problem. Luque et al. [8] define the fully cooled gas turbine flow field in terms of the following 19 variables: $p_{01h}, \rho_{1h}, \mu_{1h}, k_{1h}, c_{p1h}, \gamma_{1h}, p_{02c}, \rho_{2c}, \mu_{2c}, k_{2c}, c_{p2c}, \gamma_{2c}, p_3, y, C_x, k_w, T_{01h}, T_{02c}, T_{w1}$. Here $p_{01h}, \rho_{1h}, \mu_{1h}, k_{1h}$ and γ_{1h} are total pressure, density, dynamic viscosity, thermal conductivity, specific heat capacity at constant pressure and ratio of specific heat capacities (c_p/c_v) of the mainstream at inlet conditions. Likewise, $p_{02c}, \rho_{2c}, \mu_{2c}, k_{2c}$ and γ_{2c} are the corresponding variables for coolant at the cooling channel inlet condition. The remaining variables are: the domain-exit static pressure, p_3; the surface-normal distance, y; the characteristic length (the plate surface length in chapters 2 and 3 and the axial chord of the HPT NGVs in chapter 4), C_x; and the wall thermal conductivity, k_w. Luque et al. [8] show that these can be reduced to 18 variables of which two are temperature differences: $p_{01h}, \rho_{1h}, \mu_{1h}, k_{1h}, c_{p1h}, \gamma_{1h}, p_{02c}, \rho_{2c}, \mu_{2c}, k_{2c}, c_{p2c}, \gamma_{2c}, p_3, y, C_x, k_w, T_{02c} - T_{\Re}, T_{w1} - T_{\Re}$, where $T_{\Re}$ is the recovery and redistribution temperature (this is explored further in a moment). These are subsequently reduced via a process of dimensional analysis to 13 non-dimensional quantities

$$\theta,\ \frac{C_x\sqrt{p_{01h}\rho_{1h}}}{\mu_{1h}},\ \frac{c_{p1h}\mu_{1h}}{k_{1h}},\ \frac{p_{02c}}{p_{01h}},\ \frac{p_{01h}}{p_3},\ \frac{\rho_{2c}}{\rho_{1h}},\ \frac{\mu_{2c}}{\mu_{1h}},\ \frac{k_{2c}}{k_{1h}},\ \frac{c_{p2c}}{c_{p1h}},\ \frac{y}{C_x},\ \frac{k_w}{k_{1h}},\ \gamma_{1h},\ \gamma_{2c}$$

The first five non-dimensional groups are, in turn: the overall cooling effectiveness, θ; the mainstream Reynolds number, Re_{1h}; the mainstream Prandtl number, Pr_{1h}; the coolant-to-mainstream pressure ratio, CMPR; and the domain pressure ratio, PR. The remaining seven groups have self-evident meanings based on the variables they contain.

For HPT NGV laboratory experiments, a commonly used value of mainstream-to-coolant temperature ratio is TR = 1.2 (see, for example, Kirollos et al. [9]). This is lower than the typical engine value for large civil aircraft of TR = 2.0. A general problem arises when TR is varied, in

that the non-dimensional groups of the system change in a complex inter-related way. It is common in experiments to attempt to match Re_{1h}, Pr_{1h}, CMPR and PR to engine conditions (see, for example, Kirollos et al. [9]). Geometric similarity constraints might also mean that y/C_x is matched. Although these five important non-dimensional groups might be matched, if TR is not matched to the engine condition, it is likely that the remaining seven non-dimensional groups will be unmatched. As overall cooling effectiveness is a function of all 12 remaining groups, it would be unnatural to expect it to take the same value as at the fully matched condition. If all 12 groups cannot be matched in practice between two situations of different TR, it is necessary to know how θ scales with the remaining 7 groups. Expressed in this way the problem is prima facie complex. The purpose of this thesis is to explore a practical way forward with this scaling problem.

One of the first studies to seriously explore the issue of scaling overall cooling effectiveness with TR is that of Luque et al. [8]. The key question addressed in this paper was the impact of compressibility, and in particular the issue of compressibility effects even with the apparently incompressible cooling system ducts on account of coupling with compressible (external) regions of the flow. This problem had not previously been addressed, and the authors proposed a new TR-invariant definition of overall cooling effectiveness, θ''' (see Results VIII), based on a *recovery and redistribution temperature*. Using a conjugate low-order thermal model, they demonstrated exact collapse of θ''' for the special case of varying TR *with all other non-dimensional groups fixed to reference values.* Luque et al. [10] also showed experimentally that for temperature ratios in the range $1.05 \leq \mathrm{TR} \leq 1.22$ a good collapse of experimental data could be achieved in practice. The result of Luque et al. [10] was likely only possible because the TR range was limited, and thus changes in other non-dimensional groups were small. Taken together, these papers demonstrate the conceptual importance of the recovery and redistribution temperature, but it is difficult to know how to use this result in practice over wide TR ranges in systems in which non-dimensional groups are allowed to *vary sympathetically* with TR. It is these real systems that are the subject of this thesis, and the key distinction with previous work.

Three approaches that could be used to study the impact of TR on overall cooling effectiveness or adiabatic film effectiveness are introduced. Examples of the first two are seen in literature and it is argued that the third is new. They are:

i) *Approach 1: perturb multiple non-dimensional groups simultaneously*. Identify all system variables and derive the set of non-dimensional groups that fully define θ or η_{aw}. Perturb several groups simultaneously and quantify and explain changes in θ or η_{aw} in terms of the combined effect of changes in each non-dimensional group. This process has been used extensively in the literature (often because the interrelationship between the non-dimensional groups is not understood) to attempt to understand the effect of particular non-dimensional groups on both θ and η_{aw} (see, for example, Greiner et al. [7] and [11–16]). This approach is not adopted in this thesis because it is very difficult to understand the individual contribution of each non-dimensional group and therefore the physical interpretation is unclear. The impact of one group on θ and η_{aw} is often contaminated with the effect of an uncontrolled change in another non-dimensional group.

ii) *Approach 2: perturb each non-dimensional group individually*. Identify all system variables and derive the set of non-dimensional groups that fully define θ or η_{aw}. Here, TR must be included as a non-dimensional group. Perturb each non-dimensional group individually, whilst remaining groups take unchanged values. Quantify and explain the change in effectiveness in terms of variations in each non-dimensional group, in isolation of all other non-dimensional groups. This is the approach used by Ornano and Povey [4] for the study of the impact of TR on η_{aw}. This is regarded as an important approach to best separate fundamental effects, but has two failings in practice for the problem of the impact of TR on θ: firstly it is unclear whether it is possible to find a choice of underlying variables that allow this process in practice; secondly, the set of non-dimensional groups is so large, it is arguable that non-sympathetic variation of all groups with TR renders the results so abstract as to be meaningless in practice.

iii) *Approach 3: virtual experiment with all variables and non-dimensional groups following TR sympathetically*. Describe system in terms of system variables, domain-global boundary conditions (BCs) and cooling system BCs (discussion later). Perform virtual experiments at a range of TRs with solutions fully converged, such that all system variables and non-dimensional groups vary sympathetically with TR. Output θ trends at different TRs. Explain results in terms of changes in underlying variables, underlying non-dimensional groups, or in terms of local surface boundary conditions (full discussion in chapters 2 and 3). This is the approach adopted in this thesis. It is argued that it is the only approach that is both tractable and provides results that are non-conflated with undesired changes in uncontrolled variables.

Examples of studies that have used Approach 1 are now briefly discussed, in order to provide context to this thesis. Sweeney and Rhodes [11] studied impact of CMPR on θ with fixed TR and PR. Albert and Bogard [12] studied the impact of blowing ratio with fixed density ratio on $\bar{\eta}_{\mathrm{aw}}$ and $\bar{\theta}$. Greiner et al. [7] numerically studied the impact of simultaneously varying multiple non-dimensional groups on η_{aw}. Rutledge et al. [13] showed numerically that, when blowing ratio ($u_{1\mathrm{c}}\rho_{1\mathrm{c}}/u_{1\mathrm{h}}\rho_{1\mathrm{h}}$), density ratio ($\rho_{1\mathrm{c}}/\rho_{1\mathrm{h}}$), momentum flux ratio ($\rho_{1\mathrm{c}}u_{1\mathrm{c}}^2/\rho_{1\mathrm{h}}u_{1\mathrm{h}}^2$) and velocity ratio ($u_{1\mathrm{c}}/u_{1\mathrm{h}}$) are fixed, η_{aw} is insensitive to variations in the remaining non-dimensional groups. Fischer et al. [14] and Mc Namara et al. [15] demonstrated experimentally that, when heat capacity flux ratio ($\rho_{1\mathrm{c}}u_{1\mathrm{c}}c_{p1\mathrm{c}}/\rho_{1\mathrm{h}}u_{1\mathrm{h}}c_{p1\mathrm{h}}$) is fixed and momentum flux ratio is constrained to the range $\rho_{1\mathrm{c}}u_{1\mathrm{c}}^2/\rho_{1\mathrm{h}}u_{1\mathrm{h}}^2 \leq 0.6$, η_{aw} is insensitive to variations in the remaining non-dimensional groups. Bryant and Rutledge [16] numerically studied the impact of η_{aw} on θ for matched $h_{\mathrm{m}}/h_{\mathrm{c}}$ and Biot number. Reservations about all studies that fall under Approach 1 have been expressed, and the studies discussed in this thesis (chapters 2–4) will follow the framework of Approach 3.

The only study known to the author that has used Approach 2 is that of Ornano and Povey [4]. The authors numerically studied the sensitivity of η_{aw} to momentum flux ratio, specific heat

capacity flux ratio, blowing ratio and TR. Specific BCs were chosen that allowed each non-dimensional group to be *individually* perturbed. The study was unique in this respect. This was important because individual results were not conflacted with undesired changes in other non-dimensional groups. The effect of each non-dimensional group was quantified in three distinct regions of increasing distance from the film cooling hole, which they refered to as binary, intermediate and mixed-out regions. The individual effect of each group on η_{aw} was explained with reference to the underlying physics. They showed that in the binary region the primary influence on η_{aw} was the momentum flux ratio, because it determines the initial trajectory of the cooling film. In the vicinity of the film cooling row, the mainstream and coolant flows are unmixed and therefore it is the flow *structure* that is of primary importance. Heat capacity flux ratio dominated changes in η_{aw} in the intermediate and mixed-out regions as this parameter determines the relative ability of the coolant and entrained hot-gas flow to store heat. Blowing ratio significantly affected η_{aw} in the intermediate region as it governs the *initial* velocity ratio (u_{1c}/u_{1h}) or volume flow rate ratio and therefore determines the rate of shear interaction between coolant and mainstream, which influences the heat capacity flux ratio *within* the mixing layer. The effect of TR, *when all other non-dimensional groups were fixed*, was second order and attributed to induced changes in the density of the mixing layer, which has the affect of changing the kinematic viscosity (which governs the extent of near-wall mixing) and the volume dilation (which determines the extent to which turbulent flow structures are pushed into the mainstream). It is believed that this work is important because it was the first study to truly isolate the *independent* effect of the key non-dimensional groups on η_{aw}. In many previous studies (Approach 1 studies) the co-dependence of the non-dimensional groups was not fully appreciated, rendering the results difficult to interpret.

The rationale for Approach 3, which is perhaps the most important point of this thesis, is now reiterated. In many studies that purport to study the effect of non-dimensional groups on θ or η_{aw}, there is confusion and ambiguity about which non-dimensional groups had controlled (deliberate)

or un-controlled (often unintended) variation. The problem is intrinsic in many experimental studies in that it is impossible in practice to vary one non-dimensional group whilst keeping all others constant. On close reading of the literature, it appears that in most experimental and numerical studies this problem was simply overlooked. Studies with uncontrolled variation of certain non-dimensional groups are referred to as Approach 1, and studies in this category are difficult to meaningfully interpret. Approach 2, in which individual non-dimensional groups are *individually varied*, may be desired from a very fundamental perspective, but this problem is intractable, and of limited practical use both because of the very large number of non-dimensional groups, and because *independent variation* of non-dimensional groups is non-representative of real systems. In Approach 3, all non-dimensional groups vary naturally and sympathetically with TR as they would in a real system. Approach 3 requires very careful attention to boundary conditions, a subject which is addressed in detail in chapter 2. The result of an Approach 3 study would be a characteristic of θ or η_{aw} with TR. The contributions to this characteristic can be decomposed in three primary ways, and it is advocated to do so in terms of so-called local-surface boundary conditions because this is the only approach that allows clear physical interpretation.

In this thesis the problem of scaling overall cooling effectiveness from conventional laboratory conditions to engine conditions is addressed. For quantifying changes in overall cooling effectiveness with TR, virtual experiments are performed using a 2D low-order network model for four very different HPT NGV cooling systems (three systems in chapter 2 and a fourth system in chapter 3). In order to explain the results, changes in θ are decomposed into the individual contributions associated with each local surface BC (see chapters 2 and 3). This follows the framework of Approach 3. Low-order model results are experimentally validated in a bespoke flat-plate test facility (see Naidu and Povey [17]) and using real-engine HPT NGVs in the ECAT+ facility (see Messenger et al. [18]).

It is demonstrated that, for a system with minimal coupling between external and internal walls (typical of HPT NGV PS and early SS; coupling is discussed in detail in chapter 3), moving between a typical engine temperature ratio for large civil aircraft of 2.0 to a conventional laboratory temperature ratio of 1.2 leads to a change in effectiveness of approximately -0.040 for a mean effectiveness of 0.500. This is equivalent to a -8% change. The rate of change accelerates with decreasing temperature ratio. This result is shown to be insensitive to the cooling system network and the type of domain-global BCs imposed, and the mean value of overall cooling effectiveness at the reference TR. When the changes due to both *absolute* temperature and combustion products are considered (the engine-to-rig scaling problem) the correction offset can be both positive or negative, with a sweet-spot at TR = 1.25, for which the correction offset is zero (for systems with minimal coupling between external and internal walls).

It is believed that this is the first study to systematically quantify and explain from first principles the effect of TR on overall cooling effectiveness. This is done for a number of cooling system networks and for domain-global boundary conditions relevant to laboratory and engine testing.

The research contribution of this thesis is broken down in more detail in the next section.

1.2 Research contribution

The research contribution of this thesis is separated into three chapters (chapters 2–4). The three chapters are briefly summarised below:

i) *Chapter 2: Fundamentals of scaling of overall cooling effectiveness with temperature ratio:* the impact of temperature ratio on overall cooling effectiveness is quantified using a bespoke low-order conjugate solver. The geometry of the network model is representative of real-engine HPT NGVs and conventional correlations for heat transfer coefficients and internal pressure loss are used, in order to capture the physics relevant to accurately predicting *changes* in overall cooling effectiveness with TR. Three internal cooling system

networks and two domain-global BCs are considered. In order to explain the results, the change in θ is separated into the individual change caused by each of five local surface BCs. The key results are: θ decreases with reducing TR; the change in θ is insensitive to the internal cooling architecture, the type of domain-global BC imposed, and the surface-averaged value of θ at the reference TR; the scaling effects associated with changes in absolute temperature and mainstream gas properties are significant; there is a sweet spot for which the overall rig-to-engine correction (when accounting for the effects of TR, absolute temperature and mainstream gas properties) is 0 at TR = 1.25; and the result is very sensitive to the particular definition of θ. The work presented in this chapter is the subject of a journal paper published in *ASME Journal of Turbomachinery* [1].

ii) *Chapter 3: Impact of temperature ratio on overall cooling effectiveness: experimental validation of a scaling theory:* the theory for scaling of overall cooling effectiveness with TR (developed in chapter 2) is independently applied to a fourth cooling system. Low-order-model predictions for the change in θ with TR are made and the results are experimentally validated in a flat-plate test facility (see Naidu and Povey [17]). Experiments are performed in the range $1.07 \leq TR \leq 1.62$ with domain-global BCs of fixed Re *and* fixed domain inlet-to-exit total-to-static pressure ratio, PR. The experimental and low-order-model results are broadly in agreement with the modelling work of chapter 2, however the magnitude of the change in θ is significantly reduced. It is shown that this is due to the presence of conducting webs separating the external and internal walls of the flat plate. The work presented in this chapter is the subject of a journal paper submitted to *ASME Journal of Turbomachinery* and is currently under peer review [2].

iii) *Chapter 4: Experimental study of the impact of temperature ratio on overall cooling effectiveness of high-pressure turbine nozzle guide vanes:* the theory for scaling of overall cooling effectiveness with TR (developed in chapter 2) is experimentally validated using real-engine HPT NGVs in the ECAT+ test facility. ECAT+ (see Messenger et al. [18]) is

the second generation of the original ECAT facility (see Kirollos et al. [9]) and allows testing at engine-realistic conditions of mainstream Reynolds number (Re) and Mach number (M); coolant-to-mainstream pressure ratio (CMPR); turbulence intensity (Tu); and mainstream-to-coolant temperature ratio (TR). Experiments are performed in the range $1.08 \leq TR \leq 1.89$ with domain-global BCs of fixed PR, with fixed atmospheric exit static pressure. These experiments were performed as part of the original commissioning campaign for the facility (discussed in detail in Messenger et al. [18]). The experimental results are taken to be broadly in accord with the low-order-model predictions and experimental results of chapters 1 and 2 (the general trend of θ is relatively flat with TR), however the results do not directly validate the theory for scaling of overall cooling effectiveness with TR. The work presented in this chapter is the subject of a complete paper draft, which will shortly be submitted to a journal [3].

1.3 Guidance for turbine vane designers

In this section, two procedures for scaling overall cooling effectiveness from conventional laboratory conditions to engine conditions are outlined. These scaling procedures facilitate prediction of HPT NGV metal temperatures and comparison of the performance of various HPT NGV cooling configurations at engine conditions. It is hoped that the scaling procedures outlined in this section will be of use to turbine vane designers in both academia and industry.

1.3.1 Scaling Procedure 1: Run ECAT at TR = 1.25

Scaling Procedure 1 involves testing HPT NGVs in an engine-realistic test facility at moderate temperature ratio (TR = 1.25). One such facility is the Engine Component Aerothermal (ECAT) Facility at the University of Oxford (see Kirollos et al. [9]). The facility should be operated with domain-global BC2 (fixed PR and fixed exit-Re) with the exit Reynolds number matched to engine conditions for the flight conditions considered (e.g. cruise or maximum-take-off

conditions). The ECAT facility allows for testing at a wide range of exit Reynolds numbers by independently adjusting the back pressure (see Michaud et al. [19]).

Scaling Procedure 1 is a simple and cost-effective approach that can be used to rapidly compare the engine performance of a wide range of HPT NGV cooling configurations. ECAT is a fully annular HPT NGV test facility, which allows rapid interchange of instrumentation (for example, infrared (IR) camera position) between tests due to its modular design. In order to demonstrate the efficiency of using the ECAT facility for comparing the engine performance of HPT NGV cooling configurations, consider that a single vane module build consists of 20 HPT NGV pairs, which means that 20 separate HPT NGV cooling configurations can be tested for every module build. Accounting for the time taken to split the facility and reposition the IR cameras between tests, a minimum of two days is required to test each vane pair (i.e. obtain pressure surface (PS) and suction surface (SS) overall cooling effectiveness measurements for a fixed CMPR or a range of CMPRs), meaning that a single module build of 20 vane pairs can be characterised within 40 days (in theory).

It is demonstrated in chapter 2, using theoretical arguments and conjugate low-order-modelling techniques, that the engine value of overall cooling effectiveness is obtained when ECAT is operated at a temperature ratio of TR = 1.25. This result, illustrated in Figure 36, is obtained by superimposing three effects: moving from the reference TR (TR = 2.0) to lower-than-reference TR (see Figure 13); scaling for the effects of absolute temperature (see Figure 33); and scaling for the effects of combustion product gas properties (see Figure 34). The derived scaling chart Figure 36 is derived for system 1 (see Figure 5) with domain-global BC1 (fixed PR with fixed atmospheric exit pressure), however it is demonstrated that this result is insensitive to the choice of domain-global boundary conditions (see Figure 28), the mean value of overall cooling effectiveness at the reference TR (see Figure 30) and the details of the internal cooling system network (see Figure 31). It is difficult to quantify the (small) residual (i.e. the difference between the predicted and actual surface-averaged effectiveness at engine conditions) in this process when results are scaled according to Scaling Procedure 1. By considering the approximate spread of

surface-averaged results for $\Delta\theta^{TR=1.2}$ for two domain-global BCs (8%), mean overall cooling effectiveness values in the range $0.4 < \bar{\theta}^{TR=2.0} < 0.6$ i.e. the usual HPT NGV range (9%) and three very different internal cooling system networks (2%) it is estimated that the residual is no more than about ±0.01 for conventional HPT NGV cooling configurations when operating ECAT at TR = 1.25. This corresponds to a residual of about 2% (for an effectiveness of 0.5), which is equal to approximately 10 K at typical engine conditions for large civil aircraft.

An advantage of Scaling Procedure 1 is its simplicity, as it makes use of a generally-applicable scaling chart provided in this thesis (Figure 35). A disadvantage of this approach might be that the residual (i.e. the difference between the predicted and actual surface-averaged effectiveness at engine conditions)—due to the (weak) dependence of the final engine-to-rig correction on the applied domain-global BCs and cooling system geometry—might be larger than that associated with an alternative approach, proposed in section 1.3.2.

1.3.2 Scaling Procedure 2: Run ECAT or ECAT+ at TR determined by calibrated low-order network model

Scaling Procedure 2 involves a similar process to Scaling Procedure 1, however in this case the experiments are complimented by a calibrated low-order network model (of the style introduced in chapter 3), which is used to evaluate the required operating temperature ratio for the facility. This procedure is outlined below:

i) Develop bespoke conjugate network model representing the particular HPT NGV cooling configuration. This model could be developed using MATLAB (instructions for developing a low-order network model in MATLAB are provided in chapters 2 and 3) or a proprietary in-house conjugate heat-transfer tool.

ii) Test HPT NGVs in an engine-realistic test facility at temperature ratios in the range $1.0 < TR \leq 2.0$. These experiments could be performed in the Second-Generation High-Temperature Engine Component Aerothermal (ECAT+) Facility at the University of Oxford (see Messenger et al. [18]).

iii) Calibrate model against experimental data. Techniques for the required calibration are developed in section 3.8.4.

iv) Run calibrated model at TR in the range $1.0 < \mathrm{TR} \leq 2.0$ to evaluate the engine-to-rig correction characteristic $\overline{\Delta\theta}_{\mathrm{E\text{-}R}} = f(\mathrm{TR})$. An example of such a characteristic is shown in Figure 36.

v) Determine TR^* which satisfies $\overline{\Delta\theta}_{\mathrm{E\text{-}R}} = f(\mathrm{TR}^*) = 0$.

vi) Run ECAT or ECAT+ at TR^*. The measured overall cooling effectiveness value is equal to the corresponding engine value.

A block diagram for this scaling procedure is provided in Figure 1.

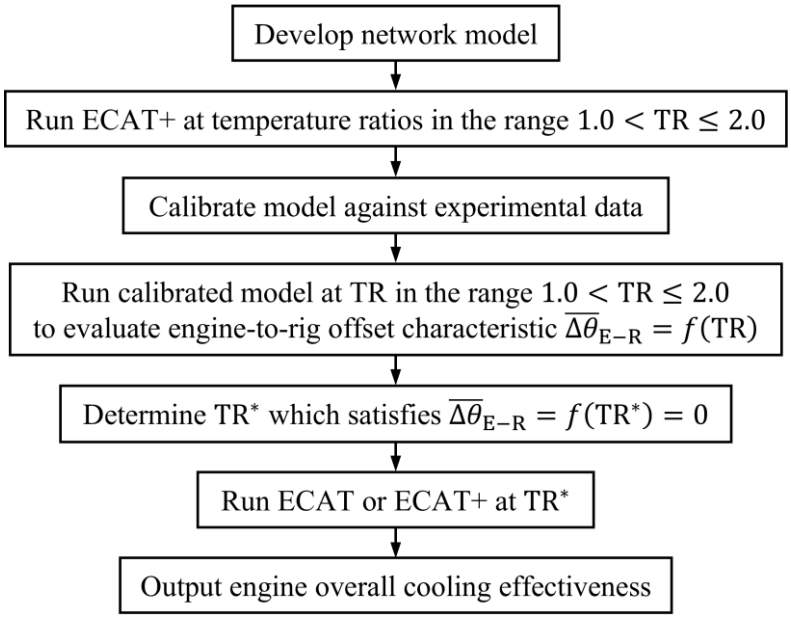

Figure 1: Block-diagram representation of Scaling Procedure 2.

An advantage of Scaling Procedure 2 might be that it has a lower residual associated with it than Scaling Procedure 1, and therefore may lead to a closer match between the predicted and actual engine overall cooling effectiveness values. This is because the scaling chart is derived using a bespoke numerical solver tailored to the particular cooling system geometry considered and run with the required domain-global boundary conditions. A disadvantage might be that the process

is more involved than that of Scaling Procedure 1, as a separate network model must be developed and calibrated to complement the experiments.

2. Fundamentals of scaling of overall cooling effectiveness with temperature ratio

In this chapter, the relationship between overall cooling effectiveness (or so-called metal effectiveness) and mainstream-to-coolant total temperature ratio (TR), for typical high-pressure turbine nozzle guide vane (HPT NGV) cooling systems, is studied. The temperature ratio range studied is that between conventional laboratory conditions (TR ≅ 1.2) and engine conditions typical of large civil aircraft (TR ≅ 2.0). The purpose is twofold: firstly, to quantify the difference in overall cooling effectiveness between conventional laboratory and engine conditions of temperature ratio; and—secondly—to understand the physical bases for the difference, separated in terms of changes in five local surface boundary conditions. This is done using a bespoke conjugate thermal network model which includes models of both the internal cooling and the external film cooling layer. Three typical cooling architectures are studied. The results allow comparison and scaling between situations at different conditions of temperature ratio.

2.1 Introduction

In this chapter, the change in overall cooling effectiveness with TR is quantified and explained for typical HPT NGV cooling systems. A cross-section diagram (cut taken through the midspan) for such a system is shown in Figure 2. A low-order conjugate thermal network model, which includes physics-based models of both the internal cooling and the external film cooling layer, and realistic gas and wall thermal properties, is used for this study. Predictions are performed for converged conjugate thermal systems at a range of temperature ratios, with boundary conditions set such that *all non-dimensional groups vary simultaneously and sympathetically with TR as they would in a real environment* subject to the same boundary conditions. The resulting trends of θ with TR represent the natural change of the entire thermal system with TR, subject to particular boundary conditions. Contributions to the change in θ with TR into effects arising from five *local-*

surface boundary conditions (discussion later) are decomposed. The five boundary conditions are: effectiveness of the mixing layer, η_{ML}; local through-wall-average wall thermal conductivity, $\overline{k}_w$; external heat transfer coefficient, h_m; internal heat transfer coefficient, h_c; and internal cooling effectiveness, λ. These five parameters form a complete set that describe θ for a zero-dimensional system. This is referred to as Approach 3.

Under Approach 3, instead of attempting to decompose the change in θ with TR in terms of these five local surface boundary conditions, one could attempt to do so in terms of either the underlying dimensional variables, or the resulting non-dimensional groups. This would be practically challenging because of the number of variables in each case and would give rise to complex and un-intuitive results non open to meaningful interpretation.

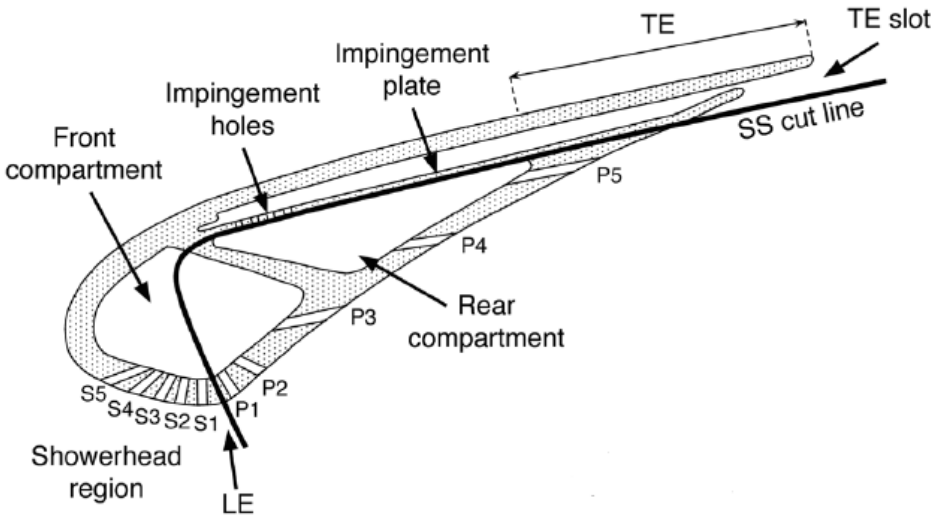

Figure 2: Cross-section diagram of a typical HPT NGV cooling system. Cut is taken through the midspan. Figure taken from Kirollos and Povey [20].

2.2 Three groups of boundary conditions

Before describing details of the numerical network model three groups of boundary condition are defined, which are referred to as *domain-global* BCs, *cooling system* BCs, and *local surface* BCs. A schematic of the domain is shown in Figure 3 with the boundary conditions marked.

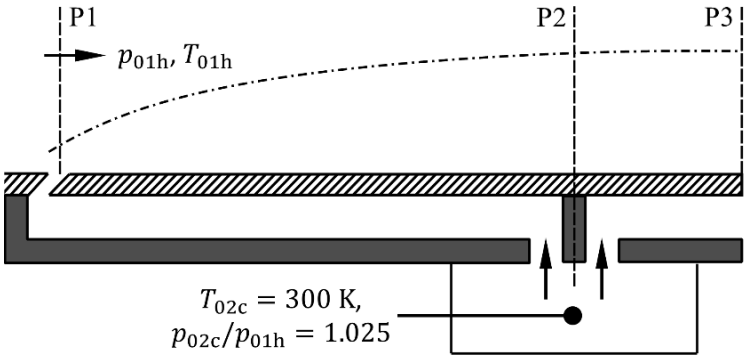

Figure 3: Schematic of cooling system BCs and locations of planes 1–3.

Three planes of interest are noted: plane 1, the inlet plane and point of coolant injection into the mainstream; plane 2, the inlet to the reverse-pass coolant duct; plane 3, the outlet plane. The three groups of boundary conditions are illustrated in Figure 4.

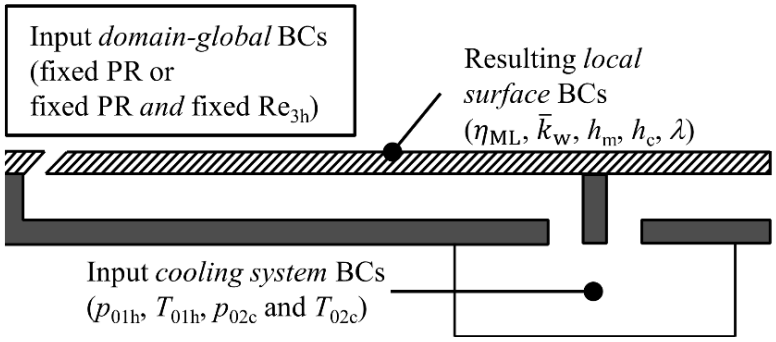

Figure 4: Schematic of the three groups of boundary conditions.

It is emphasised that the results of this study have meaning only in the context of a precisely-defined set of boundary conditions—another key point of this chapter.

Firstly, the term *domain-global BCs* refers to the boundary conditions on the mainstream flow for the implied NGV row, i.e. the conditions established in a particular experimental test facility or engine test. Studies are performed for two types of domain-global BC, which represent the common ways of running experiments, namely:

i) Fixed domain inlet-to-exit total-to-static pressure ratio, PR = 1.75, with fixed atmospheric exit pressure, p_3 = 1.0 bar. This is typical of facilities without independent backpressure control, and implies a fixed inlet total pressure (p_{01h} = 1.75 bar). With varying TR, this

implies variation in exit—and therefore surface—Reynolds number Re_{3h} by a factor of approximately 2.0 across the TR range tested (for TR = 2.0, $\mathrm{Re}_{3h} = 1.05\times10^6$; for TR = 1.2, $\mathrm{Re}_{3h} = 1.97\times10^6$).

ii) Fixed exit Reynolds number (typical of facilities with independent back-pressure control) and fixed PR. This implies inlet pressure variation in the range 0.93−1.75 bar (fixed Re_{3h}) for TR in the range $1.2 \leq \mathrm{TR} \leq 2.0$.

It is noted that, to compare trends of results subject to the two methods for setting domain-global boundary condition, one needs to choose a condition at which to match Re_{3h}. This is done, somewhat arbitrarily, at the reference temperature ratio conditions, TR = 2.0.

Second, *cooling system BCs* refer to the boundary conditions for the cooling system, that in conjunction with the domain-global BCs, set the coolant-to-mainstream pressure ratio (CMPR) and TR. Here those boundary conditions are the coolant inlet total pressure (p_{02c}) and total temperature (T_{02c}) and the corresponding values for the mainstream (p_{01h} and T_{01h}) that satisfy a particular domain-global BC approach.

In all simulations the coolant inlet total temperature is set to T_{02c} = 300 K. To achieve TR in the range $1.2 \leq \mathrm{TR} \leq 2.0$, the mainstream total temperature is varied in the range 360−600 K. CMPR (based on inlet values) has a fixed value of 1.025 for all simulations. To first order, this means that coolant-to-mainstream momentum flux ratio ($\rho_{1c}u_{1c}^2/\rho_{1h}u_{1h}^2$) is the same between simulations at different TR. Second order differences arise, however, due to, for example: changes in duct pressure loss that reduce the coolant total pressure at the coolant hole inlet; changes due to real-gas-effects in the mainstream and coolant ratios of specific heat capacities (γ_h and γ_c) that affect (very slightly) the local external Mach number distribution even for fixed domain-global PR. Nearly-constant coolant-to-mainstream momentum flux ratio across a wide range of TR implies a fairly wide range of heat capacity flow rate ratio, $\dot{m}_{1c}c_{p1c}/\dot{m}_{1h}c_{p01h}$: essentially, if $\rho_{1c}u_{1c}^2/\rho_{1h}u_{1h}^2$ is approximately constant with TR, but ρ_{1c}/ρ_{1h} varies widely with TR, then the term

$\rho_{1c}u_{1c}/\rho_{1h}u_{1h}$—which appears in the heat capacity flow rate ratio—must also vary widely. This change in heat capacity flow rate ratio is of primary importance in this system because it changes the effectiveness of the mixing layer. This effect is discussed in detail in Ornano and Povey [4]. Secondary effects arise due to changes in, for example: internal heat transfer coefficient driven by changes in channel velocity and local fluid properties.

Domain-global and cooling system boundary conditions at the reference TR, the resulting mass flow rate ratios, and geometric details of the system are summarized in Table 1.

Table 1: Domain-global and cooling system boundary conditions at the reference TR, resulting mass flow rate ratios, and geometric details of the system.

Boundary/operating conditions at reference TR		Value
Coolant plenum total temperature, T_{02c} (K)		300
Mainstream total temperature, T_{01h} (K)		600
Mainstream-to-coolant TR, (–)		2.0
Mainstream inlet Mach number, M_{1h} (–)		0.30
Mainstream exit Mach number, M_{3h} (–)		0.93
Coolant plenum total pressure, p_{02c} (bar)		1.79
Mainstream inlet total pressure, p_{01h} (bar)		1.75
Exit static pressure, p_3 (bar)		1.0
CMPR, p_{02c}/p_{01h} (–)		1.025
Coolant-to-mainstream mass flow rate ratio for reverse-pass cooling duct $\dot{m}_{1c}/\dot{m}_{1h}$ (–)	System 1	0.081
	System 2	0.084
	System 3	0.081
Coolant-to-mainstream mass flow rate ratio for the TE slot, $\dot{m}_{3c}/\dot{m}_{1h}$ (–)		0.020
Plate surface length, C_x (mm)		100
Plate width, w (m)		1
Wall thickness, t_w (mm)		1
Mainstream exit Re number, Re_{3h} (–)		1.05×10^6

Boundary conditions are chosen to be representative of those commonly established in lab experiments (see chapter 4). Conditions for all three cooling system networks are identical at the reference TR, with the exception of the coolant-to-mainstream mass flow rate ratios for the leading circuit, which take values within 4.1% of each other. These small differences arise because

of small differences in cooling mass flow caused by differences in pressure drop between the cooling system inlet and exit.

Finally, the local surface BCs refer to the local boundary conditions that *result* on the surface in a converged simulation. Here the surface distributions of five parameters are specifically referred to: effectiveness of the mixing layer, η_{ML}; local through-wall-average wall thermal conductivity, $\bar{k}_{\mathrm{w}}$; external heat transfer coefficient, h_{m}; internal heat transfer coefficient, h_{c}; and internal cooling effectiveness, λ. This choice of boundary conditions is justified in section 2.3.6.

2.3 Five local surface boundary conditions

In this section, the five *local-surface BCs* referenced in this chapter are defined and justification for their choice is provided.

2.3.1 Effectiveness of the mixing layer

Effectiveness of the mixing layer is the non-dimensional mixing layer recovery temperature or, equivalently, the non-dimensional driving temperature for heat transfer. This is defined by

$$\eta_{\mathrm{ML}}(x) = \frac{c_{\mathrm{h}}(x)T_{01\mathrm{h}} - c_{\mathrm{m}}(x)T_{0\mathrm{m}}(x)}{c_{\mathrm{h}}(x)T_{01\mathrm{h}} - c_{\mathrm{c}}(x)T_{02\mathrm{c}}} \tag{3}$$

where $T_{0\mathrm{m}}(x)$ is the mixing layer total temperature and $c_{\mathrm{m}}(x)$ is the mixing layer local recovery ratio. Recovery ratios are calculated using the stream conditions (of total pressure and temperature, gas properties, and a local static pressure calculated by treating the boundary of the mixing layer (or, for $c_{\mathrm{c}}(x)$, the boundary of the unmixed coolant stream) as a *slip line*, zero static pressure gradient in the wall-normal (or, approximately, slip-line-normal) direction. This process is discussed in more detail in the context of the numerical solver). An isentropic flow assumption is taken for Mach number, and the turbulent flow correlation for recovery factor, $r(x) = \mathrm{Pr}^{1/3}(x)$, is assumed. The validity of this correlation outside the conventional laboratory range ($T(x) > 600$ K) is unknown and further discussion of appropriate correlations for recovery factor at high absolute temperatures is encouraged. By defining Eq. (3) in this way—with individual local

recovery ratios for each term—η_{ML} is constrained between 0 and 1. This is so because of the following theoretically limiting temperatures: a theoretical maximum external temperature of $c_{\mathrm{h}}(x)T_{01\mathrm{h}}$ in the case of no cooling flow and an adiabatic wall; a theoretical minimum external temperature of $c_{\mathrm{c}}(x)T_{02\mathrm{c}}$ for the case of perfect cooling (no entrained hot gas) and an adiabatic wall.

2.3.2 Local through-wall-average wall thermal conductivity

Wall thermal conductivity, $k_{\mathrm{w}}(x,y)$, is evaluated at the local wall temperature, $T_{\mathrm{w}}(x,y)$. The local through-wall-average wall thermal conductivity is defined by

$$\bar{k}_{\mathrm{w}}(x,y) = \frac{1}{t_{\mathrm{w}}}\int_0^{t_{\mathrm{w}}} k_{\mathrm{w}}(x,y)\mathrm{d}y \tag{4}$$

where t_{w} is wall thickness.

2.3.3 External heat transfer coefficient

The local external heat transfer coefficient is based on local fluid properties and length scale, and is defined by

$$h_{\mathrm{m}}(x) = \frac{\mathrm{Nu}_{\mathrm{m}}(x)k_{\mathrm{m}}(x)}{x} \tag{5}$$

where $\mathrm{Nu}_{\mathrm{m}}(x)$ is the local external Nusselt number distribution and $k_{\mathrm{m}}(x)$ and is the local thermal conductivity of the gas in the mixing layer. A correlation for this is presented later.

2.3.4 Internal heat transfer coefficient

In like manner, the local internal (cooling-channel) heat transfer coefficient is defined by

$$h_{\mathrm{c}}(x) = \frac{\mathrm{Nu}_{\mathrm{c}}(x)k_{\mathrm{c}}(x)}{D(x)} \tag{6}$$

where $\mathrm{Nu}_{\mathrm{c}}(x)$ is the local cooling channel Nusselt number and $k_{\mathrm{c}}(x)$ the local thermal conductivity of the gas in the coolant channel. $D(x)$ is hydraulic diameter of the internal cooling channel. A correlation is presented for this later.

2.3.5 Internal cooling effectiveness

The internal cooling effectiveness is the non-dimensional internal coolant temperature defined by

$$\lambda(x) = \frac{c_{\mathrm{h}}(x)T_{01\mathrm{h}} - T_{0\mathrm{c}}(x)}{c_{\mathrm{h}}(x)T_{01\mathrm{h}} - c_{\mathrm{c}}(x)T_{02\mathrm{c}}} \tag{7}$$

where $T_{0\mathrm{c}}(x)$ is the local internal coolant temperature, and where all other variables have been defined. In the absence of lateral conduction, defining $\lambda(x)$ in this way constrains $\lambda(x)$ between 0 and 1. This is so because of the following theoretically limiting temperatures: a theoretical maximum *local* internal coolant temperature equal to the local mainstream recovery temperature (i.e. $T_{0\mathrm{c}}(x) = c_{\mathrm{h}}(x)T_{01\mathrm{h}}$); a theoretical minimum local internal coolant temperature equal to the local recovery temperature of a *hypothetical unmixed coolant stream with adiabatic wall condition* and total pressure and temperature equal to those of the coolant at plane 2 (i.e. $T_{0\mathrm{c}}(x) = c_{\mathrm{c}}(x)T_{02\mathrm{c}}$). Both situations would arise in a system with very low cooling flow and high through-wall condition.

2.3.6 Justification for choice of local surface boundary conditions

For a network with 1D conduction heat transfer in the through-wall direction (no lateral conduction), wall external surface temperature, T_{w1}, is given by

$$T_{\mathrm{w1}} = c_{\mathrm{m}}T_{0\mathrm{m}} - \left(1 + \frac{h_{\mathrm{m}}}{h_{\mathrm{c}}} + \frac{h_{\mathrm{m}}t_{\mathrm{w}}}{\bar{k}_{\mathrm{w}}}\right)^{-1} \times (c_{\mathrm{m}}T_{0\mathrm{m}} - T_{0\mathrm{c}}) \tag{8}$$

This is derived by equating the following heat transfer rate terms: convection from mixing layer to external surface; conduction in the through-wall direction; and convection from internal wall to coolant. By substituting Eq. (2), (3) and (8) into Eq. (9) one arrives at the following expression for overall cooling effectiveness for systems with 1D conduction

$$\theta = \eta_{\mathrm{ML}} + \frac{\lambda - \eta_{\mathrm{ML}}}{1 + \frac{h_{\mathrm{m}}}{h_{\mathrm{c}}} + \mathrm{Bi}} \tag{9}$$

where Biot number is the ratio of wall thermal resistance to the effective convective thermal resistance, which is defined by

$$\mathrm{Bi}(x) = \frac{h_\mathrm{m}(x)t_\mathrm{w}}{\bar{k}_\mathrm{w}(x)} \tag{10}$$

By rearrangement this is equivalent to

$$\theta = \eta_\mathrm{ML} + \frac{\lambda - \eta_\mathrm{ML}}{1 + h_\mathrm{m}\left(\frac{1}{h_\mathrm{c}} + \frac{t_\mathrm{w}}{\bar{k}_\mathrm{w}}\right)} \tag{11}$$

It is observed that, for an incompressible 1D system, overall cooling effectiveness has the functional relationship $\theta = f(\eta_\mathrm{ML}, \bar{k}_\mathrm{w}, h_\mathrm{m}, h_\mathrm{c}, \lambda)$. In this chapter, lateral conduction terms are assumed to be at least an order of magnitude smaller than through-wall conduction terms (scale disparity) and are therefore omitted from the analysis. With this assumption in mind, it can be argued that a decomposition of changes in θ with TR due to changes in each local surface BC—in isolation of changes in other local surface BCs—is sufficiently true for real systems that it can be used to give meaningful physical insight into the underlying mechanisms driving the relationship between θ and TR. It is shown later, by a linear-superposition check-sum approach, that this simplification appears valid with reasonable accuracy for the actual systems presented in this chapter. In chapter 3, a more complex system is considered, in which the adiabatic constraint on the internal wall is relaxed and in which conducting webs act to couple the external and internal walls. This latter system is shown to be fully described by eight local surface boundary conditions (one heat transfer coefficient for each of five surfaces).

2.4 Cooling system network definitions

The HPT NGV is modelled as a flat plate with two internal coolant feeds, and ejection from a single row of film cooling holes located at a notional leading-edge point ($x/C_x = 0$; plane 1; see Figure 3) and from a trailing edge (TE) slot ($x/C_x = 0.75$; plane 2; see Figure 3). The TE slot feed is forward-pass (flowing in the same direction as the external flow) in the range $0.75 \leq x/C_x < 1.00$. In the leading region of the plate ($0 \leq x/C_x < 0.75$) the internal cooling flow is of reverse-pass design (see Kirollos and Povey [20]).

Three different systems are modelled:

i) System 1, point-inlet reverse-pass. This is shown in Figure 5a. In this system there is a single feed and incremental heat pick-up along the channel. This system maximises the axial temperature variation of the coolant flow, but minimises the axial variation in wall temperature (see Kirollos and Povey [20]). Such a system is interesting both because it approaches a theoretical optimum for a cooling network, but also because it has complex coupling between internal cooling flow and the external mixing layer.

ii) System 2, distributed-inlet reverse-pass. This is shown in Figure 5b. This system is one in which there is both incremental heat pick up in the flow direction, but also mass flow addition. The system can be thought of as representing a more open internal cooling system; i.e. unguided reverse-pass flow in the direction of the sink (coolant outlet).

iii) System 3, fully-mixed reverse-pass. This is shown in Figure 5c. This is a theoretical system, not possible in practice, in which the temperature in the entire cooling duct is constant, and set to the mid-point of the inlet and outlet temperature. Conservation equations taking into account inlet flow, outlet flow, and heat transfer are satisfied for the duct as a single entity. This represents extreme (beyond physical limit) mixing of the internal cooling flow.

The purpose of studying three systems is to test the sensitivity of the general result to the specific cooling system network. The correlations for internal heat transfer coefficients and internal cooling pressure loss are discussed in sections 2.5.1 and 2.5.2.

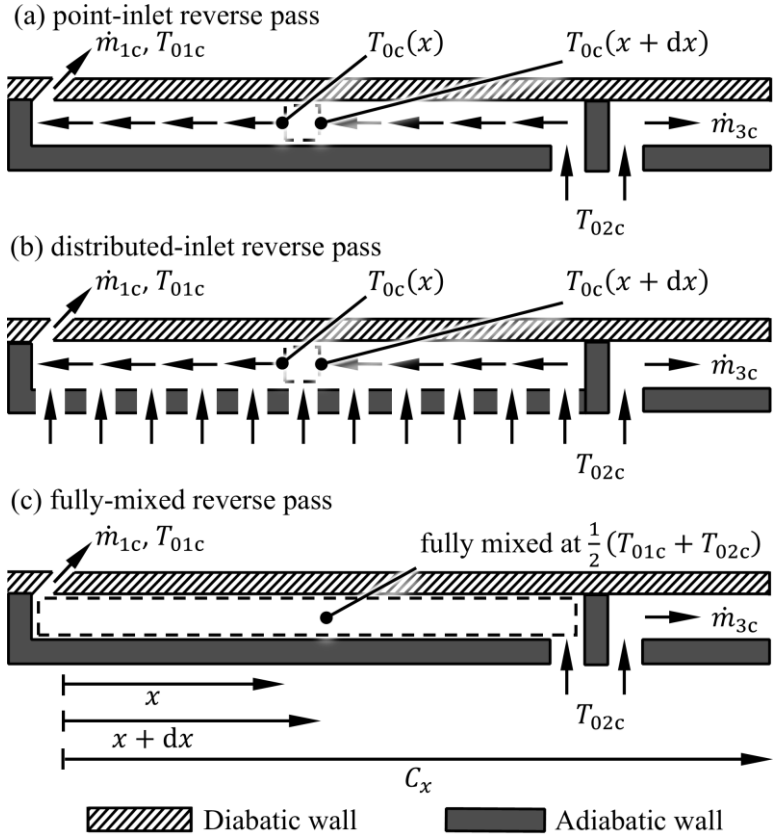

Figure 5: Cooling systems considered in chapter 2: (a) system 1, point-inlet reverse-pass; (b) system 2, distributed-inlet reverse-pass; (c) system 3, fully-mixed reverse-pass.

2.5 Details of the numerical solver

This study was performed with a bespoke conjugate thermal solver which includes models of both the internal cooling and the external film cooling layer. The solver, which was developed using the low-order-modelling techniques of Kirollos and Povey [20], has the facility to solve any cooling network of injection and ejection points for internal and external cooling flows. For the internal cooling flow, the solver takes account of heat transfer between the cooling flow and the wall, and of total pressure loss along the channels. These combined effects lead to complex coupling of heat and mass flows in the system because of the effects of: volume dilation (temperature and pressure change); changes in internal-channel Re and Nu; changes in channel total pressure loss; changes in cooling channel mass flow rate. The external film cooling is modelled using a control-volume-style entrainment-based model of a mixing layer. These models

are described in detail in this section. A block diagram describing the algorithm used by the numerical solver to evaluate the converged solution is provided in Figure 6.

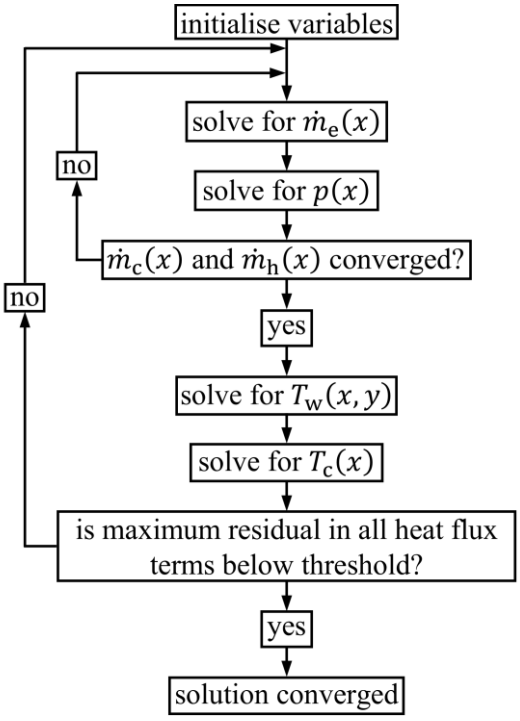

Figure 6: Block-diagram representation of low-order network-model algorithm.

2.5.1 Correlations for internal heat transfer coefficient

Local internal heat transfer coefficient, $h_c(x)$ depends on local temperature-dependant fluid properties, $h_c(x) = f(c_{pc}, k_c, u_c, \mu_c, \rho_c)$, where $c_{pc}(x)$, $k_c(x)$, $u_c(x)$, $\mu_c(x)$ and $\rho_c(x)$ are local values of specific heat capacity, thermal conductivity, channel velocity, dynamic viscosity and density of the internal coolant. Fluid properties are evaluated at each cooling-channel location for each iteration step of the solution using the evaluated distribution of $T_{0c}(x)$ at the corresponding solution step. This allows pressure loss and internal heat transfer coefficients to be updated as the numerical solver is run to convergence. The choice of duct heights (H_{1c} for the reverse-pass cooling duct and H_{3c} for the TE slot) and cross-sectional areas of the film cooling row and TE slot (A_{1c} and A_{3c}, respectively) were chosen to be representative of typical cooling systems, and to—in conjunction with other BCs—give target values of surface-average cooling effectiveness

($\bar{\theta} = 0.5$) and coolant-to-mainstream mass flow rate ratios ($\dot{m}_{1c}/\dot{m}_{1h} = 0.081$ and $\dot{m}_{3c}/\dot{m}_{1h} = 0.020$).

The specific correlations used for cooling duct heat transfer coefficients and pressure loss are now considered.

The local cooling-channel Reynolds number is defined by

$$\mathrm{Re}_c(x) = \frac{\rho_c(x) u_c(x) D(x)}{\mu_c(x)} \tag{12}$$

where $D(x)$ is hydraulic diameter of the duct. D_{1c} is the leading-circuit hydraulic diameter and D_{3c} is the TE circuit hydraulic diameter. Local cooling-channel Prandtl number is defined by

$$\mathrm{Pr}_c(x) = \frac{c_{pc}(x)\mu_c(x)}{k_c(x)} \tag{13}$$

The local cooling-channel Nusselt number is then given by the Dittus-Boelter equation (see McAdams [21]; leading constant multiplication term quoted to two significant figures).

$$\mathrm{Nu}_c(x) = 0.023 \mathrm{Re}_c(x)^{0.8} \mathrm{Pr}_c(x)^{0.4} \tag{14}$$

Local cooling-channel heat transfer coefficient is then defined by

$$h_c(x) = \frac{\mathrm{Nu}_c(x) k_c(x)}{D(x)} \tag{15}$$

Correlation (15) was used for the TE-circuit flows of all three systems, and for the leading-circuit (reverse-pass) flows of system 1 and system 3. For the leading circuit of system 2, correlation (14) was augmented by applying a multiplication factor, $K(x)$

$$\mathrm{Nu}_c(x) = 0.023 K(x) \mathrm{Re}_c(x)^{0.8} \mathrm{Pr}_c(x)^{0.4} \tag{16}$$

where $K(x)$ was set to give constant Nu *for the reference TR* (i.e. $\mathrm{Nu}_c/\mathrm{Nu}_c(0) = 1$ for $0 \le x/C_x < 0.75$) with the value set to that associated with the fluid conditions *at duct outlet*. The same distribution $K(x)$ was then used at non-reference TR, with terms $\mathrm{Re}_c^{0.8}(x)$ and $\mathrm{Pr}_c^{0.4}(x)$ being

calculated based on local fluid properties and local velocity. This was an artificial way of setting constant Nu at the reference condition, with *physically meaningful variation with TR* away from the reference condition. For the distributed-inlet flow network of system 2, primary interest is in different coupling of the system (from system 1 and system 3) due to different mass flow rate distribution, and therefore any physically-based variation in the system serves the purpose of this chapter. The resulting distribution $K(x)$ is shown in Figure 7.

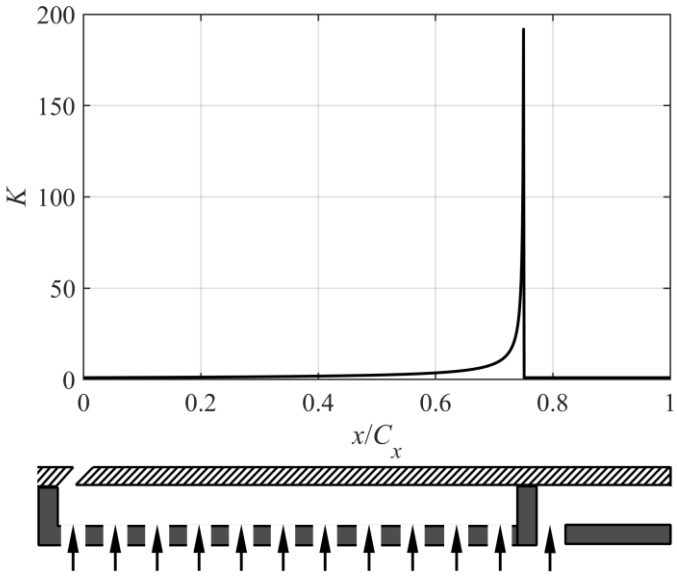

Figure 7: Distribution of multiplication factor, $K(x)$, used in correlation (16) for system 2.

Distributions $h_c(x)$ for all three systems are presented and discussed in section 2.6.

2.5.2 Correlations for cooling channel pressure loss

Friction coefficient, $f_c(x)$ was evaluated from the smooth-pipe Moody chart correlations (see, for example, Bergman et al. [22]) for fully developed turbulent flow. Considering low-order network model simulations for both domain-global boundary conditions and system 1, local cooling-channel Reynolds number varies in the range $1.17\times10^4 \le \mathrm{Re}_c \le 2.21\times10^4$ for temperature ratios in the range $1.2 \le \mathrm{TR} \le 2.0$. The applicability of smooth-pipe correlations for HPT NGVs is unknown however the choice of these correlations is justified on the basis that *changes in surface-averaged overall cooling effectiveness with TR* are the primary subject of this chapter and that any sensible correlation is likely to be sufficient for accurately quantifying these changes.

For the leading circuit, total pressure gradient at position x, $\mathrm{d}p_{0\mathrm{c}}(x)/\mathrm{d}x$, was evaluated using the *Moody friction factor equation*

$$\frac{\mathrm{d}p_{0\mathrm{c}}(x)}{\mathrm{d}x} = \frac{4f_{\mathrm{c}}(x)}{D_{1\mathrm{c}}}\frac{1}{2}u_{\mathrm{c}}(x)^2 \tag{17}$$

where u_{c} is the local channel velocity given by

$$u_{\mathrm{c}}(x) = \frac{\dot{m}_{\mathrm{c}}(x)}{\rho_{\mathrm{c}}(x)wH_{1\mathrm{c}}} \tag{18}$$

where $\rho_{\mathrm{c}}(x)$ is the local density of internal cooling flow and w is plate width. This correlation is used for systems 1–3.

Analysis of the TE circuit followed identical principles (hydraulic diameter $D_{3\mathrm{c}}$; duct height $H_{3\mathrm{c}}$).

2.5.3 Correlations for external heat transfer coefficient

The local external heat transfer coefficient was evaluated using flat plate heat transfer correlations using the local fluid properties of the external mixing layer (this concept is discussed later). Local external Reynolds number is defined by

$$\mathrm{Re}_{\mathrm{m}}(x) = \frac{\rho_{\mathrm{m}}(x)u_{\mathrm{m}}(x)x}{\mu_{\mathrm{m}}(x)} \tag{19}$$

where $\rho_{\mathrm{m}}(x)$ is the local density in the mixing layer, and $\mu_{\mathrm{m}}(x)$ is the local dynamic viscosity. The local velocity of the mixing layer, $u_{\mathrm{m}}(x)$, is that obtained when a flow of the mass-mean total pressure of the mixing layer is expanded isentropically to the static pressure set by an isentropic mainstream flow. Local external Prandtl number is defined by

$$\mathrm{Pr}_{\mathrm{m}}(x) = \frac{c_{p\mathrm{m}}(x)\mu_{\mathrm{m}}(x)}{k_{\mathrm{m}}(x)} \tag{20}$$

where $c_{p\mathrm{m}}(x)$ is the local specific heat capacity at constant pressure in the mixing layer, and $k_{\mathrm{m}}(x)$ is the local thermal conductivity.

For the Nusselt number distribution a flat plate correlation for turbulent flow (see Bergman et al. [22]) is used

$$\mathrm{Nu_m}(x) = 0.0296\mathrm{Re_m}(x)^{4/5}\mathrm{Pr_m}(x)^{1/3} \tag{21}$$

Finally, the local external heat transfer coefficient is defined by

$$h_\mathrm{m}(x) = \frac{\mathrm{Nu_m}(x)k_\mathrm{m}(x)}{x} \tag{22}$$

The flat plate correlations give results of somewhat similar form to typical external heat transfer coefficient distributions for HPT NGV pressure sides and suction sides (assuming the flow has fully transitioned in the showerhead region). They are considered sufficiently accurate for the purpose of this chapter, namely predictions of *changes* in overall cooling effectiveness with TR, because they have sound physical basis (variation of h_m with $\mathrm{Nu_m}$ and $\mathrm{Pr_m}$; dependence on local fluid properties; etc.) which allows physically-meaningful responses to changes in the system boundary conditions.

Distributions $h_\mathrm{m}(x)$ for all three systems are presented and discussed in section 2.6.

2.5.4 Definition of the external mixing layer

An *external mixing layer* is defined as the region adjacent to the wall in which the coolant ejected from the film cooling row mixes with hot gas. This is shown schematically in Figure 8.

The following assumptions are made about the behaviour of this layer:

i) Static pressure, $p(x)$, is constant in the wall-normal direction. This means that the local static pressures in the mainstream and mixing layers are the same $p_\mathrm{m}(x) = p_\mathrm{h}(x) = p(x)$. Total pressures can be—slightly—different and the boundary may be considered as being represented by a *slip line*.

ii) The mixing layer is *fully mixed*, with a mass flow rate distribution for integrated entrained hot gas, $\dot{m}_\mathrm{e}(x)$, that gives the desired mixing-layer *effectiveness distribution*, $\eta_\mathrm{ML}(x)$, for the reference temperature ratio, TR = 2.0.

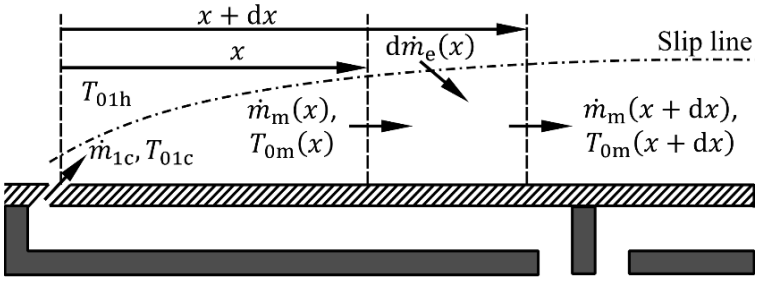

Figure 8: Schematic illustration of the fully-mixed mixing layer.

These assumptions allow calculation of the system static pressure distribution (from BCs, geometric area distribution, and simultaneous solution of both streams) and the mixing layer effectiveness distribution (from energy conservation, for entrainment subject to some similarity conditions discussed later) for any conditions of TR. Real gas properties are considered in these calculations. Though the assumption of the fully-mixed layer differs significantly from the physical situation of temperature gradient within the near-wall layer, by arbitrarily setting the entrainment rate to match the desired effectiveness distribution for the reference condition, and because there is sound physical basis for the way *changes* from this condition are calculated, it is believed to be a useful proxy-model for the particular purpose of evaluating changes in overall effectiveness with temperature ratio. Another example of the use of an assumed fully-mixed mixing layer is that of Kirollos and Povey [23], who use it for the purpose of film superposition calculations. In Kirollos and Povey [23], although individual mixing-layers take—by definition—the arbitrary thicknesses that satisfy the required single-film-cooling-row effectiveness distributions, the superposed solution is accurate. The point is that whilst layer thickness is arbitrary, much of the remaining physics is accurate.

The methods for evaluating effectiveness distribution and pressure distribution are discussed in sections 2.5.5 and 2.5.6.

2.5.5 Effectiveness distribution of the mixing layer

Effectiveness of the mixing layer at the reference temperature ratio, $\eta_{\mathrm{ML}}^{\mathrm{TR}=2.0}(x)$, is defined based on an incompressible adiabatic film effectiveness correlation (Vinton et al. [24]) for a flat plate with a single row of cooling holes

$$\eta_{\mathrm{aw}}(x) = 0.4\mathrm{e}^{-1.4x/C_x} \tag{23}$$

Now recall Eq. (3)

$$\eta_{\mathrm{ML}}(x) = \frac{c_{\mathrm{h}}(x)T_{01\mathrm{h}} - c_{\mathrm{m}}(x)T_{0\mathrm{m}}(x)}{c_{\mathrm{h}}(x)T_{01\mathrm{h}} - c_{\mathrm{c}}(x)T_{02\mathrm{c}}}$$

where each term has an individual recovery ratio distribution ($c_{\mathrm{h}}(x)$, $c_{\mathrm{m}}(x)$ and $c_{\mathrm{c}}(x)$) so as to constrain values of η_{ML} to the range $0 < \eta_{\mathrm{ML}} < 1$. For the case of TR = 2.0, Eq. (24) and Eq. (3) are equated giving

$$\eta_{\mathrm{ML}}^{\mathrm{TR}=2.0}(x) = \eta_{\mathrm{aw}}(x) \tag{24}$$

which defines $T_{0\mathrm{m}}^{\mathrm{TR}=2.0}(x)$ by rearrangement of terms. The resulting integrated entrainment rate distribution, $\dot{m}_{\mathrm{e}}^{\mathrm{TR}=2.0}(x)$, is that which satisfies conservation of mass and energy (full equation not shown).

For *non-reference* temperature-ratio it is assumed that the integrated entrained hot gas mass flow rate, $\dot{m}_{\mathrm{e}}(x)$, follows a geometric similarity argument as follows

$$\frac{\dot{m}_{\mathrm{e}}(x)}{\dot{m}_{1\mathrm{h}}} = \frac{\dot{m}_{\mathrm{e}}^{\mathrm{TR}=2.0}(x)}{\dot{m}_{1\mathrm{h}}^{\mathrm{TR}=2.0}} \tag{25}$$

That is, the *depth of the mixing layer* does not change with TR. In the situation of essentially-constant momentum flux ratio with TR, and essentially-constant external-side Mach number distribution with TR, the constraint Eq. (25) can be thought of as a similarity condition for the mixing-determining structures (for example, the penetration depth of the film and the turbulence length scale). Once $\dot{m}_{\mathrm{e}}(x)$ is determined from Eq. (25), the total temperature of the mixing layer can be calculated by mass balance

$$T_{0\mathrm{m}}(x) = \frac{\dot{m}_{1\mathrm{c}}c_{p1\mathrm{c}}T_{01\mathrm{c}} + \dot{m}_{\mathrm{e}}(x)c_{p01\mathrm{h}}T_{01\mathrm{h}}}{\dot{m}_{\mathrm{m}}(x)c_{p0\mathrm{m}}(x)} - \frac{w\int_0^x q_{\mathrm{m}}\mathrm{d}x}{\dot{m}_{\mathrm{m}}(x)c_{p0\mathrm{m}}(x)} \tag{26}$$

where c_{p1c} is specific heat capacity of cooling flow at plane 1, c_{p01h} is specific heat capacity of the mainstream flow at corresponding temperature T_{01h}, $w\int_0^x q_m \mathrm{d}x$ is the integrated (between 0 and x) external convective heat flux, and $c_{p0m}(x)$ is specific heat capacity of the mixing layer evaluated at corresponding temperature T_{0m}. Eq. (26) defines both the driving temperature for heat transfer, $c_m(x)T_{0m}(x)$, and the effectiveness of the mixing layer, $\eta_{ML}(x)$ (from Eq. (3)).

Distributions $\eta_{ML}(x)$ for all three systems are presented and discussed in section 2.6.

2.5.6 Calculation of external static pressure distribution and mainstream and coolant mass flow rate

This section describes how the external static pressure distribution, $p(x)$, and the mainstream and (forward-circuit) coolant mass flow rates, $\dot{m}_h(x)$ and $\dot{m}_{1c}$, are simultaneously calculated.

The static pressure distribution sets the static pressure at the exit of the film cooling row (and therefore the cooling flow rate). The static pressure distribution varies slightly with TR, due to changes in, for example, specific heat capacities with temperature, causing changes in the local external Mach number distribution even for fixed domain-global PR.

In the network model considered here, the cross-sectional area of the mainstream (representing the vane), $A(x)$ varies linearly from inlet to exit as shown in Figure 9. Domain-global BCs are set (either fixed exit Re and PR, or fixed PR with fixed exit pressure), which define the mainstream flow total pressure. The mainstream total temperature is defined by the given TR condition being studied. The coolant feed total pressure is defined by the coolant-to-mainstream pressure ratio.

Mass flows and pressure distributions are solved simultaneously and iteratively (to convergence) subject to the following constraints:

i) Inlet total pressures, p_{01h} and p_{02c}, and domain-exit static pressure, p_3, defined by the domain-global and cooling-system BCs (see Figure 4 and Table 1).

ii) Cooling flow total temperature $T_{02c} = 300$ K, with mainstream total temperature, T_{01h} defined by the TR under consideration.

iii) Distributions of local areas of mainstream flow and mixing layer flow, $A_{\mathrm{h}}(x)$ and $A_{\mathrm{m}}(x)$, subject to the geometrical constraint $A_{\mathrm{h}}(x) + A_{\mathrm{m}}(x) = A(x)$ i.e. the two stream areas sum to the local passage area. This is illustrated in Figure 9.

iv) Adiabatic mainstream flow, $T_{0\mathrm{h}}(x) = T_{01\mathrm{h}}$, with no loss of total pressure, $p_{0\mathrm{h}}(x) = p_{01\mathrm{h}}$.

v) Total pressure of the mixing layer defined by a simple mass average

$$p_{0\mathrm{m}}(x) = \frac{\dot{m}_{1\mathrm{c}} p_{01\mathrm{c}} + \dot{m}_{\mathrm{e}}(x) p_{01\mathrm{h}}}{\dot{m}_{\mathrm{m}}(x)} \tag{27}$$

where it is noted that the inlet total pressures $p_{01\mathrm{h}}$ and $p_{02\mathrm{c}}$ differ by only 2.5%, and that most of the entrainment happens at low Mach number (M < 0.60) limiting the impact of weaknesses in this model especially so far as changes with TR conditions are concerned.

vi) Total temperature distribution of the mixing layer for the reference TR, $T_{0\mathrm{m}}^{\mathrm{TR}=2.0}(x)$, prescribed by Eq. (23) and equality with Eq. (24), which defines a particular associated integrated entrainment rate, $\dot{m}_{\mathrm{e}}(x)$.

vii) For the non-reference TR, a geometric similarity condition is imposed on the mixing layer (see Eq. (25)) which is equivalent to the depth of the mixing layer being unchanged with TR. This allows $\dot{m}_{\mathrm{e}}(x)$ and therefore $T_{0\mathrm{m}}(x)$ to be calculated for any non-reference TR.

viii) Mass and energy conservation in each cell, including through-wall heat fluxes.

ix) The mixing layer boundary acts as a slip line, such that the static pressure either side is constant i.e. $p_{\mathrm{h}}(x) = p_{\mathrm{m}}(x) = p(x)$.

Temperature-dependent fluid properties are used in the analysis, and the (reverse-pass) forward-circuit mass flow rate, $\dot{m}_{1\mathrm{c}}$, and associated channel exit total pressure, $p_{01\mathrm{c}}$, are allowed to vary with external static pressure. For the case of the domain-global fixed PR BCs, these effects cause the coolant-to-mainstream mass flow rate ratio to change by approximately −21% as TR is varied between 2.0 to 1.2. The corresponding value for the domain-global fixed Re BC is −22%.

The primary cause of this effect is a reduction in coolant mass flow rate as TR is reduced (approximately constant coolant momentum flux as coolant density decreases with increasing coolant temperature, leading to a reduction in coolant mass flow rate per unit area).

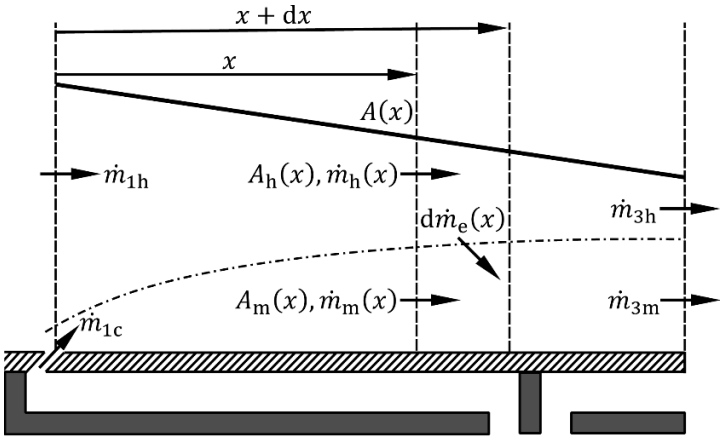

Figure 9: Schematic of the mixing layer, showing boundary conditions on the mixing process.

2.5.7 Discretisation scheme for numerical solver

For each elemental cell in the mixing layer and internal cooling duct, mass and energy conservation are satisfied, taking account of convection heat transfer with the walls, and advection terms into and out of an elemental cell. On the external surface the driving temperature difference is taken to be $c_{\mathrm{m}}(x)T_{0\mathrm{m}}(x) - T_{\mathrm{w1}}(x)$, i.e. the recovery factor of the mixing layer is considered to account for compressible flow effects. For the wall energy conservation in the through-wall direction is considered. Lateral conduction terms are omitted from the main results sections but it is shown in a later section that they are very small (length ratio, $C_x/t_{\mathrm{w}} = 100$) in comparison to through-wall terms. The solution was iterated to convergence, defined by the maximum residual in any heat flux term being less than 0.1% of the mean through-wall heat flux. This threshold was usually passed after 3 global iteration steps. A grid independence study was performed and the solution was found to be independent of mesh size for $\mathrm{d}x \leq 0.1$ mm and $\mathrm{d}y \leq 0.5$ mm. The final mesh had uniform spacing in all directions (uniform spacing mesh) with 10 cells in the through-wall direction and approximately 1×10^3 cells in the flow-wise direction. A simplified schematic of the discretisation scheme for the numerical solver for the leading circuit is shown in Figure 10.

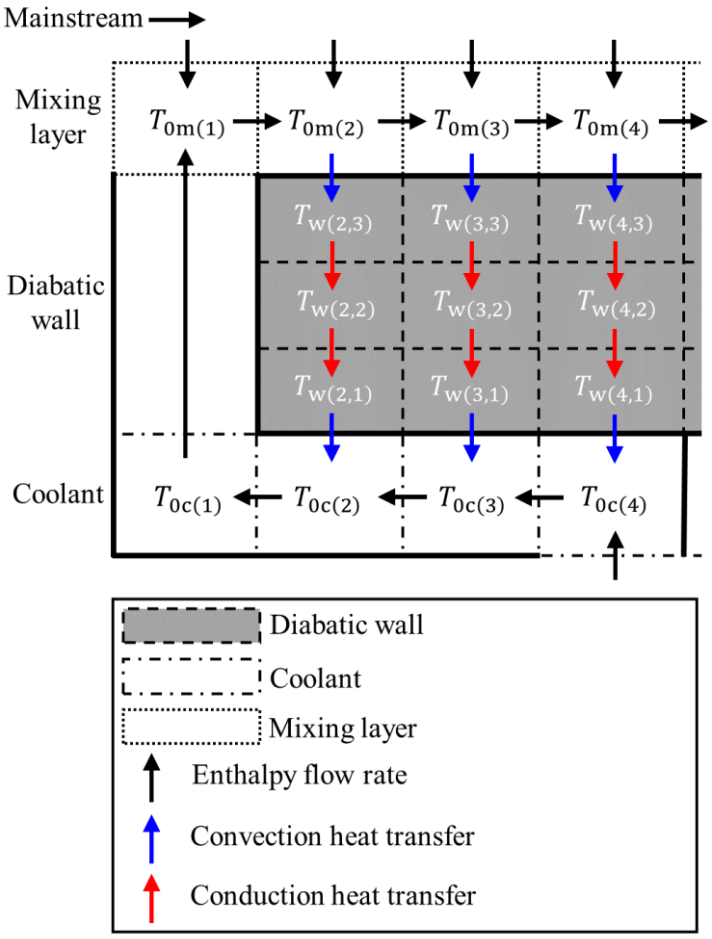

Figure 10: Discretisation scheme for numerical solver for the leading circuit with temperatures and heat flows.

2.6 Results I: Baseline local surface boundary conditions and overall cooling effectiveness distributions

In this section baseline (i.e. for reference TR = 2.0) local surface boundary conditions and overall cooling effectiveness results for the three cooling system networks (see Figure 5) are presented. These form the reference case for all comparisons later in this chapter, as temperature ratio is varied away from the reference TR. The reference TR domain-global and cooling system BCs are summarised in Table 1.

First, consider the resulting *local surface BCs* which are presented in Figure 11 for all three cooling systems.

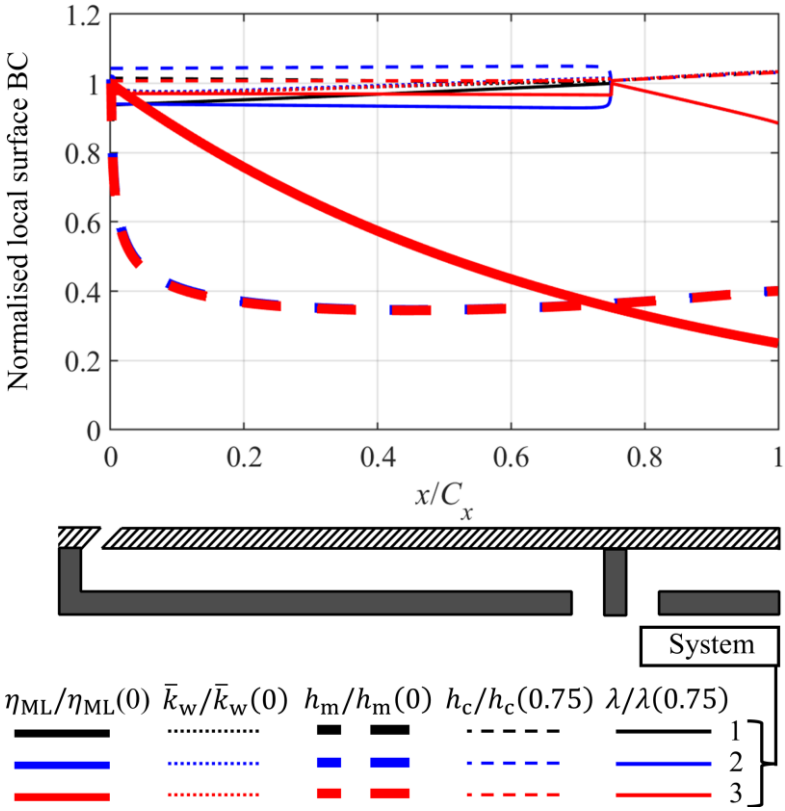

Figure 11: Local surface BCs for cooling system networks 1–3 at the reference TR. Absolute values are normalised by particular local values for system 1 (values at $x/C_x = 0$ for η_{ML}, $\bar{k}_w$ and h_m; values at $x/C_x = 0.75$ for h_c and λ).

Here distributions of five parameters are plotted: effectiveness of the mixing layer, η_{ML}; local through-wall-average wall thermal conductivity, $\bar{k}_w$; external heat transfer coefficient, h_m; internal heat transfer coefficient, h_c; and internal cooling effectiveness, λ. Because primary interest is in the characteristic trends, and in differences between the three systems, absolute values are normalised by particular local values for system 1. η_{ML}, h_m and $\bar{k}_w$, are normalised by values at the leading edge of the plate ($x/C_x = 0$) for which numerical values are: $\eta_{ML} = 0.40$, $h_m = 1773$ W m^{-2} K^{-1}, and $\bar{k}_w = 12.9$ W m^{-1} K^{-1}. h_c and λ are normalised by values at the entrance to the reverse-pass cooling duct ($x/C_x = 0.75$) for which numerical values are: $h_c = 417$ W m^{-2} K^{-1} and $\lambda = 0.994$ (small difference from unity arises due to recovery ratios).

Consider first the effectiveness distributions for the mixing layer, $\eta_{\mathrm{ML}}(x)$. The trend is for exponential decay, in line with Eq. (23). Trends for all three cooling system networks are identical because the distribution is imposed at the reference TR

Now consider the trend in external heat transfer coefficient, $h_{\mathrm{m}}(x)$. The general trend is similar to $1/x$ in the region $0 \leq x/C_x < 0.4$ due to the $1/x$ term in Eq. (22). In the region $0.4 \leq x/C_x < 1$, $h_{\mathrm{m}}(x)$ monotonically increases because the rate at which $1/x$ term decays is smaller than the rate of increase of local external Reynolds number, $\mathrm{Re}_{\mathrm{m}}(x)$, due to increasing local external velocity, $u_{\mathrm{m}}(x)$. The trends are almost identical for all three cooling system networks with second-order differences due to, for example: differences in cooling mass flow rate due to differences in pressure loss from inlet to exit of the reverse-pass cooling duct; differences in through-wall heat flux distributions between the three systems caused by slight differences in mixing layer temperature.

The local through-wall-average wall thermal conductivity, $\bar{k}_{\mathrm{w}}(x)$, is approximately constant with streamwise distance, with RMS variation from the surface-averaged value of 0.22 W m^{-1} K^{-1} and maximum variation of 0.46 W m^{-1} K^{-1}. These are equivalent to 1.7% and 3.6% of the surface-averaged value, respectively.

Now consider the internal heat transfer coefficient distribution, $h_{\mathrm{c}}(x)$. The trends for the TE circuit ($0.75 \leq x/C_x < 1$) are identical for all three cooling system networks: this is expected because this is a common part of the networks. Small differences in this region are caused by velocity variation along the channel. The values in the region of the leading circuit ($0 \leq x/C_x < 0.75$) are approximately constant, with a mean value approximately 2.9% higher for system 2 (difference in the way the distributed-inlet boundary condition was set).

Finally, consider the internal cooling effectiveness distributions, $\lambda(x)$. In the TE circuit ($0.75 \leq x/C_x < 1$), for all three cooling systems, $\lambda(x)$ starts from a value of 0.99 at $x/C_x = 0.75$ and falls approximately linearly to a value of approximately 0.88 at $x/C_x = 1.00$, as heat is picked up in the channel. In the region of the leading circuit, the trend for system 1 is approximately linear

decay between values of 0.99 ($x/C_x = 0.75$) and 0.93 ($x/C_x = 0$) as heat is picked up in the reverse-pass channel. In system 2 (distributed inlet) the fluid temperature is always much closer to the inner wall temperature (lower initial mass flow; incremental addition of coolant) and $\lambda(x)$ is in the range $0.923 < \lambda(x) < 0.927$ (i.e. approximately constant) in the region $0 \leq x/C_x < 0.75$ (i.e. the entire passage from a very short distance downstream of the inlet). For system 3, the cooling flow is fully-mixed by definition and $\lambda(x)$ takes the constant value 0.96.

Resulting overall cooling effectiveness distributions, $\theta(x)$, for all three cooling system networks at the reference TR are presented in Figure 12.

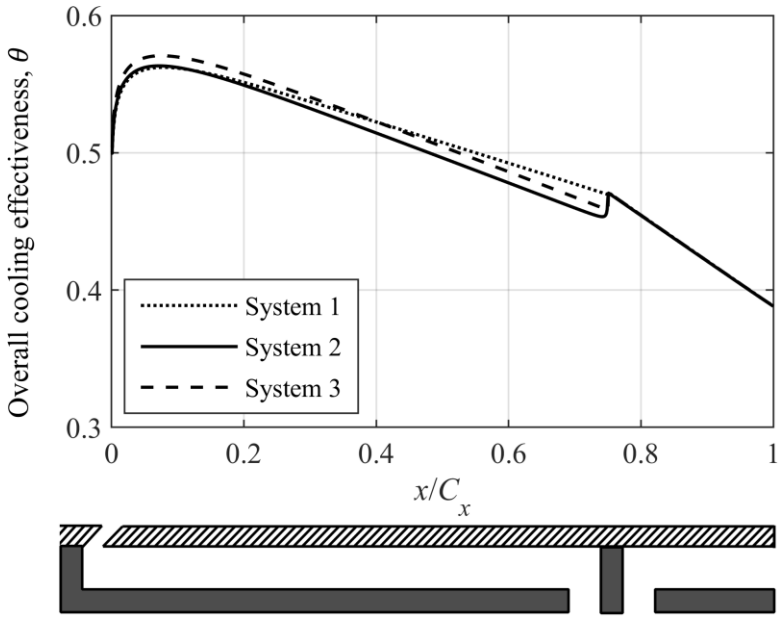

Figure 12: Overall cooling effectiveness distributions, $\theta(x)$, for cooling system networks 1–3 at the reference TR.

Distributions were similar for all three cooling system networks, with values being bounded by $0.38 < \theta(x) < 0.58$, and with mean values $\bar{\theta} = 0.500$, 0.494 and 0.500, for cooling system networks 1−3 respectively. Mean RMS difference between trends was 0.005, and maximum difference 0.014. It is interesting that the resulting trends are so insensitive to fairly large changes in the network of the design. The physical basis for the underlying trends is now described in more detail.

The sudden increase in $\theta(x)$ between $x/C_x = 0$ and $x/C_x = 0.08$ is driven by a steep reduction in external heat transfer coefficient (see Figure 11) near the leading edge as the boundary layer thickens from the leading edge. For $x/C_x > 0.08$, the trend in θ is an approximately-linear decrease from a peak at 0.56 to a minimum of 0.39. In this region the external heat transfer coefficient is approximately constant, and the trend in θ is primarily caused by an approximately linear reduction in the mixing layer effectiveness, η_{ML}.

2.7 Results II: Effect of temperature ratio on overall cooling effectiveness

In this section the effect of temperature ratio on overall cooling effectiveness is considered. Results are presented for system 1 for domain-global boundary conditions of fixed PR. It is shown later that the result is almost completely independent of the cooling system network for the types of network considered. It is also shown that the *overall* change in overall cooling effectiveness (sum of effects associated with changes in each of five local surface BCs) is relatively independent of the domain-global boundary conditions, despite significant changes associated with individual local surface BCs for the domain-global BC of fixed exit Re with fixed PR.

Predictions were performed over the TR range $1.2 \leq \mathrm{TR} \leq 2.0$ for fixed $p_{01\mathrm{h}}, p_{02\mathrm{c}}, p_{3\mathrm{h}}$, CMPR and $T_{02\mathrm{c}}$. The changes in overall cooling effectiveness distribution from that for the reference TR (Figure 12), $\Delta\theta = \theta - \theta^{\mathrm{TR}=2.0}$ are presented in Figure 13. The effect of reducing TR from the reference condition is to reduce effectiveness. This effect occurs primarily because of a reduction in the heat capacity flow rate ratio ($\dot{m}_{1\mathrm{c}}c_{p1\mathrm{c}}/\dot{m}_{1\mathrm{h}}c_{p01\mathrm{h}}$) as TR is reduced, causing a reduction in the mixing layer effectiveness. This effect, and other second-order effects, is discussed in detail in the following sections. The surface-mean change in overall cooling effectiveness from the value for the reference TR, $\overline{\Delta\theta}$, was -0.006, -0.014, -0.023 and -0.037 for TRs 1.8, 1.6, 1.4 and 1.2 respectively. As percentages of the target mean effectiveness ($\bar{\theta} = 0.500$) these are equivalent to changes of -1.23%, -2.71%, -4.60% and -7.39% respectively. This is the key result of this chapter, and remaining sections are largely dedicated to robustly examining this result, and

looking at the range of boundary conditions for which it is valid. A more complex system is considered in chapter 3, which includes coupling webs connecting the external and internal walls. It is demonstrated that the effect of the webs is to dramatically reduce the magnitude in changes of overall cooling effectiveness as one moves from the reference TR to lower-than-reference TR. It is concluded that the degree of coupling between external and internal walls must be assessed when applying the general results of Figure 13 to real systems. This is discussed in detail in chapter 3.

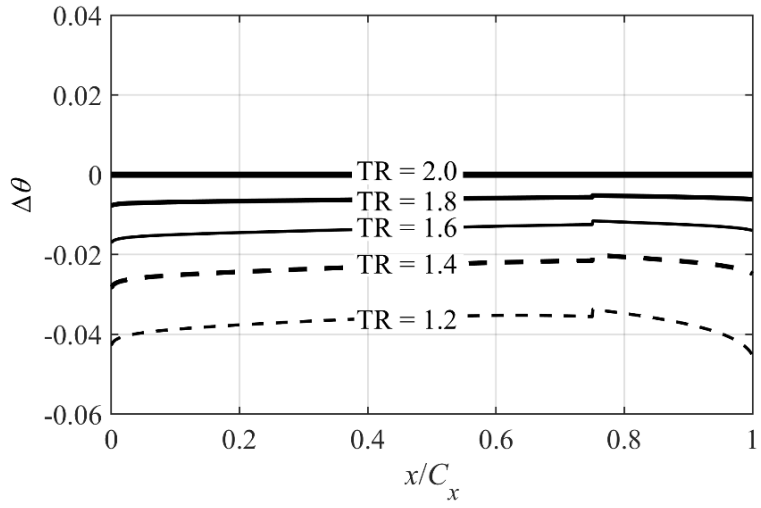

Figure 13: Distributions of change in overall cooling effectiveness, $\Delta\theta(x)$, as a function of normalised streamwise distance, x/C_x, for temperature ratios in the range $1.2 \leq \mathrm{TR} \leq 2.0$. Results are for system 1 for domain-global boundary conditions of fixed PR.

For mainstream and coolant temperatures (see, for example, Cumpsty and Heyes [25]) of 1750 K and 875 K, values which are typical of large civil engines, and based on the preferred definition of overall effectiveness (Eq. (2)), if tests were run at conventional laboratory conditions with TR = 1.2, and results were not corrected to engine conditions, scaled uncorrected results would be higher than true engine metal temperatures by 34.1 K. That is, tests at conventional laboratory temperatures overestimate component temperature based on simple scaling. So far as the trends with streamwise distance are concerned, it is observed (Figure 13) that the change varies by a factor of about 1.2 in the leading circuit and 1.3 in the region of the trailing circuit. Overall, the

result is approximately constant with streamwise distance; considering the trend for TR = 1.2, the RMS deviation from the mean value of $\Delta\theta(x)$ is 5.3% of the mean value.

For the case of the fixed PR domain-global BC this is explained by a combination of three effects. Firstly (see Figure 11) $\eta_{\mathrm{ML}}(x)$ is significantly larger at the leading edge (value of approximately 0.40) than the trailing edge (value of approximately 0.10), which, when combined with the geometric similarity mixing constraint—Eq. (25)—means greater change with TR in *absolute* values of $\eta_{\mathrm{ML}}(x)$ at the leading rather than the trailing edge: that is, the absolute reduction in $\eta_{\mathrm{ML}}(x)$ as TR is reduced is greater at the LE than the TE. The second effect is an increase in the external heat transfer coefficient as TR is reduced (due to an increase in local external Reynolds number with decreasing mainstream temperature), which acts to further decrease the overall cooling effectiveness. The trend for the second effect is an increase in magnitude with streamwise distance in the region of the leading circuit but at a lower rate than the first effect. This is explained as follows: the change in $h_{\mathrm{m}}(x)$ with TR, $\Delta h_{\mathrm{m}}(x)$, is approximately constant with streamwise distance and the sensitivity of $\theta(x)$ to changes in $h_{\mathrm{m}}(x)$ increases with streamwise distance due to an increase in the magnitude of $\lambda(x) - \eta_{\mathrm{ML}}(x)$ caused by an increase in $\lambda(x)$ and a reduction in $\eta_{\mathrm{ML}}(x)$ as one moves from the leading edge ($x/C_x = 0$) to plane 2 ($x/C_x = 0.75$). This can be understood by considering the partial derivative of Eq. (11) with respect to h_{m}. In the region of the trailing edge circuit the magnitude of the second effect decreases with streamwise distance. This can be explained as follows: sensitivity of $\theta(x)$ to changes in $h_{\mathrm{m}}(x)$ decreases with streamwise distance due to a reduction in the magnitude of $\lambda(x) - \eta_{\mathrm{ML}}(x)$ due to a combination of a reduction in $\lambda(x)$ and a (small) reduction in $\eta_{\mathrm{ML}}(x)$ as one moves from plane 2 ($x/C_x = 0.75$) to the trailing edge plane 3 ($x/C_x = 1$). The third effect is a reduction in internal cooling effectiveness as TR is reduced, which acts to further decrease the overall cooling effectiveness. This effect is explained as follows. The effect of compressibility in the system results in recovery ratios less than unity and, for temperature ratios greater than unity, this has the effect of reducing λ (compared to the case $c_{\mathrm{c}}(x) = c_{\mathrm{h}}(x) = c_{\mathrm{m}}(x) = 1$). The effect of decreasing TR

from TR = 2.0 is to amplify the magnitude of the reduction in λ caused by this compressibility effect.

In combination, and taking into account two other second-order effects (see later sections), these effects lead to the trends of Figure 13. Although this is to some extent a system-specific result, the characteristic trend is typical of most HPT NGVs. It is shown in later sections that the *overall* result of Figure 13 is insensitive to the choice of domain-global BCs (fixed PR alone, or fixed exit Reynolds number and fixed PR), but the *contributions* from individual local surface BCs are very different for different domain-global BCs.

2.8 Results III: Decomposed contributions from changes in local surface boundary conditions

In this section the overall change in θ with TR is decomposed into the effects associated with changes in five local surface BCs. The following local surface boundary conditions are chosen for this process: effectiveness of the mixing layer, η_{ML}; local through-wall-average wall thermal conductivity, $\bar{k}_{\mathrm{w}}$; external heat transfer coefficient, h_{m}; internal heat transfer coefficient, h_{c}; and internal cooling effectiveness, λ. That is, $\theta = f\left(\eta_{\mathrm{ML}}, \bar{k}_{\mathrm{w}}, h_{\mathrm{m}}, h_{\mathrm{c}}, \lambda\right)$. Though somewhat arbitrary, this choice of variables is justified with the weak analytical argument that for a simple zero-dimensional model these five parameters are sufficient to define the surface temperature. This argument has been presented. The effects associated with each of these five boundary conditions are referred to as effect 1 to effect 5. In the analysis that follows, where changes in any particular one of these local surface boundary conditions can be ascribed to changes in underlying parameters, they are done so. A schematic diagram of the cooling system network showing the region which each effect (1 to 5) is associated with, is shown in Figure 14.

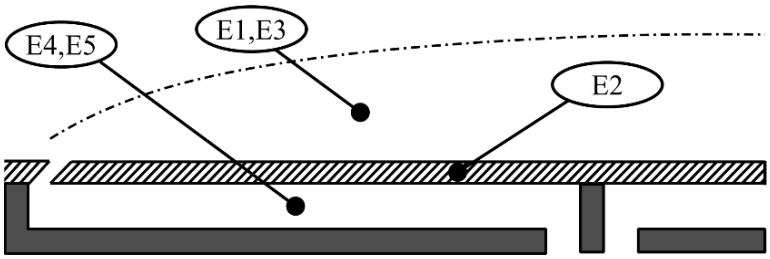

Figure 14: Schematic of the cooling system showing the regions with which each of the effects 1–5 are most associated.

Results will be presented for system 1 for fixed PR boundary conditions. It is shown later that the general result is insensitive to overall system boundary conditions (fixed PR or fixed exit Re with fixed PR) and insensitive to the internal cooling system network.

To perform these predictions, the following steps are performed:

i) Solutions are converged at each of five TR conditions corresponding to TR = 2.0, 1.8, 1.6, 1.4 and 1.2. In these simulations all fluid properties and local BCs are for the domain-global and cooling system BCs presented in Table 1. These predictions represent the natural converged state of the system at a given TR condition.

ii) From each of the five converged simulations (at five TR conditions) distributions of overall cooling effectiveness, $\theta(x)$, and distributions of each of the five local surface BCs: $\eta_{\mathrm{ML}}(x)$, $\bar{k}_{\mathrm{w}}(x)$, $h_{\mathrm{m}}(x)$, $h_{\mathrm{c}}(x)$ and $\lambda(x)$ are extracted. The result is $5\times6=30$ distributions. The structure of this data is shown in Table 1 (only average values of the underlying distributions presented).

iii) The surface-mean change in the value of $\theta(x)$ with TR, $\overline{\Delta\theta}$, represents the sensitivity of overall cooling effectiveness to TR when all variables are allowed to vary in a natural co-dependent way with TR. This has been discussed in the context of Figure 13.

To perform a simple decomposition of contributions associated with changes in each of the five local surface BCs ($\eta_{\mathrm{ML}}(x)$, $\bar{k}_{\mathrm{w}}(x)$, $h_{\mathrm{m}}(x)$, $h_{\mathrm{c}}(x)$, $\lambda(x)$), treating each local surface BC in turn, the converged simulation at the reference temperature ratio is taken, and conditions of a single

particular local surface BC from converged simulations at all other non-reference TRs are imposed. The resulting distributions $\theta'(x)$ are then compared to the original distributions $\theta(x)$. The difference, $\Delta\theta(x) = \theta'(x) - \theta(x)$, is taken to be due to the single variable that was perturbed. Later, a check-sum approach is used to test the extent of validity of this implicit linear superposition assumption. A schematic of the data that is used in this process is shown in Figure 15 for effect 1, changes in $\eta_{\mathrm{ML}}(x)$.

Each of the effects is now considered in turn. All the analysis that follows is for system 1, for the fixed PR domain-global BC.

Fully converged simulations at five TRs

TR	$\bar{\theta}$ (−)	$\bar{\eta}_{\mathrm{ML}}$ (−)	$\bar{k}_{\mathrm{w}}$ (W m^{-1} K^{-1})	$\bar{h}_{\mathrm{m}}$ (W m^{-2} K^{-1})	$\bar{h}_{\mathrm{c}}$ (W m^{-2} K^{-1})	$\bar{\lambda}$ (−)
2.0	0.4996	0.2164	12.92	669.6	421.7	0.9555
1.8	0.4935	0.2108	12.45	679.4	423.5	0.9540
1.6	0.4861	0.2042	11.98	690.3	425.2	0.9516
1.4	0.4766	0.1962	11.49	702.6	427.0	0.9471
1.2	0.4627	0.1867	10.99	716.8	428.7	0.9343

Effect 1: resulting value of $\bar{\theta}'$ when only η_{ML} is perturbed

$\bar{\theta}'$ (−)
0.4996
0.4961
0.4920
0.4870
0.4811

Figure 15: Schematic of data structure used in the process for predicting changes in overall cooling effectiveness when one local surface BC is changed—in isolation of other local surface BCs—from its value at reference TR. Example for effect 1.

2.8.1 Effect 1: Changes in overall cooling effectiveness due to changes in effectiveness of the mixing layer

The effect on θ of varying the effectiveness of the mixing layer (η_{ML})—in isolation of other local surface BCs—from its value at the reference TR is now considered. The distributions $\eta_{\mathrm{ML}}(x)$ are changed to the values they take at TRs in the range $1.2 \leq \mathrm{TR} \leq 2.0$, whilst all other local surface BCs ($\bar{k}_{\mathrm{w}}$, h_{m}, h_{c} and λ) are kept equal to the values they take in a converged simulation at the reference TR. If linear superposition can be assumed to be valid, this allows one to determine the impact on θ of changes in η_{ML} (with TR) for fixed conditions of other local surface BCs. These changes are referred to as $\Delta\theta_{\mathrm{E1}}(x)$, where the sign convention is $\Delta\theta_{\mathrm{E1}}(x) = \theta(x) - \theta(x)^{\mathrm{TR}\,=\,2.0}$. The changes $\Delta\theta_{\mathrm{E1}}(x)$ are plotted for the range $1.2 \leq \mathrm{TR} \leq 2.0$ in Figure 16.

The effect of reducing TR from the reference condition is to reduce the effectiveness of the mixing layer, which decreases θ due to higher non-dimensional driving external temperature. This

effect occurs primarily because of a reduction in the heat capacity flow rate ratio ($\dot{m}_{1c}c_{p1c}/\dot{m}_{1h}c_{p01h}$) as TR is reduced, causing a reduction in the mixing layer effectiveness. The surface-mean changes in overall cooling effectiveness from the value for the reference TR, $\overline{\Delta\theta}_{E1}$ were −0.003, −0.008, −0.013, and −0.018 for TRs 1.8, 1.6, 1.4 and 1.2 respectively. As percentages of the target mean effectiveness ($\overline{\theta} = 0.500$) these are equivalent to changes of −0.70%, −1.53%, −2.51% and −3.70% respectively.

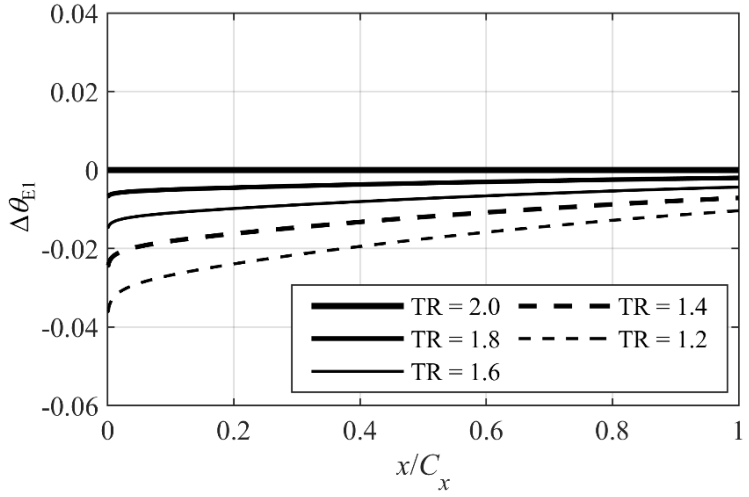

Figure 16: Change in overall cooling effectiveness when the effectiveness of the mixing layer, η_{ML}, is changed—in isolation of other local surface BCs—from its value at reference TR.

So far as the trends with streamwise distance are concerned, it is shown (Figure 16) that the change, $\Delta\theta_{E1}(x)$, is greater at the leading edge ($x/C_x = 0$) than the trailing edge ($x/C_x = 1.0$) by a factor of approximately 3.5. This is because (see also discussion in context of Figure 13) $\eta_{ML}(x)$ takes greater absolute values near the leading edge (see Figure 11) which when combined with the geometric similarity condition for mixing (Eq. (25)), means greater *absolute* change in $\eta_{ML}(x)$ near the leading edge compared with the trailing edge. The underlying physical effect is that when TR is reduced from the reference condition, a relative increase in hot-gas mass flow rate (due to increase in density that outweighs the reduction in velocity) reduces the coolant-to-mainstream mass flux ratio, reducing the effectiveness of the mixing layer.

To provide insight into second-order effects, a sensitivity analysis of all influences on $\eta_{ML}(x)$ as TR is varied is now performed. The full equation for effectiveness of the mixing layer (not

shown) arises from consideration of mass and energy conservation within the mixing layer and has the functional relationship $\eta_{\mathrm{ML}}=f\left(\dot{m}_{\mathrm{e}}, \dot{m}_{1\mathrm{c}}, c_{p01\mathrm{h}}, c_{p1\mathrm{c}}, \varepsilon, \dot{m}_{3\mathrm{c}}, c_{\mathrm{c}}, c_{\mathrm{h}}, c_{\mathrm{m}}, c_{p2\mathrm{c}}, T_{02\mathrm{c}}, T_{01\mathrm{h}}\right)$. In this equation, the recovery ratios $c_{\mathrm{h}}(x)$, $c_{\mathrm{m}}(x)$ and $c_{\mathrm{c}}(x)$ are approximately equal to unity (minimum value 0.98), and vary little with temperature ratio. Taking the approximation $c_{\mathrm{h}}(x) = c_{\mathrm{m}}(x) = c_{\mathrm{c}}(x) = 1$, and taking the further approximation of constant specific heat capacity of the coolant within the leading circuit (i.e. $c_{p1\mathrm{c}} = c_{p2\mathrm{c}}$; true to within 0.14%) the more complex functional relationship can be reduced to the form

$$\eta_{\mathrm{ML}}(x) = \frac{1 - \varepsilon(x)\left(1 + \dfrac{\dot{m}_{3\mathrm{c}}}{\dot{m}_{1\mathrm{c}}}\right)}{1 + \left(\dfrac{\dot{m}_{\mathrm{e}}(x)}{\dot{m}_{1\mathrm{c}}}\right)\left(\dfrac{c_{p01\mathrm{h}}}{c_{p1\mathrm{c}}}\right)} \tag{28}$$

where $\dot{m}_{\mathrm{e}}(x)/\dot{m}_{1\mathrm{c}}$ is the ratio of integrated (between 0 and x) entrainment mass flow rate to coolant mass flow rate at plane 1, $\dot{m}_{3\mathrm{c}}/\dot{m}_{1\mathrm{c}}$ is the ratio of trailing circuit to leading circuit coolant mass flow rate, $c_{p01\mathrm{h}}/c_{p1\mathrm{c}}$ is the specific heat capacity ratio, and $\varepsilon(x)$ is the total non-dimensional external-side heat flux between any location x and the cooling channel inlet ($x/C_x = 0.75$) i.e.

$$\varepsilon(x) = \frac{w\int_{x}^{x/C_x\,=\,0.75} q_{\mathrm{m}}\,\mathrm{d}x}{(\dot{m}_{1\mathrm{c}} + \dot{m}_{3\mathrm{c}})c_{p2\mathrm{c}}(T_{01\mathrm{h}} - T_{02\mathrm{c}})} \tag{29}$$

where the total external-side heat flux is normalised by the maximum heat pick up of the combined coolant streams (streams heated from $T_{02\mathrm{c}}$ to $T_{01\mathrm{h}}$), taking the assumption of constant specific heat capacity for coolant flow within the ducts.

In Eq. (28) η_{ML} is expressed as a function of four non-dimensional groups, i.e. $\eta_{\mathrm{ML}}=f(\dot{m}_{\mathrm{e}}(x)/\dot{m}_{1\mathrm{c}}$, $\dot{m}_{3\mathrm{c}}/\dot{m}_{1\mathrm{c}}$, $c_{p01\mathrm{h}}/c_{p1\mathrm{c}}$, $\varepsilon)$. The sensitivity of surface-averaged effectiveness, $\bar{\eta}_{\mathrm{ML}}$, to each of the four non-dimensional groups is evaluated by partial derivative of Eq. (28) with respect to each in turn. The sensitivity of the *surface-averaged* effectiveness, $\bar{\eta}_{\mathrm{ML}}$, to each group is considered in order to give insight into the physical mechanisms that drive changes in $\eta_{\mathrm{ML}}(x)$. Percentage contributions of each non-dimensional group to the overall change in surface-average film effectiveness ($\Delta\bar{\eta}_{\mathrm{ML}}$) are presented as a bar chart in Figure 17.

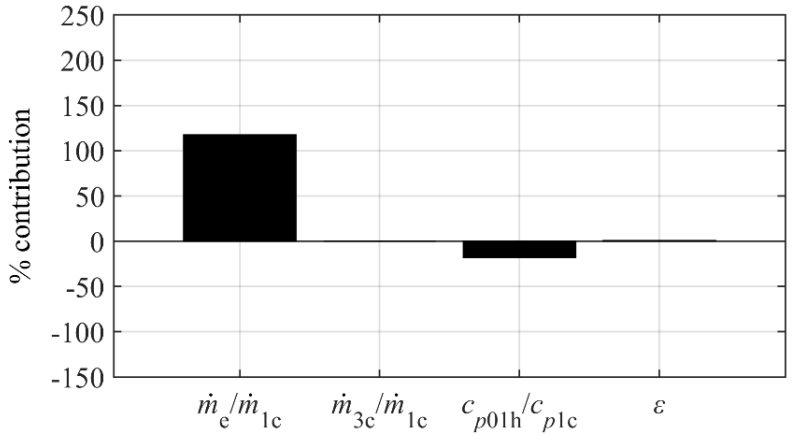

Figure 17: Percentage contributions of three underlying terms to changes in surface-averaged effectiveness of the mixing layer, $\bar{\eta}_{ML}$.

It is recalled that moving from the reference TR to lower-than-reference TR causes a reduction in $\bar{\eta}_{ML}$, which causes a reduction in θ (negative value of $\Delta\theta_{E1}$). It is shown in Figure 17 that this effect is dominated by the increase in the ratio of integrated entrained hot gas to coolant mass flow rate ($\dot{m}_e/\dot{m}_{1c}$), which is driven by reduction in coolant-to-mainstream density ratio (ρ_{1c}/ρ_{1h}) due to an increase in ρ_{1h} as TR is reduced (an effect that outweighs the decrease in mass flow with decreasing mainstream velocity with reducing TR). The magnitude of this effect is 117% of the overall change, and is offset by a 0.03% contribution associated with the change in $\dot{m}_{3c}/\dot{m}_{1c}$, a −17.8% contribution associated with the change in c_{p01h}/c_{p1c}, and a 0.35% contribution associated with the change in ε. In summary, it is the change in the ratio of integrated entrained hot gas to coolant mass flow rate and the change in heat capacity ratio that dominate the change in $\bar{\eta}_{ML}$ that gives rise to a change in θ. It is noted that the product of $\dot{m}_e(x)/\dot{m}_{1c}$ and c_{p01h}/c_{p1c} is the ratio of the heat capacity flow rates of the coolant and entrained hot gas ($\dot{m}_{1c}c_{p1c}/\dot{m}_e(x)c_{p01h}$). Due to the geometric similarity condition for mixing (Eq. (25)), this is directly proportional to the coolant-to-mainstream heat capacity flow rate ratio ($\dot{m}_{1h}c_{p01h}/\dot{m}_{1c}c_{p1c}$), which is the primary variable responsible for determining the mixing layer effectiveness (see Ornano and Povey [4]). From a dimensional-analysis standpoint this combined parameter is of predominant importance in this problem. Here the two underlying terms are treated separately, however, to identify that

the root cause of the change in coolant-to-mainstream heat capacity flow rate ratio is almost primarily related to the change in mass flow rate ratio and only secondarily dependent on the heat capacity ratio.

In summary, as one moves from the reference TR to lower-than-reference TR, η_{ML} decreases, primarily due to an increase in the ratio of integrated entrained hot gas to coolant mass flow rate. The decrease in η_{ML} leads to a decrease in θ.

2.8.2 Effect 2: Changes in overall cooling effectiveness due to changes in local through-wall-average wall thermal conductivity

The effect on θ of varying local through-wall-average (in y-direction) wall thermal conductivity ($\bar{k}_{\mathrm{w}}$)—in isolation of other local surface BCs—from its value at the reference TR is now considered. As described in section 2.8.1, the distributions $\bar{k}_{\mathrm{w}}(x)$ are changed to the values they take at TRs in the range $1.2 \leq \mathrm{TR} \leq 2.0$, whilst all other local surface BCs (η_{ML}, h_{m}, h_{c} and λ) are kept equal to the values they take in a converged simulation at the reference TR. If linear superposition can be assumed to be valid, this allows one to determine the impact on θ of changes in $\bar{k}_{\mathrm{w}}$ for fixed conditions of other local surface BCs. These changes are referred to as $\Delta\theta_{\mathrm{E2}}(x)$, where the sign convention is $\Delta\theta_{\mathrm{E2}}(x) = \theta(x) - \theta(x)^{\mathrm{TR}=2.0}$. The changes $\Delta\theta_{\mathrm{E2}}(x)$ are plotted for the range $1.2 \leq \mathrm{TR} \leq 2.0$ in Figure 18.

The effect of reducing TR from the reference condition is to decrease wall thermal conductivity, which reduces θ due to higher Biot number (less coupling of internal and external surface, so lower effect of internal cooling). Here the correlation $k_{\mathrm{w}} = 5.480 + 0.017T_{\mathrm{w}}$, which is typical for nickel alloy (see, for example, Zielińska et al. [26]), is taken; that is, a weak positive linear trend between k_{w} and T_{w}. The surface-mean changes in overall cooling effectiveness from the value for the reference TR, $\overline{\Delta\theta}_{\mathrm{E2}}$ were -0.0002, -0.0004, -0.0007, and -0.0010 for TRs 1.8, 1.6, 1.4 and 1.2 respectively. As percentages of the target mean effectiveness ($\bar{\theta} = 0.500$) these are equivalent to changes of -0.04%, -0.09%, -0.14% and -0.20% respectively. This effect is small

in the temperature range dictated by the domain-global BCs considered in this chapter. This point is revisited in the context of engine-like absolute temperatures in section 2.12.

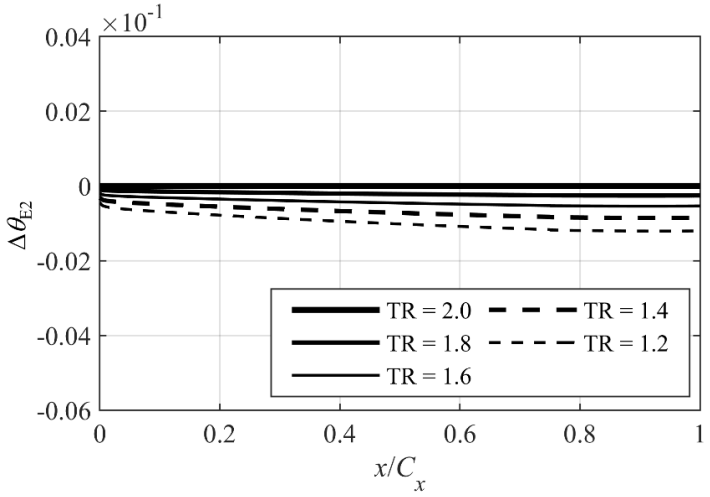

Figure 18: Change in overall cooling effectiveness when the local through-wall-average wall thermal conductivity, $\bar{k}_{\mathrm{w}}$, is changed—in isolation of other local surface BCs—from its value at reference TR.

So far as the trends with streamwise distance are concerned, it is observed (Figure 18) that the change, $\Delta\theta_{\mathrm{E2}}(x)$, is greater at the trailing edge ($x/C_x = 1.0$) than the leading edge ($x/C_x = 0$) by a factor of approximately 2.6. This effect is now explained. As we reduce TR, the absolute change in through-wall-average thermal conductivity, $\Delta\bar{k}_{\mathrm{w}}$, is larger at the trailing edge than the leading edge because the absolute change in wall temperature with TR, ΔT_{w}, is larger at the trailing edge than the leading edge. This is because the absolute wall temperature, T_{w} is greater at the trailing edge, which results from the effectiveness of the mixing layer, $\eta_{\mathrm{ML}}(x)$, decaying with axial distance (see discussion in the context of Figure 11). The greater decrease, $\Delta\bar{k}_{\mathrm{w}}$ (recall this term takes negative value with decreasing TR) at the TE, leads to a greater increase in Biot number than at the leading edge, leading to greater change $\Delta\theta_{\mathrm{E2}}$ at the trailing edge.

In summary, as one moves from the reference TR to lower-than-reference TR, $\bar{k}_{\mathrm{w}}$ decreases, due to a decrease in T_{w}. This leads to a decrease in θ because of an attendant increase in Biot number, which has the effect of reducing the impact of internal cooling on the external

temperature (acts to decouple the surfaces). The effect is quite small in comparison to other effects.

2.8.3 Effect 3: Changes in overall cooling effectiveness due to changes in external heat transfer coefficient

The effect on θ of varying external heat transfer coefficient (h_m)—in isolation of other local surface BCs—from its value at the reference TR is now considered. The distributions $h_m(x)$ are changed to the values they take at TRs in the range $1.2 \leq \mathrm{TR} \leq 2.0$, whilst all other local surface BCs (η_{ML}, $\bar{k}_w$, h_c and λ) are kept equal to the values they take in a converged simulation at the reference TR. If linear superposition can be assumed to be valid, this allows one to determine the impact on θ of changes in h_m (with TR) for fixed conditions of other local surface BCs. These changes are referred to as $\Delta\theta_{E3}(x)$, where the sign convention is $\Delta\theta_{E3}(x) = \theta(x) - \theta(x)^{\mathrm{TR}=2.0}$. The changes $\Delta\theta_{E3}(x)$ are plotted for the range $1.2 \leq \mathrm{TR} \leq 2.0$ in Figure 19.

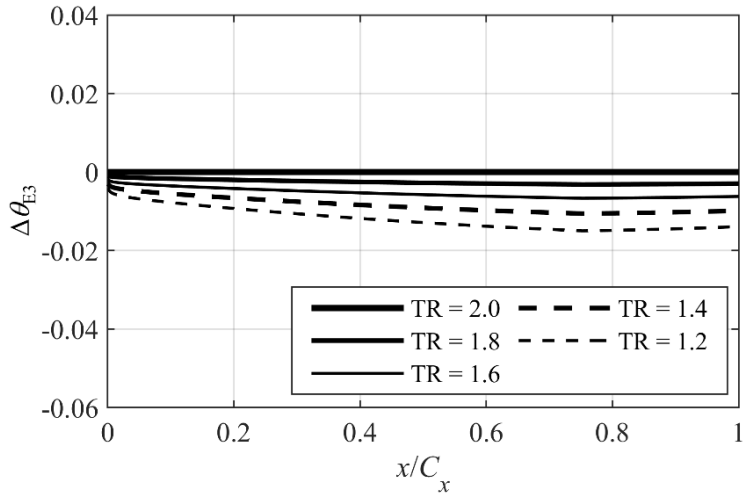

Figure 19: Change in overall cooling effectiveness when external heat transfer coefficient, h_m, is changed—in isolation of other local surface BCs—from its value at reference TR.

The effect of reducing TR from the reference condition is to increase external heat transfer coefficient, which reduces θ due to higher external heat transfer. This effect occurs because of an increase in $\mathrm{Nu}_m(x)$, which is caused by an increase in $\mathrm{Re}_m(x)$. $\mathrm{Re}_m(x)$ increases primarily because of an increase in $\rho_m(x)$ as one moves from the reference TR to lower-than-reference TR. This is due to lower absolute mainstream temperature lowering the average absolute temperature of the

mixing layer. There are smaller contributions of both positive and negative sign associated with changes in other variables. In order of decreasing absolute magnitude of effect these variables are: $k_{\mathrm{m}}(x)$, $u_{\mathrm{m}}(x)$, $\mu_{\mathrm{m}}(x)$ and $c_{p\mathrm{m}}(x)$. These smaller effects are discussed later in this section. The surface-mean changes in overall cooling effectiveness from the value for the reference TR, $\overline{\Delta\theta}_{\mathrm{E3}}$, were -0.003, -0.005, -0.009, and -0.012 for TRs 1.8, 1.6, 1.4 and 1.2 respectively. As percentages of the target mean effectiveness ($\bar{\theta} = 0.500$) these are equivalent to changes of -0.51%, -1.08%, -1.70% and -2.40% respectively.

So far as the trends with streamwise distance are concerned, it is observed (Figure 19) that the change, $\Delta\theta_{\mathrm{E3}}(x)$, is greater at the trailing edge ($x/C_x = 1.0$) than the leading edge ($x/C_x = 0$) by a factor of approximately 3.3. To explain why the magnitude of change increases with streamwise distance the sensitivity of $\theta(x)$ to $h_{\mathrm{m}}(x)$, i.e. the partial derivative of Eq. (11) with respect to $h_{\mathrm{m}}(x)$, is considered

$$\frac{\partial\theta}{\partial h_{\mathrm{m}}}(x) = \frac{-\left(\lambda(x) - \eta_{\mathrm{ML}}(x)\right)\left(\frac{1}{h_{\mathrm{c}}(x)} + \frac{t_{\mathrm{w}}}{\bar{k}_{\mathrm{w}}(x)}\right)}{\left(1 + h_{\mathrm{m}}(x)\left(\frac{1}{h_{\mathrm{c}}(x)} + \frac{t_{\mathrm{w}}}{\bar{k}_{\mathrm{w}}(x)}\right)\right)^2} \tag{30}$$

The partial derivative of Eq. (11) with respect to $h_{\mathrm{m}}(x)$ is plotted in Figure 20 as a function of x/C_x. The change in $h_{\mathrm{m}}(x)$, $\Delta h_{\mathrm{m}}(x)$, between the reference TR (TR = 2.0) and the case of TR = 1.2 (common laboratory temperature ratio) is also plotted. Terms are normalised by values at the leading edge of the plate ($x/C_x = 0$) for which numerical values are: $\partial\theta/\partial h_{\mathrm{m}} = -4.6\times10^{-5}$ W^{-1} m^2 K and $\Delta h_{\mathrm{m}} = -96$ W m^{-2} K^{-1}. It is shown that the general trend with x for the magnitude of $\partial\theta/\partial h_{\mathrm{m}}$ is to increase from the leading edge to plane 2 ($x/C_x = 0.75$) and decrease from plane 2 to the trailing edge. This trend is driven primarily by the term $\lambda(x) - \eta_{\mathrm{ML}}(x)$ (Eq. (30)), which increases with streamwise distance in the region of the leading circuit (dominated by reduction in $\eta_{\mathrm{ML}}(x)$) and decreases with streamwise distance in the region of the trailing circuit (dominated by reduction in $\lambda(x)$). Looking at the change in $h_{\mathrm{m}}(x)$ between TR = 2.0 and TR = 1.2 (common laboratory temperature ratio) it is observed that the magnitude of $\Delta h_{\mathrm{m}}(x)$ is approximately

constant over most of the surface (apart from a significant reduction at the leading edge). Taken in combination the trends for $\partial\theta/\partial h_{\mathrm{m}}$ and $\Delta h_{\mathrm{m}}(x)$ lead to an increasing trend with streamwise distance in the absolute value of term $\Delta\theta_{\mathrm{E3}}(x)$ between planes 1 and 2 and a decreasing trend between planes 2 and 3.

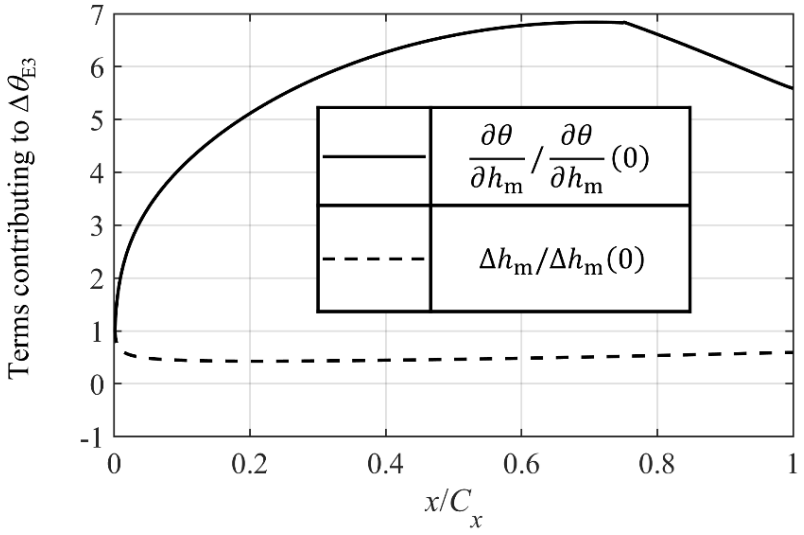

Figure 20: Terms contributing to changes in θ caused by changes in h_{m}, in isolation of other local surface BCs. Both terms are normalised by their respective values at $x/C_x = 0$.

Recall that $h_{\mathrm{m}}(x)$ increases as one moves from the reference TR to lower-than-reference TR because of an increase in $\mathrm{Nu}_{\mathrm{m}}(x)$, due to an increase in $\mathrm{Re}_{\mathrm{m}}(x)$, which is a consequence of an increase in $\rho_{\mathrm{m}}(x)$. To provide insight into second-order effects, a sensitivity analysis of all influences on $h_{\mathrm{m}}(x)$ as TR is varied is now performed. Substituting Eq. (21) into Eq. (22) external heat transfer coefficient can be expressed as

$$h_{\mathrm{m}}(x) = 0.0296x^{-1/5}\rho_{\mathrm{m}}(x)^{4/5}u_{\mathrm{m}}(x)^{4/5}\mu_{\mathrm{m}}(x)^{-7/15}k_{\mathrm{m}}(x)^{2/3}\mathrm{c}_{\mathrm{pm}}(x)^{1/3} \tag{31}$$

The approximate percentage contribution of each variable to changes in surface-averaged external heat transfer coefficient, $\bar{h}_{\mathrm{m}}$, is evaluated by considering the partial derivative of Eq. (31) with respect to each of $\rho_{\mathrm{m}}(x)$, $k_{\mathrm{m}}(x)$, $u_{\mathrm{m}}(x)$, $\mu_{\mathrm{m}}(x)$ and $c_{p\mathrm{m}}(x)$. The results are presented as a bar chart in Figure 21.

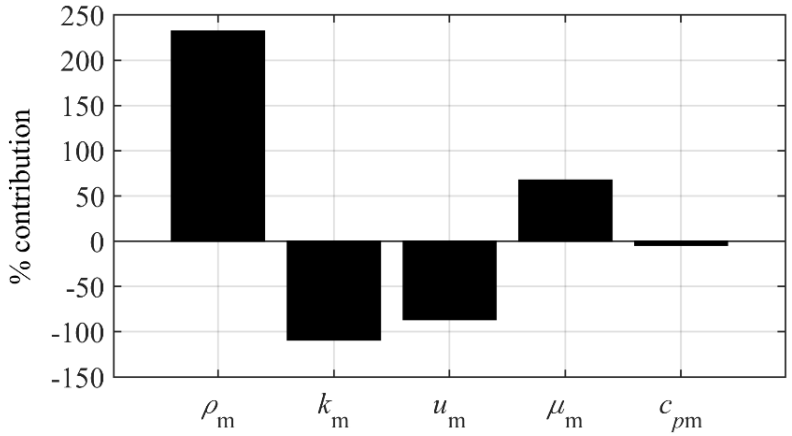

Figure 21: Percentage contributions of five underlying terms to changes in surface-averaged external heat transfer coefficient, $\bar{h}_m$.

Positive percentage contribution implies that the change in that variable—in isolation of all other variables—as one moves from the reference TR to lower-than-reference TR causes an increase in $\bar{h}_m$. Looking at the figure, it is observed that the increase in $\bar{h}_m$ with reducing TR is dominated by the increase in $\rho_m(x)$. This effect has been discussed. There is an additional contribution of the same sign caused by a decrease in $\mu_m(x)$ ($\sqrt{T_m}$ dependence; note negative exponent for μ_m in Eq. (31)) with TR, caused by a reduction in static temperature of the mixing layer, T_m, which is driven by a reduction in mainstream total temperature, T_{01h}. There are terms of opposite sign associated with decreases in k_m and u_m ($\sqrt{T_m}$ dependence; note positive exponents in Eq. (31)). The contribution associated with the change in c_{pm} is small in comparison to other terms.

In summary, as one moves from the reference TR to lower-than-reference TR, there is an increase in external heat transfer coefficient, $h_m(x)$, which causes a decrease in θ. This effect occurs because of an increase in $\mathrm{Nu}_m(x)$, which is caused by an increase in $\mathrm{Re}_m(x)$. $\mathrm{Re}_m(x)$ increases primarily because of an increase in $\rho_m(x)$ as one moves from the reference TR to lower-than-reference TR. This is due to lower absolute mainstream temperature lowering the average absolute temperature of the mixing layer. There are four additional effects, but they are substantially smaller in magnitude and partially cancel each other out.

2.8.4 Effect 4: Changes in overall cooling effectiveness due to changes in internal heat transfer coefficient

The effect on θ of varying internal heat transfer coefficient (h_c)—in isolation of other local surface BCs—from its value at the reference TR is now considered. The distributions $h_c(x)$ are changed to the values they take at TRs in the range $1.2 \leq \mathrm{TR} \leq 2.0$, whilst all other local surface BCs (η_{ML}, $\overline{k}_w$, h_m and λ) are kept equal to the values they take in a converged simulation at the reference TR. If linear superposition can be assumed to be valid, this allows one to determine the impact on θ of changes in h_c (with TR) for fixed conditions of other local surface BCs. These changes are referred to as $\Delta\theta_{E4}(x)$, where the sign convention is $\Delta\theta_{E4}(x) = \theta(x) - \theta(x)^{TR=2.0}$. The changes $\Delta\theta_{E4}(x)$ are plotted for the range $1.2 \leq \mathrm{TR} \leq 2.0$ in Figure 22.

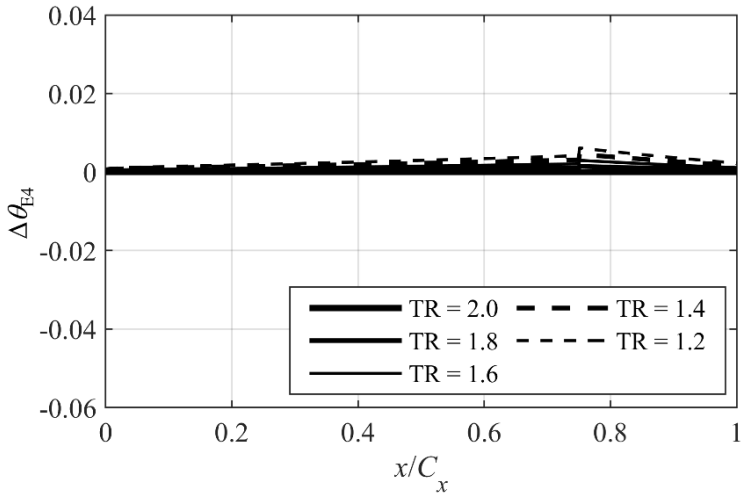

Figure 22: Change in overall cooling effectiveness when internal heat transfer coefficient, h_c, is changed—in isolation of other local surface BCs—from its value at reference TR.

The surface-mean changes in overall cooling effectiveness from the value for the reference TR, $\overline{\Delta\theta}_{E4}$, were 0.0007, 0.0014, 0.0022, and 0.0029 for TRs 1.8, 1.6, 1.4 and 1.2 respectively. As percentages of the target mean effectiveness ($\overline{\theta} = 0.500$) these are equivalent to changes of 0.14%, 0.29%, 0.43% and 0.58% respectively. That is, the impact is a small increase in overall cooling effectiveness. The effect of reducing TR from the reference condition is to very slightly increase the internal heat transfer coefficient, which slightly increases θ due to higher internal heat transfer.

This effect is now explained in detail. Substituting Eq. (14) into Eq. (15), internal heat transfer coefficient can be expressed as

$$h_{\mathrm{c}}(x) = 0.023D(x)^{-0.2}\left(\rho_{\mathrm{c}}(x)u_{\mathrm{c}}(x)\right)^{0.8} c_{p\mathrm{c}}(x)^{0.4}\mu_{\mathrm{c}}(x)^{-0.4}k_{\mathrm{c}}(x)^{0.6} \tag{32}$$

The reason for an increase in $h_{\mathrm{c}}(x)$ as TR is reduced is an increase in the product of local coolant density and velocity, $\rho_{\mathrm{c}}(x)u_{\mathrm{c}}(x)$, due to a (slight) increase in duct-averaged density, $\overline{\rho}_{\mathrm{c}}$. This is equivalent to coolant mass flow rate increasing. The physical basis for the increase in mass flow rate, is that, as TR is reduced, ρ_{c} has lower heat pick-up with local streamwise distance (from cooling channel inlet), leading to lower decrease in ρ_{c} with streamwise distance. This effect arises because at lower TR the mainstream flow has lower absolute driving temperature. Duct-averaged velocity, $\overline{u}_{\mathrm{c}}$, is approximately invariant with TR and therefore its contribution to changes in mass flow rate is second order. As one moves from the reference TR to lower-than-reference TR the following interrelated effects are observed: a very small reduction in static pressure at the leading edge, p_1; and a very small increase in dynamic head at the film cooling hole *exit*, $\rho'_{1\mathrm{c}}u'^2_{1\mathrm{c}}$; a very small increase in channel total pressure loss, $p_{02\mathrm{c}} - p_{01\mathrm{c}}$; an increase in $\overline{\rho}_{\mathrm{c}}$ due to lower mean T_{c}; a reduction in $\overline{\mu}_{\mathrm{c}}$ due to lower mean T_{c}; negligible change in $\overline{u}_{\mathrm{c}}$. Cause and effect is rather moot because all changes are arguably inter-related.

Here trends have been explained in term of duct-average values. Whilst the arguments are true, consider also that at the cooling duct inlet ($x/C_x = 0.75$) $\Delta\theta_{\mathrm{E4}}(x)$ takes its maximum value, but, apparently contradictorily, here the change in h_{c} must be attributed only to changes in u_{c}, the other variables (ρ_{c}, k_{c}, μ_{c}, and $c_{p\mathrm{c}}$) being fixed by the cooling system inlet BCs at this position, and therefore not varying with TR. The mystery is explained considering mass conservation more deeply.

It is worth noting that whilst for the fixed-PR domain-global BC the impact on θ of changes in h_{c} with TR is small, this is not the case for the domain-global BC of fixed exit-Re *and* fixed PR. It is for this reason that the effects are discussed in full, because the *mechanisms* for

sensitivities are similar for both types of domain-global BC. The effect of changing domain-global BCs is considered in section 2.9.

So far as the trends with streamwise distance are concerned, it is observed (Figure 22) that the change $\Delta\theta_{E4}(x)$ is greater at location of the cooling channel inlets ($x/C_x = 0.75$) than at the leading and trailing edges ($x/C_x = 0$ and $x/C_x = 1$ respectively). This is explained by the following logic. There is a global increase in $h_c(x)$ with decreasing TR arising from increased $\rho_c(x)$, which causes a global increase in θ. The product $\rho_c(x)u_c(x)$ is constant along the duct (conservation of mass) so this term in Eq. (32) can be thought of as being responsible for the offset but not the secondary trend. In general (for all TR conditions) there is heat pick up in the coolant flow, increasing in the streamwise direction away from the coolant inlet ($x/C_x = 0.75$). This causes an increase in $k_c(x)$ with streamwise distance ($\sqrt{T_c}$ dependence). The increase in $k_c(x)$ with streamwise distance increases $h_c(x)$ with streamwise distance (see Eq. (32)) which increases θ with streamwise distance. Because the effect is related to the square root of *absolute* temperature it is larger for TR = 2.0 than for lower temperature ratio conditions. When differences $\Delta\theta_{E4}(x)$ are taken, this leads to a negative trend of $\Delta\theta_{E4}(x)$ from the cooling channel inlets ($x/C_x = 0.75$), i.e. a maximum at $x/C_x = 0.75$ and minima at ($x/C_x = 0$ and $x/C_x = 1$ respectively). Because the heat pick up is relatively small (values of $\lambda(x)$ close to unity) the trends are approximately linear (far from reaching asymptotic condition).

To provide insight into second-order effects, a sensitivity analysis of all influences on $h_c(x)$ as TR is varied, is performed. By considering the partial derivatives of Eq. (32) with respect to each of $\rho_c(x)$, $k_c(x)$, $u_c(x)$, $\mu_c(x)$ and $c_{pc}(x)$ the approximate percentage contribution of each variable to changes in duct-averaged internal heat transfer coefficient, $\overline{h}_c$, is evaluated. The results are presented as a bar chart in Figure 23. Positive percentage contribution implies that the change in that variable—in isolation of all other variables—as one moves from the reference TR to lower-than-reference TR causes an increase in $\overline{h}_c$.

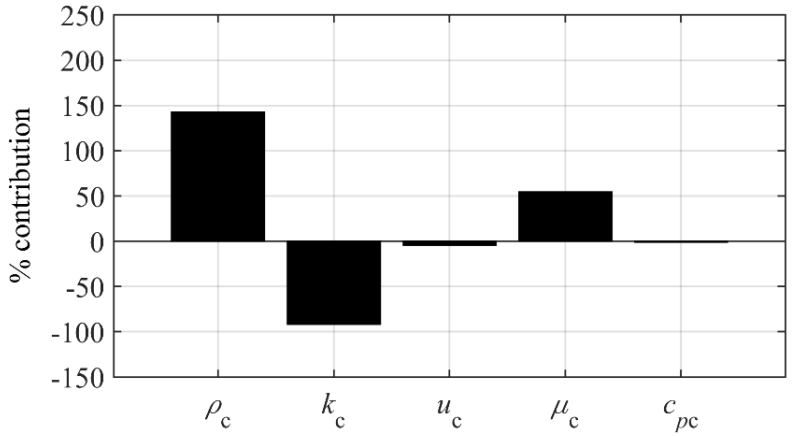

Figure 23: Percentage contributions of five underlying terms to changes in surface-average internal heat transfer coefficient, $\bar{h}_c$.

Looking at Figure 23, it is observed that the increase in $\bar{h}_c$ with reducing TR is dominated by the increase in ρ_c. This effect has been discussed. There is an additional contribution of the same sign caused by a decrease in μ_c with TR ($\sqrt{T_c}$ dependence; note negative exponent for μ_c in Eq. (32)), caused by a reduction in surface-averaged static temperature of the coolant, $\bar{T}_c$, due to a reduction in *absolute* internal convective heat transfer rate as TR is reduced. There is a term of opposite sign associated with a decrease in k_c ($\sqrt{T_c}$ dependence; note positive exponent in Eq. (32)). The contributions associated with the changes in c_{pc} and u_c are small in comparison to other terms. It is noted that, whilst the contribution of u_c to changes in *duct-averaged* internal heat transfer coefficient, $\bar{h}_c$, is small, the local effect can be significant. This apparent contradiction has been discussed.

In summary, as one moves from the reference TR to lower-than-reference TR, there is an increase in internal heat transfer coefficient, $h_c(x)$, which causes an increase in θ. This is primarily driven by an increase in coolant density, $\rho_c(x)$, as TR is reduced. This is because of lower *absolute* heat transfer rate from internal wall to coolant, resulting in lower average absolute coolant temperature. There are four additional effects, but they are smaller in magnitude and partially cancel each other out.

2.8.5 Effect 5: Changes in overall cooling effectiveness due to changes in internal cooling effectiveness

The effect on θ of varying internal cooling effectiveness (λ)—in isolation of other local surface BCs—from its value at the reference TR is now considered. The distributions $\lambda(x)$ are changed to the values they take at TRs in the range $1.2 \leq \mathrm{TR} \leq 2.0$, whilst all other local surface BCs (η_{ML}, $\bar{k}_{\mathrm{w}}$, h_{m} and h_{c}) are kept equal to the values they take in a converged simulation at the reference TR. If linear superposition can be assumed to be valid, this allows one to determine the impact on θ of changes in λ (with TR) for fixed conditions of other local surface BCs. These changes are referred to as $\Delta\theta_{\mathrm{E5}}(x)$, where the sign convention is $\Delta\theta_{\mathrm{E5}}(x) = \theta(x) - \theta(x)^{\mathrm{TR}=2.0}$. The changes $\Delta\theta_{\mathrm{E5}}(x)$ are plotted for the range $1.2 \leq \mathrm{TR} \leq 2.0$ in Figure 24.

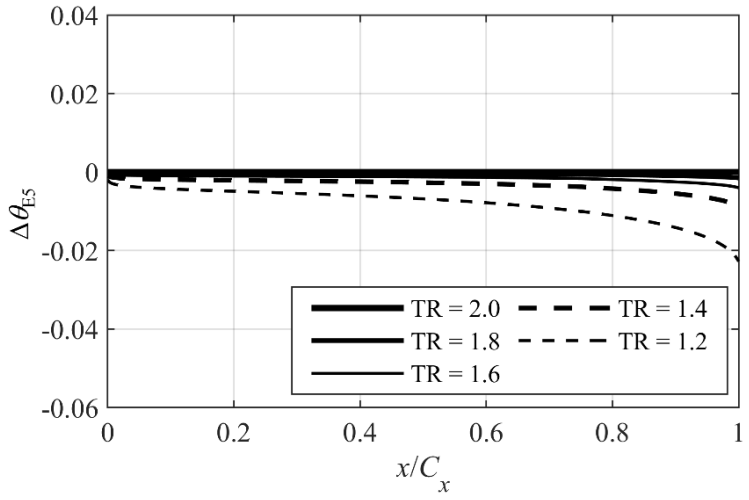

Figure 24: Change in overall cooling effectiveness when internal cooling effectiveness, λ, is changed—in isolation of other local surface BCs—from its value at reference TR.

The effect of reducing TR from the reference condition is to reduce internal cooling effectiveness (greater *non-dimensional* temperature rise in the internal cooling flow), which decreases θ. This effect occurs because of a decrease in TR itself, an effect that arises in the system due to the combination of recovery ratios (i.e. this is a manifestation of the effect of compressibility on the chosen definition of λ). There are smaller contributions of both positive and negative sign associated with changes in other variables. The surface-mean changes in overall cooling effectiveness from the value for the reference TR, $\overline{\Delta\theta}_{\mathrm{E5}}$, were -0.0006, -0.0015, -0.0032, and

-0.0081 for TR = 1.8, 1.6, 1.4 and 1.2 respectively. As percentages of the target mean effectiveness ($\overline{\theta} = 0.500$) these are equivalent to changes of -0.12%, -0.30%, -0.65% and -1.63% respectively.

So far as the trends with streamwise distance are concerned, it is observed (Figure 24) that the change, $\Delta\theta_{E5}(x)$, increases in magnitude with streamwise distance. For the TR = 1.2 case (common laboratory temperature ratio), the magnitude of correction is larger at the trailing edge than the leading edge by factor 10.6. To explain why the magnitude of correction increases with streamwise distance, the partial derivative of θ with respect to λ i.e. the partial derivative of Eq. (11) with respect to λ is considered

$$\frac{\partial\theta}{\partial\lambda}(x) = \frac{1}{1 + h_m(x)\left(\frac{1}{h_c(x)} + \frac{t_w}{\bar{k}_w(x)}\right)} \tag{33}$$

This is plotted in Figure 25 as a function of x/C_x. The change in $\lambda(x)$, $\Delta\lambda(x)$, between the reference TR (TR = 2.0) and the case of TR = 1.2 (common laboratory temperature ratio) is also plotted. Both terms are normalised by their respective values at $x/C_x = 0$, which are 0.19 and -0.012 for $\partial\theta/\partial\lambda$ and $\Delta\lambda(x)$, respectively. The general trend with x for the magnitude of $\partial\theta/\partial\lambda$ is to increase from the leading edge to a maximum at $x/C_x = 0.43$ and decrease (slightly) from $x/C_x = 0.43$ to the trailing edge. This is primarily driven by the distribution of $h_m(x)$ (see discussion in the context of Figure 11), whilst there are second order contributions from the distributions of $h_c(x)$ and $\bar{k}_w(x)$.The general trend for the magnitude of $\Delta\lambda(x)$ is quasi-exponential increase from the leading edge to trailing edge. Taken in combination, the trends for $\partial\theta/\partial\lambda$ and $\Delta\lambda(x)$ lead to an increasing trend with streamwise distance in the absolute value of $\Delta\theta_{E5}(x)$ between the leading edge and trailing edge.

As it is observed in a moment, changes in λ are dominated by changes in TR (definitional issue) and, by considering the partial derivative of λ with respect to TR, $\partial\lambda(x)/\partial$TR (not shown), one can see that the shape of the trend for $\Delta\lambda(x)$ with streamwise distance is dominated by a combination of the distributions $c_c(x)$ and $c_h(x)$. TR and the change in TR, ΔTR, are—by

definition—constant with streamwise distance. The effect of compressibility in the system (i.e. recovery ratios less than unity) is to reduce λ (compared to the case $c_c(x) = c_h(x) = c_m(x) = 1$). For temperature ratios greater than unity, the effect of decreasing TR from TR = 2.0 is to amplify the magnitude of the reduction in λ caused by this compressibility effect.

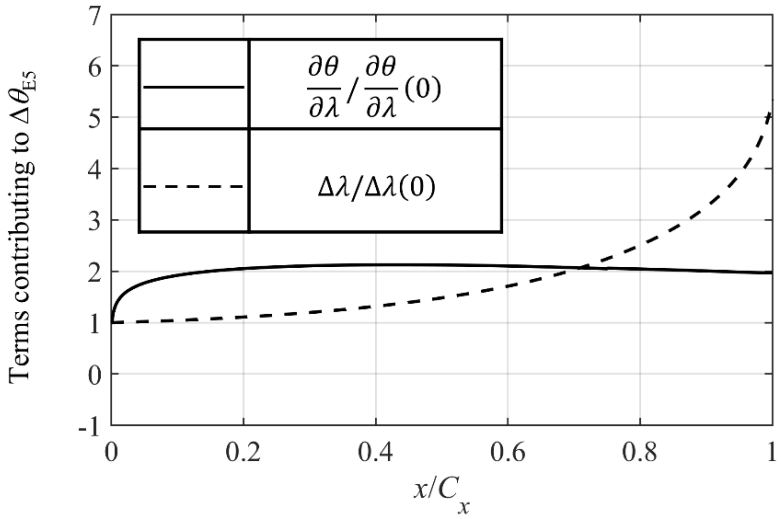

Figure 25: Terms contributing to changes in θ caused by changes in λ, in isolation of other local surface BCs. Both terms are normalised by their respective values at $x/C_x = 0$.

Recall that $\lambda(x)$ decreases as one moves from the reference TR to lower-than-reference TR, and does so definitionally because of a reduction in TR itself. This definitional change is the primary effect. To provide insight into second-order effects, a sensitivity analysis of all influences on $\lambda(x)$ as TR is varied is now performed. The full equation for internal cooling effectiveness arises from energy conservation within the internal cooling duct. Taking the approximation of constant specific heat capacity of the coolant within the leading circuit (i.e. $c_{pc}(x) = c_{p2c}$) and using a local co-ordinate system based on streamwise distance from the channel inlet, x' (where $x' = 0.75C_x - x$ for the leading circuit, and $x' = x - 0.75C_x$ for the TE circuit), applying an energy balance for the internal coolant stream gives the following distribution $\lambda(x')$

$$\begin{aligned}\lambda(x') = \lambda(0) &- \int_0^{x'} \left(\frac{\big(1-\lambda(x')\big)\mathrm{TR}}{(c_c(x') - c_h(x')\mathrm{TR})} \frac{\mathrm{d}c_h(x')}{\mathrm{d}x'} \right) \mathrm{d}x' \\ &- \int_0^{x'} \left(\frac{\lambda(x')}{(c_c(x') - c_h(x')\mathrm{TR})} \frac{\mathrm{d}c_c(x')}{\mathrm{d}x'} \right) \mathrm{d}x' - \int_0^{x'} \left(\frac{h_c(x')w}{\dot{m}_{1c}c_{p2c}} \right) \big(\lambda(x') - \varphi(x')\big) \mathrm{d}x'\end{aligned} \tag{34}$$

where an *internal surface effectiveness*, $\varphi(x)$ is defined by

$$\varphi(x) = \frac{c_{\mathrm{h}}(x)T_{01\mathrm{h}} - T_{\mathrm{w}2}(x)}{c_{\mathrm{h}}(x)T_{01\mathrm{h}} - c_{\mathrm{c}}(x)T_{02\mathrm{c}}} \tag{35}$$

where $T_{\mathrm{w}2}(x)$ is wall internal surface temperature and where the analogy to the definition of $\theta(x)$ (see Eq. (2)) is noted. The further assumption that the recovery ratios are invariant of TR is made, so that—so far as variation with TR is concerned—the functional form of Eq. (34) is $\lambda = f\left(\mathrm{TR}, \varphi, h_{\mathrm{c}}, \dot{m}_{1\mathrm{c}}c_{p2\mathrm{c}}\right)$: i.e. a function of four groups. The sensitivity of surface-averaged internal cooling effectiveness, $\bar{\lambda}$, to each of the four groups is evaluated by partial derivatives of Eq. (34) with respect to each group in turn. Percentage contributions of each variable to the overall change in surface-averaged internal cooling effectiveness ($\Delta\bar{\lambda}$) are presented as a bar chart in Figure 26. Positive percentage contribution implies that the change in that variable—in isolation of all other variables—as one moves from the reference TR to lower-than-reference TR causes a reduction in $\bar{\lambda}$ (greater rate of warming).

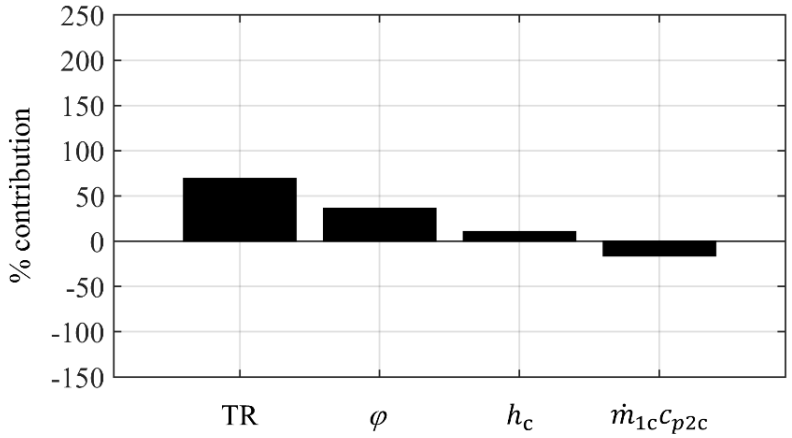

Figure 26: Percentage contributions of four underlying terms to changes in surface-averaged internal cooling effectiveness, $\bar{\lambda}$.

Looking at the figure, it is observed that the reduction in $\bar{\lambda}$ as TR is reduced is dominated by reduction in TR itself. This effect arises due to the definitions of λ and θ, in combination with distributions of recovery ratios $c_{\mathrm{c}}(x)$ and $c_{\mathrm{h}}(x)$. Though purely definitional in nature, the term is real so far as scaling between temperature ratios is concerned. A smaller effect with positive contribution arises because of a decrease in φ. This effect is now explained in detail. Moving from

the reference TR to TR = 1.2, the surface-averaged overall cooling effectiveness, $\bar{\theta}$, changes by -7.4% (see discussion in context of Figure 13), and the surface-averaged internal surface effectiveness, $\bar{\varphi}$ changes by -6.5%. That is, both the inner and outer walls move in the direction of being non-dimensionally warmer. The non-dimensionally warmer internal wall leads to a faster rate of non-dimensional warming of coolant with local streamwise distance along the duct, or a faster rate of decrease of $\lambda(x)$ (see Eq. (7)). The effect of λ decreasing (coolant becoming non-dimensionally warmer)—in isolation of other local surface BCs—is to reduce non-dimensional internal convective heat transfer rate, which has the effect of reducing θ (wall moving towards being non-dimensionally warmer).

A smaller effect also with positive contribution arises because of an increase in internal heat transfer coefficient, $h_c(x)$, as TR is reduced. This is primarily due to an increase in the product of local coolant density and velocity, $\rho_c(x)u_c(x)$, due to an increase in surface-averaged coolant density, $\bar{\rho}_c$, as one moves from the reference TR to lower-than-reference TR. This has been discussed in detail in the context of Figure 12. An increase in $h_c(x)$ leads to an increase in internal convective heat transfer rate (wall to coolant), which leads to a higher rate (with x) of temperature rise in the internal cooling flow and lower internal cooling effectiveness.

Another small effect of negative sign arises because of an increase in local coolant heat capacity flow rate, $\dot{m}_{1c}c_{p2c}$, as TR is reduced. This is primarily due to an increase in coolant mass flow rate, caused by a higher average coolant density. Higher coolant capacity flow rate leads to a lower temperature rise in the internal cooling flow and a higher surface-average internal cooling effectiveness. The effects of decreasing TR and increasing φ and h_c account for +69.2%, $+36.1\%$ and $+10.5\%$ of the overall change in λ, respectively, and are offset by a -15.8% contribution associated with changes in $\dot{m}_{1c}c_{p2c}$.

In summary, as one moves from the reference TR to lower-than-reference TR, the internal cooling effectiveness, λ, decreases (coolant becomes non-dimensionally warmer), which leads to a reduction in θ. This effect is primarily definitional, and arises directly as a result of changes in

TR, in combination with the definitions of λ and θ and distributions of recovery ratios $c_{\mathrm{c}}(x)$ and $c_{\mathrm{h}}(x)$. Though definitional in origin, it is real so far as scaling is concerned between different TR conditions. Three secondary effects arise due to changes in λ arising from internal surface effectiveness, $\varphi(x)$, internal heat transfer coefficient, $h_{\mathrm{c}}(x)$, and local coolant heat capacity flow rate, $\dot{m}_{1\mathrm{c}}c_{p2\mathrm{c}}$. These are small in comparison to the primary term.

2.8.6 Comparison of checksum of changes in overall cooling effectiveness due to each local surface boundary condition with overall change

In this section the overall change in θ, $\Delta\theta^{\mathrm{TR}=1.2}$, as one moves from the reference TR to lower than reference TR is compared with the checksum of changes in θ for each of effect 1 to effect 5 (i.e. $\sum_{j=1}^{5}\Delta\theta_{\mathrm{E}j}$). This is done (arbitrarily) for TR = 1.2, for system 1 and the domain-global BC of fixed PR. The results reported are equally valid for other choices. The comparison is shown in Figure 27.

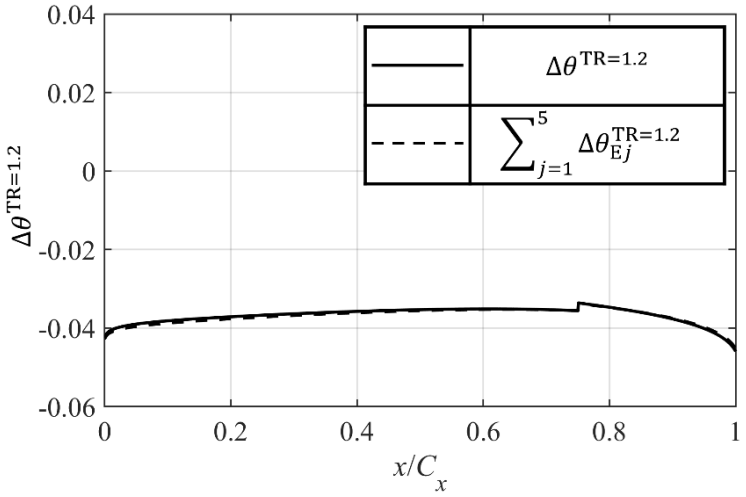

Figure 27: Comparison of overall change in cooling effectiveness with checksum of contributions from each of effect 1 to effect 5. Result is between the reference TR and TR = 1.2.

Looking at the figure, it is observed that the trends for the overall change and checksum are very similar (mean values of -0.037 and -0.037, respectively, with RMS difference between the trends of 0.0004 and maximum difference 0.0007). This demonstrates that linear superposition of the decomposed contributions (due to each of each of the five local surface BCs $\eta_{\mathrm{ML}}(x)$, $\bar{k}_{\mathrm{w}}(x)$,

$h_m(x)$, $h_c(x)$ and $\lambda(x)$) is valid to a high degree of accuracy. This justifies the assumptions made regarding the use of a one-dimensional model to do simplified decomposition of the result.

2.9 Results IV: Sensitivity of results to domain-global boundary conditions

In this section the change in overall cooling effectiveness with TR is compared for two domain-global boundary conditions common in experimental work: fixed PR (BC1); and fixed exit-Re with fixed PR (BC2). It is shown that the change in θ with TR is similar for these two commonly-used boundary conditions.

The change in θ from the reference TR to TR = 1.2 ($\Delta\theta^{TR=1.2} = \theta^{TR=1.2} - \theta^{TR=2.0}$) is presented in Figure 28 as a function of streamwise distance for both domain-global BCs.

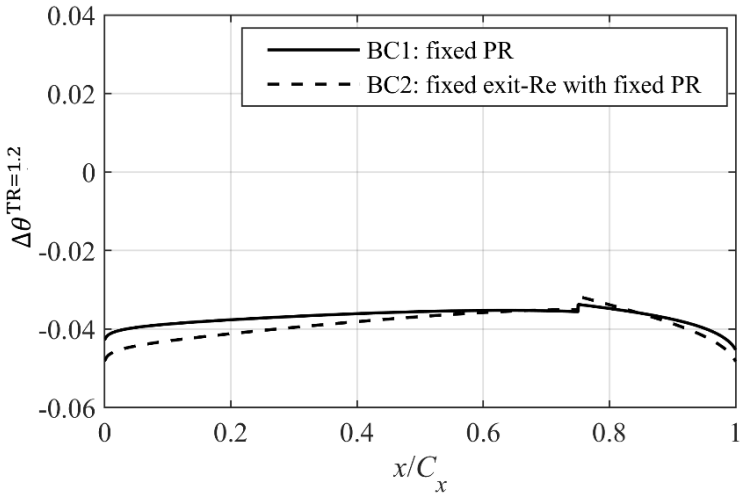

Figure 28: Changes in overall cooling effectiveness between the reference TR and TR = 1.2 as a function of streamwise distance for two domain-global boundary conditions.

Results are (arbitrarily) for system 1. The distributions, $\Delta\theta^{TR=1.2}(x)$, are similar for the two domain-global BCs, with values being bounded by $-0.049 < \Delta\theta^{TR=1.2}(x) < -0.031$, and with mean values $\overline{\Delta\theta}^{TR=1.2} = -0.037$ and -0.039, for BC1 and BC2 respectively. The RMS difference between trends was 0.003, and maximum absolute difference was 0.005. The trend for BC1 was discussed in the context of Figure 13. Although the trend for BC2 is similar, the physical bases for this is different. This will be discussed in detail.

The percentage contributions of each of effects 1–5 are now quantified and compared to changes with TR in surface-averaged $\theta(x)$, $\Delta\overline{\theta}^{\mathrm{TR}=1.2}$, for BC1 and BC2. Results are presented in Figure 29.

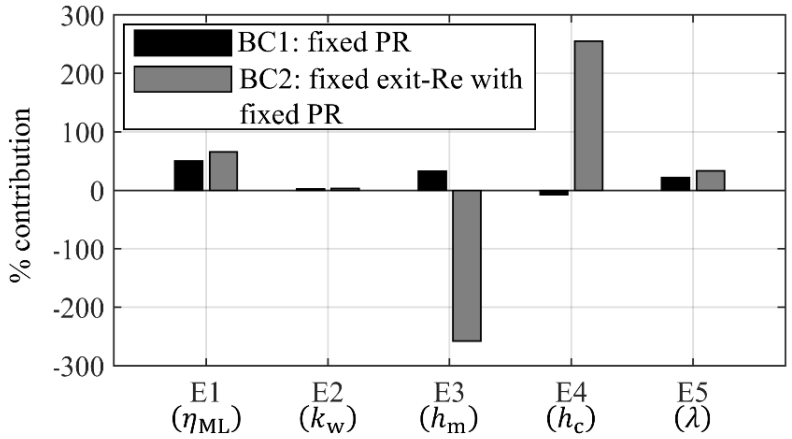

Figure 29: Percentage contributions of each of effects 1–5 to changes in surface-averaged overall cooling effectiveness for two types of domain-global BC. Results are shown for system 1.

Looking at the figure, it is observed that the percentage contributions of $\eta_{\mathrm{ML}}(x)$, $\overline{k}_{\mathrm{w}}(x)$ and $\lambda(x)$ to changes in $\overline{\theta}$ are very similar for BC1 and BC2, whereas the percentage contributions arising from $h_{\mathrm{m}}(x)$ and $h_{\mathrm{c}}(x)$ are very different for the two domain-global BCs. This is in spite of the *overall* change (Figure 28) being similar. As one moves from BC1 to BC2 the contributions from $h_{\mathrm{m}}(x)$ and $h_{\mathrm{c}}(x)$ become much larger in absolute magnitude, but have opposite sign and almost cancel each other out.

First, consider the effect of changes in $\eta_{\mathrm{ML}}(x)$ on changes in $\overline{\theta}$ as one moves from the reference TR to lower-than-reference TR. It was shown (discussion in context of Figure 16 and Figure 17) that changes in $\eta_{\mathrm{ML}}(x)$ were dominated by changes in the ratio of integrated (between 0 and x) entrainment mass flow rate and coolant mass flow rate at plane 1 ($\dot{m}_{\mathrm{e}}(x)/\dot{m}_{1\mathrm{c}}$). This, in turn, was dominated by changes in density ratio $\rho_{1\mathrm{c}}/\rho_{1\mathrm{h}}$ with TR. This change is approximately independent of the choice of domain-global BC, explaining the similar results for BC1 and BC2 in Figure 29.

The effect of changes in $\bar{k}_{\mathrm{w}}(x)$ on changes in $\bar{\theta}$ as one moves from the reference TR to lower-than-reference TR is now considered. The percentage contribution of $\bar{k}_{\mathrm{w}}(x)$ to changes in $\bar{\theta}$ is very similar for BC1 and BC2 (and much smaller in magnitude than the other effects) because changes in $\bar{k}_{\mathrm{w}}$ are caused by changes in T_{w}, which are similar for both BC1 and BC2.

The effect of changes in $h_{\mathrm{m}}(x)$ and $h_{\mathrm{c}}(x)$ on changes in $\bar{\theta}$ as one moves from the reference TR to lower-than-reference TR is now considered. As one moves from BC1 to BC2, the percentage contributions of $h_{\mathrm{m}}(x)$ and $h_{\mathrm{c}}(x)$ to changes in $\bar{\theta}$ become significantly larger in magnitude and change in sign. Despite this significant change, it happens that the combined effects of $h_{\mathrm{m}}(x)$ and $h_{\mathrm{c}}(x)$ essentially cancel for both BC1 and BC2. Consider first that it is primarily the *ratio* $h_{\mathrm{m}}(x)/h_{\mathrm{c}}(x)$ that affects $\theta(x)$ (see Eq. (11)): the absolute values $h_{\mathrm{m}}(x)$ and $h_{\mathrm{c}}(x)$ are of secondary importance. If the ratio were insensitive to the domain-global BCs it would explain this effect. It can be shown that this is so by taking the ratio of Eq. (5) and Eq. (6) and substituting in Eq. (14) and Eq. (21), as well as the definitions of Reynolds number and mass flow rate. One arrives at

$$\frac{h_{\mathrm{m}}(x)}{h_{\mathrm{c}}(x)} = \left(\left(1 + \frac{\dot{m}_{\mathrm{e}}(x)}{\dot{m}_{1\mathrm{c}}}\right)\frac{\mu_{\mathrm{c}}(x)}{\mu_{\mathrm{m}}(x)}\frac{H(x)wx}{D(x)A_{\mathrm{m}}(x)}\right)^{0.8} \times \frac{\mathrm{Pr}_{\mathrm{m}}(x)^{\frac{1}{3}}}{\mathrm{Pr}_{\mathrm{c}}(x)^{0.4}}\frac{k_{\mathrm{m}}(x)}{k_{\mathrm{c}}(x)}\frac{D(x)}{x} \tag{36}$$

In Eq. (36) $h_{\mathrm{m}}/h_{\mathrm{c}}$ as expressed a function of six groups i.e. $h_{\mathrm{m}}/h_{\mathrm{c}} = f\left(\dot{m}_{\mathrm{e}}/\dot{m}_{1\mathrm{c}}, k_{\mathrm{c}}/k_{\mathrm{m}}, \mu_{\mathrm{c}}/\mu_{\mathrm{m}}, \mathrm{Pr}_{\mathrm{m}}, \mathrm{Pr}_{\mathrm{c}}, Hwx/DA_{\mathrm{m}}\right)$. The way in which the variation of each of these groups with TR is affected by the domain-global BCs is now considered. It has already been established that the change in $\dot{m}_{\mathrm{e}}/\dot{m}_{1\mathrm{c}}$ with TR is approximately independent of the choice of domain-global BC. The fluid properties (k_{m}, μ_{m}) and Prandtl number (Pr_{m}) of the mixing layer are functions of the static temperature, $T_{\mathrm{m}}(x)$. This is determined by the external Mach number distribution (approximately invariant of TR) and the total temperature of the mixing layer, $T_{0\mathrm{m}}(x)$. $T_{0\mathrm{m}}(x)$ is determined by considering mass and energy conservation and can be shown (substitution of Eq. (29) into Eq. (26)) to be a function of six groups, $T_{0\mathrm{m}} = f\left(\dot{m}_{\mathrm{e}}(x)/\dot{m}_{1\mathrm{c}}, c_{p01\mathrm{h}}/c_{p1\mathrm{c}}, T_{01\mathrm{h}}, T_{02\mathrm{c}}, \dot{m}_{1\mathrm{c}}/\dot{m}_{3\mathrm{c}}, \varepsilon\right)$. The variation of $c_{p01\mathrm{h}}/c_{p1\mathrm{c}}$ with TR is approximately independent of the choice of domain-global BC.

The cooling system BCs T_{01h} and T_{02c} are fixed, and are therefore inherently independent of the choice of domain-global BC. The groups $\dot{m}_{1c}/\dot{m}_{3c}$ and ε are approximately unchanged with TR. For these reasons T_{0m} is essentially unaltered with the change in domain-global BCs. Consequently, the effects of changes in k_m, μ_m and Pr_m on h_m/h_c are approximately independent of the choice of domain-global BC. So far as Pr_c is concerned, the variation with TR of internal coolant fluid properties k_c, μ_c and c_{pc} are relatively small (see discussion in the context of Figure 23) and similar for both domain-global BCs (driven by θ which is similar for both BCs) and therefore the change in Pr_c with TR is relatively small, and the change between BC1 and BC2 at a given TR even smaller. Finally, the group Hwx/DA_m is determined by geometry and does not depend on the domain global BCs. In practice then, all six of the groups on which h_m/h_c is functionally dependent have a variation with TR that is similar for BC1 and BC2. This means that h_m/h_c has similar variation with TR for both domain-global BCs. For this reason, even though there is a significant decrease in the magnitude of both h_m and h_c for low-TR conditions for BC2 (the decrease in h_m is caused by a decrease in k_m with TR, where it is noted that Re_m and therefore Nu_m are approximately invariant of TR due to the constraint of fixed exit Re; the decrease in h_c is caused by a reduction in Re_c due to a decrease in ρ_c as one reduces p_{02c} with TR in order to maintain a fixed CMPR), because the ratio h_m/h_c is approximately preserved with TR there is little impact on $\overline{\theta}$.

Finally, the effect of changes in $\lambda(x)$ on changes in $\overline{\theta}$ as one moves from the reference TR to lower-than-reference TR is considered. It was shown in Results III that changes in $\lambda(x)$ were dominated by changes in TR. This was described as a definitional issue. This definitional issue is independent of the choice of domain-global BC, explaining the similar results for BC1 and BC2 in Figure 29.

In summary changes in $\theta(x)$ with TR are similar for both types of domain-global BCs common in experimental work (maximum difference between trends of Figure 28 is 13.5% of the mean value of $\Delta\theta^{TR=1.2}$ for BC1). This is because θ is functionally dependent on η_{ML}, $\overline{k}_w$, h_m/h_c,

and λ, and the changes of these groups with TR are similar for the two types of domain-global BC.

2.10 Results V: Sensitivity of results to mean value of overall cooling effectiveness

In this section the sensitivity of the results to the mean value of overall cooling effectiveness is considered. Results are arbitrarily presented for system 1, but are equally applicable to other systems. Three values of mean overall cooling effectiveness at the reference TR, $\bar{\theta}^{\mathrm{TR}=2.0}$= 0.4, 0.5, 0.6, which cover the usual range for HPT NGVs (see, for example, Rhee et al. [27]), are explored. These mean values are achieved by introducing modified correlations for effectiveness of the mixing layer, $\eta'_{\mathrm{ML}} = k_1\eta_{\mathrm{ML}}$, local external Nusselt number, $\mathrm{Nu}'_{\mathrm{m}} = k_2\mathrm{Nu}_{\mathrm{m}}$, and local cooling-channel Nusselt number, $\mathrm{Nu}'_{\mathrm{c}} = k_3\mathrm{Nu}_{\mathrm{c}}$, where k_1, k_2 and k_3 are constants. These constants are constrained to the ranges $0.5 \le \mathrm{k}_1 \le 2.5$ (so that η'_{ML} at the leading edge is constrained to the range 0.2–1.0), $1 \le k_2 \le 2$ and $1 \le k_3 \le 2$ to ensure that plausible deviations from the baseline correlations are considered. There are infinite combinations of k_1, k_2 and k_3 that set a given value of $\bar{\theta}^{\mathrm{TR}=2.0}$. For the $\bar{\theta}^{\mathrm{TR}=2.0}$= 0.4 condition the following is done: vary k_1 alone; vary k_1 and k_2 together. For the $\bar{\theta}^{\mathrm{TR}=2.0}$= 0.6 condition the following is done: vary k_1 alone; vary k_3 alone. By doing so, extrema in the solution range (details beyond scope of discussion) are set. In Figure 30 results are presented for the surface-mean change in overall cooling effectiveness, $\overline{\Delta\theta}$, as a function of TR, for $\bar{\theta}^{\mathrm{TR}=2.0}$= 0.4, 0.5 and 0.6. The range of TR was $1.1 \le \mathrm{TR} \le 2.0$. Values of k_1, k_2 and k_3 are presented in the figure, and were chosen to represent solution-extrema. It is observed that all changes $\overline{\Delta\theta} = f(\mathrm{TR})$ are similar. The mean (across TR conditions) of the local RMS difference between lines (for all lines) normalized by the local value of $\Delta\theta$ was -0.085 (i.e. 8.5% of the local value). The conclusion is that the general result is insensitive to the mean value of overall cooling effectiveness in the usual HPT NGV range $0.4 < \bar{\theta}^{\mathrm{TR}=2.0} < 0.6$. Interrogating

the results (beyond the scope of this discussion) shows that physical arguments presented in the preceding sections remain valid at all mean values of overall cooling effectiveness considered.

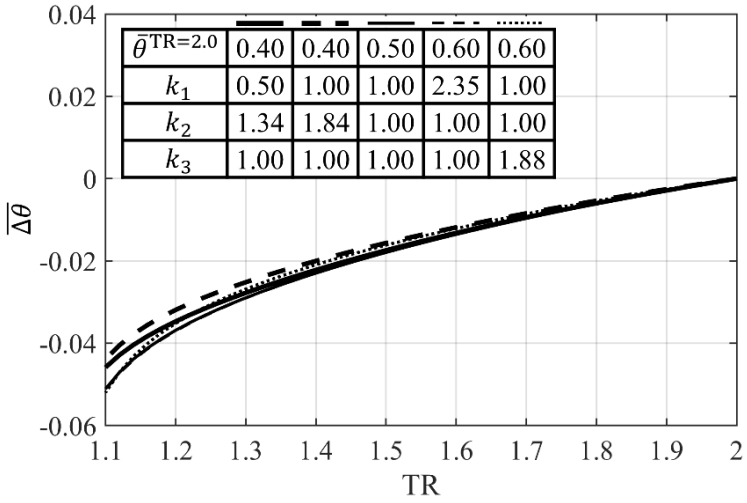

Figure 30: Magnitude of surface-mean change in overall cooling effectiveness, $\overline{\Delta\theta}$, as a function of TR, for three values of mean overall cooling effectiveness, $\bar{\theta}^{TR=2.0}$, for different combinations of k_1, k_2 and k_3.

In summary, the general results of this study are insensitive to the mean value of overall cooling effectiveness. This result is important because it demonstrates that the required correction offset for scaling overall cooling effectiveness from conventional laboratory to engine conditions is insensitive—over a fairly wide range—to non-dimensional operating temperature of the part.

2.11 Results VI: Sensitivity of results to internal cooling system network

In this section results are compared for internal cooling systems 1 to 3 (see Figure 5), to understand the sensitivity of the results to the cooling system network. These three networks represent a fairly wide design range for HPT NGV cooling systems.

In Figure 31, trends are presented for $\Delta\theta^{TR=1.2}$ for all three cooling systems and the fixed-PR domain-global BC, BC1.

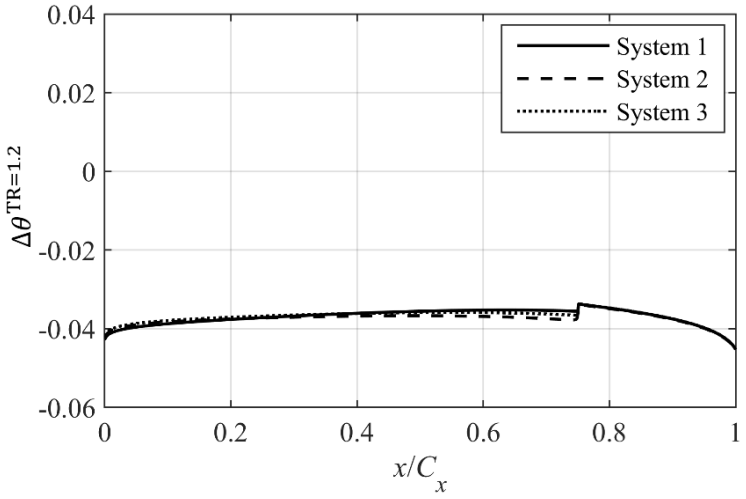

Figure 31: Distributions of change in overall cooling effectiveness between the reference TR to TR = 1.2, $\Delta\theta^{TR=1.2}$, for cooling systems 1–3.

Although results are not presented, the same conclusions hold true for BC2. The trend for system 1 was discussed in the context of Figure 13. The trends for systems 2 and 3 are extremely similar (mean values within 0.45% of each other; mean RMS difference between trends of 0.0007; maximum difference of 0.0023). The conclusion is that the general trend for the change in θ with TR is relatively independent of network choice (maximum difference between trends is 6.2% of the surface-averaged value of $\Delta\theta^{TR\,=\,1.2}$ for system 1).

In order to explain why the trends in $\Delta\theta^{TR\,=\,1.2}$ are very similar for each system, the percentage contributions to $\Delta\theta^{TR\,=\,1.2}$ associated with each of five local surface BCs are compared. These are presented in Figure 32 for each of the three systems. Results are for BC1, but the general conclusions are equally applicable to BC2. Looking at the figure, it is observed that the percentage contribution of each local surface BC is almost identical between systems. This result is now discussed in detail. The five effects driving changes in $\overline{\theta}$ with TR are changes in $\eta_{\mathrm{ML}}(x)$, $\overline{k}_{\mathrm{w}}(x)$, $h_{\mathrm{m}}(x)$, $h_{\mathrm{c}}(x)$ and $\lambda(x)$. It was shown in Results III that the contribution of $\overline{k}_{\mathrm{w}}(x)$ to changes in $\overline{\theta}$ with TR is second order and it was shown in Results IV that $\overline{\theta}$ is insensitive to the absolute values of $h_{\mathrm{m}}(x)$ and $h_{\mathrm{c}}(x)$ as long as the ratio $h_{\mathrm{m}}(x)/h_{\mathrm{c}}(x)$ is preserved when TR is varied. Changes in $\overline{\theta}$ with TR are therefore driven by changes in $\eta_{\mathrm{ML}}(x)$, $h_{\mathrm{m}}(x)/h_{\mathrm{c}}(x)$ and $\lambda(x)$ with TR. Changes in

$\eta_{\mathrm{ML}}(x)$ and $h_{\mathrm{m}}(x)/h_{\mathrm{c}}(x)$ with TR are caused primarily by changes in $\dot{m}_{\mathrm{e}}(x)/\dot{m}_{1\mathrm{c}}$ with TR (see Results IV), whilst changes in $\lambda(x)$ are dominated by changes in TR (definitional issue, see discussion in the context of Figure 24 and Figure 26). The differences in $\dot{m}_{\mathrm{e}}(x)/\dot{m}_{1\mathrm{c}}$ (for fixed TR) between systems originate from variation in channel pressure loss and internal convective heat transfer rate. These effects are small, so $\dot{m}_{\mathrm{e}}(x)/\dot{m}_{1\mathrm{c}}$ is approximately the same for all three cooling systems at a given TR. Thus, changes in $\eta_{\mathrm{ML}}(x)$ and $h_{\mathrm{m}}(x)/h_{\mathrm{c}}(x)$ with TR are similar for all three cooling networks. TR itself is an input parameter, so inherently independent of cooling system choice. Thus, for a given TR, $\lambda(x)$ is approximately unchanged between cooling system network choices. The conclusion is that changes with TR in $\eta_{\mathrm{ML}}(x)$, $h_{\mathrm{m}}(x)/h_{\mathrm{c}}(x)$ and $\lambda(x)$ and, therefore, $\overline{\theta}$ are approximately independent of the choice of cooling system.

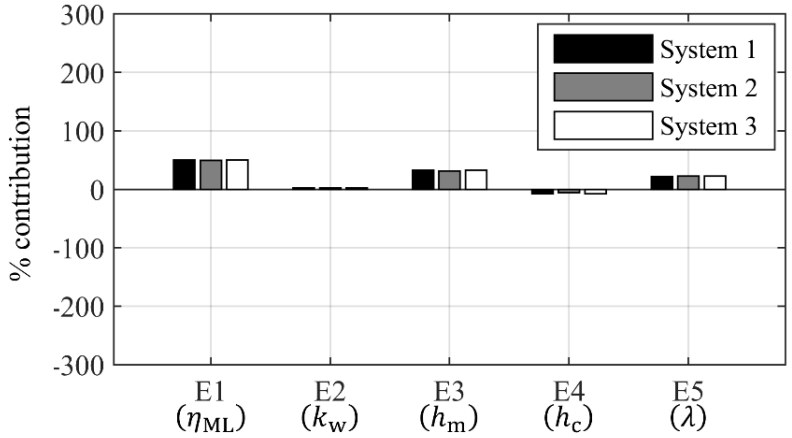

Figure 32: Percentage contribution of each of five local surface BCs to changes in surface-averaged overall cooling effectiveness for systems 1 to 3 (domain-global BC of fixed PR).

In summary, it is concluded that the general results are insensitive to the cooling system network over a fairly wide design range that includes most HPT NGV cooling systems. It is further shown that changes due to each of the five local surface BCs are relatively similar in magnitude in all cases: that is, the driving effects are similar for this range of cooling systems.

2.12 Results VII: Sensitivity to absolute temperature

In this section the sensitivity of the results to the absolute temperature is considered. Typical engine mainstream and coolant total temperatures for large civil aircraft are 1750 K and 875 K (see, for example, Cumpsty and Heyes [25]). To independently consider the impact of absolute temperature and TR the following are taken: engine conditions as $T_{02c} = 875$ K and T_{01h} defined by TR; conventional laboratory conditions as $T_{02c} = 300$ K with T_{01h} defined by TR. Fluid properties for air were taken from Poferl et al. [28] for high (engine) absolute temperatures and Oldfield and Guo [29] for low (rig) absolute temperatures. θ at engine (high) absolute temperatures is referred to as $\theta_{\mathrm{HT}}(x)$, and θ at rig (low) absolute temperatures is referred to as $\theta_{\mathrm{LT}}(x)$. The change in overall cooling effectiveness as one moves from the engine absolute temperatures to rig absolute temperatures is referred to as $\Delta\theta_{\mathrm{ABS}}(x) = \theta_{\mathrm{LT}}(x) - \theta_{\mathrm{HT}}(x)$. It is shown that (at fixed TR) there is an increase in the magnitude of $\theta(x)$ as one moves from high absolute temperature (typical engine values) to low absolute temperature (typical rig values). That is, cooling performance is overestimated at typical rig conditions.

The changes with absolute temperature in overall cooling effectiveness distribution at fixed TR for TRs in the range $1.2 \leq \mathrm{TR} \leq 2.0$, $\Delta\theta_{\mathrm{ABS}}(x)$, are shown in Figure 33 for system 1 and the fixed-PR domain-global BC, BC1.

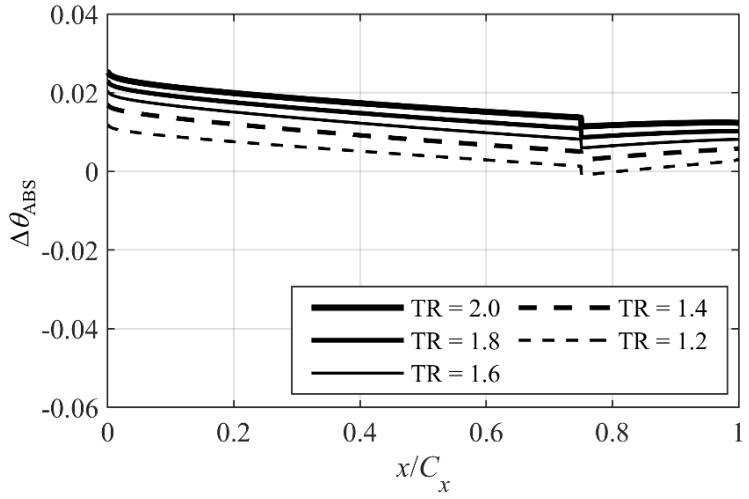

Figure 33: Distributions of change in overall cooling effectiveness, $\Delta\theta_{ABS}(x)$, as one moves from high absolute temperature to low absolute temperature as a function of normalised streamwise distance, x/C_x, for fixed temperature ratios in the range $1.2 \leq TR \leq 2.0$ (system 1 and domain-global boundary conditions of fixed PR).

The effect of moving from high absolute temperature to low absolute temperature *at fixed TR* is to increase effectiveness. This is caused by four effects. The first effect is an increase in $\theta(x)$ due to an increase in $h_c(x)$, which is caused by an increase in the product $\rho_c(x)u_c(x)$, due to an increase in $\bar{\rho}_c$ resulting from a decrease in $T_c(x)$ as one moves from high absolute temperature to low absolute temperature. The second effect is a reduction in $\theta(x)$ due to an increase in $h_m(x)$, which is primarily driven by an increase in $\rho_m(x)$ and decrease in $\mu_m(x)$ as one moves from high absolute temperature to low absolute temperature. The third effect is an increase in $\theta(x)$ due to an increase in $\eta_{ML}(x)$, which is caused by an increase in the ratio of coolant heat capacity flow rate to entrained hot-gas heat capacity flow rate ($\dot{m}_{1c}c_{p1c}/\dot{m}_e(x)c_{p01h}$), which is primarily due to an increase in the coolant-to-mainstream specific heat capacity (c_{p1c}/c_{p01h}) caused by a decrease in c_{p01h} as absolute temperature is reduced. The final effect is a reduction in $\theta(x)$ due to a decrease in $\bar{k}_w(x)$ due to a decrease in T_w as absolute temperature is reduced. There is an additional, second order contribution associated with an increase in $\lambda(x)$ as absolute temperature is reduced.

The surface-mean changes in overall cooling effectiveness as absolute temperature is reduced, $\overline{\Delta\theta}_{ABS}$, were +0.016, +0.014, +0.011, +0.008 and +0.004 for TRs 2.0, 1.8, 1.6, 1.4 and 1.2,

respectively. As percentages of the mean effectiveness at high absolute temperature at each TR (0.483, 0.479, 0.475, 0.468 and 0.458 for TRs 2.0, 1.8, 1.6, 1.4 and 1.2, respectively) these are equivalent to changes of +3.41%, +2.91%, +2.42%, +1.80% and +0.97% respectively.

So far as the trends with streamwise distance are concerned, the positive values $\Delta\theta_{\mathrm{ABS}}(x)$ (physical basis has been discussed) reduce with axial distance as one moves from LE to the TE (factor of 1.8). This effect occurs primarily because the absolute increase in $\eta_{\mathrm{ML}}(x)$ as absolute temperature is reduced is greater at the LE than the TE (see full discussion of this effect in the context of Figure 13 and Figure 16).

In summary, the effect of moving from high absolute temperature (engine) to low absolute temperature (rig) is an increase in $\theta(x)$, which is caused by the sum of effects of increases in $h_{\mathrm{c}}(x)$, $h_{\mathrm{m}}(x)$ and $\eta_{\mathrm{ML}}(x)$ and a decrease in $\bar{k}_{\mathrm{w}}(x)$. The implication is that overall cooling effectiveness is overestimated at lower absolute temperatures by typically 3.20% ($\bar{\theta} = 0.5$, TR = 2.0).

2.13 Results VIII: Effect of combustion product gas properties

In this section the effect on the results of changing gas properties for the mainstream gas from those for combustion products (engine conditions) to air (conventional lab conditions) at high absolute temperature is considered. Simulations are done over a range of TR, taking $T_{02\mathrm{c}}$ = 875 K and $T_{01\mathrm{h}}$ defined by TR. It is shown that—for fixed TR—there is an increase in the magnitude of $\theta(x)$ as gas properties are changed from those for combustion products to those for air. θ evaluated using gas properties for combustion products is referred to as $\theta_{\mathrm{CP}}(x)$, and θ evaluated using gas properties for air is referred to as $\theta_{\mathrm{Air}}(x)$. The change in overall cooling effectiveness as we change from gas properties (GP) for combustion products to those for air is referred to as $\Delta\theta_{\mathrm{GP}}(x) = \theta_{\mathrm{Air}}(x) - \theta_{\mathrm{CP}}(x)$. Fluid properties for combustion products arising from burning kerosene in air (stoichiometric) were taken from Poferl et al. [28]. For the mixing layer the fluid

properties c_{pm}, k_m, R_m, γ_m and μ_m are assumed to take the mass-averaged values of the mainstream (combustion products) and coolant (air) gasses at the local temperature of the mixing layer, T_m. The changes in overall cooling effectiveness distribution at fixed TR for TRs in the range $1.2 \leq \mathrm{TR} \leq 2.0$, $\Delta\theta_{GP}(x)$, are shown in Figure 34 for system 1 and the fixed-PR domain-global BC, BC1.

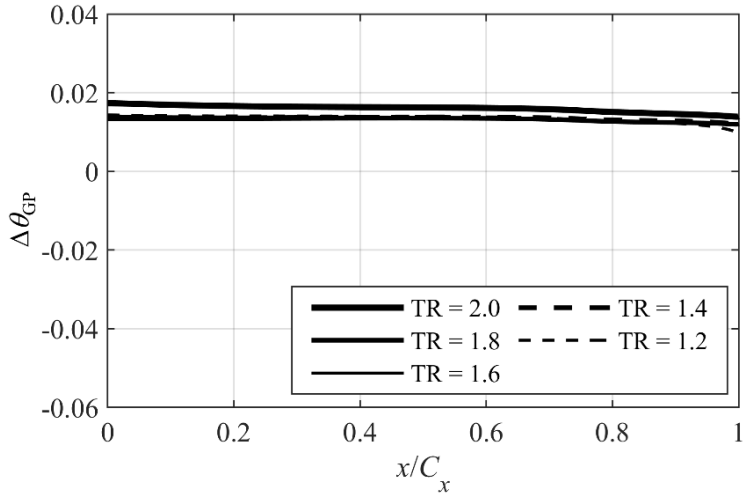

Figure 34: Distributions of change in overall cooling effectiveness, $\Delta\theta_{GP}(x)$, as one changes from fluid properties for combustion products to those for air at fixed TR (in range $1.2 \leq \mathrm{TR} \leq 2.0$) as a function of normalised streamwise distance, x/C_x (system 1 and domain-global boundary conditions of fixed PR).

The effect of changing the mainstream gas from combustion products to air *at fixed TR* is to increase the overall cooling effectiveness. This is caused by two effects. The first effect is a decrease in $h_m(x)$, which is primarily driven by a decrease in $k_m(x)$. The second effect is an increase in $\eta_{ML}(x)$ due to an increase in the ratio of coolant heat capacity flow rate to entrained hot-gas heat capacity flow rate ($\dot{m}_{1c}c_{p1c}/\dot{m}_e(x)c_{p01h}$) caused by an increase in coolant-to-mainstream specific heat capacity ratio (c_{p1c}/c_{p01h}) due to a decrease in c_{p01h} as one changes the mainstream gas properties from those for combustion products to those for air. There are second order contributions of positive sign from increases in $h_c(x)$ and $\lambda(x)$ and of negative sign from a decrease in $\bar{k}_w(x)$ as one changes from combustion products to air.

The surface-mean changes in overall cooling effectiveness as one moves from combustion products to air, $\overline{\Delta\theta}_{GP}$, were +0.016, +0.013, +0.013, +0.013 and +0.014 for TRs 2.0, 1.8, 1.6,

1.4 and 1.2 respectively. As percentages of the mean effectiveness for the cases with combustion products at each TR (0.467, 0.466, 0.461, 0.454 and 0.445 for TRs 2.0, 1.8, 1.6, 1.4 and 1.2, respectively), these equate to changes of +3.42%, +2.85%, +2.83%, +2.97% and +3.04%.

So far as the trends with streamwise distance are concerned, the change in overall cooling effectiveness, $\Delta\theta_{GP}(x)$ is approximately constant with streamwise distance. This is explained by a balance between two primary effects. The first effect—in isolation—would drive a reduction in the magnitude of $\Delta\theta_{GP}(x)$ with streamwise distance because the *absolute* increase in $\eta_{ML}(x)$ as one changes from combustion products to air is greater at the LE than the TE (see full discussion of this effect in the context of Figure 13 and Figure 16). The second effect—in isolation—would drive an increase in the magnitude of $\Delta\theta(x)$ with streamwise distance because the *absolute* decrease in $h_m(x)$ as one changes from combustion products to air is greater at the TE than LE. This second effect occurs primarily because the absolute decrease in both $k_m(x)$ and $c_{pm}(x)$ is greater at the TE than LE due to an increase in the ratio $\dot{m}_e(x)/\dot{m}_{1c}$ i.e. an increase in entrainment rate with streamwise distance (recall that $k_m(x)$ and $c_{pm}(x)$ are evaluated as mass average values at the local mixing layer temperature T_m).

In summary, the effect of changing from combustion products to air is an increase in $\theta(x)$. This is caused by the combined effects of a decrease in $h_m(x)$ and an increase in $\eta_{ML}(x)$. There are second order contributions of positive sign from increases in $h_c(x)$ and $\lambda(x)$ and negative sign from a decrease in $\bar{k}_w(x)$.

2.14 Results IX: Engine-to-rig scaling example

The overall correction offset for scaling from typical engine conditions for large civil aircraft to conventional laboratory conditions is now considered. As an example, consider a case where one moves from typical engine condition for large civil aircraft of $T_{01h} = 1750$ K and $T_{02c} = 875$ K (i.e. TR = 2.0) and combustion products to conventional lab conditions of $T_{01h} = 360$ K and $T_{02c} = 300$ K (i.e. TR = 1.2). This is done two ways. In the first method (M1) correction offsets

are summed for: TR effects in air between the reference TR and TR = 1.2 (i.e. the result of Figure 13 in Results II); effect of moving from high *absolute* temperature to low absolute temperature, $\Delta\theta_{\mathrm{ABS}}^{\mathrm{TR}=2.0}(x)$ (i.e. the result of Figure 33 in Results IV) for TR = 2.0; and the effect of moving from gas properties for combustion products to gas properties for air for TR = 2.0, $\Delta\theta_{\mathrm{GP}}^{\mathrm{TR}=2.0}(x)$ (i.e. the result of Figure 34 in Results VII).

The sum of these effects for this engine-to-rig scaling is referred to as $\Delta\theta_{\mathrm{E-R}}^{\mathrm{M1}}(x)$ where $\Delta\theta_{\mathrm{E-R}}^{\mathrm{M1}}(x) = \Delta\theta^{\mathrm{TR}=1.2}(x)+\Delta\theta_{\mathrm{ABS}}^{\mathrm{TR}=2.0}(x)+\Delta\theta_{\mathrm{GP}}^{\mathrm{TR}=2.0}(x)$. The individual terms and the sum are shown in Figure 35.

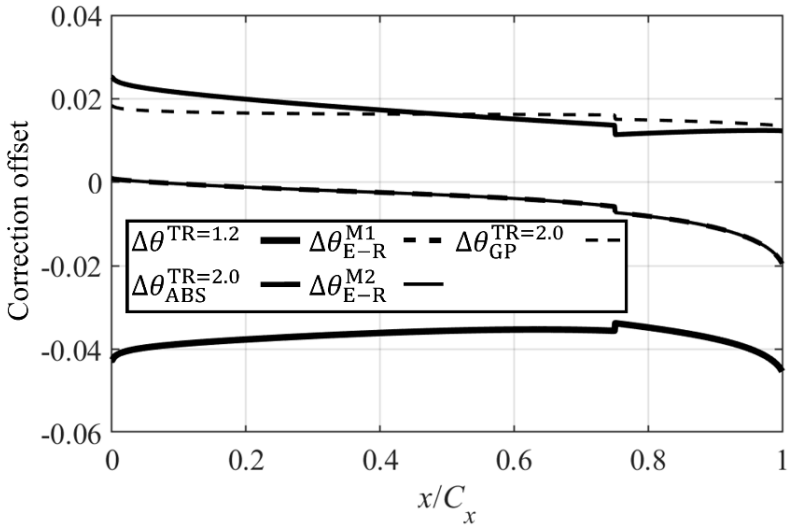

Figure 35: Example of engine-to-rig scaling offsets calculated using two methods: a superposition approach $\Delta\theta_{\mathrm{E-R}}^{\mathrm{M1}}(x) = \Delta\theta(x)+\Delta\theta_{\mathrm{ABS}}^{\mathrm{TR}=2.0}(x)+\Delta\theta_{\mathrm{GP}}^{\mathrm{TR}=2.0}(x)$; and a direct simulation approach $\Delta\theta_{\mathrm{E-R}}^{\mathrm{M2}}(x)$.

The sign convention is inherited from the underlying terms, and is such that $\Delta\theta_{\mathrm{E-R}}^{\mathrm{M1}}(x)$ should be added to the engine condition to scale to the rig condition. In the second method (M2) the engine condition and the rig condition are directly computed and the difference is taken. This is referred to as $\Delta\theta_{\mathrm{E-R}}^{\mathrm{M2}}(x)$. The sign convention is as for $\Delta\theta_{\mathrm{E-R}}^{\mathrm{M1}}(x)$. This ends up being mathematically identical to the first method because the two simulations of method 2 form a subset of the four simulations of method 1 i.e. it is merely a consistency check. This is also shown in Figure 35. In this example the system 1 network with the fixed-PR domain-global BC is used.

Looking at Figure 35 it is first noted that methods M1 and M2 give identical results, showing consistency ($\Delta\theta^{M1}_{E-R}(x) = \Delta\theta^{M2}_{E-R}(x) = \Delta\theta_{E-R}(x)$). The overall engine-to-rig correction is negative in sign, increasing from LE to TE in an approximately linear manner over most of the range of streamwise distance, and with average value $\overline{\Delta\theta}_{E\text{-}R} = -0.0045$ (-0.90% of $\bar{\theta} = 0.5$). For the purpose of scaling between engine and rig results it is a welcome co-incidence that the relatively large (in absolute terms) correction offsets sum to a small value. To provide a look-up graph that may be of practical use, this analysis is repeated for all TR in the range $1.1 \leq TR \leq 2.0$, to calculate the characteristic $\overline{\Delta\theta}_{E\text{-}R} = f(TR)$. For each TR, the trend with streamwise distance is the sum of the line for the relevant TR from Figure 8, the line TR = 2.0 from Figure 28, and the line TR = 2.0 from Figure 29.

The surface-mean value is given as a function of TR in Figure 36. The correction offset is approximately -0.019 for TR = 1.1, and approximately +0.032 for TR = 2.0, and has a decreasing gradient with TR as TR increases. For TR = 1.25 the characteristic has a value of zero.

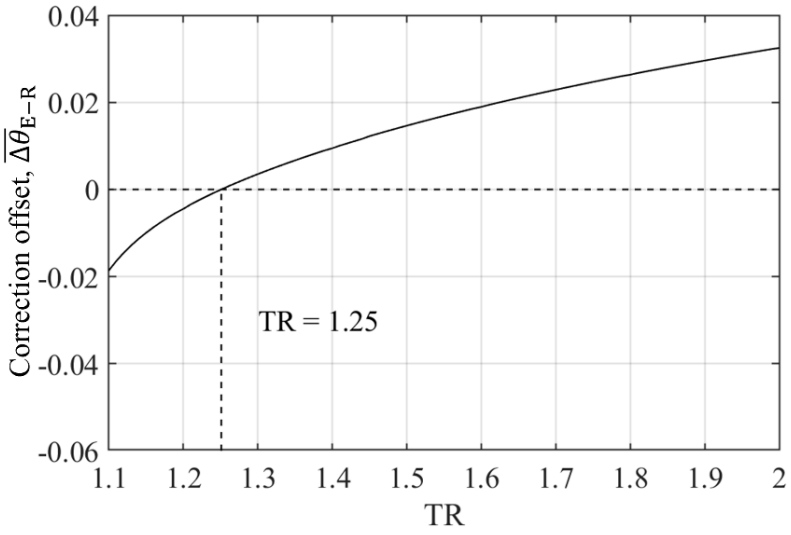

Figure 36: Overall engine-to-rig correction offset $\overline{\Delta\theta}_{E\text{-}R}$ as a function of TR.

The conclusion is that laboratory experiments can both under-estimate or over-estimate engine values of overall cooling effectiveness but only by a very small margin. Testing at TR = 1.25 there is no required correction offset between conventional laboratory and engine conditions. For practical purposes this can be regarded as a key result of this chapter.

2.15 Results X: Sensitivity to definitions of overall cooling effectiveness

In this section the sensitivity of the results to the definition of overall cooling effectiveness is considered. The results—so far—have been presented in terms of the following definition of overall cooling effectiveness (Eq. (2))

$$\theta(x) = \frac{c_{\mathrm{h}}(x)T_{01\mathrm{h}} - T_{\mathrm{w1}}(x)}{c_{\mathrm{h}}(x)T_{01\mathrm{h}} - c_{\mathrm{c}}(x)T_{02\mathrm{c}}}$$

This is the preferred definition in chapters 2 and 4 because it has three particular advantages. Firstly, it limits the range of θ to $0.0 \leq \theta \leq 1.0$. This is so because of the following theoretically limiting temperatures: a theoretical maximum external temperature of $c_{\mathrm{h}}(x)T_{01\mathrm{h}}$ in the case of no cooling flow and an adiabatic wall; a theoretical minimum external temperature of $c_{\mathrm{c}}(x)T_{02\mathrm{c}}$ for the case of perfect cooling (no entrained hot gas) and an adiabatic wall. Secondly, the definition of Eq. (2) accounts for compressibility effects in the hot stream and mixing layer through the use of the recovery ratios $c_{\mathrm{h}}(x)$ and $c_{\mathrm{c}}(x)$. The third advantage of this definition is the close parallel with the chosen definition of η_{ML}, which was defined so as to limit the range of η_{ML} to $0.0 \leq \eta_{\mathrm{ML}} \leq 1.0$ and to account for compressibility effects in the hot stream and mixing layer. It is noted that Michaud et al. [30] used the same definition (Eq. (2)) but their recovery ratio distribution, $c_{\mathrm{c}}(x)$, was calculated using the Mach number distribution associated with a mixing layer with entrainment rate distribution that satisfied a particular desired distribution of $\eta_{\mathrm{ML}}(x)$. In the case considered in this chapter, the recovery ratio distribution was calculated using the Mach number distribution associated with a *hypothetical perfect cooling film* (no entrainment). This very subtle distinction ensures that θ is *strictly* limited to the range $0.0 \leq \theta \leq 1.0$. This pedantic distinction arises because of the co-dependence of Mach number distribution and entrainment rate because the external static pressure distribution is affected by the mass flow rate (and corresponding cross-sectional area) of the mixing layer.

Taking the change in overall cooling effectiveness with TR (result of Figure 14) the surface-mean, $\overline{\Delta\theta}$, is computed for each TR, and plotted as a function of TR (i.e. $\overline{\Delta\theta} = f(\mathrm{TR})$) in Figure 37.

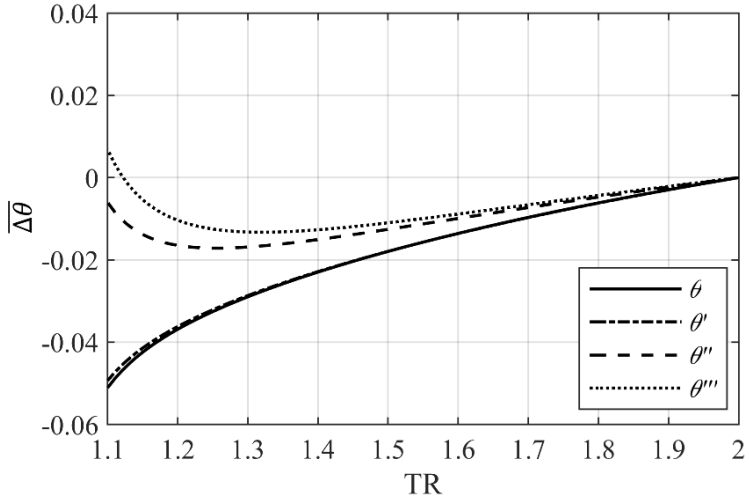

Figure 37: Magnitude of surface-mean of the change in overall cooling effectiveness, $\overline{\Delta\theta}$, as a function of TR, for four definitions of overall cooling effectiveness.

The trend is non-linear, with an increase in gradient as one moves from the reference TR to lower-than-reference TR. This trend is now compared with trends arising from three other definitions of overall film cooling effectiveness.

In previous work from the same group (see Kirollos et al. [9] and Michaud et al. [31]) an alternative definition of effectiveness has been used, in which the terms $c_{\mathrm{h}}(x)T_{01\mathrm{h}}$ and $c_{\mathrm{c}}(x)T_{02\mathrm{c}}$ in the denominator are replaced by $T_{01\mathrm{h}}$ and $T_{02\mathrm{c}}$, giving

$$\theta'(x) = \frac{c_{\mathrm{h}}(x)T_{01\mathrm{h}} - T_{\mathrm{w1}}(x)}{T_{01\mathrm{h}} - T_{02\mathrm{c}}} \tag{37}$$

i.e. total temperatures are used in place of recovery temperatures in the denominator. Justifications for using $T_{02\mathrm{c}}$ instead of $c_{\mathrm{c}}(x)T_{02\mathrm{c}}$ in the denominator might be as follows: firstly, within the cooling duct the flow is entirely incompressible, so any effect in the conjugate system arising from the *internal cooling* is associated with a limiting temperature unaffected by compressibility (recovery) effects; on the external surface the only region in which compressibility effects are significant (the late surface) is one in which η_{ML} takes low values (very dilute cooling flow in the mixing layer). The fundamental justification for using $T_{01\mathrm{h}}$ in place of $c_{\mathrm{h}}(x)T_{01\mathrm{h}}$ in the

denominator is less clear, but likely arises from historical convention. The trend for the average change (from the reference TR) in $\theta'(x)$ with TR ($\overline{\Delta\theta'}$) is shown, as a function of TR, in Figure 37. The trend is extremely similar to that for $\overline{\Delta\theta}$. This can be understood by performing a similar analysis to that leading to Eq. (11), but for $\theta'(x)$, through which it can be shown that $\theta'(x)$ is rendered into the form $\theta'(x) = \beta_1(x)\theta(x)$ where $\beta_1(x) = (c_{\mathrm{h}}(x)\mathrm{TR} - c_{\mathrm{c}}(x))/(\mathrm{TR} - 1)$. It is observed that over a wide range of TR $\beta_1 \cong 1$, giving $\theta' \cong \theta$.

Although there is little difference in practice between using θ' and θ, it is argued that θ' is incomplete for two reasons: it does not make use of the two theoretically limiting temperatures and therefore does not constrain overall cooling effectiveness between 0 and 1; it has a weaker parallel with the chosen definition of η_{ML}(see Eq. (3)).

A third definition which is probably that in widest use (see, for example, Albert and Bogard [12], Williams et al. [32], Nathan et al. [33] and Dyson et al. [34]) is one in which recovery temperatures are used in neither the numerator or denominator. It is

$$\theta''(x) = \frac{T_{01\mathrm{h}} - T_{\mathrm{w1}}(x)}{T_{01\mathrm{h}} - T_{02\mathrm{c}}} \tag{38}$$

This parameter is not used in this chapter because it fails to account for compressibility and does not use either of the two limiting temperatures in the system. This means both that overall cooling effectiveness is not constrained to a rational range, and that artificial sensitivity to TR is introduced (this is discussed in a moment). The trend for the average change (from the reference TR) in $\theta''(x)$ with TR ($\overline{\Delta\theta''}$) is shown, as a function of TR, in Figure 37. As one moves from the reference TR to lower-than-reference TR, $\overline{\Delta\theta''}$ decreases from zero (by definition) at TR = 2.0, to a minimum at TR = 1.24. Below TR = 1.24, $\overline{\Delta\theta''}$ increases asymptotically to a limiting TR of unity. This can be understood by performing a similar analysis to that leading to Eq. (11), but for θ'', through which $\theta''(x)$ is rendered into the form $\theta''(x) = \beta_1(x)\theta(x) + \beta_2(x)$ where $\beta_2(x) = \big(1 - c_{\mathrm{h}}(x)\big)\mathrm{TR}/(\mathrm{TR} - 1)$. It is observed that, as one decreases TR towards unity, $\beta_2(x)$

increases asymptotically. The combination of a reduction in $\theta(x)$ and increase in $\beta_2(x)$ as one decreases TR leads to the trend for $\overline{\Delta\theta''}$ in Figure 37. Using this common definition the correction $\overline{\Delta\theta''}$ *explodes* at low TR as an artefact of failing to include compressibility in the definition.

Finally, consider a definition proposed by Luque et al. [8], which included a so-called recovery and redistribution parameter, $\Re(x)$, designed to account for compressibility effects and the redistribution of heat transferred from the compressible external flow domain to the supposedly (i.e. notwithstanding the transfer of heat from the compressible side, which—in fact—is coupling to a compressible region) incompressible internal flow domain. The definition of overall cooling effectiveness, $\theta'''(x)$, was

$$\theta'''(x) = \frac{\Re(x)T_{01\mathrm{h}} - T_{\mathrm{w1}}(x)}{\Re(x)T_{01\mathrm{h}} - T_{02\mathrm{c}}} \tag{39}$$

This defines an overall cooling effectiveness that is invariant of TR for the particular case *of all other non-dimensional groups being fixed as TR is varied.* This situation is of theoretical interest, but does not correspond to the typical engine-to-rig scaling problem, in which non-dimensional groups *vary sympathetically with TR* (key distinction with this study). This is plotted for completeness in Figure 37.

In summary, the results are highly dependent on the definition of overall cooling effectiveness, and care needs to be given to the definition of this parameter. There are rational reasons to use a fully compressible form of this parameter and the form of Eq. (2) is recommended.

2.16 Results XI: sensitivity to lateral conduction

In this section the main results, for the case when lateral conduction terms are included, are presented and it is demonstrated that the results are insensitive to lateral conduction.

Resulting overall cooling effectiveness distributions, $\theta(x)$, for system 1 at the reference TR and air at low absolute temperature, when lateral conduction terms are turned off and on, are presented in Figure 38.

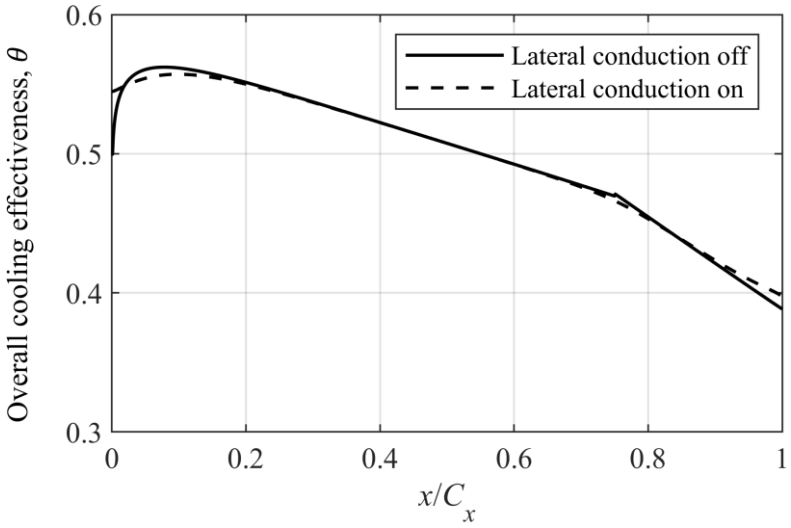

Figure 38: Comparison of overall cooling effectiveness distributions, $\theta(x)$, for cooling system network 1 at the reference TR and air at low absolute temperature when lateral conduction terms are turned off and on.

The results are very similar in form when lateral conduction terms are turned on. That is, an increase in $\theta(x)$ with streamwise distance to a maximum value at approximately $x/C_x = 0.10$ and a subsequent reduction in $\theta(x)$ as one moves towards the TE. RMS difference between trends was 0.004, and maximum difference 0.045. Two salient effects of turning on lateral conduction terms are noted: the gradient of the local change in $\theta(x)$ at the inlet to the TE circuit ($x/C_x = 0.75$) has reduced magnitude (i.e. the local distribution of $\theta(x)$ in this region is more smooth); and the value of $\theta(x)$ at the LE is larger, with a smaller subsequent increase in $\theta(x)$ in the range $0.00 \leq x/C_x \leq 0.10$. These phenomena arise because the effect of lateral conduction is to redistribute heat in the streamwise direction, which acts to reduce the magnitude of local gradients in $\theta(x)$ with streamwise distance.

The resulting changes in overall cooling effectiveness distribution, $\Delta\theta^{\mathrm{TR}=1.2}(x)$, when lateral conduction terms are turned off and on are presented in Figure 39.

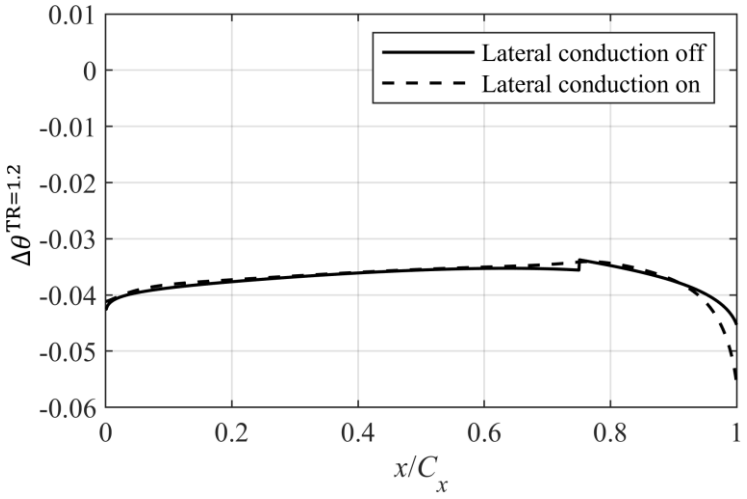

Figure 39: Changes in overall cooling effectiveness between the reference TR and TR = 1.2 as a function of streamwise distance when lateral conduction terms are turned off and on. Results are for system 1, domain-global boundary conditions of fixed PR and air at low absolute temperature.

Looking at Figure 39, it is demonstrated that the effect of reducing TR from the reference condition is to reduce effectiveness. The results are almost identical when lateral conduction terms are turned on but the local distribution of $\Delta\theta(x)$ at the TE-circuit inlet (x/C_x = 0.75) is smoother due to the effect of lateral heat redistribution (this effect has been discussed). RMS difference between trends was 0.0012, and maximum difference 0.0014. These correspond to percentage differences of 3.3% and 3.9% respectively i.e. they are very small differences. This is because the lateral conduction heat flow terms are very small compared to the corresponding through-wall heat flow terms. This is best understood by considering that the length scale most associated with lateral conduction i.e. the wall thickness is a factor of 100 smaller than the length scale most associated with through-wall conduction i.e. the streamwise length.

In summary, the presence of lateral conduction terms has a very small effect on all mechanisms driving changes in overall cooling effectiveness with temperature ratio (these were discussed in Results III). The corresponding impact on the results presented in previous sections is therefore very small.

2.17 Conclusions

In this chapter, the relationship between overall cooling effectiveness (or so-called *metal effectiveness*) and mainstream-to-coolant total temperature ratio (TR) is considered. The problem is considered using both fundamental scaling arguments and using results from a low-order numerical network model. Results have been presented for three different cooling system networks, and two types of domain-global BCs (the macro-boundary-conditions relevant to laboratory or engine tests).

The key conclusion of this chapter is that (for low absolute temperature and for air) overall cooling effectiveness decreases as one moves from the reference TR to lower-than-reference TR. Moving between a typical engine temperature ratio for large civil aircraft of 2.0 to a common laboratory temperature ratio of 1.2 leads to a change in effectiveness of approximately -0.040 for a mean effectiveness of 0.500. This is equivalent to a -8% change. The rate of change accelerates with decreasing temperature ratio. The result was surprisingly insensitive to the cooling system network and the type of domain-global boundary conditions imposed. When the changes due to both *absolute* temperature and combustion products are considered (the engine-to-rig scaling problem) the correction offset can be both positive or negative, with a sweet-spot at TR = 1.25, for which the correction offset is zero.

It is argued using a simple zero-dimensional model that the overall cooling effectiveness can be expressed—crudely—as a function of five local surface boundary conditions, and that insights can be gained by decomposing results into contributions arising from each. There is some dependence of the results on the type of domain global boundary conditions. For the fixed-PR BC, a reduction in θ is caused by reductions in η_{ML}, λ and an increase in h_{m} as one moves from the reference TR to lower-than-reference TR whilst the contributions from changes in $\overline{k}_{\mathrm{w}}$ and h_{c} are second order. For the BC of fixed exit Re *and* fixed PR, a reduction in θ is caused by a combination of reductions in η_{ML}, λ, h_{m} and h_{c} as one moves from the reference TR to lower-than-reference TR, whilst the contribution from changes in $\overline{k}_{\mathrm{w}}$ was small.

There are seven supplementary conclusions:

i) Sensitivity to domain-global BCs. The change in θ as one moves from the reference TR to lower-than-reference TR was relatively insensitive to the domain-global BCs. This means the general results are applicable to both fixed PR and fixed exit Re with fixed PR BCs.

ii) Sensitivity to mean value of overall cooling effectiveness. The change in θ as one moves from the reference TR to lower-than-reference TR was relatively insensitive to the value of $\overline{\theta}$ at the reference TR. This means the general results are applicable to a wide range of $\overline{\theta}$ values.

iii) Sensitivity of results to internal cooling system network. The change in θ as one moves from the reference TR to lower-than-reference TR was highly insensitive to the details of the internal cooling network (mean corrections $\Delta\theta^{\mathrm{TR}=1.2}$ were within 0.45% of each other for three cooling network styles). This means that the general results are applicable to a wide range of internal cooling networks.

iv) Sensitivity to absolute temperature. The effect at fixed TR of moving from high absolute temperature (engine conditions) to low absolute temperature (conventional laboratory conditions) is an increase in the mean value of θ. For engine conditions of temperature ratio and absolute temperature ($T_{01\mathrm{h}} = 1750$ K, $T_{02\mathrm{c}} = 875$ K), there is a mean change in θ of +0.016 (+3.2% of $\overline{\theta} = 0.5$) when moving to conventional lab conditions of absolute temperature ($T_{01\mathrm{h}} = 600$ K, $T_{02\mathrm{c}} = 300$ K). The implication is that overall cooling effectiveness is overestimated at lower absolute temperatures by typically 3.41%.

v) Combustion product effects. The effect at fixed TR of changing gas properties for the mainstream gas from combustion products (engine conditions) to air (conventional lab conditions) at high absolute temperature is an increase in θ. At engine conditions of temperature ratio, there is a mean change in θ of +0.016 (+3.2% of $\overline{\theta} = 0.5$). Overall cooling effectiveness is overestimated by using air instead of combustion products.

vi) Engine-to-rig scaling. Taking the effect of TR, absolute temperature, and combustion products together, laboratory experiments can under-estimate or over-estimate overall cooling effectiveness. Moving from engine conditions of temperature ratio, absolute temperature and mainstream gas properties, to rig conditions in the range 1.2 < TR < 1.4, there is a mean change in θ which falls in the range $-0.005 < \overline{\Delta\theta} < 0.010$, i.e. within 2.0% of $\overline{\theta} = 0.5$. That is, the correction is small for the conventional laboratory range. There is a sweet-spot for TR = 1.25, at which condition the correction offset between engine and rig conditions is zero. For practical purposes this can be regarded as a key result of this chapter.

vii) Sensitivity to definitions of overall cooling effectiveness. The variation of overall cooling effectiveness with TR is highly dependent on the definition of overall cooling effectiveness used, and care needs to be given to the definition of this parameter. There are compelling rational reasons to use a fully compressible form of this parameter and the form of Eq. (2) is recommended.

It is believed that this is the first study to systematically quantify and explain from first principles the effect of TR on overall cooling effectiveness. This is done for a number of cooling system networks and for domain-global boundary conditions relevant to laboratory and engine testing. The resulting scaling charts allow scaling of overall effectiveness data between typical low-temperature-ratio laboratory tests and engine temperature ratios.

3. Impact of temperature ratio on overall cooling effectiveness: experimental validation of a scaling theory

In this chapter, an experimental study of the impact of mainstream-to-coolant temperature ratio on overall cooling effectiveness (or so-called metal effectiveness, θ) is presented. Experimental measurements of overall cooling effectiveness of a fully-cooled (internal and film) flat plate were performed in the mainstream-to-coolant temperature ratio (TR) range $1.07 \leq \mathrm{TR} \leq 1.62$. The high-temperature-capable facility used for the study was purpose built for these tests (see Naidu and Povey [17]). The experimental data show that overall cooling effectiveness (θ) decreases with decreasing temperature ratio. This result is in accord with the modelling work of Naidu and Povey [17]—some of which is rehearsed in this chapter—and the theoretical work of chapter 2. The experimental data of this chapter are compared to those studies, and it is found that all three results are in broad agreement so far as the trend with TR is concerned. The correction in overall cooling effectiveness between engine (TR = 2.0) and conventional rig (TR = 1.2) conditions is approximately $\Delta\theta = -0.017$ (for surface-averaged overall cooling effectiveness of $\theta = 0.51$). The correction is relatively small. By decomposing the results into the individual changes associated with each local surface boundary condition, the change in overall cooling effectiveness with temperature ratio is explained in terms of changes in: external heat transfer coefficient (responsible for −582% of the overall effect); internal heat transfer coefficients for Surface 2−5 (+396%, +11.6%, +69.3% and +1.24%, respectively); film effectiveness of the mixing layer (+111%); wall thermal conductivity (+49.7%); and internal cooling effectiveness (+43.1%). Several significant effects are shown to be in competition.

The results of this chapter are—to the authors' knowledge—the first published data validating the theory of scaling of overall cooling effectiveness between different temperature ratio conditions (e.g. between conventional laboratory conditions and engine conditions).

3.1 Introduction

Research in the open literature relating to overall thermal performance of components could be categorised as being of a bottom-up or top-down philosophy (see discussion in Kirollos et al. [9]). *Bottom-up* refers to studies in which individual local surface boundary conditions are established in experiments (including computational experiments) designed to decouple these boundary conditions from each other as much as possible. In this approach, individual boundary conditions (BCs) can be coupled later, via an analytical or computational model, for prediction of the overall cooling effectiveness (θ) of the fully-coupled system (see, for example, Williams et al. [32]). Whilst this approach has several advantages (e.g. the results of decoupled experiments possibly have more clear physical interpretation), one disadvantage is that errors in the measurements of individual local surface BCs can accumulate in the final prediction of θ. In recent literature, the overall cooling effectiveness (θ) of engine components has been measured directly in highly coupled environments with a high degree of non-dimensional similarity to the engine conditions. This latter approach would be regarded as *top-down* in philosophy. The top-down approach is advantageous because it allows direct component validation in an engine-realistic environment at an early stage of the design process, leading to faster and more accurate design evaluation. In order to gain physical insight into underlying mechanisms, the underlying boundary conditions are generally inferred by decoupling the result using a model (see, for example, Michaud et al. [35]). Here the disadvantage might be that the uncertainty in individual boundary conditions could be large. Interestingly, design extrapolation (redesign to move the design in a particular direction, for example) is little impaired by this increased uncertainty, because the relationship between a set of boundary conditions is often known to a higher degree of accuracy then the individual boundary conditions themselves. This is discussed in detail in Michaud et al. [35].

The scaling of overall cooling effectiveness (θ) between conventional laboratory (TR = 1.2; see, for example, Kirollos et al. [9]) and engine conditions (TR = 2.0) of temperature ratio is a matter that is of both academic and practical interest. A robust and validated scaling theory for

this process would allow experimental data at moderate temperature ratio to be used to infer engine conditions. This would allow engine-realistic test vehicles like the ECAT facility (see Kirollos et al. [9]) to be used for direct engine performance validation, without the need to operate at actual engine temperature ratios (see, e.g. the ECAT+ facility, discussed in Messenger et al. [18]).

This chapter confines itself to the problem of the scaling of overall cooling effectiveness with temperature ratio for air, for domain-global (row inlet to row exit; other boundary conditions are distinguished later) boundary conditions of fixed mainstream outlet-Re, Re_D, *and* fixed domain inlet-to-exit total-to-static pressure ratio, PR, for a flat plate with a mean cooling effectiveness of approximately 0.50. Re_D is defined based on the outlet velocity and the cooling hole diameter (in the flat plate facility the passage width and height are arbitrarily large, so the cooling hole length scale is more relevant to the scaling problem). In the theoretical work of chapter 2, it is shown that there are significant scaling effects associated with the changes between high absolute temperature (engine) and low absolute temperature (typical rig); and combustion products (engine) and air (typical rig), but that the sensitivities of the general result (change in overall cooling effectiveness with TR for air at low absolute temperature) to domain-global boundary conditions (fixed-PR vs fixed outlet-Re *and* fixed PR; see chapter 2), cooling system design, and mean overall cooling effectiveness are very low. That is, though this chapter confines itself to a very specific problem, the results (see chapter 2) are widely applicable.

The experimental measurements cover the range $1.07 \leq \mathrm{TR} \leq 1.62$. Experiments were performed on a heavily cooled (both internal and film) flat-plate test article, with domain-global boundary conditions of fixed Re_D *and* fixed PR. In this study, the controlling dimensionless groups change in a natural co-dependent way with temperature ratio. The philosophy of different frameworks for attack of this problem is discussed extensively in chapter 2. The prime purpose of this chapter is experimental validation of the broadly-applicable scaling theory of chapter 2,

independently modelled for a system-specific application (same application as this chapter) by Naidu and Povey [17].

In this chapter, physical experiments and complementary virtual experiments that align with the framework of Approach 3 (see chapter 1) are used. The experiment was designed and built with the sole purpose of validating the scaling theory developed in chapter 2, and is operated with non-dimensional groups that vary sympathetically with TR with domain-global boundary conditions of fixed outlet-Re *and* fixed PR. The virtual experiments are an aerothermal proxy for the physical experiment, with all relevant physics modelled (see later sections). The virtual experiment has tuning parameters to achieve a best match of absolute value of θ with the physical experiment; this still allows comparison of trends of θ with TR. The virtual experiment also allowed decomposition of changes in θ with TR into the effects of five local surface BCs.

3.2 Test facility

The high-temperature test facility developed expressly for this study is described in detail by Naidu and Povey [17]. The facility is a transient open-loop blowdown tunnel, with mainstream and coolant air introduced from pressurized tanks (60 m^3 at 27.6 bar). The flow is controlled using an inline pressure regulator and choked venturi nozzles and exhausts to the atmosphere. The mainstream was heated using a 1 MW electrical heater. A unique feature of the facility is the large operational range of both temperature and temperature ratio (capability $0.50 \leq \mathrm{TR} \leq 2.30$). In chapter 3 experiments were operated in the range $1.07 \leq \mathrm{TR} \leq 1.62$. They were performed with a fixed coolant temperature ($T_{0\mathrm{c,in}} = 290$ K) and varying mainstream temperature ($310\ \mathrm{K} < T_{0\mathrm{1h}} < 470$ K). Test conditions for the current experiments are summarised in Table 2; the full operational range of the facility is also presented.

A schematic cross-section of the facility working section is shown in Figure 40. The flow-path is of rectangular cross-section. The lower wall of the test section is a fully cooled flat plate test piece (described subsequently); the upper wall is a full-width infrared (IR) window (Zinc Selenide with anti-reflective coating) allowing the entire mainstream-facing side of the flat plate

to be visualised in its entirety (FLIR A655sc cameras). The underside of the flat plate forms one wall of the coolant plenum and can be visualised through a second full-width IR window (see Figure 40). The ability to take full surface IR measurements of both the mainstream-facing and cooling-facing walls of the test article is a second unusual feature of the facility. The working section is instrumented with inlet total pressure and total temperature rakes upstream of the flat plate, and static pressure tappings downstream of the flat plate. Total pressure and total temperature are also measured in the coolant plenum. Mainstream and coolant mass flow rates are measured using choked sonic-venturi nozzles.

Table 2: Test facility operating conditions for the experiments of chapter 3 (full facility operating range shown in parentheses).

Boundary condition	Symbol	Range
Mainstream-to-coolant temperature ratio (–)	T_{01h}	310–470 (290–600)
Mainstream total temperature, T_{01h} (K)	TR	1.07–1.62 (0.50–2.30)
Mainstream total pressure (bar)	p_{01h}	1.55–1.96 (1–10)
Coolant-to-mainstream total pressure ratio (–)	CMPR	1.0170–1.0238 (low–high)
Mainstream outlet-Re based on hole diameter (–)	Re_D	1.34×10^4–1.82×10^4 (1.50×10^4–3.15×10^4)
Mainstream outlet Mach number (–)	M	0.290–0.305 (low–1.0)
Turbulence length scale (mm)	l	3.00 (low–high)
Turbulence intensity (%)	Tu	10.0 (low–high)

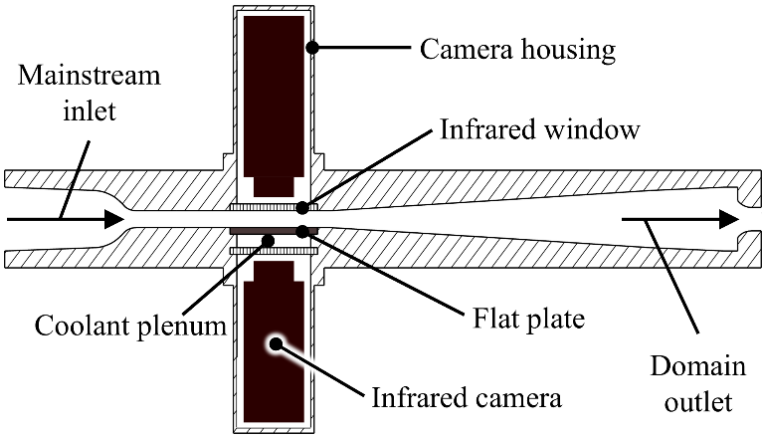

Figure 40: Defeatured cross-section of the working section, showing infrared cameras and flat-plate test article.

In-situ calibration of the cameras was performed using the low-conductivity isothermal-patch method of Michaud et al. [31]. The calibration gauges were 8 mm diameter copper discs mounted

on Macor and instrumented with K-type thermocouples. The calibration assembly was recessed into the flat plate to create a flush surface. Separate overall cooling effectiveness data are presented for IR temperature measurements calibrated according to three methods:

i) *Calibration Method 1*: black-body calibration only i.e. raw values converted to black-body-equivalent temperatures using the black-body calibration curve supplied by the manufacturer.

ii) *Calibration Method 2*: real-time in-situ calibration using the isothermal patch method with *total surrounding radiant flux* (or background radiation), $q^*(t)$, correction. This follows the work of Michaud et al. [31], Kirollos and Povey [36] and Michaud et al. [30]. In the method a simple (one-dimensional, with additional background radiation) model of the optical system is developed using known (measured) emissivity and transmittance values for the optical windows and target surfaces. A real-time background radiation term is evaluated that reconciles the real-time recorded camera temperature at the location of the isothermal calibration patch with the measured (calibration thermocouple) temperature at the same location. The background radiation term is used in conjunction with the radiation model to correct camera temperatures at all other locations.

iii) *Calibration Method 3*: real-time in-situ calibration using the isothermal patch method with a *temperature offset correction*. In this method a simple real-time temperature offset between the black-body-equivalent IR camera measurement and thermocouple temperature measurement at the locations of the calibration patches is determined. The temperature offset, $\Delta T_{CP}(t)$, is applied uniformly across the entire surface: $T_S(x,y,t) = T_{bb}(x,y,t)+\Delta T_{CP}(t)$.

Overall cooling effectiveness data based on IR temperature measurements obtained using Calibration Method 1 are primarily discussed in this chapter, but the corresponding results for measurements obtained using Calibration Method 2 and Calibration Method 3 are briefly discussed in section 3.10.

3.3 Design of the flat-plate test article

The working section of the facility (see Naidu and Povey [17]) houses a cooled rectangular flat-plate (215 mm by 115 mm in size) laser sintered from Inconel 718. The design used is shown in Figure 41a to Figure 41d. The design has internal cooling and film cooling design features typical of some modern civil aeroengines. There are three identical cooled *modules* in the streamwise direction, and six identical modules in the lateral direction (18 modules in total). On the internal side, coolant enters individual modules through a rectangular slot, and passes in the reverse-flow direction along an internal channel incorporating 45° V-shaped broken-rib turbulators (0.50 mm high). The purpose of the V-shaped turbulators is to increase the internal heat transfer coefficient and therefore increase the coupling between external and internal flow domains, which leads to more pronounced and interesting scaling effects with TR. Each module exhausts through three equally spaced 2.00 mm diameter circular holes. Each module in both the streamwise and lateral direction is separated from neighbouring modules by webs with thickness w. Design parameters are summarised in Table 3.

A schematic of a single coolant module of the flat plate is shown in Figure 42, with key dimensions indicated. The design is related to typical civil aeroengine designs by a scale factor of two (hole size; hole spacing; wall thicknesses; channel height etc.) The global design is based on the reverse-pass cooling designs of Kirollos and Povey [20] and [37–38] in which the adiabatic film effectiveness decreases in the same direction as the coolant potential increases, leading to flatter overall cooling effectiveness with streamwise distance. This type of design is particularly interesting for the present study because it also maximises the coupling between the internal and external systems leading to more pronounced scaling effects with temperature ratio than some other systems. Further details of the facility design, experimental setup, and operation of the facility are given in Naidu and Povey [17].

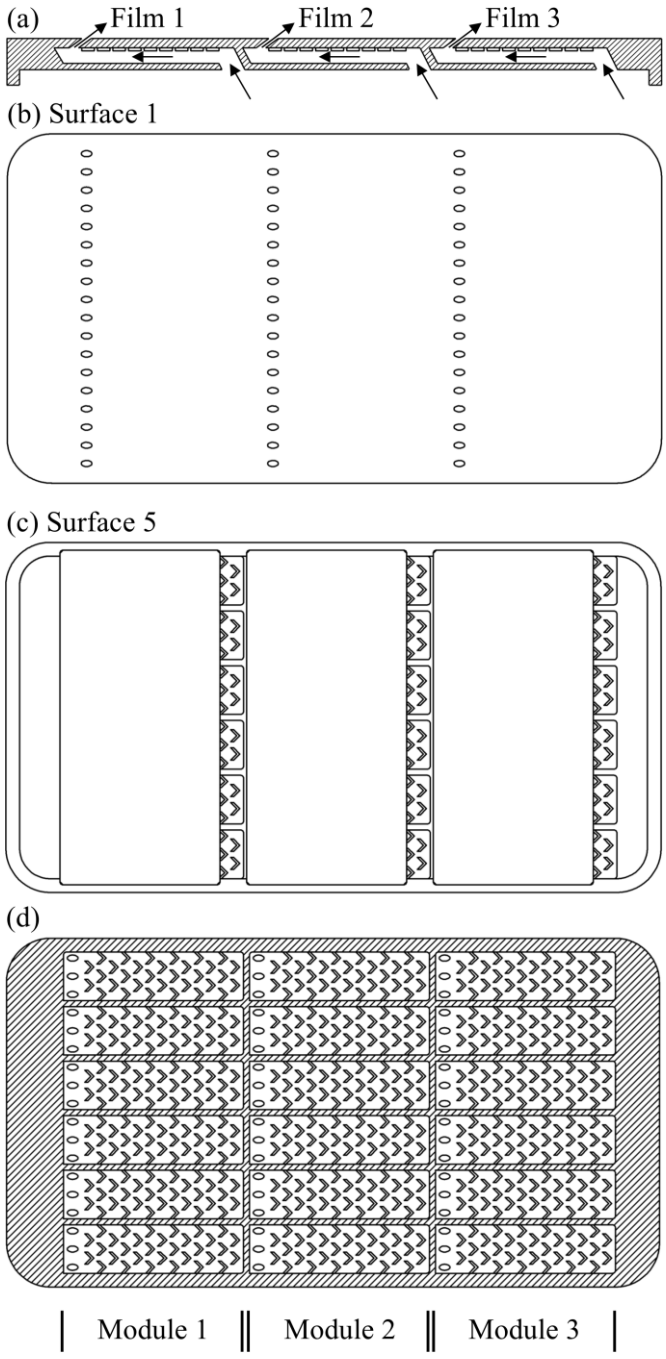

Figure 41: (a) drawing of flat-plate cross-section; (b) drawing of flat-plate external wall; (c) drawing of flat-plate internal wall; and (d) drawing of flat-plate internal surface showing ribs.

Table 3: Summary of key dimensions.

Parameter	Symbol	Value
Height of internal channel (mm)	H	5.00
Length of streamwise module (mm)	L	60.0
External wall thickness (mm)	t_{w1}	3.00
Internal wall thickness (mm)	t_{w2}	2.00
Web thickness (mm)	w	2.00
Width of lateral module (mm)	W	20.0
Hole angle (°)	α	35.0

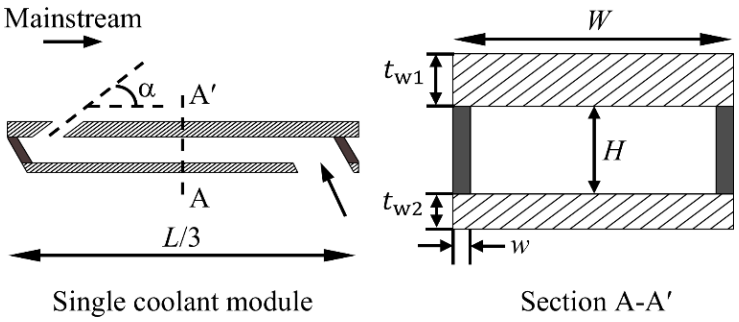

Figure 42: Schematic of a single coolant module of the flat plate showing key dimensions.

3.4 Boundary conditions for experiments

In this chapter three groups of boundary conditions are referred to: domain-global BCs; cooling system BCs; and local surface BCs. A comprehensive discussion of the physical significance of these boundary conditions is provided in chapter 2. The key points are briefly revisited in the context of chapter 3. The domain-global BCs relate to the conditions on the mainstream flow established in the test facility. In this chapter experiments are performed for domain-global boundary conditions of fixed outlet-Re *and* fixed PR. Inlet pressure variation in the range 1.25–2.08 bar was required for fixed $\mathrm{Re}_D = 1.50\times10^4$ for the TR range $1.07 \leq \mathrm{TR} \leq 1.62$. The cooling system BCs are the conditions relevant to the inlet to the internal cooling channels. When combined with the domain-global BCs, they set the particular CMPR and TR for a given run. Total temperature at inlet to the cooling channel was approximately the same for all runs ($T_{0c,in} = 290$ K) and approximately constant with time during a run. The mainstream total temperature was varied in the range 310–470 K in order to achieve temperature ratios in the range $1.07 \leq \mathrm{TR} \leq 1.62$. There is a slow time variation of temperature during a run which is described

in more detail in section 3.7.2. A schematic of the system is shown in Figure 43, in which the cooling system BCs and four planes of interest are indicated: Plane 1 is the domain inlet and the point at which coolant from row 1 is injected into the mainstream; planes 2 and 3 mark the downstream positions at which coolant is injected into the mainstream from cooling rows 2 and 3, respectively; and plane 4 is the domain exit.

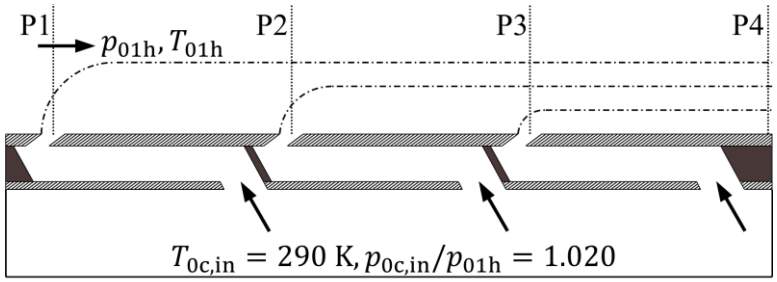

Figure 43: Schematic of cooling system BCs and locations of planes 1–4.

In chapter 3 eight local surface BCs are referred to: film effectiveness of the mixing layer, η_{ML}; wall thermal conductivity, k_w; external heat transfer coefficient, h_m; internal heat transfer coefficient on surface i (i = 2, 3, 4, 5), h_{ci} (four heat transfer coefficients in total); and internal cooling effectiveness, λ (see section 3.5 for further discussion). Changes in overall cooling effectiveness from a reference condition with TR = 2.0 are referred to throughout this chapter; this temperature ratio is so chosen to be representative of typical engine conditions for large civil aircraft (also consistent with chapter 2). Domain-global and cooling system BCs are summarised in Table 4 for the for the reference case condition with TR = 2.0, and for the lowest temperature ratio condition of TR = 1.2. Resulting coolant-to-mainstream mass flow rate ratios for each of the three reverse-pass cooling ducts are also given.

Table 4: Domain-global and cooling system boundary conditions for TR = 2.0 and TR = 1.2.

Boundary condition		Value for TR = 2.0	Value for TR = 1.2
Coolant plenum total temperature, $T_{0c,in}$ (K)		290	290
Mainstream total temperature, T_{01h} (K)		580	348
Mainstream-to-coolant temperature ratio, TR (–)		2.0	1.2
Mainstream outlet Mach number, M (–)		0.30	0.30
Coolant plenum total pressure, $p_{0c,in}$ (bar)		2.74	1.47
Mainstream inlet total pressure, p_{01h} (bar)		2.68	1.44
Exit static pressure, p_4 (bar)		2.52	1.35
CMPR, $p_{0c,in}/p_{01h}$ (–)		1.020	1.020
Mainstream outlet-Re number based on cooling hole diameter, Re_D (–)		1.50×10^4	1.50×10^4
Coolant-to-mainstream mass flow rate ratio for cooling row j, $\dot{m}_{jc}/\dot{m}_{1h}$ (–)	Row 1	0.0141	0.0109
	Row 2	0.0142	0.0110
	Row 3	0.0156	0.0121

3.5 Eight local surface boundary conditions

In the Approach 3 method used in this chapter, the change in θ with deliberate change in TR is decomposed into changes in a complete set of local surface boundary conditions. This is possible by using a—calibrated—virtual experiment to determine the sympathetic variation in non-dimensional groups other than TR, and to use these changes to calculate the changes in a set of local surface boundary conditions.

In chapter 2, it was demonstrated that for a 1D incompressible system, overall cooling effectiveness can be expressed as

$$\theta = \eta_{\mathrm{ML}} + \frac{\lambda - \eta_{\mathrm{ML}}}{1 + h_{\mathrm{m}}\left(\frac{1}{h_{\mathrm{c}}} + \frac{t_{\mathrm{w}}}{\bar{k}_{\mathrm{w}}}\right)} \tag{40}$$

where η_{ML} is the effectivness of the mixing layer, $\bar{k}_{\mathrm{w}}$ the local through-wall averge wall thermal conductivity, h_{m} the external heat transfer coefficient, h_{c} the internal heat transfer coeffcient, and λ the internal cooling effectiveness. The local wall thickness, t_{w}, can be regarded as a constant for the system, or could be combined with $\bar{k}_{\mathrm{w}}$ to form a wall thermal resistance.

The form of (40) is $\theta = f\left(\eta_{ML}, \bar{k}_w, h_m, h_c, \lambda\right)$. That is, θ is a function of five local surface boundary conditions. This is true when lateral conduction effects are small in comparison to through-wall conduction effects: true for many real systems of interest. It was demonstrated that linear superposition of the isolated contributions of each local surface BC to the change in overall cooling effectiveness closely matches the overall change as TR is varied (with sympathetic variation of all other non-dimensional groups), demonstrating that the local surface BCs form a complete set and provide a full explanation for the change in θ with TR.

Chapter 2 is now diverged from in two important respects: there are conductive webs connecting the outer and inner walls; the assumption of an adiabatic inner wall is relaxed. This requires additional complexity for the minimum set of local surface boundary conditions to represent the problem. Two changes to the local surface boundary conditions are made: firstly, in place of a through-wall average wall conductivity, $\bar{k}_w$, a local wall thermal conductivity, $k_w(x,y,z)$, based on the local temperature, $T_w(x,y,z)$, is used; secondly, in place of a single internal heat transfer coefficient, h_c, individual heat transfer coefficients on each of the inner wall surfaces S2 to S5, h_{c2}, to h_{c5}, respectively, are used. The nomenclature for the surfaces is shown in Figure 44.

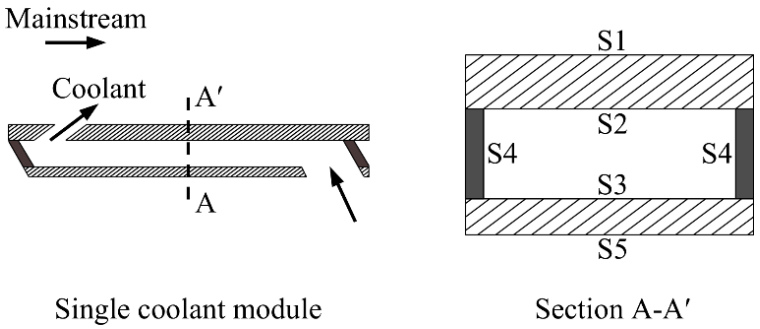

Figure 44: Schematic of a single coolant module, and a section diagram showing surfaces S1 to S5.

The new functional relationship is $\theta = f\left(\eta_{ML}, k_w, h_m, h_{c2}, h_{c3}, h_{c4}, h_{c5}, \lambda\right)$. That is, θ is represented as a function of eight local surface boundary conditions, not five.

The local surface boundary conditions are now described in turn.

3.5.1 Film effectiveness of the mixing layer

Film effectiveness of the mixing layer is the non-dimensional temperature of the mixing layer directly adjacent to the external surface of the flat plate (driving temperature for external heat transfer). The energy-based method of Kirollos and Povey [23], in which there is a mixing layer associated with each cooling film, which can entrain gas (and therefore enthalpy flow rate) from preceding layers (or the mainstream in the case of the first mixing layer), is used. The Kirollos and Povey [23] model is preferred—particularly for the present purpose—because it satisfies energy conservation unlike some better-known models for film superposition. The model is discussed in more detail in section 3.6.2. Film effectiveness of the mixing layer is defined by

$$\eta_{\mathrm{ML}}(x,y) = \frac{T_{01\mathrm{h}} - T_{0\mathrm{m}}(x,y)}{T_{01\mathrm{h}} - T_{0\mathrm{c,in}}} \tag{41}$$

where $T_{0\mathrm{m}}(x,y)$ is the local total temperature of the mixing layer. An incompressible definition is used in chapter 3 but it is noted that, for systems with high Mach number, the compressible definition adopted by chapter 2 should be used.

3.5.2 Wall thermal conductivity

Wall thermal conductivity, $k_{\mathrm{w}}(x,y,z)$, is evaluated at the local wall temperature $T_{\mathrm{w}}(x,y,z)$. This is in contrast to using local *through-wall average* wall thermal conductivity in chapter 2. The additional complexity here is justifed because greater through-wall temperature variation is expected in the system considered in this chapter than the system of chapter 2.

3.5.3 External heat transfer coefficient

The external heat transfer coefficient is defined by

$$h_{\mathrm{m}}(x,y) = \frac{\mathrm{Nu}_{\mathrm{m}}(x,y)k_{\mathrm{m}}(x,y)}{x} \tag{42}$$

where $\mathrm{Nu}_{\mathrm{m}}(x,y)$ is external Nusselt number, $k_{\mathrm{m}}(x,y)$ is thermal conductivity of the gas in the mixing layer, and x is the local streamwise distance. A correlation for external Nusselt number is provided in section 3.6.4.

3.5.4 Internal heat transfer coefficients

For internal surfaces 2–4 (see Figure 44) the internal heat transfer coefficients are given by

$$h_{ci}(x,y) = \frac{\mathrm{Nu}_{ci}(x,y)k_{\mathrm{c}}(x,y)}{D_{\mathrm{c}}} \tag{43}$$

where $\mathrm{Nu}_{ci}(x,y)$ is the local internal Nusselt number for surface i ($i = 2, 3, 4$), $k_{\mathrm{c}}(x,y)$ is local thermal conductivity of the coolant flow and D_{c} is hydraulic diameter of the internal cooling channel. A correlation for internal Nusselt number is provided in section 3.6.6: the same form of equation for surfaces 2–4 is taken but different multiplication factors are used to account for different augmentation (due to turbulators etc).

For Surface 5 (which faces the coolant plenum), it is asusmed that the coolant is fully mixed at the temperature and pressure of the cooling channel inlet. The internal heat transfer coefficient for Surface 5 is given by

$$h_{c5}(x,y) = \frac{\mathrm{Nu}_{c5}(x,y)k_{\mathrm{c,in}}}{D_{\mathrm{plen}}} \tag{44}$$

where $\mathrm{Nu}_{c5}(x,y)$ is the corresponding Nusselt number, $k_{\mathrm{c,in}}$ is coolant thermal conductivity at the cooling channel inlet, and D_{plen} is hydraulic diameter of the coolant plenum. A correlation for Nu_{c5} is provided in section 3.6.6.

3.5.5 Internal cooling effectiveness

Internal cooling effectiveness is the local non-dimensional temperature of the internal coolant. This is defined by

$$\lambda(x,y) = \frac{T_{01\mathrm{h}} - T_{0\mathrm{c}}(x,y)}{T_{01\mathrm{h}} - T_{0\mathrm{c,in}}} \tag{45}$$

where $T_{0\mathrm{c}}(x,y)$ is local internal coolant total temperature. Here an incompressible definition (parallel with the chosen definitions of θ and η_{ML}) is used. For a discussion of compressible definitions, see chapter 2.

3.6 2D low-order conjugate aerothermal network model

The virtual experiment is a low-order conjugate aerothermal network model of the test plate, with all relevant physics modelled. The network model is two-dimensional (streamwise direction; through-wall direction) and includes conductive, convective and advective heat transfer terms. Surfaces S2 to S5 (see Figure 44) refer—respecively—to the following: the external wall facing the mainstream air; the external wall facing the coolant channel; the internal wall facing the coolant channel; the internal surface of the webs separating the modules in the lateral direction; and the internal wall facing the coolant plenum. The networking of flow in the model is designed to represent the test article (Figure 41a to Figure 41d). The algorithm used by the numerical solver to evaluate the converged solution is similar to that described by the block diagram of Figure 6.

Advection in the external and internal fluid domain are modelled, as is conduction in the solid and convection at the fluid-solid interface. In the internal cooling channels, there is a streamwise change in temperature as heat is transferred to the cooling flow as well as pressure loss from duct inlet to outlet due to friction. In the wall, only through-wall conduction was modelled (no lateral conduction); this simplification can be shown to have a negligible effect on the result for most practical cooling system designs (scale disparity). The external and internal walls are additionally directly coupled with conduction terms representing the through-wall webs that separate the modules in the lateral direction. The modelling of this is discussed in more detail in section 3.6.1. The coolant mass flow for each row was calculated by using the experimentally measured plate coolant capacity characteristics for each row blowing in isolation, and the *local* CMPR. This was evaluated using the local static pressure inferred from the run total pressure and an isentropic Mach number distribution taken from a CFD simulation (see Naidu and Povey [17]). Local fluid properties were evaluated using the correlations of Oldfield and Guo [29]. Wall thermal conductivity was modelled using a best fit to experimental data of the form $k_w = 0.017T_w + 5.480$, which is typical of nickel alloys (see, e.g., Zielińska et al. [26]).

The solution of the low-order network model was found to be independent of mesh size with 100 nodes per streamwise module in the streamwise direction, ten nodes in the through-wall direction (six nodes in the external wall, four nodes in the internal wall) and two nodes in the through-wall webs (uniform spacing mesh). This gave a total cell count of 3600 cells.

3.6.1 Coupling between external and internal walls due to conduction through webs

In this section, the modelling for conduction through the webs separating the modules in the lateral direction is explained. The network model has no concept of temperature variation in the lateral direction i.e. temperature varies only in the streamwise and through-wall directions. In the model, the temperature difference across a web is therefore the difference between the surface 2 and surface 3 temperatures (see Figure 44), i.e. $T_{S2} - T_{S3}$. In the model, the heat flows into and out of the webs, Q_A and Q_B respectively, are calculated. These terms are not equal because there is a heat flow from the web to coolant within the channel, Q_C. By continuity $Q_A = Q_B + Q_C$. The three heat flow terms are shown in Figure 45.

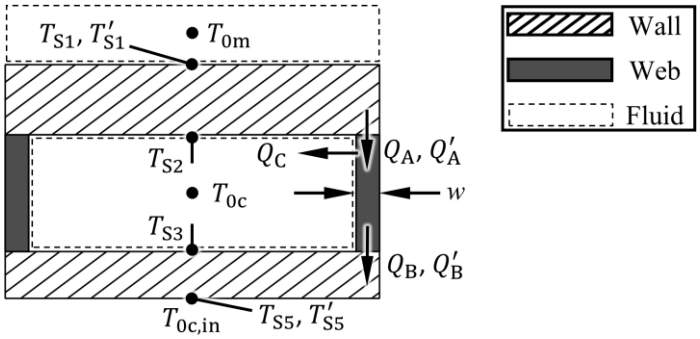

Figure 45: Schematic representation of a lateral cross section of single coolant module.

Because there is no concept of lateral variation of temperature in the network model, there is no effect of local reduction in temperature due to the heat-sink effect of the web on the outer wall, nor the effect of local augmentation of temperature due to the local heat-source effect of the web on the inner wall. Without a correction the heat flows Q_A and Q_B would be overestimated. *Uncorrected* heat flows Q'_A and Q'_B are referred to and marked in Figure 45. Correction is performed by multiplying the conduction equations by a constant $K_{web} < 1$, where the constant is

evaluated using a fully-resolved (streamwise, lateral, though-wall) FEA simulation of a 10 mm long (streamwise length) section of the plate (including all six lateral modules) with boundary conditions of surface-averaged gas temperatures (T_{0m}, T_{0c} and $T_{0c,in}$) and local heat transfer coefficients (for Surface 1–5) from a converged low-order network model simulation. The streamwise length is arbitrary, as its purpose is simply to account for lateral temperature variation on through-web heat flows. Because wall temperatures are not specified, the three-dimensional internal temperature field can develop.

K_{web} is defined to be the value that reconciles the though-web heat flows, per unit temperature difference between Surface 1 and Surface 5, between the low-order network model and the fully-resolved FEA simulation i.e.

$$K_{web} = \frac{1}{2} \times \left(\frac{Q_A}{Q'_A} + \frac{Q_B}{Q'_B} \right) \times \frac{(T'_{S1} - T'_{S5})}{(T_{S1} - T_{S5})} \tag{46}$$

For the evaluation of Q'_A and Q'_B, the low-order conjugate aerothermal network model is run with $K_{web} = 1$. Though-web heat flows are evaluated by using the temperatures of the cells in the external (T_{S2}) and internal walls (T_{S3}) immediately adjacent to the webs. Q'_A and Q'_B are taken to be the surface-averaged web heat flows and T'_{S1} and T'_{S5} are taken to be the surface-averaged temperatures of Surface 1 and Surface 5, respectively. For Q_A and Q_B a 3D FEA simulation is run, taking Q_A and Q_B to be the surface-averaged web heat flows and T_{S1} and T_{S5} to be the surface-averaged temperatures of Surface 1 and Surface 5, respectively. Using Eq. (46), the value of the correction factor is determined to be $K_{web} = 0.59$. This correction accurately accounts for lateral temperature non-uniformity, rendering the through-wall heat flux in the 2D network model the same as the 3D FEA simulations.

3.6.2 Film effectiveness of the mixing layers

The coolant mixing layers were modelled using an entrainment-based approach (mainstream gas entering successive mixing layers) with heat loss to the wall. The model consists of three

sequential fully mixed cooling films, with each mixing layer entraining relatively hotter gas from the preceding layer. This is illustrated schematically in Figure 46.

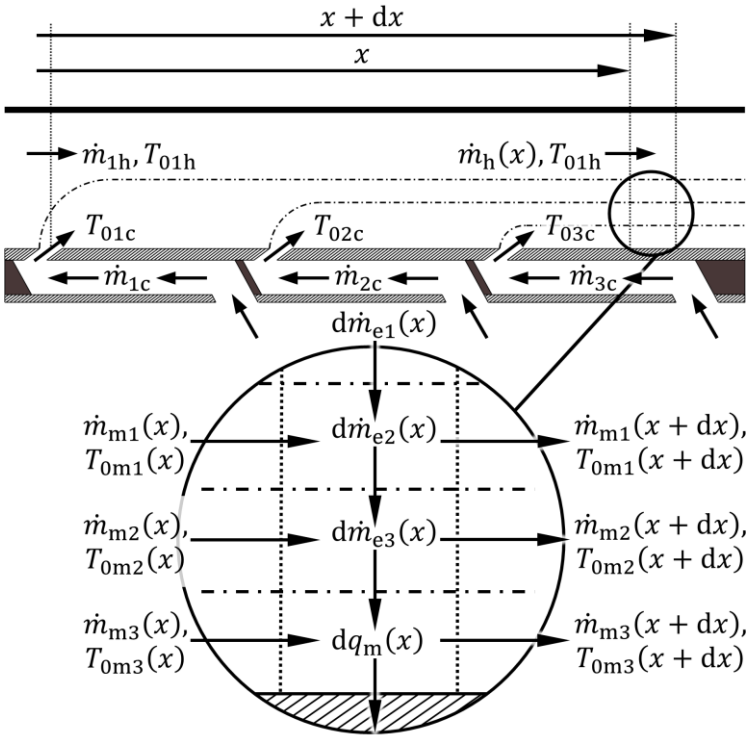

Figure 46: Schematic illustration of the mixing layers.

The driving temperature for external surface heat transfer is taken to be the total temperature of the mixing layer adjacent to the surface. The method is the energy-based film superposition approach of Kirollos and Povey [23]. Implementation of the method is now briefly explained.

Adiabatic film effectiveness is defined by

$$\eta(x) = \frac{T_{01\mathrm{h}} - T_{\mathrm{aw}}(x)}{T_{01\mathrm{h}} - T_{0\mathrm{c,in}}} \tag{47}$$

where $T_{\mathrm{aw}}(x)$ is adiabatic wall temperature and where it is recalled $T_{01\mathrm{h}}$ is mainstream total temperature and $T_{0\mathrm{c,in}}$ is total temperature at the cooling channel inlet.

For the reference case condition with TR = 2.0, the adiabatic wall temperature, $T_{\mathrm{aw}}(x)$, is evaluated from an adiabatic CFD simulation (see Naidu and Povey [17]). $\eta(x)$ is evaluated using Eq. (47). The scalar tracking method outlined by Thomas and Povey [39] is used to identify the

contribution by mass fraction, $\eta_j(x)$, of each cooling film (j = 1, 2, 3) to the overall distribution $\eta(x)$. The mass fractions obey the relationship $\eta(x) = \eta_1(x)+\eta_2(x)+\eta_3(x)$. For each cooling film j, the mass-entrainment-rate distribution with streamwise distance, $\dot{m}_{ej}(x)$, is evaluated by considering continuity of mass flow rate and conservation of energy for fully-mixed mixing layer. It is assumed that coolant specific heat capacity is constant within the cooling channel ($c_{pc}(x) = c_{pc,in}$). This leads to the following relationship (for derivation see Kirollos and Povey [23])

$$\dot{m}_{ej}(x) = \dot{m}_{jc}\frac{c_{pc,in}}{c_{p1h}}\frac{\left(1-\eta_j(x)\right)}{\eta_j(x)} \tag{48}$$

It is assumed that the mass-entrainment-rate distributions $\dot{m}_{ej}(x)$ are unaffected by through-wall heat flux. These distributions are used in the low-order network model simulation at the reference TR.

To calculate mass-entrainment-rate distributions at non-reference TRs, a geometric similarity argument is used. Both the physical experiment and the low-order network model are run with the same coolant-to-mainstream momentum flux ratio at all TRs. It is therefore reasonable to assume similar aerodynamic behaviour so far as the interaction of cooling jets and mainstream is concerned (similar penetration into freestream, and similar mixing). If the mixing process is assumed to be *geometrically* similar (same layer thickness etc), the implication is that the mass-entrainment-rate into each mixing cooling layer, $\dot{m}_{ej}(x)$, is proportional to the inlet mainstream mass flow rate $\dot{m}_{1h}$. That is, the following assumption is made

$$\frac{\dot{m}_{ej}(x)}{\dot{m}_{1h}} = \left(\frac{\dot{m}_{ej}(x)^{TR=2.0}}{\dot{m}_{1h}{}^{TR=2.0}}\right) \tag{49}$$

This is discussed further in chapter 2.

The total temperature of each mixing layer j, $T_{0mj}(x)$, is then evaluated by considering mass flow rate continuity and conservation of energy. For the mixing layer immediately adjacent to the wall, heat flow into (or out of) the wall is accounted for: i.e. the *diabatic* system is modelled. The external driving (diabatic) wall temperature (incompressible assumption) is just the total

temperature of the mixing layer adjacent to the surface, $T_{0\mathrm{m}}(x)$. The effectiveness of the surface mixing layer is

$$\eta_{\mathrm{ML}}(x) = \frac{T_{01\mathrm{h}} - T_{0\mathrm{m}}(x)}{T_{01\mathrm{h}} - T_{0\mathrm{c,in}}}$$

3.6.3 Static pressure distribution and total pressure of the mixing layer

The evaluation of the external static pressure, $p(x)$, and total pressure of the mixing layer, $p_{0\mathrm{m}}(x)$, is now discussed. These parameters are combined with the distribution $T_{0\mathrm{m}}(x)$ to determine the fluid properties of the mixing layer, which are in turn used in the correlations for the external heat transfer coefficient. The following constraints are applied in the network model:

i) The sum of the cross-sectional areas of the mainstream flow and each cooling films is equal to the cross-sectional area of the passage, i.e. $A(x) = A_{\mathrm{h}}(x)+A_{\mathrm{m1}}(x)+A_{\mathrm{m2}}(x)+A_{\mathrm{m3}}(x)$. This is shown schematically in Figure 47.

ii) The cross-sectional area of the passage is constant, i.e. $A(x) = A$ (see Figure 47).

iii) The mainstream flow is isentropic and adiabatic, i.e. $p_{0\mathrm{h}}(x) = p_{01\mathrm{h}}$ and $T_{0\mathrm{h}}(x) = T_{01\mathrm{h}}$.

iv) The boundaries of the mixing layer associated with each cooling film can be considered as a slip line with constant static pressure across the boundary, i.e. $p_{\mathrm{m}j}(x) = p_{\mathrm{h}}(x) = p(x)$. For a discussion of this see chapter 2.

v) The total pressure of each mixing layer, $p_{0\mathrm{m}j}(x)$, at a particular streamwise position x, is the mass-flow-rate-average total pressure of all flows entering the layer.

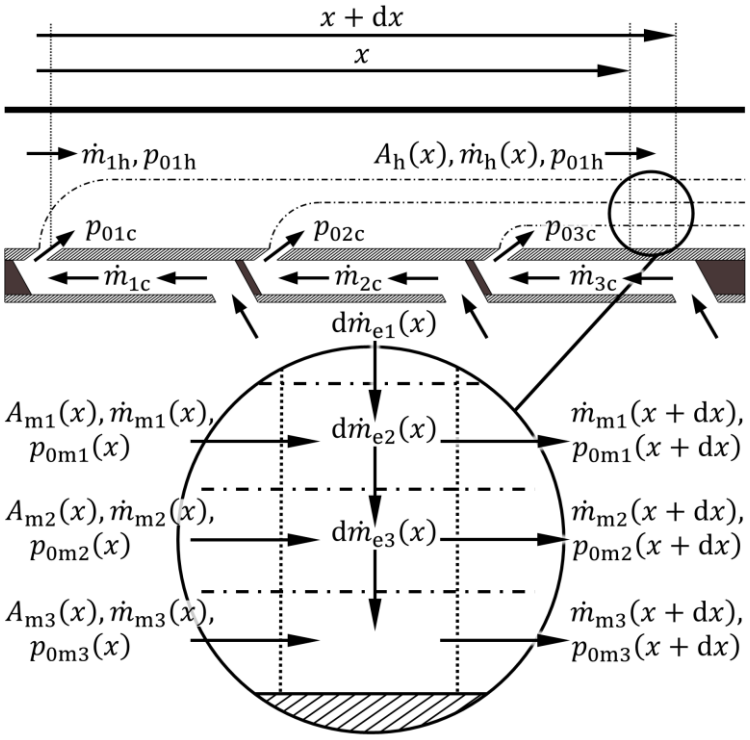

Figure 47: Schematic of the test article, defining cross-sectional areas and total pressures of the system.

The mainstream total pressure is evaluated using Eq. (50), which is derived by combining the definitions of Mach number and Reynolds number with the isentropic equations

$$p_{01\mathrm{h}} = \frac{\mathrm{Re}_D \mu_{4\mathrm{h}}}{D\mathrm{M}} \sqrt{\frac{RT_{01\mathrm{h}}}{\gamma_{4\mathrm{h}}}} \left(1 + \frac{\gamma_{4\mathrm{h}} - 1}{2} \mathrm{M}^2\right)^{\frac{\gamma_{4\mathrm{h}}+1}{2(\gamma_{4\mathrm{h}}-1)}} \tag{50}$$

where R is the specific gas constant.

Re_D, M and $T_{01\mathrm{h}}$ are known boundary conditions for a given condition. The mainstream dynamic viscosity, $\mu_{4\mathrm{h}}$, and specific heat capacity ratio, $\gamma_{4\mathrm{h}}$, are evaluated at the domain outlet. The external static pressure distribution, $p(x)$ is obtained by combining the isentropic Mach number distribution, $\mathrm{M}_{\mathrm{h}}(x)$, obtained from a CFD simulation (see Naidu and Povey [17]) with the calculated value of $p_{01\mathrm{h}}$

$$p(x) = p_{01\mathrm{h}} \left(1 + \frac{\gamma_{\mathrm{h}}(x) - 1}{2} \mathrm{M}_{\mathrm{h}}(x)^2\right)^{-\frac{\gamma_{\mathrm{h}}(x)}{\gamma_{\mathrm{h}}(x)-1}} \tag{51}$$

3.6.4 Correlations for external heat transfer coefficient

The correlations used to evaluate the local external heat transfer coefficient are now described. External Reynolds number is defined by

$$\mathrm{Re_m}(x) = \frac{\rho_\mathrm{m}(x) u_\mathrm{m}(x) x}{\mu_\mathrm{m}(x)} \tag{52}$$

where $\rho_\mathrm{m}(x)$, $u_\mathrm{m}(x)$ and $\mu_\mathrm{m}(x)$ are density, velocity and dynamic viscosity, respectively, of the mixing layer adjacent to the surface. The external Prandtl number is defined by

$$\mathrm{Pr_m}(x) = \frac{c_{p\mathrm{m}}(x)\mu_\mathrm{m}(x)}{k_\mathrm{m}(x)} \tag{53}$$

where $c_{p\mathrm{m}}(x)$ and $k_\mathrm{m}(x)$ are specific heat capacity and thermal conductivity, respectively, of the mixing layer adjacent to the surface.

External Nusselt number was defined using a correlation for a flat plate in parallel flow (see Bergman et al. [22])

$$\mathrm{Nu_m}(x) = 0.0296 \mathrm{Re_m}(x)^{4/5} \mathrm{Pr_m}(x)^{1/3} \tag{54}$$

Finally, recalling Eq. (42), local external heat transfer coefficient is defined by

$$h_\mathrm{m}(x) = \frac{\mathrm{Nu_m}(x) k_\mathrm{m}(x)}{x}$$

3.6.5 Correlations for cooling channel pressure loss

Friction coefficient for the internal cooling channels, $f_\mathrm{c}(x)$, was evaluated from the smooth-pipe Moody chart correlations (see, for example, Bergman et al. [22]). At streamwise position x, $\mathrm{d}p_{0\mathrm{c}}(x)/\mathrm{d}x$, was evaluated using a modified version of the *Moody friction factor equation*

$$\frac{\mathrm{d}p_{0\mathrm{c}}(x)}{\mathrm{d}x} = \frac{4K_1 f_\mathrm{c}(x)}{D_\mathrm{c}} \frac{1}{2} u_\mathrm{c}(x)^2 \tag{55}$$

where K_1 is a multiplication factor that depends on the channel design, D_c is the hydraulic diameter of the cooling channel and $u_c(x)$ is the local channel velocity given by

$$u_c(x) = \frac{\dot{m}_c(x)}{\rho_c(x)(W-w)H} \tag{56}$$

where $\dot{m}_c(x)$ is the local coolant mass flow rate, $\rho_c(x)$ is the local density of the internal cooling flow, W is the width of one module and H is the height of the internal cooling channel. It is recalled that the web width is w. Friction factor is enhanced by the presence of 45° V-shaped broken-rib turbulators on Surface 2, for which a multiplication factor of value $K_1 = 7.00$ has been experimentally determined (see Han and Zhang [40]).

3.6.6 Correlations for internal heat transfer coefficient

The correlations used to evaluate the local internal heat transfer coefficient are now described. Internal Reynolds number is defined by

$$\mathrm{Re}_c(x) = \frac{\rho_c(x)u_c(x)x}{\mu_c(x)} \tag{57}$$

where $\mu_c(x)$ is dynamic viscosity of the internal coolant evaluated at the local temperature of the flow. For the uncalibrated low-order network model, internal Reynolds number varies in the range $0.62\times10^4 \le \mathrm{Re}_c \le 1.28\times10^4$ for temperature ratios in the range $1.2 \le \mathrm{TR} \le 2.0$. Internal Prandtl number is defined by

$$\mathrm{Pr}_c(x) = \frac{c_{pc}(x)\mu_c(x)}{k_c(x)} \tag{58}$$

where $c_{pc}(x)$ and $k_c(x)$ are specific heat capacity and thermal conductivity of the internal coolant, respectively.

Internal Nusselt number for Surfaces 2–5 was defined by a modified version of the Dittus-Boelter equation (see McAdams [21]; leading constant multiplication factor quoted to two significant figures)

$$\mathrm{Nu}_{ci}(x) = 0.023 K_{2i} \mathrm{Re}_{\mathrm{c}}(x)^{0.8} \mathrm{Pr}_{\mathrm{c}}(x)^{0.4} \tag{59}$$

where $K_{2\mathrm{i}}$ is a multiplication factor particular to surface i (where i = 2–5 for S2–S5). Particular multiplication factors are described in a moment.

Recalling Eq. (43), the local internal heat transfer coefficients for Surfaces 2–4 are defined by

$$h_{ci}(x,y) = \frac{\mathrm{Nu}_{ci}(x,y) k_{\mathrm{c}}(x,y)}{D_{\mathrm{c}}}$$

Internal heat transfer is enhanced by the presence of 45° V-shaped broken-rib turbulators on Surface 2. Multiplication factors, K_{22} = 3.77 (Surface 2), and $K_{23} = K_{24}$ = 2.03 (Surface 3 and 4) are used. These values come from experimental correlations (see Han and Zhang [40]). Finally, for Surface 5 it is asusmed that the coolant is fully mixed at the temperature and pressure at the cooling channel inlet. Recalling Eq. (44), internal heat transfer coefficient for Surface 5 is given by

$$h_{c5}(x) = \frac{\mathrm{Nu}_{c5}(x) k_{\mathrm{c,in}}}{D_{\mathrm{plen}}}$$

where $\mathrm{Nu}_{c5}(x)$ is defined by Eq. (59) with multiplication factor K_{25} = 1.00.

3.7 Experimental processing and results

In this section, the full-surface experimental result, corrections for transient behaviour, corrections for off design conditions, and uncertainty analysis are presented. Summary results of the effect of TR on overall cooling effectiveness are presented in section 3.8. The full-surface experimental result is considered first.

3.7.1 Full-surface distribution of overall cooling effectiveness

Full-surface overall cooling effectiveness measurements were performed on both Surface 1 (outer wall facing mainstream) and Surface 5 (inner wall facing coolant plenum) for temperature ratio

conditions in the range $1.07 \leq \mathrm{TR} \leq 1.62$. The design values for Re_D, M and CMPR are: $\mathrm{Re}_D = 1.50\times10^4$; M = 0.30; and CMPR = 1.020.

Typical full-surface cooling effectiveness distributions on Surface 1 and Surface 5 are shown in Figure 48.

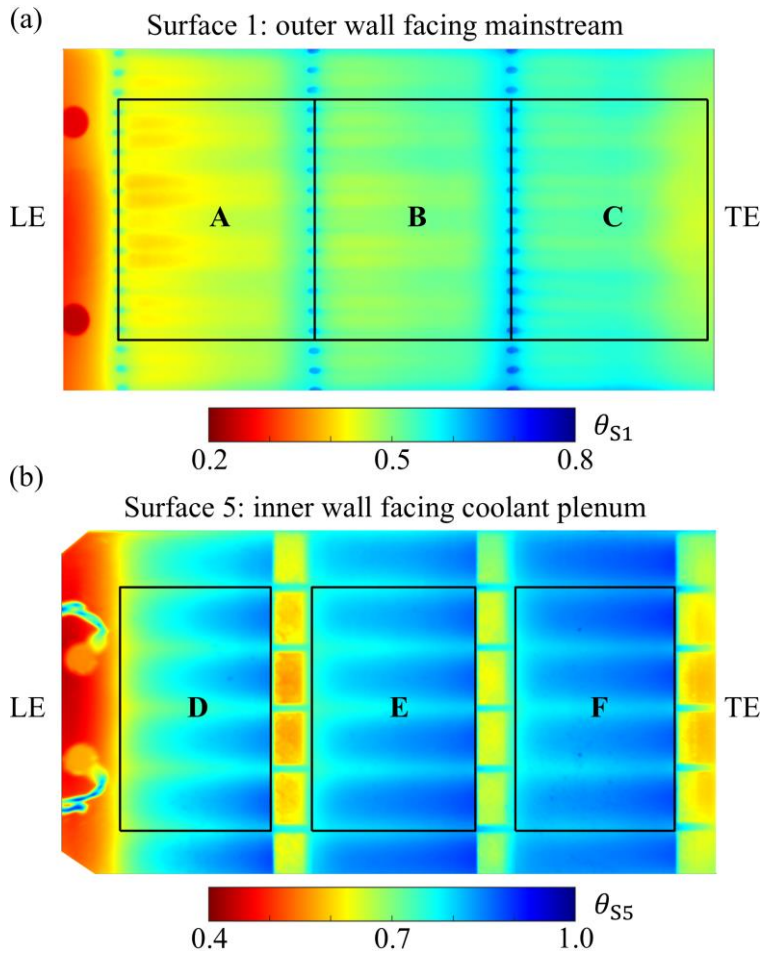

Figure 48: Overall cooling effectiveness measurements on: (a) Surface 1 (outer wall facing mainstream); and (b) Surface 5 (inner wall facing coolant plenum). The leading edge (LE) and trailing edge (TE) are marked. Averaging regions A, B and C (on Surface 1) and corresponding regions D, E and F (on Surface 5) are marked.

These data were from the end of a run with maximum temperature ratio of TR = 1.52. Overall cooling effectiveness is defined by

$$\theta(x,y) = \frac{T_{01\mathrm{h}} - T_{\mathrm{S}}(x,y)}{T_{01\mathrm{h}} - T_{0\mathrm{c,in}}} \tag{60}$$

where $T_{\mathrm{S}}(x,y)$ is the local surface temperature. Here an incompressible definition (for discussion see chapter 2) is taken.

Looking at Figure 48, the overall cooling effectiveness on Surface 1 (outer wall facing mainstream) increases in the streamwise direction i.e. the direction from leading edge (LE) to trailing edge (TE). This is due to increasing film effectiveness in the streamwise direction. On Surface 5 (inner wall facing coolant plenum) the overall cooling effectiveness decreases in the reverse direction (TE to LE), which is the direction of coolant flow, and the direction in which the cooling potential decreases. On this surface the temperature is almost equal to the local coolant flow temperature. The in-situ calibration patches are visible as two circular regions near the LE of the plate. There is excellent repeatability in the lateral direction (six repeating modules), and the general behaviour of the three streamwise modules is similar. The quality of the data is superb, and the entirety of Surface 1 and Surface 5 can be visualised in the images.

3.7.2 Transient behaviour of test piece

The transient behaviour is now considered. Specific averaging regions A, B, and C on Surface 1 and exactly corresponding regions D, E and F on Surface 5 are considered. These are marked in Figure 48. Full surface average results are also considered (entirety of Surface 1 and Surface 5).

As an example of the transient characteristics, a run with a maximum temperature ratio of TR = 1.52 is considered. Temperature characteristics for the mainstream flow, $T_{01h}(t)$, coolant flow, $T_{0c,in}(t)$, and for averaging regions A–F (T_A to T_F) are shown in Figure 49. The air heater is turned on at approximately $t = 0$ s and turned off at about $t = 300$ s. In this period the mainstream air temperature increases from approximately 305 K to approximately 445 K. The coolant temperature remains relatively constant at approximately 295 K. The characteristics of surface temperature $T_A(t)$ to $T_F(t)$ are of similar general form to $T_{01h}(t)$, but—of course—with a delay caused by the transient surface response time of the test article. Further discussion of the temperature characteristics (and corresponding pressure characteristics) are presented in Naidu and Povey [17].

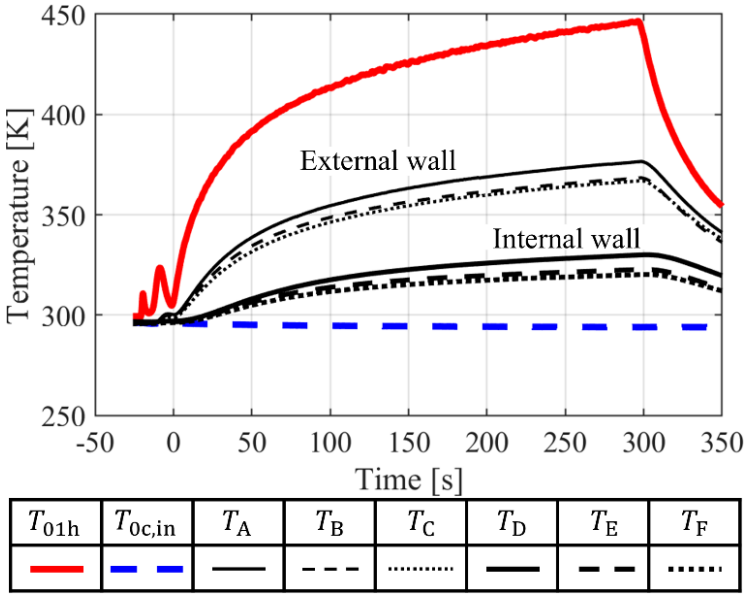

Figure 49: Transient temperature characteristics of the mainstream flow, coolant flow, regions A, B and C on Surface 1 and regions D, E, and F on Surface 5.

The characteristics $T_A(t)$ to $T_F(t)$ can be cast as overall cooling effectiveness characteristics $\theta_A(t)$ to $\theta_F(t)$ (using Eq. (60)). These are shown in Figure 50.

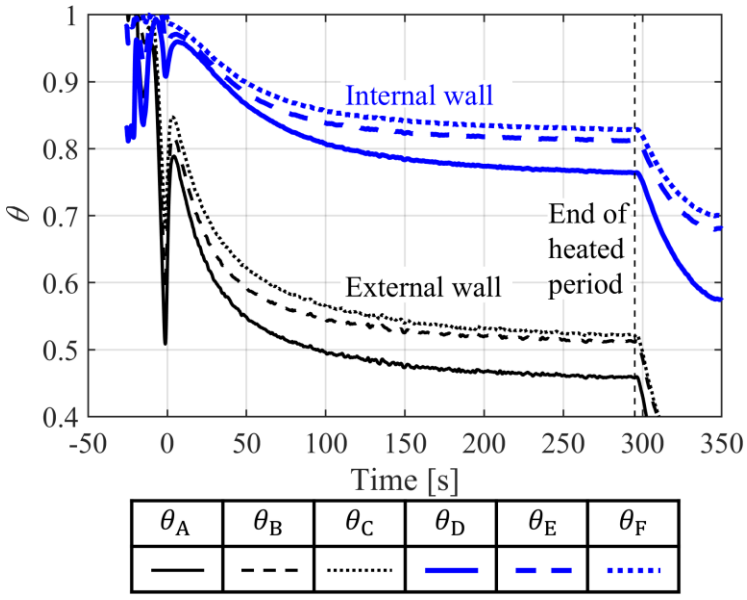

Figure 50: Transient overall cooling effectiveness characteristics for the six averaging regions.

All six characteristics have similar form: an initial transient lasting approximately 100 s after the heater has been switched on, followed by a more stable period of about 200 s duration leading up to the heater being switched off. The time constant of the test article based on the mean wall

temperature from a 2D network model (described later in section 3.7.3) is approximately τ_{model} = 18 s. Although the time constant of the mainstream flow is over three times longer than this (approximately τ_{flow} = 55 s, see Figure 49), the test article never achieves true steady state, and a small correction is necessary. This correction is considered now.

3.7.3 Correction for transient behaviour

In the experiment, the flow time constant (τ_{flow} = 55 s) was measured to be approximately 3.1 times the test article time constant (τ_{model} = 18 s), and the overall test time (300 s) was approximately 5.4 times the flow time constant. The test article comes close to a quasi-steady-state condition, but a small correction is required to determine the exact *inferred instantaneously steady state* (IISS) values of overall cooling effectiveness from the measured (transient) values. It is shown in this section that the magnitudes of correction at 100, 200 and 300 s are approximately 2.2%, 0.7% and 0.5%. These are small corrections, but performing a time-dependent correction allows one to use more of the available data in the final result. To perform this small correction for unsteady behaviour, the low-order network model was modified to run as an unsteady solver. Time-dependent mainstream and coolant inlet temperature boundary conditions and domain-global BCs (Re_D, M and CMPR) were obtained directly from experimental measurements. The initial wall temperature distributions are uniform with value equal to the average experimental surface temperature at t = 0 s (isothermal initial condition).

The predicted temporal temperature characteristics from the transient low-order network model are shown in Figure 51. The mainstream temperature, $T_{01h}(t)$, and coolant inlet temperature, $T_{0c,in}(t)$, are from an experimental run (same data as Figure 49), and are the temporal boundary conditions on the network model. The surface-averaged coolant duct temperature, $\overline{T}_{0c}(t)$, the surface-averaged near-wall mixing layer temperature, $\overline{T}_{0m}(t)$, and the surface-averaged outer and inner wall temperatures, $\overline{T}_{S1}(t)$ and $\overline{T}_{S5}(t)$ respectively, are the network model outputs. It is noted that they are of very similar form to the measured external and internal wall temperature trends shown in Figure 49. Corresponding surface-averaged IISS values (prime notation is used

to distinguish them) $\overline{T}'_{S1}(t)$ and $\overline{T}'_{S5}(t)$ are also shown. The transient network model was run for a time period corresponding to that of the heated period (from $t = 0$ s to approximately $t = 300$ s). The surface-averaged IISS values are slightly higher than the uncorrected values in the initial period of the run ($0 < t < 100$ s) but in the latter period of the run ($t > 100$ s) the two characteristics rapidly converge. Although only surface-averaged values are considered in this section, the results are based on a 2D (streamwise and through-wall directions) solver which was calibrated against the experimental data. Calibration is discussed in section 3.7.4.

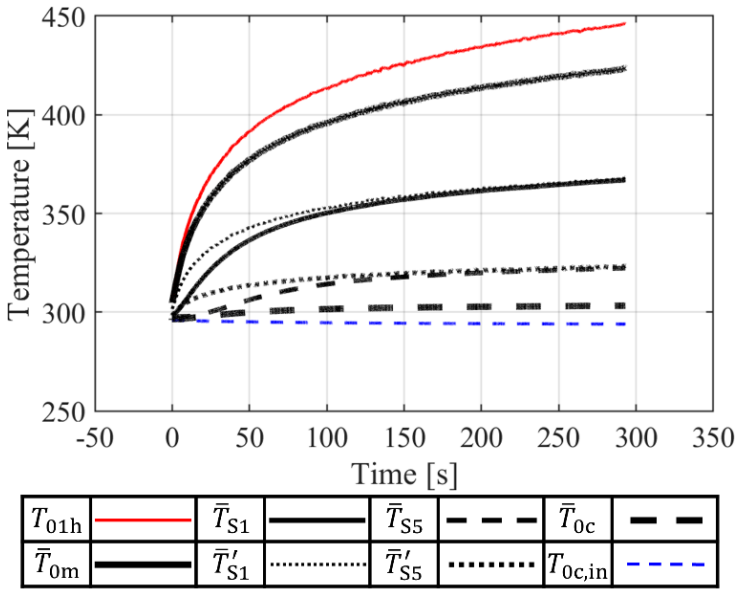

Figure 51: Temperatures characteristics from the 2D transient thermal network model.

Overall cooling effectiveness characteristics corresponding to $\overline{T}_{S1}(t)$, $\overline{T}_{S5}(t)$, $\overline{T}'_{S1}(t)$ and $\overline{T}'_{S5}(t)$ (referred to as $\overline{\theta}_{S1}(t)$, $\overline{\theta}_{S5}(t)$, $\overline{\theta}'_{S1}(t)$ and $\overline{\theta}'_{S5}(t)$) are shown in Figure 52. As expected (on the basis of back-of-the-envelope time-constant arguments), the pairs of data (IISS trend and corresponding unsteady trend) are strongly converging, the difference corresponding to approximately 2.2%, 0.7% and 0.5% of the maximum value of θ (i.e. unity) at 100, 200 and 300 s. This is most clearly seen by looking at the residuals $\overline{\theta}'_{S1}(t) - \overline{\theta}_{S1}(t)$ and $\overline{\theta}'_{S5}(t) - \overline{\theta}_{S5}(t)$. These are shown in Figure 53.

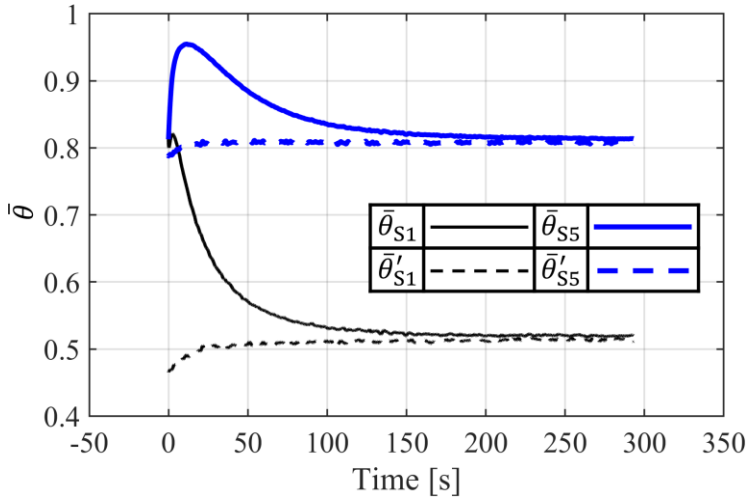

Figure 52: Transient ($\bar{\theta}_{S1}(t)$ and $\bar{\theta}_{S5}(t)$) and inferred instantaneously steady state ($\bar{\theta}'_{S1}(t)$ and $\bar{\theta}'_{S5}(t)$) surface-averaged overall cooling effectiveness characteristics from the 2D transient thermal network model.

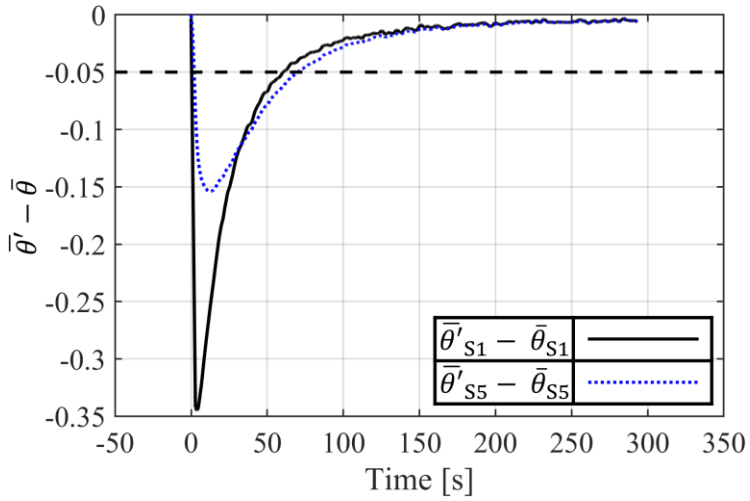

Figure 53: Residuals $\bar{\theta}'_{S1}(t) - \bar{\theta}_{S1}(t)$ and $\bar{\theta}'_{S5}(t) - \bar{\theta}_{S5}(t)$.

In addition to evaluating the magnitudes of the residuals, the residuals are used to transform the experimentally measured uncorrected data $\bar{\theta}(x,t)$ to equivalent IISS values $\bar{\theta}'(x,t)$. This correction is performed on a per-run basis; the particular residual functions arising from the particular (run-specific) mainstream and coolant inlet temperature traces, $T_{01h}(t)$ and $T_{0c,in}(t)$, respectively. This allows the use of entire time-series data in the analysis presented later in this chapter. In section 3.7.4 the local trends (function of x as well as t) and the calibration of the network model against experimental data are discussed.

3.7.4 Calibration of transient solver and application for determining spatial distributions $\bar{\theta}'(x,t)$ from $\bar{\theta}(x,t)$

In section 3.7.3 surface-averaged results were discussed to illustrate the typical magnitude of the correction to IISS values. In this section the calibration of the transient solver, and the application of the correction to IISS values as a function of both time and streamwise distance, x, is discussed. The transient solver uses six correlations, each representing one of six local surface BCs: $\eta_{ML}(x,t)$ is defined by Eq. (41); $h_m(x,t)$ is defined by Eq. (42); $h_{ci}(x,t)$ (i = 2, 3, 4) are defined by Eq. (43) with individual multiplication factors (K_{2i}) for each surface i; and $h_{c5}(x,t)$ is defined by Eq. (44). To tune the network model against the experimental data calibration coefficients (C_1 to C_6) are used in each of the six correlations. They are introduced as multipliers. The nominal value of these multipliers is unity, but optimum values of these multipliers that minimise the root-mean-square (RMS) deviation of the low-order-model data and experimental data are found. The correction is performed on a per-run basis, using laterally-averaged streamwise-varying time-based data for Surface 1 and Surface 5 (i.e. $\bar{\theta}_{S1}(x,t)$ and $\bar{\theta}_{S5}(x,t)$).

The maximum and minimum values that multipliers C_1 to C_6 take across all the data (all experimental runs in this chapter) are summarised in Table 5.

Table 5: Values of the calibration coefficients C_1 to C_6 for each correlation.

Correlation no.		Calibration coefficient	Min. value	Max. value	Max-to-min ratio
1	(η_{ML})	C1	0.96	1.07	1.11
2	(h_m)	C2	0.93	1.04	1.12
3	(h_{c2})	C3	0.98	1.10	1.12
4	(h_{c3})	C4	1.33	1.73	1.30
5	(h_{c4})	C5	1.19	1.48	1.24
6	(h_{c5})	C6	1.34	1.74	1.30

It is observed that for C_1 to C_3, the maximum deviation from unity is 0.10, demonstrating accurate applicability of the original correlations. The multipliers C_4 to C_6 deviate more from unity suggesting poorer applicability of the underlying correlations. Looking at the maximum-to-minimum value ratio for individual coefficients (last column of table) it is observed that values

lie in the range 1.11 to 1.30. The limited extent of this range shows that the minimisation algorithm is relatively stable. Once the calibration coefficients (C_1 to C_6) are determined for a particular run, the (corrected) laterally-averaged IISS overall cooling effectiveness characteristics, $\overline{\theta}'_{S1}(x,t)$ and $\overline{\theta}'_{S5}(x,t)$, can be evaluated from the uncorrected characteristics, $\overline{\theta}_{S1}(x,t)$ and $\overline{\theta}_{S5}(x,t)$. The process for this is as follows.

The starting point is a converged calibrated *transient solution* which has experimentally-measured mainstream and coolant inlet temperatures as inputs, $T_{01h}(t)$ and $T_{0c,in}(t)$, and which has six calibrated correlations (for $\eta_{ML}(x,t)$, $h_m(x,t)$, $h_{c2}(x,t)$, $h_{c3}(x,t)$, $h_{c4}(x,t)$ and $h_{c5}(x,t)$) with calibration coefficients (C_1 to C_6) particular to the individual run. For each timestep of the converged transient network model solution a supplementary steady-state solution, which has experimentally-measured mainstream and coolant inlet temperatures, $T_{01h}(t)$ and $T_{0c,in}(t)$, and pressures, $p_{01h}(t)$, $p_{0cin}(t)$ and $p_{4h}(t)$, as inputs, is run. By taking the difference between the two solutions the residuals $\overline{\theta}'_{S1}(x,t) - \overline{\theta}_{S1}(x,t)$ and $\overline{\theta}'_{S5}(x,t) - \overline{\theta}_{S5}(x,t)$ are evaluated at each streamwise position and timestep. The residuals are calculated using only information from the calibrated transient network model and corresponding supplementary steady-state solution. Once the residuals are evaluated, the experimentally-measured characteristics, $\overline{\theta}_{S1}(x,t)$ and $\overline{\theta}_{S5}(x,t)$, are corrected to get the corresponding corrected-IISS characteristics $\overline{\theta}'_{S1}(x,t)$ and $\overline{\theta}'_{S5}(x,t)$. A somewhat arbitrary decision needs to be made about *which* (time-series) data to correct, and data is chosen for which the surface-averaged residual has a magnitude less than 0.05. This cut-off value is chosen such that sufficient data points are presented to facilitate analysis of the trends of $\overline{\theta}$ with TR, whilst not presenting an excessive amount of data such that the contrary trends associated with each run (discussed in section 3.8.3) cause confusion to the reader and distract from the main points being discussed.

Consider the spatial distributions of the predicted (by the transient network model) uncorrected ($\overline{\theta}_{S1}(x,t)$ and $\overline{\theta}_{S5}(x,t)$) overall cooling effectiveness characteristics, presented in

Figure 54, for three different times t = 100, 200 and 290 s. The data are for the same run as shown in Figure 49.

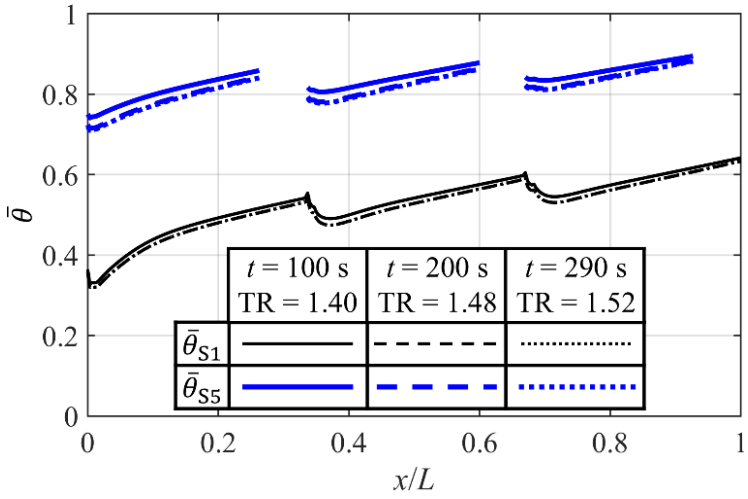

Figure 54: Low-order-model-based predictions of spatial distributions of overall cooling effectiveness $\bar{\theta}_{S1}(x,t)$ and $\bar{\theta}_{S5}(x,t)$, for t = 100, 200 and 290 s from a converged solution calibrated against an experimental run.

The temperature ratios corresponding to these time stamps are $T_{01h}/T_{0c,in}$ = 1.40, 1.48 and 1.52. As mentioned in the context of Figure 48, on both Surface 1 and Surface 5, the general trend in the streamwise direction is increasing overall cooling effectiveness. The trend with TR is that overall cooling effectiveness decreases with TR: this is the prime subject of this chapter, and it is dealt with comprehensively in section 3.8. Here the magnitude of the correction to the IISS trends is of concern. The spatial distribution of the residuals $\bar{\theta}'_{S1}-\bar{\theta}_{S1}$ and $\bar{\theta}'_{S5}-\bar{\theta}_{S5}$ (corresponding to the Figure 54 data) are shown in Figure 55. It is observed that the absolute values of the correction terms are small, and well-behaved spatially. The mean residuals for t = 100, 200 and 290 s are, respectively, $\Delta\bar{\theta}_{S1}$ = −0.0221, −0.0070 and −0.0051 and $\Delta\bar{\theta}_{S5}$ = − 0.0278, −0.0081 and −0.0052. It is complex to ascribe a meaningful additional uncertainty due to the process of correcting to IISS values, but—given the data are extremely well-behaved—the arising additional uncertainty is assumed to be at least an order of magnitude smaller than the value of the correction itself, i.e. extremely small (of order 0.1% of the surface-averaged value of θ).

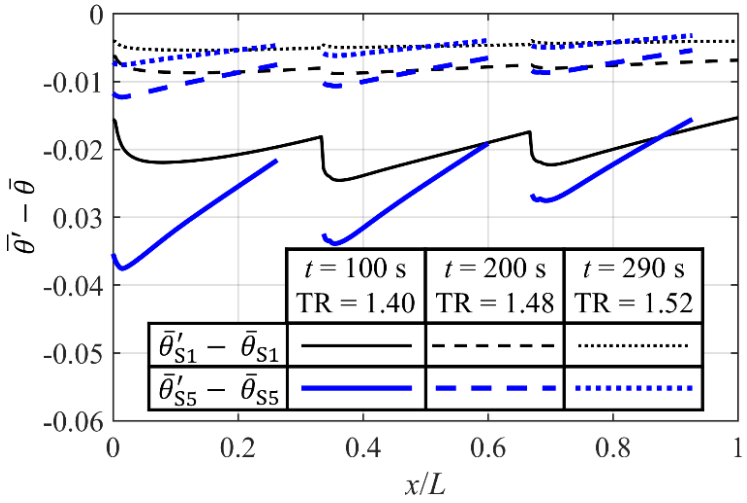

Figure 55: Predicted spatial distributions of the overall cooling effectiveness residuals $\bar{\theta}'_{S1}-\bar{\theta}_{S1}$ and $\bar{\theta}'_{S5}-\bar{\theta}_{S5}$ for t = 100, 200 and 290 s.

3.7.5 Correction for off-design conditions of Re_D, M and CMPR

During experiments, Re_D, M and CMPR were held close to their design values ($Re_D = 1.50\times10^4$; M = 0.30; and CMPR = 1.020) but there was uncontrolled variation (sympathetic with changes in temperature ratio) in the ranges: $1.34\times10^4 \leq Re_D \leq 1.82\times10^4$; $0.290 \leq M \leq 0.305$; and $1.0170 \leq CMPR \leq 1.0238$. All data is corrected back to its design point by performing simulations to assess the sensitivity to off-design conditions of Re_D, M and CMPR. These simulations were performed using the 2D low-order conjugate aerothermal network model. Simulations were performed for temperature ratios in the range $1.01 \leq TR \leq 2.00$.

In these simulations, because the sensitivity to each variable is very low, the variables were studied independently of each other (assumed linear superposition). Additional CFD simulations were performed to determine the following inputs to the aerothermal network model: adiabatic film effectiveness, and associated entrainment rate distribution, at the reference TR for off-design conditions of M and CMPR; isentropic Mach number distribution for off-design conditions of M. These simulations were similar to those presented in Naidu and Povey [17], but for Mach number in the range $0.290 \leq M \leq 0.310$ and CMPR in the range $1.0180 \leq CMPR \leq 1.0220$. These CFD data are not shown, but were used to correct the network model at off-design conditions. Adiabatic film effectiveness is assumed to be insensitive to changes in Re_D—in isolation of all other non-

dimensional groups—and therefore the baseline distribution of η (obtained from the CFD simulation at the reference TR with Re_D, M and CMPR taking their design values) is used as input to the aerothermal network model when studying the sensitivity to this variable. This assumption is supported by previous studies: for example, the experimental results of Mehendale and Han [41]. Additionally, it is assumed that the isentropic Mach number distribution is insensitive to changes in Re_D and CMPR.

The low-order-model-estimated impacts on overall cooling effectiveness arising from off-design conditions of Re_D, M and CMPR are shown in Figure 56. Results are shown for Surface 1 and Surface 5 for engine conditions (TR = 2.0) and conventional lab conditions (TR = 1.2) of temperature ratio. Individual data points (converged network model simulations) and best-fit curves are presented. The data are presented as correction offsets for off-design Re_D, M and CMPR: frame a, b and c, respectively. The following observations are made:

i) The change due to uncontrolled variation in Re_D is greater than that due to uncontrolled variation in M and CMPR. This is primarily via the impact of Re_D on h_m and $h_{\mathrm{c}2}$.

ii) The sensitivity of corrections to TR is small.

iii) The magnitude of the correction offsets is similar for Surface 1 and Surface 5, but the form is very different.

The data in Figure 56 is used (in conjunction with additional data at a wider range of TR) to correct experimental data at off-design conditions of Re_D, M and CMPR back to the nominal operating point. Taking all data used in this study, the average corrections were 0.28% and 1.00% for Surface 1 and Surface 5, respectively. The corrections are small in magnitude and can be accurately performed.

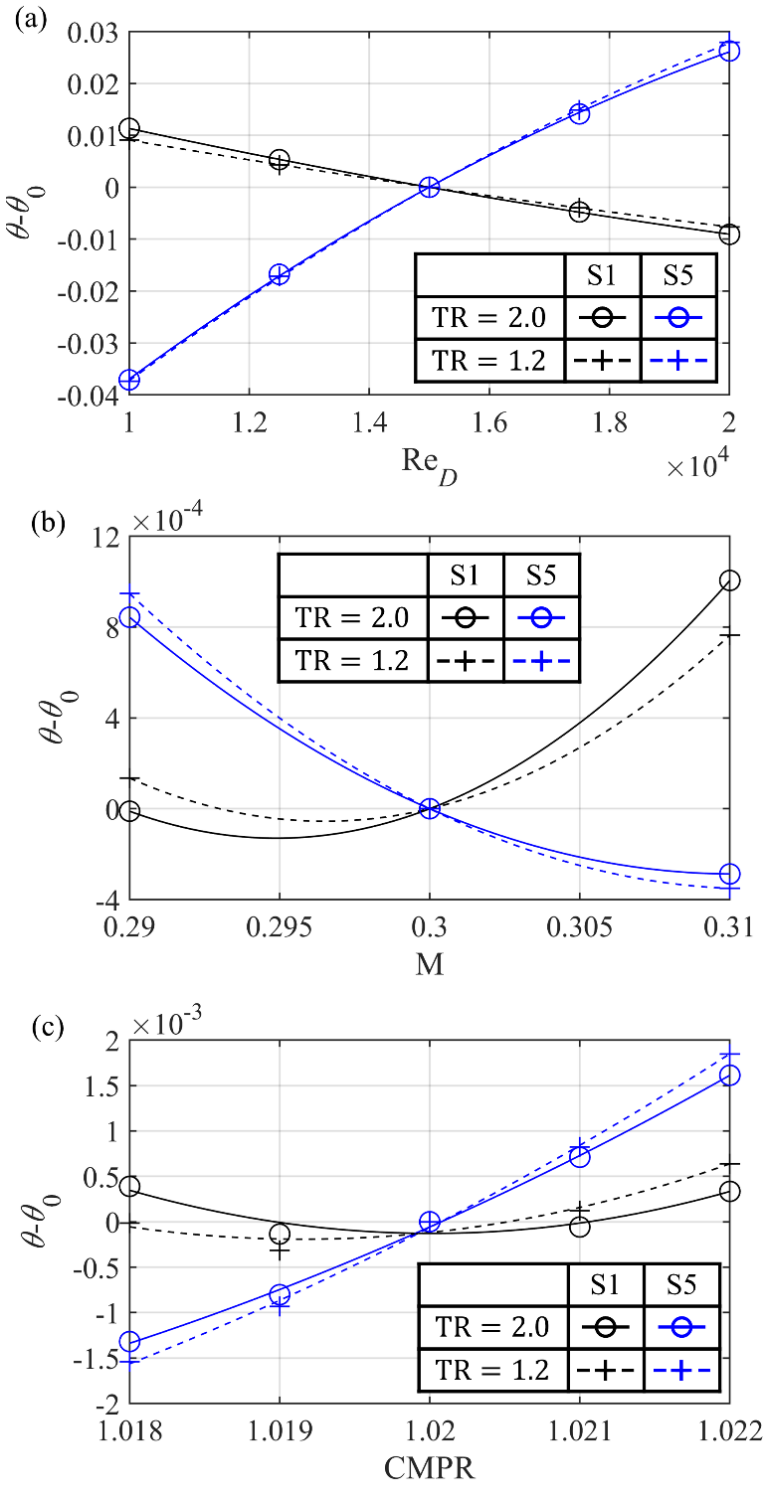

Figure 56: Low-order-model-estimated differences in overall cooling effectiveness from the design condition arising from uncontrolled variations in: (a) Re_D; (b) M; and (c) CMPR.

3.7.6 Uncertainty in overall cooling effectiveness

In this section uncertainty in the measurement of overall cooling effectiveness is considered. Two types of uncertainty are considered:

i) The absolute uncertainty in a single measurement of θ, as a function of θ and TR. This is referred to as U_θ. This is the value relevant for assessing the absolute accuracy of an overall cooling effectiveness measurement of a part. This can be thought of as an overall uncertainty that arises from combined bias uncertainties in the measurement chain. It is assumed that the length of the time window used to average overall cooling effectiveness data is of sufficient length for precision errors in the underlying temperature measurements to be insignificant.

ii) The uncertainty in a *change* in overall cooling effectiveness ($\Delta\theta$) from a particular reference point (TR_{ref}, θ_{ref}). This is referred to as $U_{\Delta\theta}$. This is the value relevant to assessing the *trend* of overall cooling effectiveness with TR, which is the prime purpose of this chapter. This can be thought of as an overall uncertainty that arises from combined *bias-variation uncertainties* in the *change* in absolute temperatures as one moves from a particular reference condition of temperature ratio to a new operating point. These uncertainties arise because the bias error of a particular thermocouple (or IR camera system) has a particular characteristic with absolute temperature (not constant). Conceptually, whilst the bias error at a particular reference temperature may be relatively large, the change in bias error moving away from that temperature will generally be smaller, and will be a function of the change in temperature from the reference point. Thus the uncertainty in $\Delta\theta$ will generally be smaller than the uncertainty in θ. The concept of bias-variation-uncertainty is developed in a moment.

First consider the uncertainty (U_θ) in absolute values of effectiveness. For mainstream and coolant flow inlet temperatures, the quoted bias uncertainty (two standard deviations) for K-type

thermocouple measurements is taken as U_T = 1.1 K. For surface temperatures measured using the IR camera system (calibrated in-house against a black-body calibrator) a bias uncertainty of U_T = 2.0 K is taken. The uncertainty analysis was performed using a Monte Carlo perturbation of Eq. (60), for normally distributed bias errors, with two-standard-deviation limits of $\pm U_T$ in the underlying temperatures.

The absolute uncertainty in θ, U_θ, was evaluated by performing a Monte Carlo simulation in the range $0.0 < \theta \leq 1.0$ and $1.0 < \mathrm{TR} \leq 2.0$ with 100 steps in each axis, with 1.0×10^6 simulations per point, i.e., 1.0×10^{10} simulations in total. The results are presented as a function of θ and TR in Figure 57.

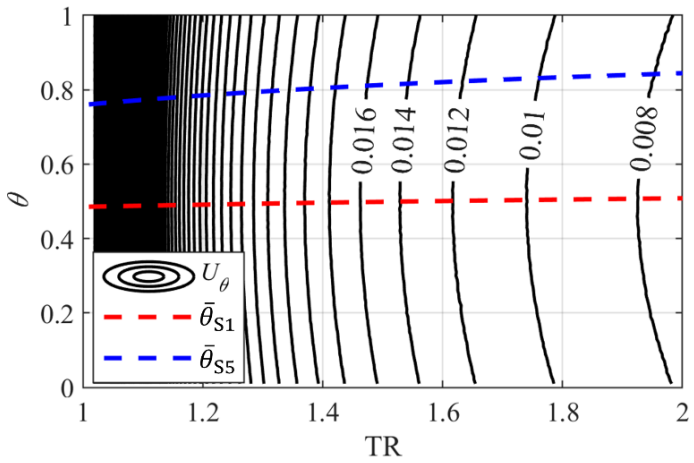

Figure 57: Uncertainty in θ, U_θ, as a function of θ and TR.

The uncertainty is a weak function of θ but a strong function of TR. In the figure surface-averaged overall cooling effectiveness characteristics from the calibrated 2D aerothermal network model (details of calibration algorithm are provided in section 3.8.4) for Surface 1 and Surface 5 (the trends are discussed in detail later) are overlayed. At the reference temperature ratio of TR = 2.0, the uncertainties for Surface 1 and Surface 5 are U_θ = 0.0074 and 0.0076, respectively. As a percentage of the design values of surface-averaged overall cooling effectiveness ($\bar{\theta}_{S1}$ = 0.50; $\bar{\theta}_{S5}$ = 0.80), these correspond to uncertainties of 1.48% and 0.95%. The uncertainty increases rapidly moving towards lower temperature ratios because absolute uncertainties in underlying variables are a larger proportion of the temperature differences in the numerator and denominator

of Eq. (60). Uncertainty limits derived from Figure 57 are used when presenting experimental trends of θ.

Now consider the uncertainty ($U_{\Delta\theta}$) in the change in surface-averaged overall cooling effectiveness ($\Delta\theta$) from a particular reference point. Assuming a fixed total temperature at the cooling channel inlet ($T_{0\mathrm{cin}} = 290$ K), the change in surface-averaged overall cooling effectiveness from any reference point (TR = $\mathrm{TR_{ref}}$; $\theta = \theta_{\mathrm{ref}}$) is expressed in terms of the *changes* in mainstream total temperature ($\Delta T_{01\mathrm{h}}(\mathrm{TR}) = T_{01\mathrm{h}}(\mathrm{TR}) - T_{01\mathrm{h,ref}}$) and surface temperature ($\Delta T_{\mathrm{S}}(\mathrm{TR}) = T_{\mathrm{S}}(\mathrm{TR}) - T_{\mathrm{S,ref}}$)

$$\Delta\theta(\mathrm{TR}) = \frac{(1-\theta_{\mathrm{ref}})\Delta T_{01\mathrm{h}}(\mathrm{TR}) - \Delta T_{\mathrm{S}}(\mathrm{TR})}{\Delta T_{01\mathrm{h}}(\mathrm{TR}) + T_{0\mathrm{cin}}(\mathrm{TR_{ref}} - 1)} \tag{61}$$

Looking at Eq. (61), it is observed that the uncertainty in $\Delta\theta$ is the result of uncertainties in $\Delta T_{01\mathrm{h}}$ and ΔT_{S}. Here bias-variation-uncertainty is referred to. These uncertaintes are functions of the temperatures themselves i.e. $U_{\Delta T_{01\mathrm{h}}}(\Delta T_{01\mathrm{h}})$ and $U_{\Delta T_{\mathrm{S}}}(\Delta T_{\mathrm{S}})$. Whilst the absolue bias error (of a particular thermocouple or IR camera system) is represented as a normal distribution at a particular reference point, the change in the *unknown* offset has a low gradient with absolute temperature. This is evidenced by the fact that instruments can record small temperature *changes* with much greater accuracy than the bias uncertainty. For very large changes in temperature it would be more natural to assume the quoted bias uncertainty prevails for the *change*. The question arises, how does one model the degree or correlation (or bias-variation-uncertainty) between two points of temperature?

The bias-variation-uncertainty, $U_{\Delta T}$, in a single measurement of a *change* in temperature, ΔT, from a reference point is now defined. One cannot know the exact form for $U_{\Delta T}(\Delta T)$, however assumptions can be made based on three known constraints:

i) At a particular reference point, the temperatures are fully correlated and repeat experiments will always give the same result, regardless of the overall bias uncertainty in θ_{ref}. That is $U_{\Delta T}(0) = 0$. And, therefore, $U_{\Delta\theta} = 0$ for $\Delta\theta = 0$.

ii) $U_{\Delta T}$ increases with increasing ΔT, because the correlation between temperatures reduces as one moves further away from the reference point.

iii) $U_{\Delta T}(\Delta T) = U_T$ for sufficiently large ΔT. That is, as one moves sufficiently far from the reference point, the temperatures become completely uncorrelated. The bias-variation-uncertainty in ΔT is now equal to the bias uncertainty in the underlying temperature measurements.

Based on these three constraints, a linear profile for $U_{\Delta T}(\Delta T)$ is assumed in the range $\Delta T = \pm 290$ K, increasing in magnitude from 0 at $\Delta T = 0$ to U_T at $\Delta T = \pm 290$ K, such that the linear region covers the full range of temperatures in the system considered in this chapter. For temperatures outside of this range, $U_{\Delta T}$ takes a constant value of $U_{\Delta T}(\Delta T) = U_T$. $U_{\Delta T}$ is presented as a function of ΔT in Figure 58 for both mainstream total temperature and surface temperature.

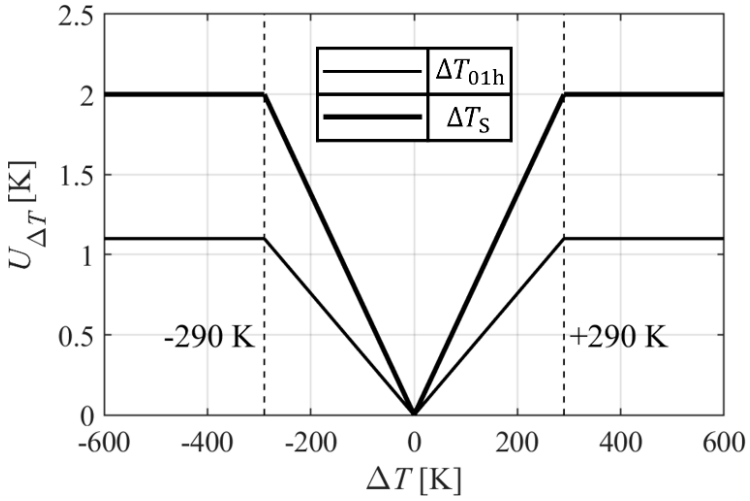

Figure 58: Assumed uncertainty in ΔT due to bias-variation-uncertainty for mainstream total temperature and surface temperature.

For a particular measurement of a change in temperature, ΔT, normally distributed bias-variation uncertainty is assumed. The uncertainty in the change in overall cooling effectiveness ($\Delta\theta$) from a particular reference point (TR_{ref}, θ_{ref}) was evaluated using a Monte Carlo perturbation of Eq. (61) for normally distributed bias-variation-uncertainty in ΔT_{01h} and ΔT_S. A decision must be made regarding how to set the value of ΔT_S as one moves away from the reference point. ΔT_S is

evaluated using the characteristic trend of $\bar{\theta}$ vs TR derived from the calibrated 2D aerothermal network model (this trend is discussed in section 3.8.4). It is noted, by re-arranging Eq. (61), that ΔT_s can be expressed in the form $\Delta T_s = (1 - \theta_{ref} - \Delta\theta)\Delta T_{01h} - T_{0cin}\Delta\theta$. For small values of $\Delta\theta$ ($\Delta\theta \cong 0$), this reduces to the form $\Delta T_s \cong (1 - \theta_{ref})\Delta T_{01h}$. That is, ΔT_s is approximately independent of the exact form of the characteristic trend— $\theta = f(\mathrm{TR})$—and therefore uncertainty limits derived using the network model can be applied to the experimental data with little loss of accuracy.

Simulations were performed at 100 discrete points along the characteristic trend for 100 different reference temperature ratios in the range $1.0 < \mathrm{TR}_{ref} \leq 2.0$, with 1.0×10^6 simulations per point, i.e., 1.0×10^{10} simulations in total, for both Surface 1 and Surface 5. For ΔT_{01h} and ΔT_S measurements, the bias-variation-uncertainty trends of Figure 58 are taken. The results are presented as a function of TR and reference temperature ratio, TR_{ref}, for Surface 1 in Figure 59 and Surface 5 in Figure 60.

For reference temperature ratios in the range $1.0 < \mathrm{TR}_{ref} \leq 2.0$, the ranges of reference overall cooling effectiveness are $0.485 < \theta_{ref} \leq 0.508$ and $0.760 < \theta_{ref} \leq 0.845$ for Surface 1 and Surface 5, respectively. In general, for a particular reference temperature ratio, moving along the TR-axis (vertically in the figure) is equivalent to moving along the corresponding characteristic trend of $\Delta\theta$ vs TR. That is, whilst a particular *reference TR* is fixed, the actual underlying temperature ratio varies (sympathetically with $\Delta\theta$) as one moves along the TR-axis.

For the data in the rest of this chapter, only the reference temperature $\mathrm{TR}_{ref} = 2.0$, i.e. the engine condition, is considered. This is marked by the dashed red line. It is the uncertainty distribution along this line that is of most importance. The variation of $U_{\Delta\theta}$ moving away from the particular reference condition $\mathrm{TR}_{ref} = 2.0$ to lower temperature ratios is now considered. The results for Surface 1 and Surface 5 are plotted in Figure 61.

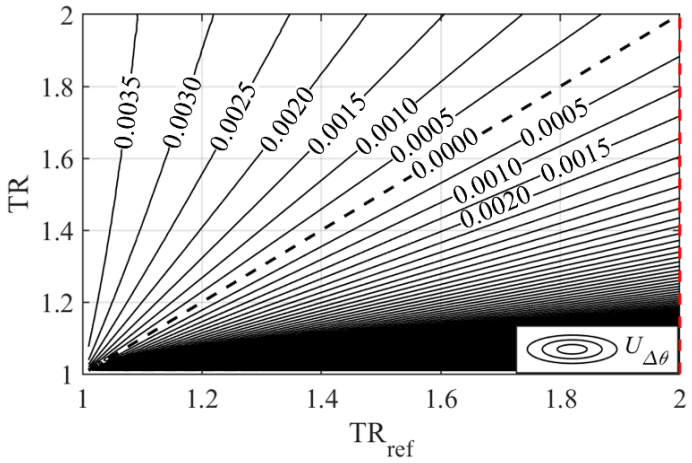

Figure 59: Uncertainty in $\Delta\theta$ (change from the reference effectiveness), $U_{\Delta\theta}$, as a function of TR and TR_{ref} for Surface 1.

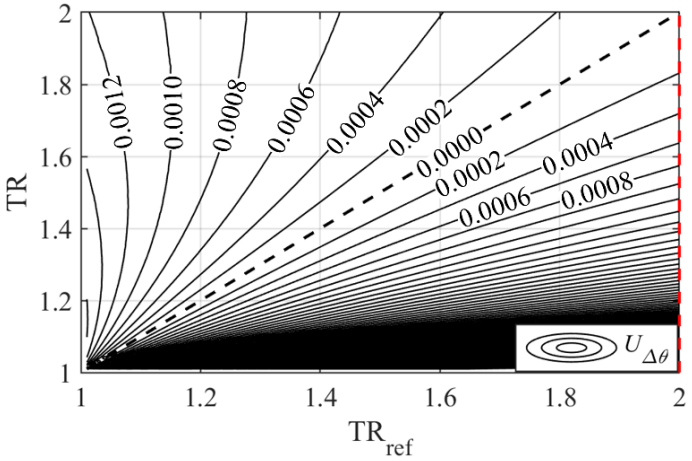

Figure 60: Uncertainty in $\Delta\theta$ (change from the reference effectiveness), $U_{\Delta\theta}$, as a function of TR and TR_{ref} for Surface 5.

Looking at the figure, the following observations are made: $U_{\Delta\theta} = 0$ at $TR = TR_{ref} = 2.0$, i.e. the bias-variation uncertainty in temperature change is zero when the temperature change is zero; $U_{\Delta\theta}$ increases as one moves from the reference TR to lower-than-reference TR; $U_{\Delta\theta}$ explodes as one approaches TR = 1.0; and uncertainty is higher for Surface 1 measurements than for Surface 5 measurements.

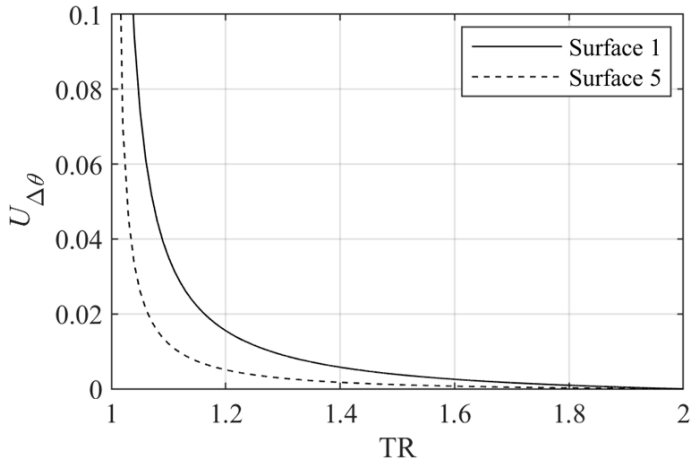

Figure 61: Uncertainty in $\Delta\theta$ (change from the reference effectiveness), $U_{\Delta\theta}$, as a function of TR for Surface 1 and Surface 5 for the reference TR = TR_{ref} = 2.0.

At conditions corresponding to conventional laboratory experiments (TR = 1.2), the uncertainties in $\Delta\theta$ for Surface 1 and Surface 5 are 0.015 and 0.0051, respectively. The corresponding changes in θ—as will be observed later—are $\Delta\theta = -0.017$ and -0.060. That is, moving from typical engine conditions for large civil aircraft to conventional laboratory conditions, the uncertainties are equal to approximately 90.5% and 8.49% of the changes themselves. Uncertainty limits derived from Figure 61 are used when presenting experimental trends of $\Delta\theta$.

3.8 Impact of temperature ratio on overall cooling effectiveness

The key result of this chapter, which is the impact of temperature ratio on overall cooling effectiveness, is now considered. Laterally averaged results for the flat plate are first considered, followed by surface-averaged results.

3.8.1 Laterally-averaged experimental results

The experimentally measured distributions (with streamwise distance) of laterally averaged overall cooling effectiveness are shown in Figure 62 for TR = 1.19, 1.34 and 1.54.

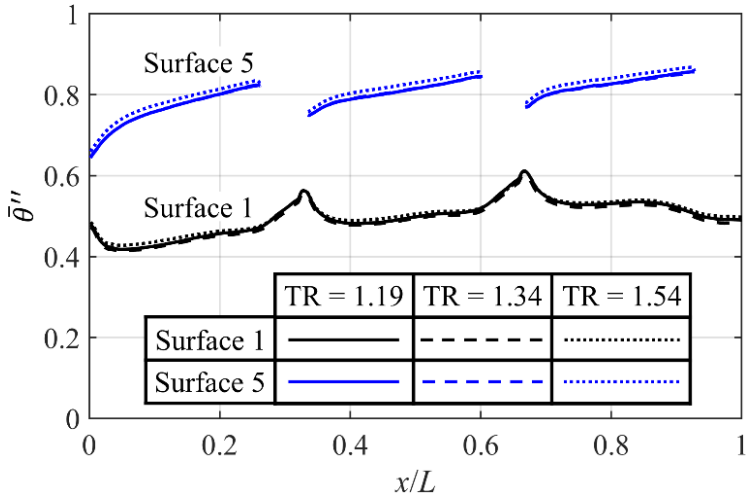

Figure 62: Experimentally-measured results of laterally-averaged overall cooling effectiveness as a function of streamwise position for TR = 1.19, 1.34 and 1.54.

The data in the figure have been averaged over the time period corresponding to the period in which both the Surface 1 and Surface 5 surface-averaged transient correction residuals ($\bar{\theta}'_{S1}(t) - \bar{\theta}_{S1}(t)$ and $\bar{\theta}'_{S5}(t) - \bar{\theta}_{S5}(t)$) are less than 0.05 (see Figure 52 to Figure 55 and associated discussion). The data have been corrected for both transient effects and off-design conditions of Re_D, M and CMPR.

The trends of overall cooling effectiveness with streamwise distance, with reference to the local surface boundary conditions, are first described. The distributions of these are inferred from calibrated low-order network model simulations at each temperature ratio. Consider first Surface 1. There is a slight increase with streamwise distance in the overall cooling effectiveness due to the combined effects of film superposition and a decrease in external heat transfer coefficient with increasing boundary layer thickness (see Naidu and Povey [17] for discussion of trends in $\eta_{ML}(x)$ and $h_m(x)$ with streamwise distance). The average effectiveness (across all data) was 0.50. Surface 5 has a similar (increasing) trend with streamwise distance. Discontinuities in the profile are cooling channel inlets (no internal wall). This trend is primarily driven by two effects: firstly, an increase with streamwise distance in overall cooling effectiveness of Surface 1 (this has been discussed); secondly, a reduction in internal cooling effectiveness as one moves from inlet to exit

of the cooling channel (the internal flow direction is opposed to the mainstream flow). The mean value of overall cooling effectiveness for Surface 5 is 0.80.

Now consider the trend with TR. For three very different temperature ratios (TR = 1.19, 1.34 and 1.54) the data are extremely similar, showing low sensitivity of this result to TR. This result is examined in much greater detail later in section 3.8.3, where a much larger data set is considered and the results are discussed in the context of experimental uncertainty.

3.8.2 Laterally-averaged low-order-model results

The low-order-model-predicted results corresponding to the data of Figure 62 are shown in Figure 63.

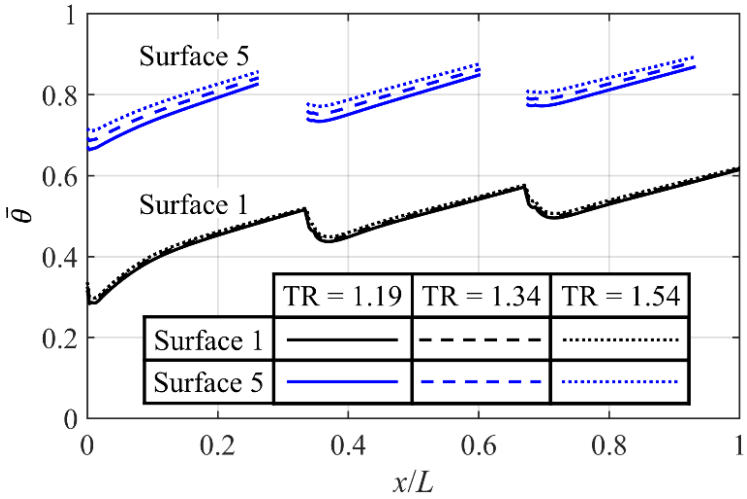

Figure 63: Low-order-model-predicted results of laterally-averaged overall cooling effectiveness as a function of streamwise position for TR = 1.19, 1.34 and 1.54.

The low-order-model has been calibrated against the entire experimental data (across all time series and temperature ratios) with a single set of calibration coefficients (C_1 to C_6) for correlations for $\eta_{ML}(x)$, $h_m(x)$ and $h_{ci}(x)$ ($i = 2, 3, 4, 5$). The process for this calibration is described in section 3.8.4. The general trends with streamwise position are similar to the experimental data (increasing overall cooling effectiveness with streamwise position and a local reduction at the interface between each module). The surface-averaged values match the experimental data (across the entire data set) as closely as possible within the constraints imposed during the calibration process (described in section 3.8.4). Small differences in local gradient

(with streamwise distance) of overall cooling effectiveness arise due to limitations in the low-order network model: for example, neither local internal heat transfer coefficient enhancement due to internal coolant impingement, nor local reduction in external film effectiveness due to jet lift off are modelled. The purpose of this study is to understand the *change with temperature ratio* in surface-averaged overall cooling effectiveness, and therefore an exact match of spatial distributions is not required. With this in mind, the focus was achieving sufficient similarity of spatial distributions, with the primary emphasis being the physical basis for correlations.

So far as the trend with TR is concerned, a small monotonic increase in overall cooling effectiveness with TR is observed, with a larger change in $\bar{\theta}(x)$ with TR for Surface 5. This result is discussed in detail in section 3.8.4.

3.8.3 Surface-averaged experimental results

Experimental measurements of surface-averaged overall cooling effectiveness as a function of TR are presented in Figure 64.

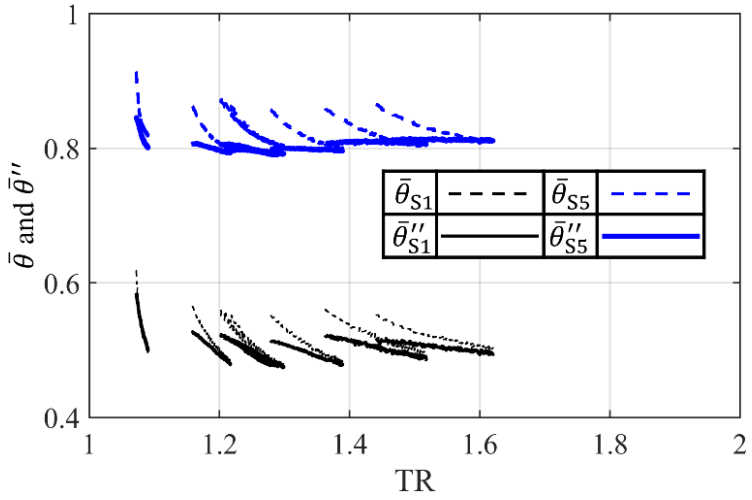

Figure 64: Uncorrected ($\bar{\theta}_{S1}$ and $\bar{\theta}_{S5}$) and corrected ($\bar{\theta}''_{S1}$ and $\bar{\theta}''_{S5}$) surface-averaged overall cooling effectiveness measurements on Surface 1 and Surface 5.

Data are presented for Surface 1 and Surface 5. Uncorrected data ($\bar{\theta}_{S1}$ and $\bar{\theta}_{S5}$) and data corrected for both transient effects and off-design conditions of Re_D, M and CMPR ($\bar{\theta}''_{S1}$ and $\bar{\theta}''_{S5}$) are both presented. In all, there are 8 experimental runs covering the TR range $1.07 < TR < 1.62$. The time-series of data that has been selected corresponds to the time period in which both the transient

correction residuals ($\bar{\theta}'_{S1} - \bar{\theta}_{S1}$ and $\bar{\theta}'_{S5} - \bar{\theta}_{S5}$) are less than 0.05. Over the entire data series of 8 runs, the time-average corrections for transient effects for Surface 1 and Surface 5 were $\Delta\bar{\theta} = -0.010$ and -0.012, respectively, and the time-average corrections for off-design conditions of Re_D, M and CMPR were $\Delta\bar{\theta} = +0.0012$ and -0.0071. The corresponding temperature-ratio-average corrections were $\Delta\bar{\theta} = -0.014$ and -0.016 (transient effects) and $\Delta\bar{\theta} = +0.0014$ and -0.0080 (off-design conditions of Re_D, M and CMPR). These corrections are relatively small.

Consider the trend with TR of the corrected overall cooling effectiveness ($\bar{\theta}''_{S1}$ and $\bar{\theta}''_{S5}$). Taking the entire data set (all runs) a small decrease in overall cooling effectiveness with decreasing temperature ratio is observed. This is the primary result of this chapter and is discussed in detail in section 3.8.4. Considering runs *individually*, it is observed that there is a small decrease in corrected overall cooling effectiveness with *increasing* TR; that is, the reverse trend from the underlying trend for all runs. The small contrary trend associated with individual runs appears to be associated with the transient correction methodology. This is evident when considering the trends with TR (not shown) for $\bar{\theta}''_{S1}$ and $\bar{\theta}''_{S5}$ from the calibrated 2D transient thermal network model (i.e. the data presented in Figure 52 but for all runs and corrected for off-design conditions of Re_D, M and CMPR), which *do* collapse on to a global trend of *reducing* overall cooling effectiveness with *reducing* TR. The implication is that the accuracy of transient correction is insufficient for the purpose. This could result from a need to improve physics in the low-order network model, or a need to improve the optimisation algorithm. The experiment was purpose-designed for this study and the calibrations have very been carefully performed, however. The contrary trend is a matter of great interest, and any experimental or theoretical study that could further investigate both the cause of this trend and improvements to the transient correction methodology is encouraged. The widest possible range of time-series data has been included in order to explicitly expose this unresolved aspect of the data presented in this chapter.

3.8.4 Comparison of low-order network model results and experimental results

The trend of overall cooling effectiveness with TR is now considered: the key result of this chapter. A functional-best-fit of the entire experimental data series is performed by running the calibrated low-order network model at every TR.

In this process, the network model was run at the nominal conditions of Re_D, M and CMPR. $p_{01\mathrm{h}}$, $p_{0\mathrm{c,in}}$ and $T_{01\mathrm{h}}$ were allowed to vary sympathetically with TR ($T_{0\mathrm{c,in}}$ had fixed value of 290 K). Coolant mass flow rate was determined using an experimentally measured capacity characteristic. Mainstream mass flow rate was evaluated from a combination of the nominal boundary conditions and facility geometry. This ensures that the network model conditions are a direct parallel of the corrected experimental conditions as TR is varied. In the *uncalibrated* network model it is recalled that correlations for the local surface BCs $h_{\mathrm{m}}(x)$ and $h_{ci}(x)$ (i = 2, 3, 4, 5) come from literature, and that the distribution $\eta_{\mathrm{ML}}(x)$ is evaluated by combining the adiabatic film effectiveness— $\eta(x)$—from a CFD simulation (for the reference condition, TR = 2.0) with conservation of energy and mass continuity arguments applied within the mixing layers, with the result then scaled using an entrainment-based model to obtain film effectiveness distributions at other conditions of TR.

Results from the uncalibrated low-order network model are compared to the corrected experimental results of surface-averaged overall cooling effectiveness ($\bar{\theta}''_{\mathrm{S1}}$ and $\bar{\theta}''_{\mathrm{S5}}$; see Figure 64) in Figure 65. The uncalibrated network model is in reasonable absolute agreement with the experimental data on Surface 1, with a temperature-ratio-average difference (across all data) of $\Delta\bar{\theta} = +0.0059$. For Surface 5, the agreement is less good with an average difference of $\Delta\bar{\theta} = +0.066$. To close the differences between the uncalibrated network model and the experimental data, the model is calibrated by allowing multipliers (β_1 to β_6) in each of the six equations defining the local surface BCs $\eta_{\mathrm{ML}}(x)$, $h_{\mathrm{m}}(x)$ and $h_{ci}(x)$ (i = 2, 3, 4, 5). The process is as follows. The uncalibrated network model (β_1 to β_6 equal to unity) is first run at every temperature ratio to determine the uncalibrated characteristics of surface-averaged overall cooling

effectiveness, $\bar{\theta}_{S1}(TR)$ and $\bar{\theta}_{S5}(TR)$. The weighted-root-mean-squared (RMS) difference between low-order-model data and experimental data is then determined, where a weighting factor, which is inversely proportional to the absolute experimental uncertainty (data of Figure 57), is used. The purpose of this is to allocate greater weighting to more accurate data, and lesser weighting to less accurate data. An optimisation routine is used to find the values β_1 to β_6 which minimise the weighted-RMS difference between the low-order-model trend and the experimental data in overlapping regions of TR (intermittent regions in the range $1.07 < TR < 1.62$). Best fit values equal to 1.33, 1.33, 1.35, 1.68, 1.55 and 1.69, were obtained for β_1 to β_6, respectively. The values for β_1 to β_3 are reasonably close to unity, demonstrating accurate applicability of the original correlations. The values for β_4 to β_6 deviate more from unity, which is attributed primarily to uncertainty in the multiplication factor K_2 used in the correlation represented by Eq. (59). Although here a single set of coefficients is found that reconciles the entire experimental data series for a particular time range (defined by the transient correction residuals being less than 0.05), it is worth nothing that these coefficients deviate from unity in a similar way to coefficients C_1 to C_6, determined in the context of the unsteady correction over a wider time range. This is unsurprising, given that the purpose of the coefficients is to calibrate rather general correlations for the specific test case presented in this chapter.

The calibrated network model results are also shown in Figure 65. The temperature-ratio-average deviation (across all data) after calibration was $\Delta\bar{\theta} = +0.012$ on Surface 1 and $\Delta\bar{\theta} = +0.011$ on Surface 5. The calibrated network model is in good agreement with the experimental data in both form, and—by virtue of calibration—absolute values. Absolute error limits to 95% confidence are also plotted for the average of each time-series of experimental data (each run). As discussed in the context of Figure 57, the absolute error increases at lower TR. The network model and experimental data agree within experimental uncertainty limits for all runs. The general trend is for slightly reducing overall cooling effectiveness with reducing temperature ratio. The trend of overall cooling effectiveness with TR is now explored in more detail.

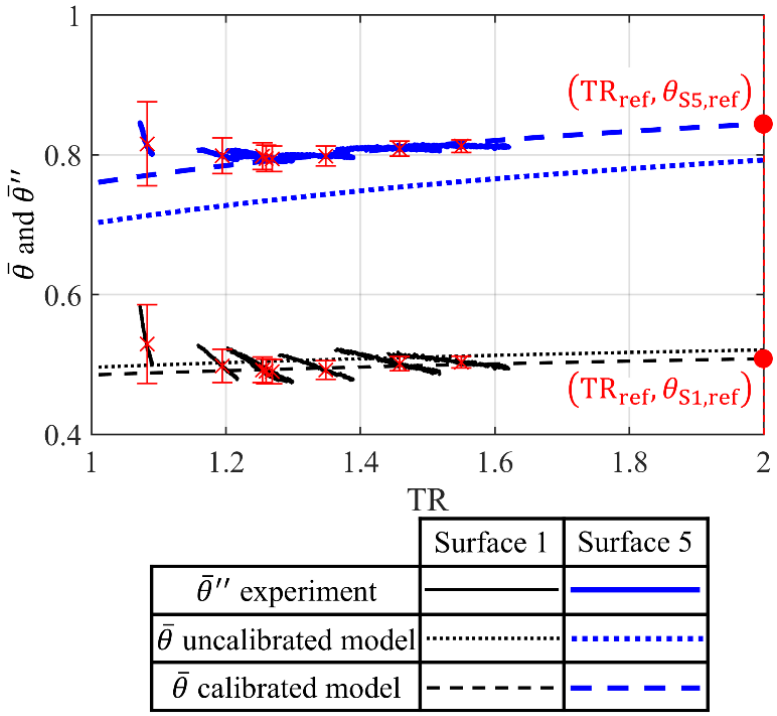

Figure 65: Corrected ($\bar{\theta}''_{S1}$ and $\bar{\theta}''_{S5}$) surface-averaged overall cooling effectiveness measurements on Surface 1 and Surface 5 compared to uncalibrated and calibrated results of the low-order aerothermal network model.

Taking now the engine condition of TR (TR = 2.0) as the reference temperature ratio, reference overall effectiveness values $\theta_{S1,ref}$ and $\theta_{S5,ref}$ are defined as the surface-averaged values of the calibrated network model at TR = 2.0. Differences from these points, i.e. values that represent the corrections from the engine temperature ratio, are presented in Figure 66. Differences for both the experimental data and low-order network model results are taken from the same reference points. 95% confidence limits for the experimental data are also shown.

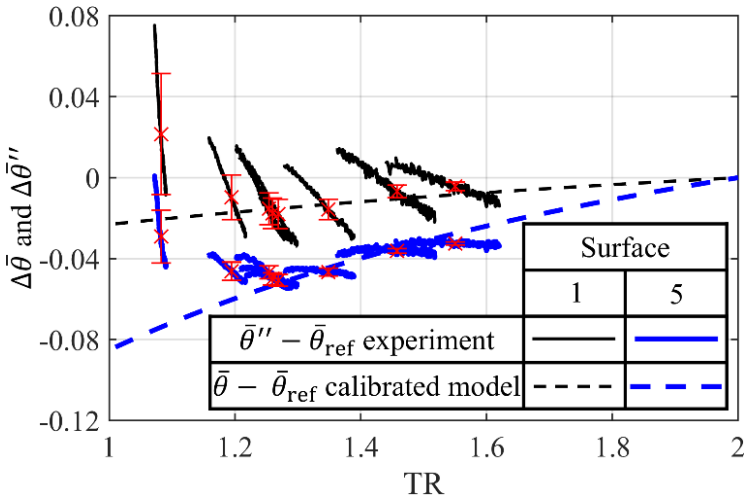

Figure 66: Magnitude of the change in surface-averaged overall cooling effectiveness as a function of TR on Surface 1 and Surface 5.

Both Surface 1 (external surface facing the mainstream) and Surface 5 (inner surface facing coolant plenum) have a mildly accelerating decrease in effectiveness with decreasing TR. Taking the data-set in its entirety, there is good agreement between the experimental data and the low-order-model results, with the overall trends being similar, and with all Surface 1 data agreeing within errors. For Surface 5, four time-averaged data points do not agree within errors, however three of these points lie in the range TR ≤ 1.25, where measurement errors start to explode and become increasingly difficult to quantify. The agreement between time-averaged Surface 5 data and the network model is very good for temperature ratios in the range TR > 1.25 (primary range of interest). It is interesting that for Surface 1 in particular, the characteristics for *individual* runs are poorly aligned with the trend from the low-order network model. This aspect of the data is unresolved, though it is noted that the measured and predicted offsets are very small, and the experimental error increases with decreasing TR The individual-run trends for Surface 5 are in better agreement with the low-order-model trend.

The magnitude of the correction moving from a typical engine condition for large civil aircraft of TR = 2.0 to a conventional lab condition of TR = 1.2 is a reduction in overall cooling effectiveness of approximately 0.017 for Surface 1 and 0.060 for Surface 5. The magnitude of

these small but significant corrections, and the general trends of Figure 66 can be regarded as the key result of this chapter.

3.8.5 Comparison to chapter 2

A similar modelling exercise, for a system of the same general type (internal and external cooling), but with more sophisticated and comprehensive treatment of the boundary conditions and the interaction of these with the system, was performed in chapter 2. In the system of chapter 2, the inner wall was treated as adiabatic, so only the outer wall was considered. This may be compared to Surface 1 in the system studied in this chapter. Just the result for domain-global BCs of fixed outlet-Re *and* fixed PR (result of Figure 37 in chapter 2; marked as Cartlidge and Povey [1]) is considered. This is compared to the result from this chapter in Figure 67.

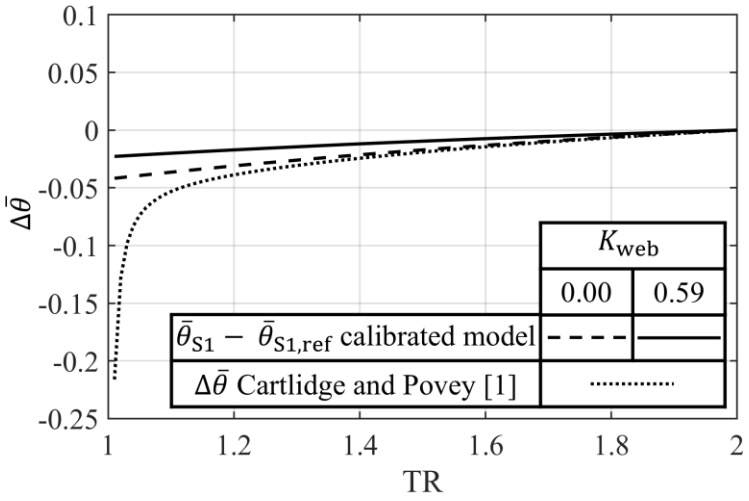

Figure 67: Magnitude of the change in surface-mean overall cooling effectiveness as a function of TR on Surface 1 with and without conducting terms associated with lateral webs.

Consider first the comparison to converged result for the calibrated thermal network model, which is marked $K_{\mathrm{web}} = 0.59$. The result of chapter 2 is of very similar form to the result of chapter 3, but differs in magnitude by a factor of 2.3. The difference is explained by the presence of a conduction term in the system considered in this chapter (not present in the system of chapter 2), which couples the external and internal walls due to the presence of webs (separating each module in the lateral direction). To demonstrate that this is the origin of the difference, the result of chapter 3 is modified by running the calibrated network model to convergence with the conduction in the

webs set to zero. This result is marked $K_{web} = 0$ in Figure 67. This result is now in good agreement with the result of chapter 2: in the range $1.2 \leq TR \leq 2.0$ (the primary range of interest) there is an average difference of 11.2%. At low temperature ratios ($TR < 1.2$), the trends diverge. This is explained by the fact that the system in chapter 2 is highly compressible ($M = 0.93$), whereas the current system (subject of this chapter) is incompressible ($M = 0.30$). The trends diverge in the region $TR < 1.2$ because of the increasing significance of compressibility on the distribution of $\theta(x)$ with reducing TR, both for purely definitional reasons (i.e. the presence of recovery ratios in the definition of $\theta(x)$ used in chapter 2) and physical reasons (i.e. the impact of compressibility effects on the surface temperature distribution). The combined effects of compressibility cause the denominator of Eq. (2) in chapter 2 to approach 0, which causes $\theta(x)$ to explode.

3.8.6 Summary of key results

The key results regarding the impact of TR on overall cooling effectiveness are as follows:

i) For the system of chapter 3, which represents a heavily cooled (internal and film cooling) turbine component, there is a reduction in external surface overall cooling effectiveness moving from the reference TR ($TR = 2.0$) to the conventional rig TR ($TR = 1.2$). The magnitude of the reduction was approximately 0.013.

ii) So far as the trend of overall cooling effectiveness with TR is concerned, there is now corroborating evidence from a number of sources showing that the general result is robust to cooling system design variation (three designs in chapter 2; a fourth in chapter 3), the mean value of overall cooling effectiveness (see chapter 2), and the domain-global boundary conditions (see chapter 2). Based on these somewhat independent studies, there is reasonable confidence in the general result.

iii) This magnitude of the reduction in cooling effectiveness with reducing TR is strongly dependent on coupling between the internal and external wall. When the coupling term is reduced to zero, the magnitude of the reduction in cooling effectiveness moving from $TR = 2.0$ to $TR = 1.2$ increases to approximately 0.031. This is approximately 1.81 the size

of the correction when there are lateral webs between channels. When applying rule-of-thumb corrections, good judgement must be exercised as to the degree of coupling between inner and outer wall.

It is noted (with reference to chapter 2) that in chapter 3 effects due to absolute temperature, combustion product gas properties, or definitions of overall cooling effectiveness have not been considered. It is shown in chapter 2 that there is a significant offset in the correction factor when one moves from conventional laboratory conditions of absolute temperature ($T_{01\mathrm{h}}$ = 600 K) to engine conditions of absolute temperature ($T_{01\mathrm{h}}$ = 1750 K) and also when one moves from air to combustion products. These effects are discussed in more detail in chapter 2. The definition of overall cooling effectiveness can also significantly change the trend of correction factor in a compressible environment. This is beyond the scope of this study but is also considered in chapter 2.

3.9 Decoupling underlying effects

In this section the calibrated low-order network model is used to decompose the overall changes in $\bar{\theta}_{\mathrm{S1}}(x)$ and $\bar{\theta}_{\mathrm{S5}}(x)$ with TR into the effects associated with changes in local surface BCs. The following local surface boundary conditions are chosen for this process: film effectiveness of the mixing layer, $\eta_{\mathrm{ML}}(x)$; wall thermal conductivity, $k_{\mathrm{w}}(x,z)$; external heat transfer coefficient, $h_{\mathrm{m}}(x)$; internal heat transfer coefficients for Surface i, $h_{\mathrm{c}i}(x)$ (i = 2, 3, 4, 5); and internal cooling effectiveness, $\lambda(x)$. That is, $\theta = f\left(\eta_{\mathrm{ML}}, k_{\mathrm{w}}, h_{\mathrm{m}}, h_{\mathrm{c2}}, h_{\mathrm{c3}}, h_{\mathrm{c4}}, h_{\mathrm{c5}}, \lambda\right)$. The choice of local surface BCs is somewhat arbitrary, but this particular selection is based on an analytical argument presented in chapter 2. This argument is the result of a simplified one-dimensional network model of the system in which there is conduction heat transfer in the through-wall direction only (i.e. no lateral conduction). It was shown in chapter 2 that a simple checksum of changes in $\bar{\theta}(x)$ due to changes in each local surface BC—in isolation of all other local surface BCs—predicts the overall change with high accuracy. This gives confidence that the boundary conditions form a closed set.

Consequently, the mechanism for changes in $\bar{\theta}_{S1}(x)$ and $\bar{\theta}_{S5}(x)$ with TR can be explained with reference to the changes in individual local surface BCs (in isolation of all other local surface BCs). The effects associated with the changes in each of these eight boundary conditions are referred to as effect 1 to effect 8. A schematic diagram of the cooling system network showing the region most associated with each effect (E1 to E8), is shown in Figure 68.

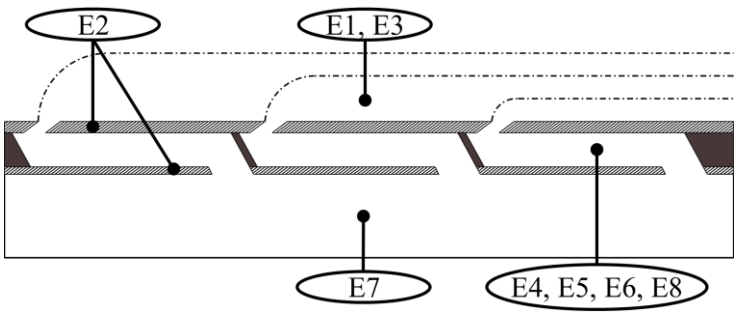

Figure 68: Schematic of the cooling system showing the regions most associated with each of effects 1–8.

The results will be presented for domain-global boundary conditions of fixed outlet-Re *and* fixed PR. To perform these predictions, the method of chapter 2 (see discussion in the context of Figure 15 in chapter 2) is used. This study is valuable for understanding the scaling process between conventional laboratory and engine conditions in the practical situation of co-dependent variation of all non-dimensional groups as temperature ratio is varied. The percentage contributions to the changes in $\bar{\theta}(x)$ of each of effects 1–8 as one moves from the reference TR (TR = 2.0) to lower-than-reference TR (the trend is mildly accelerating, but TR = 1.9 is taken for the analysis. This choice is arbitrary but chosen such that the change in TR is sufficiently small that linear superposition of the changes in $\bar{\theta}(x)$ due to changes in each local surface BC is accurate (i.e. sums to the overall change)) are presented in Figure 69. Results are shown for Surface 1 and Surface 5. Recall that surface-averaged overall cooling effectiveness decreases as one moves from the reference TR to lower-than-reference TR.

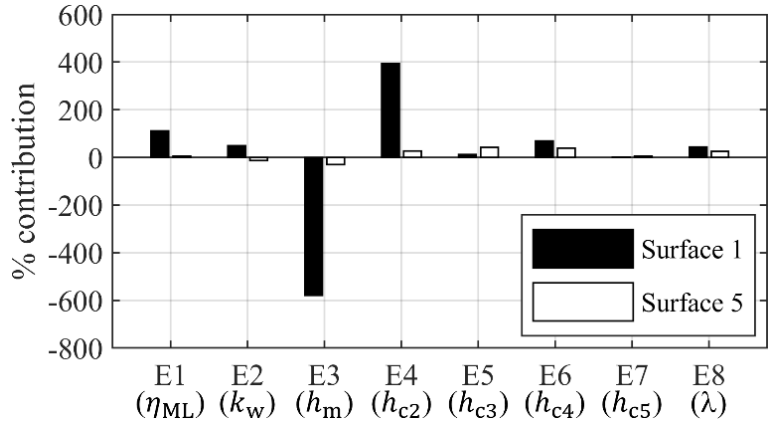

Figure 69: Percentage contributions of eight local surface boundary conditions to changes in surface-averaged overall cooling effectiveness for Surface 1 and Surface 5.

Consider first the results for Surface 1. It is observed that the change in $\overline{\theta}_{S1}(x)$ with decreasing TR is dominated by two effects: a decrease in $h_m(x)$ which acts to *increase* $\overline{\theta}_{S1}(x)$ because this represents decreased mainstream-side heat transfer; a decrease in $h_{c2}(x)$ which acts to *decrease* $\overline{\theta}_{S1}(x)$ because this represents less internal cooling. The six other effects are of smaller magnitude and act to decrease $\overline{\theta}_{S1}(x)$ with decreasing TR: a decrease in $\eta_{ML}(x)$ leading to increased non-dimensional driving temperature for heat transfer; a decrease in $h_{c4}(x)$ leading to less internal heat transfer; a decrease in $k_w(x,z)$ acting to reduce coupling of the external surface with the internal cooling channel system; a decrease in $\lambda(x)$ (coolant is non-dimensionally warmer) leading to reduced internal heat transfer; and decreases in $h_{c3}(x)$ and $h_{c5}(x)$ leading to reduced heat transfer on the plenum-facing wall, and consequently reduced through-web heat transfer.

Now looking at the results for Surface 5, it is observed that the change in $\overline{\theta}_{S5}(x)$ as one moves from the reference TR to lower-than-reference TR is explained by: reductions in $h_{ci}(x)$ (i = 2, 3, 4, 5) which act to reduce internal cooling and therefore reduce $\overline{\theta}_{S5}(x)$ by increasing the relative impact of the through-web heat transfer; reductions in $h_m(x)$ and $k_w(x,z)$ which both act to decrease through-web heat transfer, thus increasing $\overline{\theta}_{S5}(x)$; a reduction in $\eta_{ML}(x)$ which increases external driving temperature, and therefore increases through-web heat transfer, reducing $\overline{\theta}_{S5}(x)$; and finally a reduction in $\lambda(x)$ which reduces $\overline{\theta}_{S5}(x)$ due to less channel-side heat transfer because of reduced cooling potential.

The primary physical mechanisms driving changes in each local surface BCs as TR is changed are now discussed. A more detailed analysis is presented in chapter 2, but some of the key arguments are rehearsed here. As one moves from the reference TR to lower-than-reference TR:

i) the reduction in $\eta_{\mathrm{ML}}(x)$ is primarily caused by an increase in the entrained-hot-gas-to-coolant specific heat capacity flow rate ratio, $\dot{m}_{\mathrm{e}}(x)c_{p1\mathrm{h}}/(\dot{m}_{1\mathrm{c}}+\dot{m}_{2\mathrm{c}}+\dot{m}_{3\mathrm{c}})c_{p\mathrm{c,in}}$, where the main contribution is from an increase in the mass flow rate ratio, $\dot{m}_{\mathrm{e}}(x)/(\dot{m}_{1\mathrm{c}}+\dot{m}_{2\mathrm{c}}+\dot{m}_{3\mathrm{c}})$;

ii) the reduction in $k_{\mathrm{w}}(x,z)$ is caused by a decrease in absolute wall temperature, $T_{\mathrm{w}}(x,z)$;

iii) the reduction in $h_{\mathrm{m}}(x)$ is primarily attributed to a decrease in $\rho_{\mathrm{m}}(x)$ due to a reduction in mainstream total pressure, resulting from the constraint of fixed outlet Reynolds number, which lowers the total pressure of the mainstream and therefore the mixing layer;

iv) the reductions in $h_{\mathrm{c}i}(x)$ (i = 2, 3, 4, 5), are principally due to a decrease in $\rho_{\mathrm{c}}(x)$ due to a reduction in coolant total pressure (BC of fixed CMPR and consequence of mainstream total pressure decreasing with reducing TR as result of fixed outlet-Re BC);

v) the reduction in $\lambda(x)$ is primarily caused by a decrease in overall cooling effectiveness of Surfaces 2–4 ($\bar{\theta}_{\mathrm{S2}}(x)$, $\bar{\theta}_{\mathrm{S3}}(x)$ and $\bar{\theta}_{\mathrm{S4}}(x)$), implying non-dimensionally warmer internal surfaces, and an increase in non-dimensional coolant temperature.

3.10 Impact of IR in-situ calibration method on results

In this section the impact of the IR calibration method on the overall cooling effectiveness results is considered. Results have already been presented for Calibration Method 1 (data of Figure 66) and now consider Calibration Method 2 and Calibration Method 3. The purpose of an in-situ calibration is to correct the IR temperature measurement (the so-called black-body-equivalent temperature) for non-unity target surface emissivity (grey body as opposed to black body) and associated background radiation influence, and IR window transmissivity.

3.10.1 Calibration Method 2

This method uses a calibration patch mounted on the target surface to evaluate a real-time residual background radiant flux that reconciles the temperature as measured by the IR camera at the calibration patch location with the temperature measured by a thermocouple at the same location. It is assumed that the residual radiant flux (which is referred to as *total surrounding radiant flux*) is uniform across the entire surface. A full discussion of the method is given Kirollos et al. [36] and Michaud et al. [30]. By considering the radiation terms incident on the IR temperature sensor, and assuming a diffuse surface and uniform emissivity and transmittance, the local black-body-equivalent IR temperature (as measured by the IR camera with the factory black-body calibration) is given by

$$T_{\mathrm{bb}}(x,y,t)^4 = \tau\varepsilon T_{\mathrm{S}}(x,y,t)^4 + \tau(1-\varepsilon)T_{\mathrm{R}}(t)^4 + (1-\tau)T_{\mathrm{opt}}(t)^4 \tag{62}$$

where τ is transmittance of the IR window, ε is emissivity of the flat-plate surface, $T_{\mathrm{S}}(x,y,t)$ is the local surface temperature and $T_{\mathrm{R}}(t)$ and $T_{\mathrm{opt}}(t)$ are the (assumed uniform) surrounding enclosure and IR window temperatures, respectively. For the experiments of chapter 3, the values $\tau = 0.91$ and $\varepsilon = 0.945$ are taken.

A *total surrounding radiant flux*, $q^*(t)$ is then defined

$$q^*(t) = \sigma\frac{\tau(1-\varepsilon)T_{\mathrm{R}}(t)^4 + (1-\tau)T_{\mathrm{opt}}(t)^4}{1-\tau\varepsilon} \tag{63}$$

where σ is the Stefan-Boltzmann constant.

By substituting Eq. (62) into Eq. (63), and taking the black-body-equivalent IR temperature and the thermocouple temperature at the location of the calibration patch, $q^*(t)$ is expressed in the following form

$$q^*(t) = \sigma\frac{T_{\mathrm{bb}}\left(x_{\mathrm{CP}},y_{\mathrm{CP}},t\right)^4 - \tau\varepsilon T_{\mathrm{S}}\left(x_{\mathrm{CP}},y_{\mathrm{CP}},t\right)^4}{1-\tau\varepsilon} \tag{64}$$

For each experimental run and for both Surface 1 and Surface 5, $q^*(t)$ is experimentally evaluated using Eq. (64). For $T_{\mathrm{bb}}(x_{\mathrm{CP}},y_{\mathrm{CP}},t)$, the equivalent-black-body IR temperature averaged over all pixels contained within both calibration patches is used and, for $T_{\mathrm{S}}(x_{\mathrm{CP}},y_{\mathrm{CP}},t)$, the average temperature measurement of the two calibration patch thermocouples is used. By substituting Eq. (63) into Eq. (62), the real-time-corrected local surface temperature, $T_{\mathrm{S}}(x,y,t)$, is then defined by

$$T_{\mathrm{S}}(x,y,t) = \frac{1}{\tau\varepsilon}\left(T_{\mathrm{bb}}(x,y,t)^4 - \frac{(1-\tau\varepsilon)}{\sigma}q^*(t)\right)^{0.25} \tag{65}$$

Eq. (65) is substituted into Eq. (60) to evaluate the real-time-corrected overall cooling effectiveness, $\theta^*(x,y,t)$. Corrections for transient effects and for off-design conditions of Re_D, M and CMPR are then applied, as described in previous sections. This corrected data is referred to as $\theta^{*\prime\prime}(x,y,t)$.

Total surrounding radiant flux time-series characteristics for each run are plotted in Figure 70 as a function of mainstream total temperature, $T_{01\mathrm{h}}$. Data is plotted for the time period in which both transient residuals, $\overline{\theta}^{*\prime}_{\mathrm{S1}}(x,t) - \overline{\theta}^{*}_{\mathrm{S1}}(x,t)$ and $\overline{\theta}^{*\prime}_{\mathrm{S5}}(x,t) - \overline{\theta}^{*}_{\mathrm{S5}}(x,t)$ are less than 0.05.

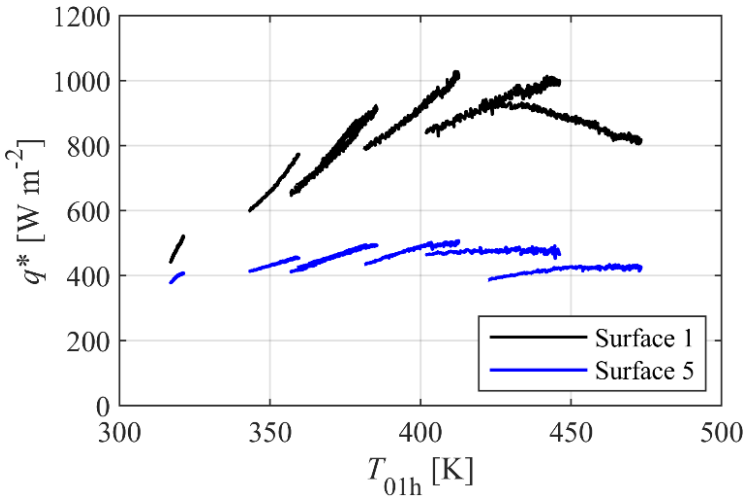

Figure 70: Total surrounding radiant flux as a function of $T_{01\mathrm{h}}$ for Surface 1 and Surface 5.

It is expected that q^* will be correlated with the background temperature, T_{R}, which is expected to be loosely correlated with the external flow temperature, $T_{01\mathrm{h}}$. Looking at the figure and looking first at the trend for Surface 1, it is observed that the primary trend for q^* is to increase

with increasing T_{01h} although the individual time series do not collapse well to a single global trend. It is noted additionally that, for the run with maximum temperature ratio TR = 1.62, the opposite trend is seen i.e. q^* decreases with increasing TR. The trend for this run is surprising because q^* has previously been shown in the literature to increase with T_{01h} throughout the heated period (see, for example, Kirollos et al. [36]). For completeness, the corresponding q^* data for Surface 5 is plotted. This surface faces the coolant plenum, where the driving temperature is that of the internal flow ($T_{0c,in}$). The q^* data are relatively constant, as expected, and of lower absolute value than for Surface 1, as expected.

The final characteristics for $\theta^{*\prime\prime}$ are shown in Figure 71, where the change in $\theta^{*\prime\prime}$ from the reference condition of TR = 2.0 is plotted.

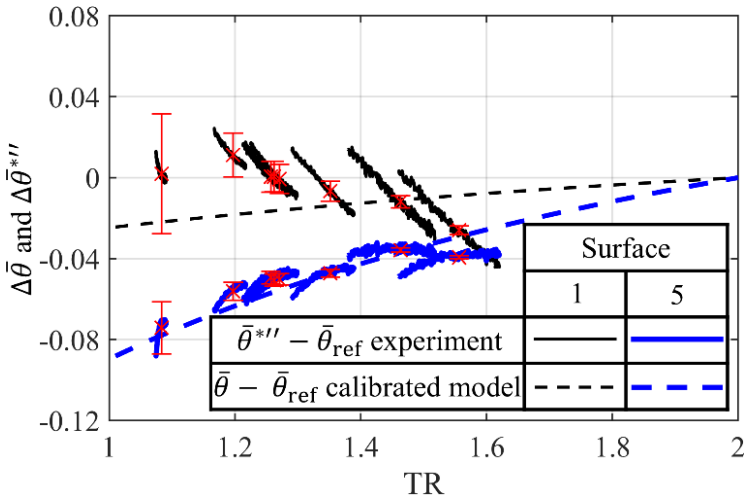

Figure 71: Magnitude of the change in surface-averaged overall cooling effectiveness as a function of TR on Surface 1 and Surface 5, when IR temperature measurements are corrected with Calibration Method 2.

This plot is the equivalent of Figure 66, but for $\theta^{*\prime\prime}$. For the reference condition, the result of the calibrated network model is used, for which $\bar{\theta} = 0.51$. The network model was re-calibrated using the method described previously. The resulting multipliers β_1–β_6 took values 1.18, 1.18, 1.19, 1.31, 1.27 and 1.32, respectively. The corresponding trends for θ from the calibrated network model are also shown in Figure 71. Error bars for the time-series average values of $\theta^{*\prime\prime}$ are also included. In order to evaluate the error bars, the uncertainty analysis outlined earlier is repeated

but, for surface temperatures, the quoted bias uncertainty for K-type thermocouple measurements is taken as U_T = 1.1 K. In this analysis uncertainty in emissivity and transmittance is not accounted for, nor for the effects associated with assuming uniformity of the background radiation term. Consequently, the error bars likely underestimate the true uncertainty.

3.10.2 Calibration Method 3

In this technique a correction is evaluated that has the effect of setting the black-body-equivalent IR temperature measured by the camera equal the calibration patch temperature at the location of the patch. Similar techniques have been used extensively in the literature (see, for example, [32–33] and [42–43]). The simple assumption is made that the temperature offset is the same across the entire surface. Defining the temperature offset at the location of the calibration patch

$$\Delta T_{\mathrm{CP}}(t) = T_{\mathrm{S}}\left(x_{\mathrm{CP}},y_{\mathrm{CP}},t\right) - T_{\mathrm{bb}}\left(x_{\mathrm{CP}},y_{\mathrm{CP}},t\right) \tag{66}$$

the *real-time-corrected* local surface temperature is then defined at all other locations

$$T_{\mathrm{S}}(x,y,t) = T_{\mathrm{bb}}(x,y,t) + \Delta T_{\mathrm{CP}}(t) \tag{67}$$

This gives one the real-time-corrected overall cooling effectiveness, $\theta^{**}(x,y,t)$. The corrections for transient effects and for off-design conditions of Re_D, M and CMPR are then applied as described in previous sections. This corrected data is referred to as $\theta^{**\prime\prime}(x,y,t)$.

The time-series characteristics for the correction term $\Delta T_{\mathrm{CP}}(t)$ are plotted in Figure 72 as a function of mainstream total temperature, $T_{01\mathrm{h}}$. Data is plotted for the time period in which both transient residuals, $\overline{\theta}^{**\prime}_{\mathrm{S1}}(x,t) - \overline{\theta}^{**}_{\mathrm{S1}}(x,t)$ and $\overline{\theta}^{**\prime}_{\mathrm{S5}}(x,t) - \overline{\theta}^{**}_{\mathrm{S5}}(x,t)$, are less than 0.05.

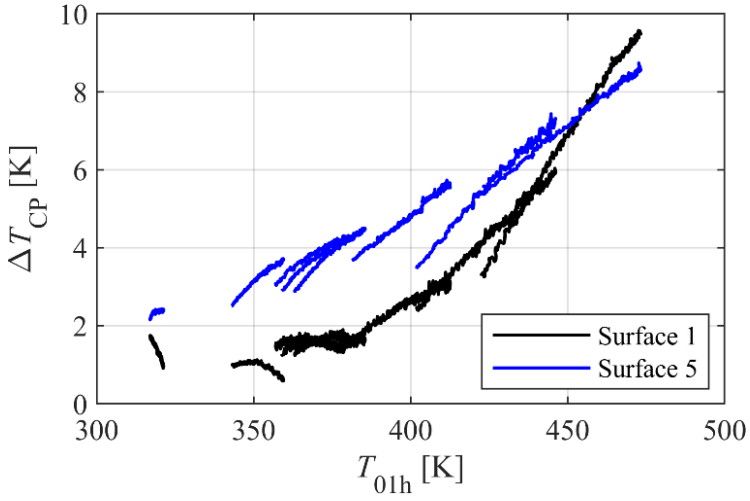

Figure 72: The correction term $\Delta T_{CP}(t)$ as a function of T_{01h} for Surface 1 and Surface 5.

ΔT_{CP} is expected to be loosely correlated with q^* which, as has been shown, is loosely correlated with T_{01h}. Looking at the figure, it is observed that ΔT_{CP} increases with T_{01h} and that the data collapses reasonably well onto a single trend for each surface.

The final characteristics for $\theta^{**\prime\prime}$ are shown in Figure 73, where the change in $\theta^{**\prime\prime}$ from the reference condition of TR = 2.0 is plotted. This plot is the equivalent of Figure 66, but for $\theta^{**\prime\prime}$.

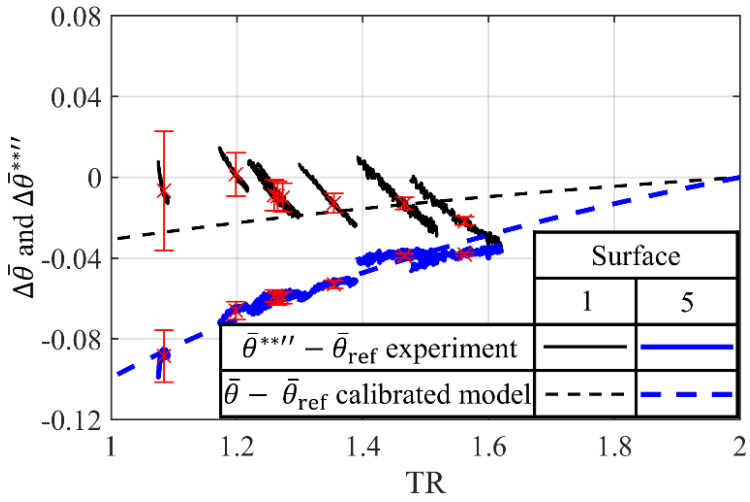

Figure 73: Magnitude of the change in surface-averaged overall cooling effectiveness (from the reference condition) as a function of TR on Surface 1 and Surface 5, when IR temperature measurements are corrected with Calibration Method 3.

For the reference condition, the result of the calibrated network model is used, for which $\bar{\theta} = 0.48$. The network model was re-calibrated using the method described previously. The resulting

multipliers β_1–β_6 took values 1.72, 1.71, 1.69, 1.22, 1.41 and 1.21, respectively. The corresponding trends for θ from the calibrated network model are also shown in Figure 73. Error bars for the time-series average values of $\theta^{**\prime\prime}$ are also included. As with Calibration method 2, for surface temperatures the quoted bias uncertainty for K-type thermocouple measurements is taken as U_T = 1.1 K.

Looking at Figure 73, it is observed that the results are very similar to those of Calibration Method 2 (Figure 71). The general trend for Surface 1 is relatively flat, with poor agreement between individual-run characteristics and the network model. The results for Surface 5 show a strong decrease in overall cooling effectiveness with reducing TR, and the agreement with the calibrated network model is very good.

A final observation is that the experimental data for Calibration Method 3 is very similar in both form and magnitude to the experimental data for Calibration Method 2. This can be understood by taking the first-order Taylor approximation of Eq. (65) about $T_{\mathrm{bb}}(x,y,t)^4$

$$T_{\mathrm{S}}(x,y,t) = \frac{1}{\tau\varepsilon} T_{\mathrm{bb}}(x,y,t) - 0.25 \frac{(1-\tau\varepsilon)}{\sigma\tau\varepsilon} q^*(t) T_{\mathrm{bb}}(x,y,t)^{-3} \times \left(T_{\mathrm{bb}}(x,y,t)^4 - \frac{(1-\tau\varepsilon)}{\sigma} q^*(t) \right)^{-0.75} \tag{68}$$

By substituting Eq. (64) and Eq. (66) into Eq. (68) (full derivation not shown), it can be shown that Eq. (67) is equivalent to Eq. (65) when the following conditions apply: the product of emissivity and transmittance is non-unity but sufficiently close to unity ($\tau\varepsilon \cong 1$); and the temperature offset at the location of the calibration patch is non-zero but sufficiently small ($\Delta T_{\mathrm{CP}}/T_{\mathrm{bb}} \ll 1$). When these conditions apply, Calibration Method 3 is equivalent to Calibration Method 2. It is noted that, when the product of emissivity and transmittance is *precisely* equal to unity ($\tau\varepsilon = 1$) and the temperature offset is *precisely* zero ($\Delta T_{\mathrm{CP}} = 0$), all three calibration methods give identical results. The equivalence of calibration methods 2 and 3 for the conditions $\tau\varepsilon \cong 1$ and $\Delta T_{\mathrm{CP}}/T_{\mathrm{bb}} \ll 1$ is potentially significant for applications with high uncertainty in the values of

transmittance and emissivity as the result of the in-situ calibration (regardless of which method is chosen) is independent of these parameters when the above criteria are satisfied. For such applications, Calibration Method 3 could be used to approximate the results for Calibration Method 2 with a high degree of accuracy.

Although it is believed that IR temperature measurements should be corrected for grey-body and surrounding radiation effects, there are unresolved questions about all data in this thesis using in-situ calibration techniques, so the analysis in this chapter is focused on results for Calibration Method 1. Further investigation of calibration methods for high-accuracy IR measurements is strongly encouraged and discussion in the community on this topic would be welcomed.

3.11 Conclusions

In this chapter, the impact of mainstream-to-coolant temperature ratio on overall cooling effectiveness for systems with both film and internal cooling and domain-global boundary conditions of fixed outlet-Re *and* fixed PR is studied. This is done with reference to three sources of information: experimental measurements from a purpose-built flat-plate test facility (see Naidu and Povey [17]); results of a calibrated 2D aerothermal network model of the test article; and the theoretical results of chapter 2. It is shown that the experimental results and calibrated-model results are in good agreement, both showing a decrease in overall cooling effectiveness with decreasing TR. Moving between a typical engine temperature ratio for large civil aircraft (TR = 2.0) and a conventional laboratory temperature ratio (TR = 1.2) leads to a change in overall cooling effectiveness on the external surface of approximately -0.017 for a mean effectiveness of 0.508. This is equivalent to a -3.3% change. The internal surface facing the cooling plenum is generally of less consequence, but a corresponding change in overall cooling effectiveness of -0.060 for a mean effectiveness of 0.845 (a -7.1% change) is demonstrated. The rate of change has a mild acceleration with decreasing temperature ratio.

The form of the experimental and calibrated-model results of chapter 3 were in good agreement with the—rather independent—theoretical results of chapter 2, but with a significant

difference in magnitude of correction. It is demonstrated that this is because there is coupling between external and internal walls (due to the webs separating each module in the lateral direction) in the system considered in chapter 3. These coupling terms act to significantly reduce the magnitude of change in overall cooling effectiveness with temperature ratio. This shows that quantifying the degree of external-internal coupling is important when applying the results presented in this chapter. Importantly, there appears to be three corroborating sources of evidence for the trends of overall cooling effectiveness with temperature ratio.

By decomposing the change in overall cooling effectiveness with temperature ratio into effects associated with each of eight local surface boundary conditions, it is shown that the change in external overall cooling effectiveness with decreasing TR is dominated by two effects: a decrease in external heat transfer coefficient (h_m), which acts to *increase* overall cooling effectiveness (θ_{S1}) because this represents decreased mainstream-side heat transfer; and a decrease in heat transfer coefficient on the inner surface of the external wall (h_{c2}), which acts to *decrease* overall cooling effectiveness because this represents less internal cooling. This is consistent with the observation that the external overall cooling effectiveness is dominated by the ratio of external-side-to-internal side heat transfer coefficients (h_m/h_{c2}), as discussed in chapter 2. Effects associated with heat transfer coefficients on three additional internal surfaces (h_{c3}, h_{c4}, and h_{c5}), the film effectiveness of the mixing layer (η_{ML}), the material conductivity in (k_w), and the internal cooling effectiveness (λ), are also important, but significantly smaller in magnitude.

A theory for correcting overall cooling effectiveness measurements between conventional facility (TR = 1.2) and engine (TR = 2.0) conditions is an important topic for engine component validation. The ability to do this robustly opens the door to component validation studies in laboratory conditions, offering the possibility of both higher accuracy and lower costs and corresponding full-engine testing. The author believes this is the first serious experimental demonstration of the scaling theory proposed in chapter 2. Further corroborating studies,

particularly in purpose-built facilities in which there is good control of boundary conditions, are encouraged.

4. Experimental study of the impact of temperature ratio on overall cooling effectiveness of high-pressure turbine nozzle guide vanes

The effect of temperature ratio (TR) on overall cooling effectiveness is an important topic for scaling between conventional laboratory and engine conditions. A scaling theory for this problem has been developed (see chapter 2), but there is limited experimental validation of that theory. The purpose of this chapter is to address that problem. Experimental measurements of fully-cooled real-engine high-pressure turbine nozzle guide vanes over the range $1.08 \leq TR \leq 1.89$ are presented. This covers the range between conventional laboratory conditions (TR = 1.2) and near-engine conditions ($TR \cong 2.0$) of temperature ratio. Experiments were performed in the ECAT+ facility at the University of Oxford, an engine-realistic facility operating at engine-matched conditions of Mach number, Reynolds number and coolant-to-mainstream pressure ratio, and with wide coolant-to-mainstream temperature ratio capability. It is shown that the trend of metal effectiveness with TR is relatively flat, a result that is in accord with recent theoretical work.

4.1 Introduction

Scaling of overall cooling effectiveness (θ) from conventional laboratory conditions (TR = 1.2) to engine conditions (TR = 2.0) of temperature ratio is a subject that is of both academic and practical interest. A validated scaling theory would allow the use of experimental results from engine-realistic test facilities operating at moderate temperature ratio and low absolute temperature (see, for example, the ECAT facility, discussed in Kirollos et al. [9]) to accurately predict overall cooling effectiveness at engine conditions of temperature ratio. In the theoretical study of chapter 2 it was shown that at low absolute temperature, there was a decrease in overall cooling effectiveness with decreasing TR. A correction was evaluated (for a particular system representative of a HPT NGV) to be -0.040 when moving between TR = 2.0 and TR = 1.2. The

situation is complicated though, as there are also sensitivities to: changes in domain global BCs; mean value of overall effectiveness; internal cooling system design; absolute temperature; combustion product effects; and definitions of overall cooling effectiveness. It was shown that when scaling between conventional laboratory and engine conditions (including combustion product effects) there was a sweet-spot for TR = 1.25, at which condition the correction offset between engine and rig conditions was zero. This is a happy co-incidence, as this temperature ratio is advantageous (low experimental uncertainty, and relatively inexpensive) for laboratory testing. To understand the context of the work of this chapter it is recommended that chapter 2 is read first.

In this chapter, the scaling of overall cooling effectiveness with temperature ratio for high-pressure turbine (HPT) nozzle guide vanes (NGVs) is considered. Fully cooled engine parts were used for the study. Experiments were performed in the ECAT+ facility at the University of Oxford, over the mainstream-to-coolant temperature ratio range $1.08 \leq TR \leq 1.89$. The *domain-global* (row inlet to row exit) boundary conditions (BCs) for tests were fixed inlet-to-exit total-to-static pressure ratio (PR) and fixed atmospheric exit static pressure. Measurements were taken over the range $1.08 \leq TR \leq 1.89$, for fixed coolant-to-mainstream pressure ratio (CMPR). The controlling dimensionless groups were allowed to change in a natural co-dependent way with temperature ratio. This is referred to as *Approach 3* in chapter 1.

4.1.1 Literature on overall cooling effectiveness measurements

Related literature is now briefly reviewed. There have been a small number of experimental studies of overall cooling effectiveness of flat plates and simplified NGVs (Rhee et al. [27], [32–33] and [43–46]). These studies have been performed in the TR range $1.06 < TR < 1.70$, and do not study the impact of TR on θ.

There are even fewer studies in environments with a high degree of engine similarity. Several early studies were performed in the Annular Sector Heat Transfer Facility, with engine-representative values of coolant-to-mainstream pressure ratio (CMPR), inlet turbulence

intensity (Tu) and Mach number (M) (Luque et al. [10], Kirollos and Povey [36] and [47–49]). In the first study in this facility, Luque and Povey [47] measured full-surface overall cooling effectiveness distributions of HPT NGVs, using a thermochromic liquid crystals technique. Later, Luque et al. [48] improved the experimental technique with the use of infrared (IR) cameras, and experimentally characterised the overall cooling effectiveness of HPT NGVs with a novel leading-edge cooling architecture (*dendritic* cooling hole passages). Work in the facility inspired a new theory for TR-invariant definitions of overall cooling effectiveness for systems in which all non-dimensional groups are fixed (see Luque et al. [8]), and the theory was demonstrated experimentally HPT NGVs (see Luque et al. [10]). Luque et al. [49] conducted experiments with two separate coolant gasses: air and a *foreign gas* mixture of SF_6 and Ar. The purpose of using a foreign gas mixture was to match density ratio and blowing ratio to engine conditions (in addition to matched CMPR, Tu and M). They showed that overall cooling effectiveness *trends* were very similar for the two cases (aerodynamically matched situations due to matched CMPR), but the absolute effectiveness values were significantly lower when for the tests with foreign gas. They demonstrated via an analytical model that this was primarily due to a reduction in coolant-to-mainstream heat capacity flow-rate ratio when the foreign gas mixture was used. In the same facility, Kirollos and Povey [36] performed an extensive experimental investigation of the effect of coolant-to-mainstream mass flow rate ratio (varied by varying CMPR) on overall cooling effectiveness of cast and laser sintered HPT NGVs. Trends were similar for both parts, and generally showed improvement in overall effectiveness with coolant mass flow rate (many other details discussed in the paper).

In a more recent study, Michaud et al. [30] experimentally studied the impact of in-service deterioration on overall cooling effectiveness of HPT NGVs in the ECAT facility, with engine-representative conditions of CMPR, M, Re, and turbulence intensity. They showed that deteriorated parts have a reduced overall cooling effectiveness with respect to new parts, which they attributed to: an increase in external heat transfer coefficient due to increased surface roughness; and a reduction in trailing-edge (TE) slot coolant capacity.

4.1.2 Current study

In chapter 4, the impact of temperature ratio on overall cooling effectiveness is assessed for an annular cascade of HPT NGVs in an environment with a very high degree of non-dimensional similarity with the engine condition. In the experiments the framework of Approach 3 is adopted, in that the governing non-dimensional groups are allowed to vary sympathetically with TR. Experiments are operated at temperature ratios in the range $1.08 \leq TR \leq 1.89$ with domain-global BCs of fixed PR with fixed atmospheric exit static pressure. Results are compared to the low-order-model-predicted trends of chapters 2 and 3.

4.2 Test facility

In this section the test facility used for conducting the experiments of chapter 4, and the instrumentation and methods used for measuring and processing data, are discussed.

Overall cooling effectiveness measurements were conducted in the Second-Generation High-Temperature Engine Component Aerothermal (ECAT+) Facility at the University of Oxford (see Messenger et al. [18]). This facility is the second generation of the original ECAT facility (see Kirollos et al. [9]), with the most significant upgrades being the increased operational ranges of both absolute temperature and mainstream-to-coolant temperature ratio (TR). This is an engine-realistic blowdown facility capable of testing an annular cascade of high-pressure turbine (HPT) nozzle guide vanes (NGVs) at engine-representative conditions of mainstream outlet Mach number (M) and Reynolds number (Re); coolant-to-mainstream total pressure ratio (CMPR); and TR. Mainstream air is introduced from three hot pressure vessels (total volume 115.5 m^3 at 51 bar) and coolant air is introduced from one cold pressure vessel (volume 20 m^3 at 51 bar). Air is supplied to the vessels from two water-cooled reciprocating compressors (total 380 kW) with exit driers. Mainstream flow passes through a 200 kW inline air heater—situated between the compressors and the pressure vessels—to heat it to the target temperature. Mainstream and coolant flows were controlled using proportional-integral-derivative (PID) pressure controllers to set constant pressure upstream of both the mainstream and coolant critical-flow venturi nozzles

(CFVNs). The flow path is of cross-section similar to that of a combustor contraction. Mainstream flow enters the NGV row at plane 1 and the mixed-out flow exits at plane 2. The locations of planes 1 and 2 are indicated in Figure 74 a–b.

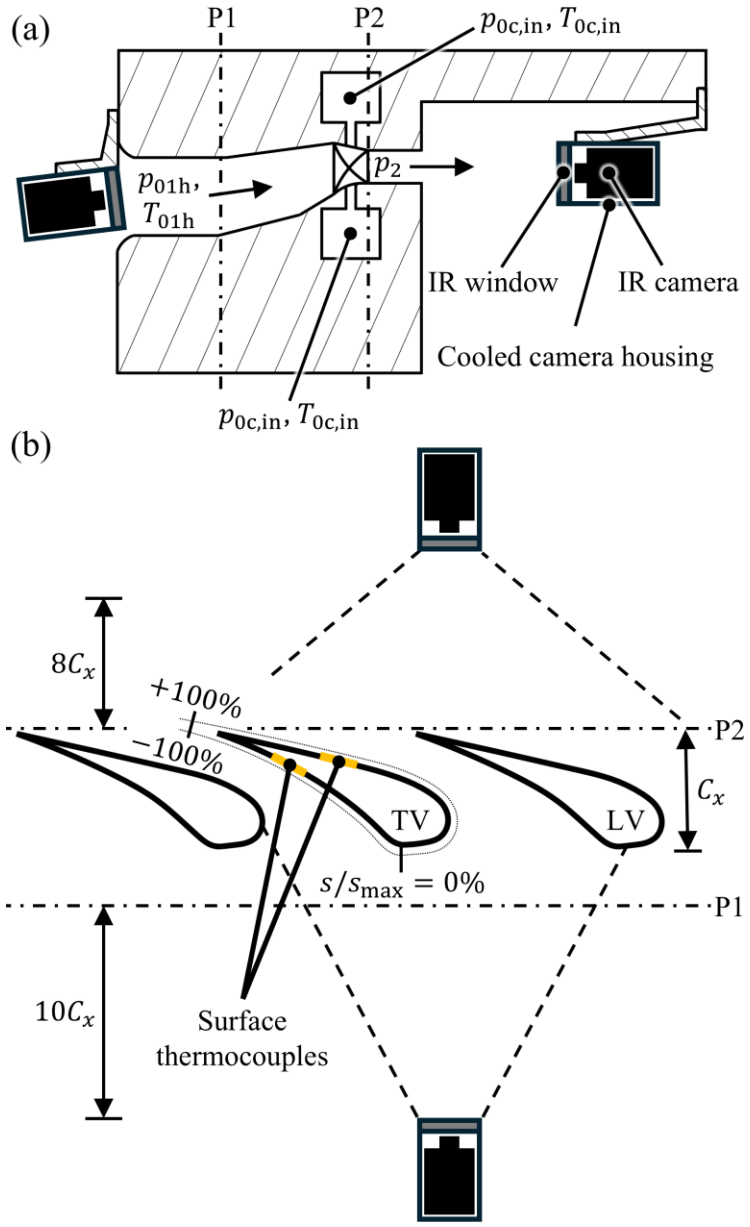

Figure 74: Details of the test facility including: (a) defeatured cross-section of the working section, showing infrared cameras and HPT NGV cascade; and (b) unwrapped schematic of the HPT NGV cascade.

Coolant is introduced from the hub and case and is injected into the external flow domain via film cooling holes on the airfoil and the hub and case platforms (all film cooling holes were open in the experiments of chapter 4). The locations of all air feeds are marked in Figure 75a.

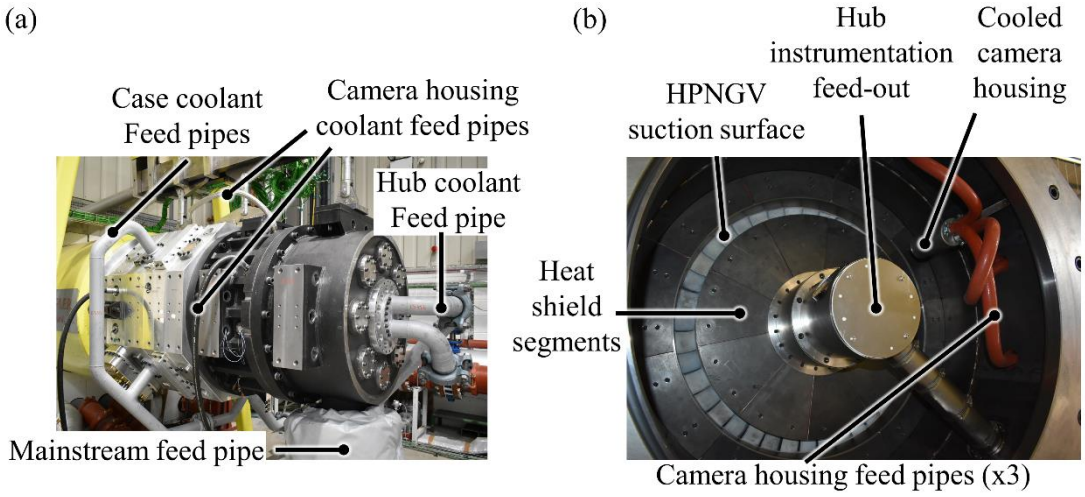

Figure 75: (a) photograph of the test facility; and (b) downstream view of the working section, showing the HPT NGV cascade, downstream IR camera and hub instrumentation feed-out.

The facility has a large range operational range of temperature and temperature ratio ($1.0 \leq \mathrm{TR} \leq 2.1$). In chapter 4 experiments were operated in the range $1.08 \leq \mathrm{TR} \leq 1.89$. They were performed with a fixed coolant temperature ($T_{0\mathrm{c,in}} = 290$ K) and varying mainstream temperature ($313 \leq T_{01\mathrm{h}} \leq 548$ K). Test conditions for the current experiments are summarised in Table 6.

Table 6: Test facility operating conditions. Ranges used in the experiments of chapter 4 are indicated, with the full facility operating range shown in parentheses.

Parameter	Symbol	Range
Mainstream total temperature (K)	$T_{01\mathrm{h}}$	313–548 (290–600)
Mainstream-to-coolant temperature ratio (–)	TR	1.08–1.89 (1.0–2.1)
Mainstream total pressure (bar)	$p_{01\mathrm{h}}$	1.67–1.84 (1–10)
Coolant-to-mainstream total pressure ratio (–)	CMPR	1.017–1.024 (low–high)
Mainstream outlet Mach number (–)	M	0.87–0.96 (0–3.7)
Domain inlet-to-exit total-to-static pressure ratio (–)	PR	1.64–1.80 (1–100)

Several details of the test facility are provided in Figure 74 and Figure 75, including: a defeatured cross-section of the working section (Figure 74a); an unwrapped schematic of the NGV cascade (Figure 74b); a photograph of the test facility (Figure 75a); and a downstream view of the working section (Figure 75b).

4.2.1 Instrumentation and data processing

The working section is instrumented with measurement rakes for mainstream inlet (i.e. plane 1) total pressure and total temperature measurements; and tappings for cascade exit (i.e. plane 2) static pressure measurements. For mainstream inlet total pressure and total temperature measurements, two rakes of eight sensors placed approximately three axial chords upstream of the cascade (i.e. 16 measurements for p_{01h} and 16 measurements for T_{01h}) were used.

Inlet measurement rakes were held in place by a cassette (see Figure 76a), which is placed into a groove in the external casing. For exit static pressure measurements, one vane pair was instrumented with 10 tappings each on both the hub and case platforms (i.e. 20 static pressure tappings in total) and pressure transducers were connected to the tappings using a combination of stainless steel tubes, compression fittings and Scanivalve tubulation. Total pressure and total temperature are also measured in the coolant plena (both hub and case). Mainstream and coolant mass flow rates are measured using choked sonic-venturi nozzles. All pressure transducers used for measuring working section and coolant plena pressure were mounted on the external surface of the test facility. The models of pressure transducer used in chapter 4 were: Druck Adroit 6200 series (for mainstream and coolant inlet total pressures and mass flow rates); and First Sensor CTE8000 series (for exit static pressure measurements). The quoted accuracies for these models are, respectively, 0.04% and 0.2% of full-scale output (FSO). Voltage signals from the pressure transducers were acquired using two National Instruments (NI) 80-channel NI PXIe-6345 cards. The thermocouple signals were acquired by a NI PXIe-6361 card. The logging frequency was 500 Hz for all channels. Data was logged using NI LabVIEW and processed using MATLAB. All rakes used for measuring mainstream and coolant inlet total pressure and total temperature are shown in Figure 76b.

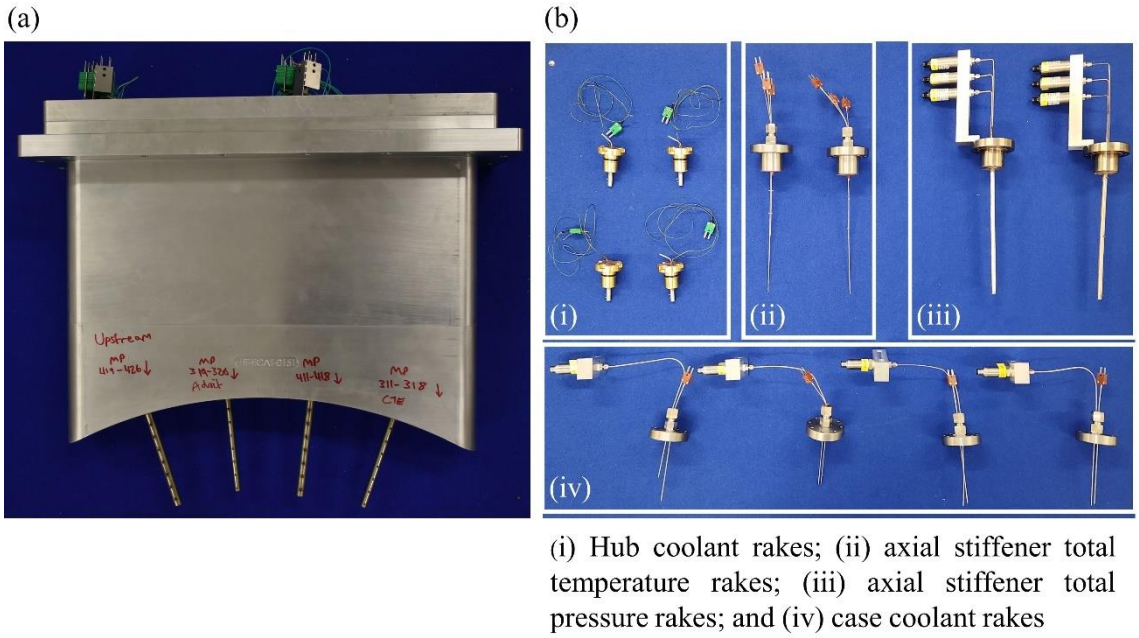

Figure 76: Photographs of the instrumentation including: (a) Upstream cassette with total pressure and total temperature rakes; and (b) total pressure and total temperature rakes for axial stiffener, case and hub.

For overall cooling effectiveness measurements, one IR camera was situated approximately 10*L* upstream of the NGV cascade and one IR camera was situated approximately 8*L* downstream of the cascade. The approximate locations of the cameras are shown in Figure 74a–b. The model of IR camera used in chapter 4 was the Micro-Epsilon thermoIMAGER TIM 640 thermalIMAGER (spectral range: 7.5–13 μm). Images were recorded at a frequency of 32 Hz. A 15° lens for the upstream camera and a 33° degree lens for the downstream camera were used. For both IR cameras, the field of view (FOV) contained one full vane pair (i.e. both the leading vane and trailing vane). The upstream IR camera was used to measure overall cooling effectiveness of the pressure surface (PS) and early suction surface (SS) and the downstream IR camera was used to measure overall cooling effectiveness of the late SS. As the cameras were mounted inside the working section, bespoke air-cooled camera enclosures were designed. These are capable of keeping the cameras close to ambient temperature during a hot run. Silicon feed pipes, mounted to internal fittings within the facility, were used to supply coolant (one pipe each for both coolant

inlet and outlet) and electronic cables for data acquisition. This arrangement is shown in Figure 75b (downstream camera).

IR data were recorded using TIMConnect and output video files were processed in MATLAB. The procedure for processing output video files is now described. Raw image data, $R(x,y)$, for each pixel are 16-bit image values representing the radiation count measured at the corresponding bolometric pixel. Raw image values are determined by converting RAVI files (output video file format for TIMConnect) to YUV files and extracting data for every pixel of every frame of every video. Raw image values are converted to black-body-equivalent IR temperatures, $T_{bb}(x,y)$ using the inferred conversion curve for the particular IR camera. The conversion curves (mapping $R(x,y)$ to $T_{bb}(x,y)$) for each camera were inferred by evaluating best-fit curves that represent the functional relationship $T_{bb} = f(R)$. The temperature data used for curve fitting were obtained from snapshots (performed using TIMConnect) taken at reference time stamps throughout a run. Corresponding raw image data were extracted from the YUV files. A distinction between *conversion curve* and *calibration curve* is drawn because—in the context of IR cameras—calibration curves typically map *radiation count* to T_{bb} whereas, in chapter 4, conversion curves are used to map *raw image values* (proxy for radiation count) to T_{bb}. In-situ calibration of the cameras was performed using the low-conductivity isothermal-patch method of Michaud et al. [31]. A separate calibration patch was installed on both the PS and SS of the trailing vane (TV). The calibration gauges were 4 mm diameter copper discs mounted on Kapton tape and instrumented with K-type thermocouples. The calibration assemblies were recessed into the vane surface to create a flush surface. The thermocouples were adhered to the copper disks with Resbond 989 alumina adhesive, and the copper disks were held in place with Duralco 4703 epoxy resin. The copper disks were coated with black paint.

Four methods for calibrating IR temperature measurements are considered in this chapter. Calibration Methods 1–3 were discussed comprehensively in chapter 3. Those methods are briefly

rehearsed here and an additional fourth calibration method is introduced. The four calibration methods are summarised below:

i) *Calibration Method 1:* black-body calibration only i.e. raw values converted to black-body-equivalent temperatures using the black-body conversion curve supplied by the manufacturer.

ii) *Calibration Method 2:* real-time in-situ calibration using the isothermal patch method with *total surrounding radiant flux* (or background radiation), $q^*(t)$, correction. This follows the work of Michaud et al. [31], Kirollos and Povey [36], Parker and Povey [50], Michaud et al. [30], and chapter 3.

iii) *Calibration Method 3:* real-time in-situ calibration using the isothermal patch method with a *temperature offset correction*. The temperature offset, $\Delta T_{CP}(t)$, is applied uniformly across the entire surface: $T_S(x,y,t) = T_{bb}(x,y,t)+\Delta T_{CP}(t)$.

iv) *Calibration Method 4:* in-situ calibration by evaluating a conversion curve, using entire time series data for a particular run, mapping raw image values to surface temperatures. The conversion curve is determined—separately for each run—by evaluating the best-fit curve that represents the functional relationship between the measured (via thermocouple) calibration-patch temperature, $T_S\left(x_{CP},y_{CP},t\right)$, and the raw image data measured by the IR camera on the calibration patch, $R\left(x_{CP},y_{CP},t\right)$ (i.e. the best-fit curve that represents the functional relationship $T_S = f(R)$ at the location of the calibration patch). When evaluating $R\left(x_{CP},y_{CP},t\right)$, raw image data is averaged over all pixels containing the calibration patch. The best fit is a third-order polynomial of the form $T_{CP} = a\times\overline{R}^3 + b\times\overline{R}^2 + c\times\overline{R} + d$ (the form is arbitrary and is chosen based on observations of the goodness of fit for the experimental data presented later in this chapter). It is assumed that the derived conversion curve represents the mapping between the local surface temperature, $T_S(x,y,t)$, and the local

raw image value, $R(x,y,t)$—for all x and y—and the best-fit curve is applied uniformly over the surface: $T_S(x,y,t) = a \times R(x,y,t)^3 + b \times R(x,y,t)^2 + c \times R(x,y,t) + d$.

In the main results sections (sections 4.6.1, 4.6.2 and 4.6.3) analysis is focused on Calibration Method 2, as calibration methods based on a physical model are preferred. This is in contrast to chapter 3, which focused primarily on Calibration Method 1 (see chapter 3 for justification). Separate overall cooling effectiveness data based on IR temperature measurements calibrated according to the other calibration methods is presented in sections 4.8.1, 4.8.2 and 4.8.3.

4.3 Boundary conditions for experiments

In this chapter three groups of boundary conditions are referred to: domain-global BCs; cooling system BCs; and local surface BCs. A comprehensive discussion of the physical significance of these boundary conditions is provided in chapter 2. The key points are briefly revisited in the context of this chapter. The domain-global BCs relate to the conditions on the mainstream flow, established in the test facility, at inlet to the HPT NGV cascade. In chapter 4 experiments are performed for domain-global boundary conditions of fixed domain inlet-to-exit total-to-static pressure ratio, PR, with fixed atmospheric exit static pressure, p_2 = 1.0 bar. Fixed inlet pressure of p_{01h} = 1.73 bar was required for fixed PR = 1.73. The cooling system BCs are the conditions relevant to the inlet to the internal cooling channels. When combined with the domain-global BCs, they set the particular CMPR and TR for a given run. Total temperature at inlet to the cooling channel was approximately the same for all runs ($T_{0c,in}$ = 290 K) and approximately constant with time during a run. The mainstream total temperature was varied in the range 313−548 K in order to achieve temperature ratios in the range $1.08 \leq TR \leq 1.89$. There is a slow time variation of temperature during a run which is described in more detail in section 4.5.3. A schematic of the system is shown in Figure 74a, in which the cooling system BCs and four planes of interest are indicated: Plane 1 is the domain inlet; and plane 2 is the domain exit.

In this chapter five local surface BCs are referred to: film effectiveness of the mixing layer, η_{ML}; through-wall average wall thermal conductivity, $\bar{k}_w$; external heat transfer coefficient, h_m; internal heat transfer coefficient, h_c; and internal cooling effectiveness, λ (see section 4.4 for further discussion). Changes in overall cooling effectiveness from a reference condition with TR = 2.0 are referred to throughout this chapter; this is so chosen to be representative of typical engine conditions for large civil aircraft (also consistent with chapters 2 and 3).

4.3.1 Transient PR and CMPR characteristics

Diameters were selected for the hub and case CFVNs that would minimise the magnitude of differences $CMPR_{case} - CMPR$ and $CMPR_{hub} - CMPR$ for a regulated run (such that both pressure ratios are close to the target value and the magnitude of the difference $CMPR_{case} - CMPR_{hub}$ is minimised). $CMPR_{case}$ is evaluated using the average case coolant plenum total pressure and the average mainstream total pressure; and $CMPR_{hub}$ is evaluated using the average hub coolant plenum total pressure and the average mainstream total pressure. For CMPR, the average coolant plenum total pressure (averaged over four measurements in both the hub and case i.e. eight measurements in total) and the average mainstream total pressure (averaged over 16 measurements) are used. The PID gains were tuned for both mainstream and coolant controllers in order to achieve stable CMPR and PR transient characteristics, with reasonable settling times for both pressure ratios. The PLC was operated in pressure control mode (this is discussed in detail in Messenger et al. [18]), which means that the boundary conditions on the facility were fixed total pressure upstream of both mainstream and coolant CFVNs. These BCs were set in order to achieve constant mainstream inlet total pressure and cooling channel inlet total pressure (and therefore constant PR and CMPR) throughout a run; however—as will be observed in a moment—the combination of this boundary condition and the facility temperature characteristics resulted in second-order transient characteristics for PR and CMPR throughout the settled period of the run. Corrections to overall cooling effectiveness for off-target pressure ratios

are discussed in section 4.5.6 and an alternative method for setting boundary conditions on the facility in order to achieve steady PR and CMPR throughout a run is discussed shortly.

The resulting characteristics for PR and CMPR are shown in Figure 77 a–b for a typical run with maximum temperature ratio of TR = 1.88.

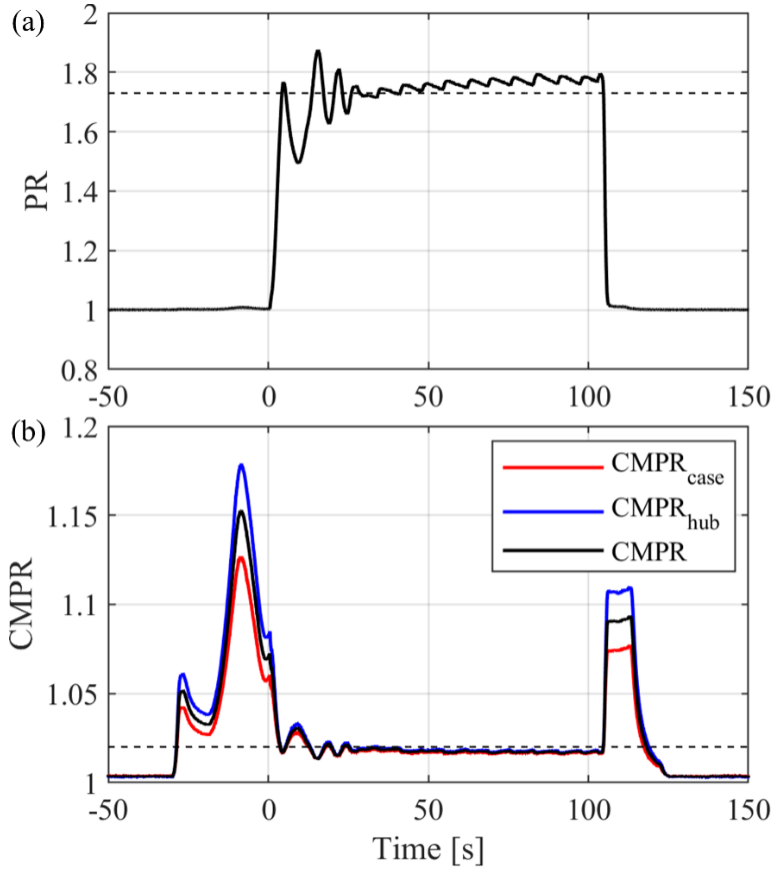

Figure 77: (a) Transient PR characteristics; and (b) transient CMPR characteristics.

The target values of each pressure ratio (PR = 1.73 and CMPR = 1.020) are also marked on the figure. Looking at Figure 77a, it is observed that PR is approximately unity in the quiescent period prior to the start of the run ($t < 0$). The mainstream run valve (see Messenger et al. [18]) was opened at $t = 0$ and a sharp rise in PR to near-target conditions is observed. The settling time for the mainstream pressure control system was approximately 27 s (roughly 25% of the total run time). For the settled period ($27 \leq t \leq 105$ s), it is observed that the general trend for PR is to increase—slightly—with time. This effect is driven by three effects: mainstream total pressure upstream of the CFVN is fixed (boundary condition on the facility); T_{01h} increases with time

throughout a run (test facility characteristic; discussed in Messenger et al. [18]) and mainstream mass flow rate increases with time throughout a run (total pressure upstream of CFVN is fixed and corresponding total temperature decreases with time. The combination of these three effects—in conjunction with an approximately constant vane capacity throughout a regulated run—causes an increase in p_{01h} and therefore T_{01h} throughout a run. The latter effect is a facility characteristic, discussed in Messenger et al. [18]). Looking at the figure, it is also observed that the data exhibits a—slight—oscillatory behaviour. This second order trend is a direct result of the programmable logic computer (PLC) characteristics—the PLC updates the valve position every few seconds (i.e. not instantaneously). The mainstream run valve was closed at $t = 105$ s and a corresponding sharp reduction in PR to unity is observed. Considering the time period for which the mainstream control system was settled for this particular run ($27 \leq t \leq 105$ s), the time-averaged PR was PR = 1.76 and the RMS deviation of all data points from this value was 0.019. As a percentage of the mean value of PR − 1, this corresponds to a value of 2.46% i.e. the steadiness of the data is high.

Looking now at Figure 77b it is observed that CMPR is approximately unity in the quiescent period ($t < -30$ s). The coolant run valve (see Messenger et al. [18]) is opened at $t = -30$ s and a sharp rise in CMPR is observed. The settling time for the coolant pressure control was approximately 30 s. At $t = 0$ (coolant pressure control system settled), the value of CMPR was 1.07. The mainstream run valve was opened at $t = 0$ and a sharp reduction in CMPR to near-target conditions is observed. The settling time was approximately 27 s (as dictated by the settling time of the mainstream pressure control, which was discussed above). For the settled period ($27 \leq t \leq 105$ s), it is observed that the general trend for CMPR is to decrease—slightly—with time. This is driven primarily by p_{01h} (and therefore PR) increasing with time throughout a run (for approximately constant cooling channel inlet total pressure, $p_{0c,in}$). This has been discussed. For completeness, it is noted that the mainstream run valve was closed at $t = 105$ s, which leads

to a sharp rise in CMPR as $p_{0c,in}$ drops to atmospheric pressure (i.e. 1.0 bar), and the coolant run valve was closed at t = 115 s, which causes a rapid reduction in CMPR to approximately unity.

Looking at the figure, it is also observed that the difference between $CMPR_{case}$ and $CMPR_{hub}$ was small. Considering the time period for which the mainstream and coolant control systems were settled for this particular run ($27 \leq t \leq 105$ s), the time-averaged CMPR was CMPR = 1.018 and the RMS deviation of all data points from this value was 6.8×10^{-4}. As a percentage of the mean value of CMPR − 1, this corresponds to a value of 3.87% i.e. the steadiness of the data is high. The RMS value of $CMPR_{case} - CMPR_{hub}$ was 0.0013. As a percentage of the mean value of CMPR − 1, this corresponds to a value of 7.35% i.e. the difference between hub and case coolant-to-mainstream pressure ratio measurements was small. The RMS difference from the nominal value for PR and CMPR was 0.033 and 0.0023, respectively. As percentages of the nominal values of PR − 1 and CMPR − 1, these correspond to percentage differences of 4.37% and 13.0%. These values are relatively small; however corrections to overall cooling effectiveness data for off-target PR and CMPR are discussed in section 4.5.6. It is noted that, whilst the target PR and CMPR were achieved with high accuracy, steadiness and stability, it is recommended that the PLC is operated in active control mode (discussed in detail in Messenger et al. [18]) in future campaigns. When operated in this mode, the PLC updates the values of the target control pressures in real-time, in order to maintain fixed PR and CMPR throughout a run (instead of setting a fixed total pressure upstream of both the mainstream and coolant CFVNs, as in the experiments considered in chapter 4).

Measured domain-global and cooling system BCs are summarised in Table 7 for the two typical runs. Here a run corresponding to near-engine conditions with TR = 1.84 and a run with a conventional laboratory temperature ratio condition of TR = 1.26 are chosen. All measured values in the table are averaged over the time period for which the mainstream and coolant control systems were settled.

Table 7: Measured domain-global and cooling system boundary conditions, at TR = 1.84 and TR = 1.26.

Boundary/operating condition	Value for TR = 1.84	Value for TR = 1.26
Coolant plenum total temperature, $T_{0c,in}$ (K)	290	290
Mainstream total temperature, T_{01h} (K)	534	365
Mainstream-to-coolant temperature ratio, TR (–)	1.84	1.26
Outlet Mach number, M (–)	0.94	0.93
Domain inlet-to-exit total-to-static pressure ratio, PR	1.76	1.75
Coolant plenum total pressure, $p_{0c,in}$ (bar)	1.82	1.78
Mainstream inlet total pressure, p_{01h} (bar)	1.79	1.75
Exit static pressure, p_2 (bar)	1.02	1.00
CMPR, $p_{0c,in}/p_{01h}$ (–)	1.017	1.016

4.4 Five local surface boundary conditions

Local surface boundary conditions are the BCs resulting on the HPT NGV surface when the cascade is subject to particular domain-global and cooling system BCs. In chapter 2 it was demonstrated that for an incompressible system with a diabatic external wall and an adiabatic internal wall; no conducting webs connecting the two walls; and one-dimensional conduction heat transfer (i.e. no lateral conduction), overall cooling effectiveness can be expressed in the form:

$$\theta = \eta_{ML} + \frac{\lambda - \eta_{ML}}{1 + h_m\left(\frac{1}{h_c} + \frac{t_w}{\bar{k}_w}\right)} \tag{69}$$

where η_{ML} is film effectiveness of the mixing layer, $\bar{k}_w$ is local through-wall average wall thermal conductivity, h_m is external heat transfer coefficient, h_c is internal heat transfer coefficient and λ is internal cooling effectiveness.

For this system, the functional relationship is $\theta = f\left(\eta_{ML}, \bar{k}_w, h_m, h_c, \lambda\right)$. In chapter 2 it was argued that the five terms in the parentheses are the local surface BCs and it was demonstrated by linear superposition of isolated changes in θ—due to changes in each individual BC—that the chosen local surface BCs form a closed set. Consequently, a full explanation for the overall change in θ with TR is provided by consideration of the variation of each local surface BC with TR. In chapter 3, a more complex incompressible system was studied. This system consisted of a diabatic external wall and a diabatic internal wall; conducting webs connecting the two walls; and one-

dimensional conduction heat transfer (i.e. no lateral conduction). Similar arguments were followed to demonstrate that the system consisted of eight local surface BCs (similar BCs to those of chapter 2 but with one heat transfer coefficient for each of five surfaces). For the NGV geometry considered in this chapter, both the external and internal walls of the cooling channel are diabatic and there is a degree of coupling between both walls. Whilst it could therefore be argued that there are eight local surface BCs relevant to the system considered here, as was the case in chapter 3, the five local surface BCs presented in chapter 2 are chosen for the analysis presented in this chapter. The reason for this is twofold: So far as the external surface is concerned (the most relevant surface for the analysis of chapter 4), it was demonstrated in chapter 3 that two of the additional three local surface BCs introduced (h_{c3} and h_{c5} in chapter 3) have second order contributions to changes in θ with TR; and the third additional BC introduced in chapter 3 (h_{c4}) has a significant contribution to changes in θ with TR for the geometry considered in that chapter but—for the NGVs considered in this chapter—the only region with a significant degree of coupling between external and internal walls is the late SS. It is therefore expected the contribution of h_{c4} to changes in surface-averaged overall cooling effectiveness to be second order for the HPT NGV geometry considered here. Each local surface BC is now briefly considered in turn.

4.4.1 Film effectiveness of the mixing layer

Film effectiveness of the mixing layer, η_{ML}, is the non-dimensional recovery temperature of the near-wall mixing region (driving temperature for heat transfer). Effectiveness of the mixing layer is defined by

$$\eta_{ML}(x,y) = \frac{c_h(x,y)T_{01h} - c_m(x,y)T_{0m}(x,y)}{c_h(x,y)T_{01h} - c_c(x,y)T_{0c,in}} \tag{70}$$

where $c_h(x,y)$ is mainstream recovery ratio, $c_m(x,y)$ is mixing layer recovery ratio, $T_{0m}(x,y)$ is mixing layer total temperature and $c_c(x,y)$ is the recovery ratio of a *hypothetical unmixed coolant stream with adiabatic wall condition* and total pressure and temperature equal to those of the

coolant at the outlet of the cooling system. Here a compressible definition (for discussion see chapter 2) is used. In chapter 4, $c_c(x,y)$ is approximated by using total pressure and temperature equal to those of the coolant at inlet to the cooling channel (assumptions of low pressure loss and heat pickup in the cooling channels—typical of internal cooling architectures for HPT NGVs used in large civil aircraft). Using the low-order network model of chapter 2 the error in absolute values of θ introduced by this assumption is estimated to be of the order 0.01% i.e. it is very small. For evaluation of recovery ratios a CFD-predicted isentropic Mach number distribution at the vane surface (see Amend et al. [51]) is taken and the turbulent flow correlation for recovery factor, $r(x,y) = \mathrm{Pr}^{1/3}(x,y)$, is assumed. Effectiveness of the mixing layer quantifies the degree to which coolant injected into the external flow domain reduces the driving temperature for heat transfer. In chapter 3, a separate film effectiveness was assigned to each of three mixing layers resulting from the injection of three film cooling rows into the external flow domain. A sophisticated entrainment-based model, which considers conservation of both mass and energy, was used to determine the effectiveness of each mixing layer. In the network model of chapter 3, subsequent mixing layers stack, such that the layer closest to the external surface is always that formed by the cooling film from the preceding row of film cooling holes. In the analysis of chapter 3, the effectiveness of the mixing layer closest to the external surface defines the driving temperature for heat transfer. In this chapter, the geometry also contains multiple rows of film cooling holes; however such comprehensive treatment of individual rows is not required. A single near-wall mixing layer, for which the effectiveness quantifies the combined contributions of all cooling films to the non-dimensional driving temperature for heat transfer, is referred to throughout the rest of this chapter.

4.4.2 Local through-wall average wall thermal conductivity

Wall thermal conductivity, $k_w(x,y,z)$, is evaluated at the local wall temperature, $T_w(x,y,z)$. The local through-wall-average wall thermal conductivity is defined by

$$\bar{k}_{\mathrm{w}}(x,y) = \frac{1}{t_{\mathrm{w}}} \int_0^{t_{\mathrm{w}}} k_{\mathrm{w}}(x,y,z)\mathrm{d}z \tag{71}$$

where t_{w} is wall thickness.

4.4.3 External heat transfer coefficient

External heat transfer coefficient is defined by

$$h_{\mathrm{m}}(x,y) = \frac{\mathrm{Nu}_{\mathrm{m}}(x,y)k_{\mathrm{m}}(x,y)}{x} \tag{72}$$

where $\mathrm{Nu}_{\mathrm{m}}(x,y)$ is external Nusselt number and $k_{\mathrm{m}}(x,y)$ is thermal conductivity of the near-wall mixing layer (it is noted that in chapters 2 and 3, Nusselt number was evaluated using properties of the near-wall mixing layer).

4.4.4 Internal heat transfer coefficient

Internal heat transfer coefficient is defined by

$$h_{\mathrm{c}}(x,y) = \frac{\mathrm{Nu}_{\mathrm{c}}(x,y)k_{\mathrm{c}}(x,y)}{D_{\mathrm{c}}} \tag{73}$$

where $\mathrm{Nu}_{\mathrm{c}}(x,y)$ is internal Nusselt number, $k_{\mathrm{c}}(x,y)$ is thermal conductivity of the internal coolant and D_{c} is hydraulic diameter of the internal cooling channel.

4.4.5 Internal cooling effectiveness

The internal cooling effectiveness is the non-dimensional internal coolant temperature defined by

$$\lambda(x) = \frac{c_{\mathrm{h}}(x)T_{01\mathrm{h}} - T_{0\mathrm{c}}(x)}{c_{\mathrm{h}}(x)T_{01\mathrm{h}} - c_{\mathrm{c}}(x)T_{0\mathrm{c,in}}} \tag{74}$$

where $T_{0\mathrm{c}}(x)$ is the local internal coolant temperature, and where all other variables have been defined. Here a compressible definition (for discussion see chapter 2) is used.

4.5 Experimental processing and results

In this section, corrections for total surrounding radiant flux, the full-surface experimental result, corrections for transient behaviour and corrections for off-target conditions are presented. The

low-order-model methods of chapter 3 are used for evaluating corrections for transient effects and off-design operating points. Summary results of the effect of TR on overall cooling effectiveness are presented in section 4.6. Corrections for total surrounding radiant flux are considered first.

4.5.1 Correction for total surround radiant flux

This chapter focuses primarily on overall cooling effectiveness data based on IR temperature measurements calibrated according to Calibration Method 2. As discussed in chapter 3, this technique uses an isothermal calibration patch mounted on the vane surface—in combination with a simple radiation model—to evaluate a residual radiant flux, in real-time, that reconciles the black-body-equivalent temperature at the location of the calibration patch with the measured (via thermocouple) temperature at this location. It is assumed that the residual radiant flux (which is referred to as *total surrounding radiant flux*) is uniform across the entire surface and use this term—in combination with the simple radiation model—to correct all black-body-equivalent IR temperatures over the surface. The reader is referred to Kirollos and Povey [36], Michaud et al. [30] and chapter 3 for full discussion of the method and the assumptions involved in the processing. Briefly, by considering the sum of radiation terms incident on the IR temperature sensor, and assuming a diffuse surface, the local black-body-equivalent IR temperature (as measured by the IR camera with the factory black-body calibration) is given by

$$T_{\mathrm{bb}}(x,y,t)^4 = \tau(x,y)\varepsilon(x,y,\beta)T_{\mathrm{S}}(x,y,t)^4 + \tau(x,y)\big(1-\varepsilon(x,y,\beta)\big)T_{\mathrm{R}}(t)^4 + \big(1-\tau(x,y)\big)T_{\mathrm{opt}}(t)^4 \tag{75}$$

where $\tau(x,y)$ is transmittance of the IR window, $\varepsilon(x,y,\beta)$ is emissivity of the vane surface, β is the IR camera viewing angle i.e. the angle subtended between the surface normal and the axis connecting the point (x,y) to the corresponding bolometric pixel, $T_{\mathrm{S}}(x,y,t)$ is the local surface temperature, and $T_{\mathrm{R}}(t)$ and $T_{\mathrm{opt}}(t)$ are the (assumed uniform) surrounding enclosure and IR window (Crystran Zinc Selenide with anti-reflective coating) temperatures, respectively.

In order to simplify the analysis, the following additional assumptions are made:

i) The NGV surface is an ideal diffuse (Lambertian) surface. That is, emissivity is independent of viewing angle i.e. $\varepsilon(x,y,\beta) \cong \varepsilon(x,y)$. It has been shown in previous literature (see, for example, the experimental results of Warren et al. [52]) that emissivity has weak dependence on viewing angles in the approximate range $\beta < 45°$ but gradually decreases with increasing viewing angles in the range $\beta \geq 45°$. Based on back-of-the-envelope calculations, the maximum viewing angle in either FOV (upstream or downstream camera) is estimated to be 37.7° i.e. below the critical value for which angular dependence becomes significant. Based on the experimental data presented in Warren et al. [52] the maximum error in ε, incurred by assuming negligible angular dependence, is estimated to be 0.8% i.e. the error is very small. It is however noted that the estimated maximum viewing angle (37.7°) in the data presented later in this chapter is close to the critical value (45°) and it is argued that a more sophisticated analysis of viewing angles would be justified for sanity checking purposes.

ii) Transmittance and emissivity are spatially uniform i.e. $\varepsilon(x,y) \cong \varepsilon$ and $\tau(x,y) \cong \tau$. These assumptions are typical in IR thermography (see, for example, Kirollos and Povey [36], Michaud et al. [30] and chapter 3). The assumption of spatially-uniform vane surface emissivity is deemed reasonable as the vane surface is coated uniformly in thermal barrier coating (TBC). Likewise, the assumption of spatially-uniform IR window transmittance is deemed reasonable (symmetric geometry of the window and camera housing); however it would be useful to verify these assumptions via further theoretical and experimental studies.

Based on the above assumptions, Eq. (75) is recast in the form

$$T_{\mathrm{bb}}(x,y,t)^4 = \tau\varepsilon T_{\mathrm{S}}(x,y,t)^4 + \tau(1-\varepsilon)T_{\mathrm{R}}(t)^4 + (1-\tau)T_{\mathrm{opt}}(t)^4 \tag{76}$$

For the experiments of chapter 4, the values $\tau = 0.91$ and $\varepsilon = 0.995$ are used. The former value was supplied by the manufacturer (valid for wavelengths in the range 7–14 μm) and the latter value was experimentally determined via an in-house calibration.

A *total surrounding radiant flux*, $q^*(t)$ is then defined

$$q^*(t) = \sigma \frac{\tau(1-\varepsilon)T_{\mathrm{R}}(t)^4 + (1-\tau)T_{\mathrm{opt}}(t)^4}{1-\tau\varepsilon} \tag{77}$$

where σ is the Stefan-Boltzmann constant.

By substituting Eq. (76) into Eq. (77), and taking the black-body-equivalent IR temperature and the surface temperature at the location of the calibration patch, $q^*(t)$ is expressed in the following form

$$q^*(t) = \sigma \frac{T_{\mathrm{bb}}\left(x_{\mathrm{CP}},y_{\mathrm{CP}},t\right)^4 - \tau\varepsilon_{\mathrm{CP}}T_{\mathrm{S}}\left(x_{\mathrm{CP}},y_{\mathrm{CP}},t\right)^4}{1-\tau\varepsilon_{\mathrm{CP}}} \tag{78}$$

where $\varepsilon_{\mathrm{CP}}$ is emissivity of the calibration patch. For the experiments of chapter 4, the value $\varepsilon_{\mathrm{CP}} = 0.97$ (Autotek black paint) is used. This value was determined from an in-house bench experiment. For $T_{\mathrm{bb}}\left(x_{\mathrm{CP}},y_{\mathrm{CP}},t\right)$, T_{bb} is averaged over all pixels contained within the calibration patch and, for $T_{\mathrm{S}}\left(x_{\mathrm{CP}},y_{\mathrm{CP}},t\right)$, the measured (via thermocouple) calibration-patch temperature is used.

For each experimental run and for both the PS and SS, $q^*(t)$ is experimentally evaluated using Eq. (78). By substituting Eq. (77) into Eq. (76), the real-time-calibrated local surface temperature, $T_{\mathrm{S}}(x,y,t)$, is then defined by

$$T_{\mathrm{S}}(x,y,t) = \frac{1}{\tau\varepsilon}\left(T_{\mathrm{bb}}(x,y,t)^4 - \frac{(1-\tau\varepsilon)}{\sigma}q^*(t)\right)^{0.25} \tag{79}$$

Total surrounding radiant flux time-series characteristics for each run are plotted in Figure 78 as a function of mainstream total temperature, $T_{01\mathrm{h}}$.

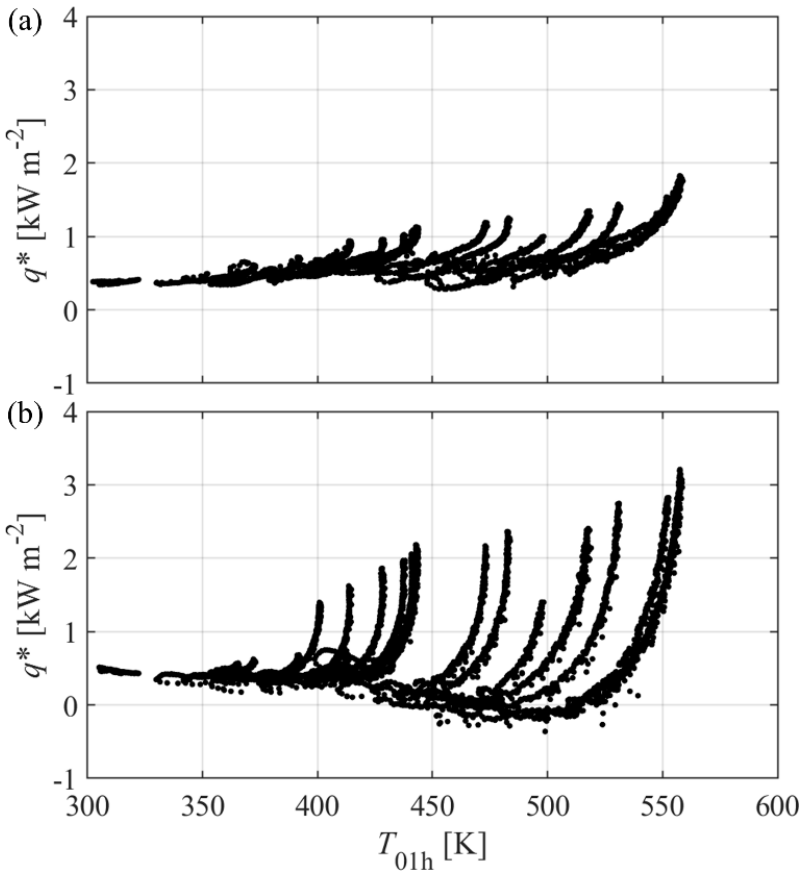

Figure 78: Total surrounding radiant flux as a function of T_{01h} for (a) PS; and (b) SS.

Data for the PS are presented in the top row (frame a) and data for the SS are presented in the bottom row (frame b). Data is plotted for the time period in which the mainstream and coolant control systems were settled. For the run discussed in the context of Figure 77, this corresponds to the time period $t > 27$ s. q^* is expected to correlate with the background temperature, T_R, which is expected to loosely correlate with the external flow temperature, T_{01h}.

Looking at the figure and looking first at the trend for the PS (frame a), it is observed that the primary trend for q^* is to increase with increasing T_{01h} although the individual time series do not collapse well to a single global trend. Now looking at the trend for the SS (frame b), it is observed that the trend for q^* *for an individual run* is to rapidly increase with increasing T_{01h}, at a higher rate than the corresponding data for the PS, and—again—the individual time series do not collapse well to a single global trend. Data for the SS typically have higher absolute values than the corresponding data for the PS. This result has been observed in similar experiments (see, for

example, the experimental results of Kirollos and Povey [36]). By setting $T_R = T_{opt} \cong T_{0c,in} = 290$ K (i.e. isothermal conditions at the minimum temperature in the system) and substituting into Eq. (77), the minimum value of the total surrounding radiant flux is expected to be approximately 400 W m^{-2}. Looking at Figure 78, it is observed that several data points, particular for the SS, lie in the range $q^* < 400$ W m^{-2} and therefore appear to take non-physical values. The reason for this is unknown, however it is noted that a very wide range of data has been presented, in order to expose this problem. Further discussion of this phenomenon in the community would be welcomed.

A sanity check of the q^* values is now performed for the PS. Firstly, it is assumed that the dominant contribution to the surrounding radiant flux is from the surrounding enclosure. Mathematically, this is expressed as $(1-\tau)T_{opt}(t)^4 \ll \tau(1-\varepsilon)T_R(t)^4$. By re-arranging Eq. (77), an approximation to the surrounding enclosure temperature, $T_R(t)$, can be evaluated as a function of time for each run. The value at the end of the run is taken. For the run discussed in the context of Figure 76, this corresponds to the time $t = 105$ s. This is repeated for all runs and the corresponding data points are added to Figure 79.

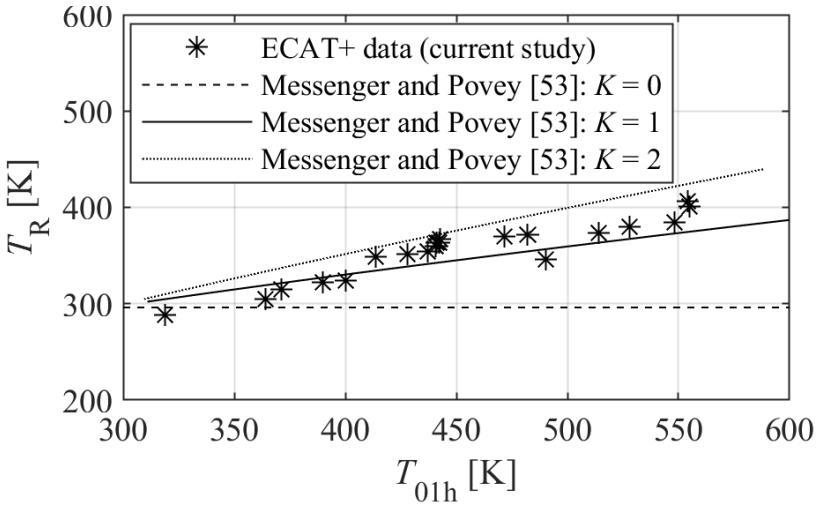

Figure 79: Equivalent surrounding enclosure temperature for the PS, at the end of the run, with comparison to 2D transient thermal facility model (see Messenger and Povey [53]).

In order to sanity check the values, the 2D transient thermal facility model described in Messenger and Povey [53] is used. The model, which was carefully calibrated against existing ECAT data,

predicts transient temperature characteristics of the test facility for particular tank temperatures and facility boundary conditions (i.e. control pressures upstream of coolant and mainstream CFVNs). In order to predict the surrounding enclosure temperature characteristics for typical runs, the model is run with a range of mainstream tank temperatures that achieve temperature ratios in the range $1.07 \leq \mathrm{TR} \leq 2.16$ at the end of the run, and the transient characteristic of the hottest section of the working section, $T_{\mathrm{WS,max}}(t)$, is extracted. By assuming that emission from the surface of the working section is the dominant component of the surrounding radiant flux incident on the NGV surface, the approximation $T_{\mathrm{R}} \cong T_{\mathrm{WS,max}}$ is then made. The working section temperatures predicted by the model are strongly affected by—amongst other factors—the form of the correlation used for Nusselt number in the working section. Whilst all Nusselt number correlations used in the model were carefully calibrated against existing ECAT data (see Kirollos et al. [9]), there exists some uncertainty in these correlations. In order to define uncertainty bands for the values of T_{R} predicted by the model, a multiplier—K—is introduced for the Nu correlation used in the working section (Eq. (1) in Messenger and Povey [53]). It is assumed that K lies in the range $0 \leq K \leq 2$ (that is, the maximum error in the predicted value of Nu at any position in the working section is ±100% of the predicted local value with $K = 1.0$) and the simulations are repeated for all tank temperatures with K values $K = 0$, 1 and 2, and all data are added to Figure 79. Looking at the figure, it is observed that all experimental data is correlated very closely with the predicted values from the model with $K = 1.0$. That is, the model and experiment are very closely aligned. Furthermore, it is observed that all data points—except for one—lie within the margin of error for the predicted value of T_{R}, arising from the assumed uncertainty in the Nusselt number correlation. The RMS deviation between experiment and model prediction (with $K = 1.0$) is 11.3 K. As a percentage of the mean value (across all 21 runs) of T_{R} (predicted by the model with $K = 1.0$), this corresponds to a value of 3.3%. This demonstrates that—so far as values at the end of the run (the quasi-steady point) are concerned—the experimentally measured total surrounding radiant flux values for the PS are physically plausible.

Several suggestions for the extension of this analysis are now discussed. It is hoped that future studies will validate the total surrounding radiant flux characteristics measured in the experiments and investigate the cause of the apparent non-physical values of q^* (particularly those used to correct SS measurements). These points are summarised below:

i) The transient thermal facility model of Messenger and Povey [53] does not currently have the capability to predict the temperature characteristics of surrounding enclosure components downstream of the NGV cascade, so an equivalent sanity check for the total surrounding radiant flux used to correct SS measurements is not included. It is recommended that the model is extended to include this capability, so that the preceding analysis can be performed in order to sanity check this data.

ii) It would be informative to compare the approximate experimentally-measured surrounding enclosure temperature characteristic, $T_{\mathrm{R}}(t)$, for the entire time series (not just the end point) for each individual run, to a prediction from the transient thermal facility model. One approach is to run the model in so-called "multi-run mode" (see Messenger and Povey [53]), which models the transient temperature characteristics of the facility in the quiescent period between runs. This ensures that the initial temperatures of the facility are accurately modelled, leading to a more realistic prediction of all transient temperature profiles for the entire time series of each run.

iii) It is recommended that the transient temperature characteristic of the IR window, $T_{\mathrm{opt}}(t)$, for an individual run is experimentally measured or predicted—by implementation of a simple transient thermal model of the window. This would allow Eq. (77) to be used—in combination with the characteristic of the IR window, $T_{\mathrm{opt}}(t)$—to evaluate the transient surrounding enclosure temperature profile, $T_{\mathrm{R}}(t)$, for each run. This would allow direct comparison of the experimentally-measured surrounding enclosure temperature with the transient thermal facility model, without needing to make the assumption $(1-\tau)T_{\mathrm{opt}}(t)^4 \ll \tau(1-\varepsilon)T_{\mathrm{R}}(t)^4$, as discussed above.

iv) The temperature of the surrounding enclosure, $T_R(t)$, should be directly measured for each experimental run. This could be done by installing thermocouples within the surrounding enclosure components both upstream and downstream of the NGV cascade. This would allow direct validation—in combination with Eq. (77) and a prediction, or experimental measurement, of $T_{opt}(t)$—of the experimentally-measured q^* values, measured using the isothermal-patch method outlined for Calibration Method 2.

4.5.2 Full-surface distribution of overall cooling effectiveness

Full-surface overall cooling effectiveness measurements were performed on both the PS and the SS for temperature ratio conditions in the range $1.08 \leq TR \leq 1.89$. The target values for PR and CMPR are: PR = 1.73; and CMPR = 1.020. Typical full-surface cooling effectiveness distributions on PS and SS are shown in Figure 80.

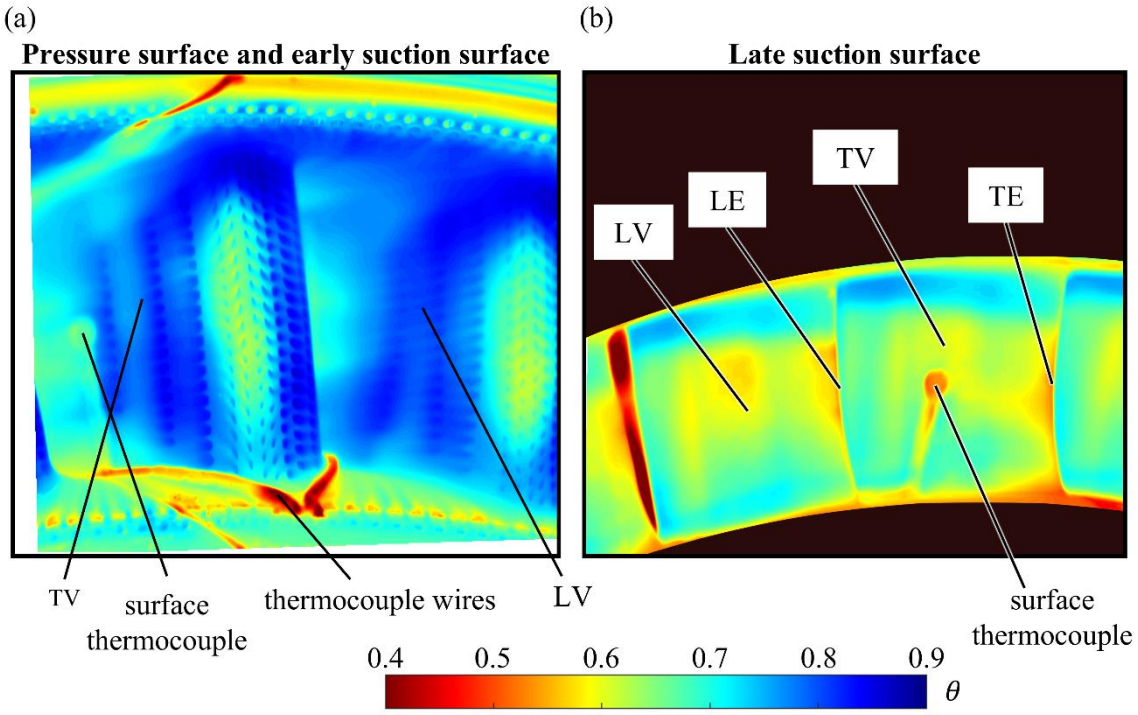

Figure 80: Overall cooling effectiveness measurements on: (a) Pressure surface (PS) and early suction surface (SS); and (b) late SS. Leading vane (LV) and trailing vane (TV) are marked. Leading edge (LE) and trailing edge (TE) are marked for SS TV.

These data were from the end of a run with maximum temperature ratio of TR = 1.88 (same run as that discussed in the context of Figure 77). The blank regions correspond to sections of the IR

images that are removed following an affine transformation. The purpose of the transformation is to align images from all runs and is required because the orientation of both cameras changes—slightly—between runs. Overall cooling effectiveness is defined by

$$\theta(x,y) = \frac{c_{\mathrm{h}}(x,y)T_{01\mathrm{h}} - T_{\mathrm{S}}(x,y)}{c_{\mathrm{h}}(x,y)T_{01\mathrm{h}} - c_{\mathrm{c}}(x,y)T_{0\mathrm{c,in}}} \tag{80}$$

where all terms have been defined previously. $T_{\mathrm{S}}(x,y)$ is taken to be the calibrated IR temperature, which is evaluated using Eq. (79). Here a compressible definition (for discussion see chapter 2) is used. Overall cooling effectiveness values presented in chapter 4 have been arbitrarily offset (same offset value for all data) in order to achieve a surface-averaged (over the PS and SS) value of 0.73 at the reference temperature ratio of TR = 2.0, which is in the range of typical engine operation for large civil aircraft.

Looking at Figure 80a, there is a hot spot (region of low overall cooling effectiveness) in the vicinity of the leading edge (LE). This is due to the high external heat transfer coefficient (boundary layer of the external flow is extremely thin in this region). As one moves away from the LE—along the PS or early SS—overall cooling effectiveness increases due to a reduction in external heat transfer coefficient, as the boundary layer thickens, and an increase in film effectiveness of the mixing layer caused by the superposition effect of cooling films. In the trailing-edge (TE) region of the PS, overall cooling effectiveness decreases with streamwise position (away from the LE) due to an increase in external heat transfer coefficient (external flow accelerates, leading to an increase in Reynolds number) and a reduction in film effectiveness of the mixing layer (due to entrainment of hot gas in the near-wall mixing region). Now looking at Figure 80b, the overall cooling effectiveness of the late SS decreases with streamwise position (away from the LE) due to a reduction in film effectiveness of the mixing layer as hot gas is entrained in the near-wall mixing region. It is also observed that there are bands of high cooling effectiveness along the late SS in the regions near the hub and case platforms. This effect is caused by upwash and downwash from the hub and case platform film cooling holes. The in-situ

calibration patches are visible as circular regions on the PS and SS of the TV. The entirety of the PS; the early SS ($s/s_{max} < 8\%$ for the leading vane (LV) and $s/s_{max} < 15\%$ for the TV); and the late SS ($s/s_{max} > 40\%$) can be visualised in the images.

4.5.3 Transient behaviour of HPT NGVs

Transient behaviour is now considered. Surface average results (PS and SS) are considered. The averaging regions (i.e. each vane surface) are shown in Figure 80. As an example of the transient characteristics, a run with a maximum temperature ratio of TR = 1.88 is considered. Temperature characteristics for the mainstream flow, $T_{01h}(t)$, coolant flow, $T_{0c,in}(t)$, and vane surface for LV and TV (PS and SS) ($\bar{T}_{PS,LV}$, $\bar{T}_{PS,TV}$, $\bar{T}_{SS,LV}$, $\bar{T}_{SS,TV}$) are shown in Figure 81.

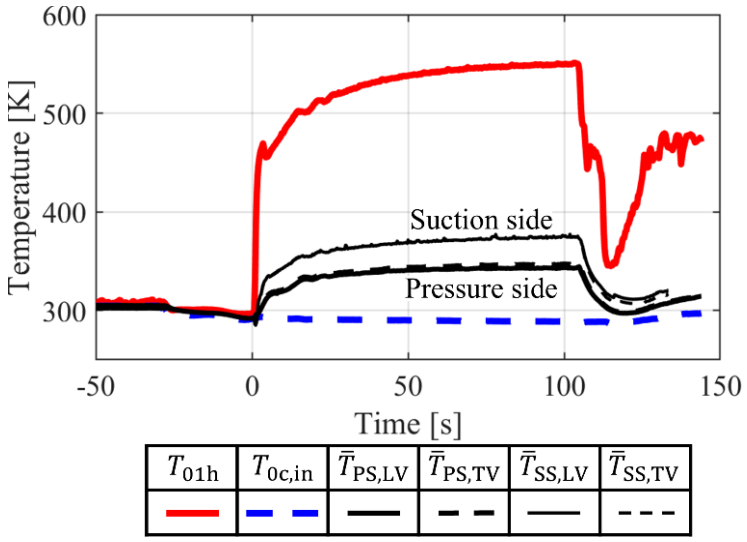

Figure 81: Transient temperature characteristics of the mainstream flow, coolant flow, leading vane and trailing vane (pressure surface and suction surface).

All temperatures in the figure have been arbitrarily offset (same offset value for all temperatures) by the value that achieves a time-averaged (over the time period for which the mainstream and coolant control systems were settled) cooling channel inlet total temperature of $T_{0c,in} = 290$ K. The mainstream run valve is opened at approximately $t = 0$ s and turned off at about $t = 105$ s. In this period the mainstream air temperature increases from approximately 300 K to approximately 550 K. The coolant temperature remains relatively constant at approximately 290 K. The

characteristics of surface temperature $\overline{T}_{\mathrm{PS,LV}}(t)$ to $\overline{T}_{\mathrm{SS,TV}}(t)$ are of similar general form to $T_{01\mathrm{h}}(t)$, but with a short delay caused by the transient surface response time of the HPT NGVs.

The increased level of noise on the suction surface temperature characteristics results from large vibrations of the downstream camera during a run. These vibrations are accounted for when performing the in-situ calibration of the IR measurements by implementing an algorithm that tracks the co-ordinates of the centre of the calibration patch as a function of time. The objective function of the algorithm is to track the co-ordinates of the point with maximum temperature within a small window of the IR data that always contains the calibration patch throughout a run. This objective function is used for two reasons: temperature of calibration patch is typically higher than the external surface, because the calibration patch is thermally isolated from the internal cooling channel; and the maximum temperature of the calibration patch typically occurs at the centre, because the patch is symmetric and there are small radial and circumferential conduction terms resulting from the surrounding external wall being at a lower temperature than the calibration patch (heat flow is in the direction from the centre of the calibration patch to the surrounding cooled external wall).

Further discussion of the temperature characteristics (and corresponding pressure characteristics) is presented in Messenger et al. [18]. The characteristics $\overline{T}_{\mathrm{PS,LV}}(t)$ to $\overline{T}_{\mathrm{SS,TV}}(t)$ can be expressed as overall cooling effectiveness characteristics $\overline{\theta}_{\mathrm{PS,LV}}(t)$ to $\overline{\theta}_{\mathrm{SS,TV}}(t)$ (using Eq. (80)). These are shown in Figure 82. All four characteristics have similar form: an initial transient lasting approximately 30 s after the heater has been switched on, followed by a more stable period of about 75 s duration leading up to the mainstream run valve being shut. The time constant of the HPT NGVs based on the wall temperatures from a 1D network model (described in section 4.5.4) is approximately $\tau_{\mathrm{model}} = 2.3$ s. Even though the time constant of the mainstream flow is more than 11 times longer than this (approximately $\tau_{\mathrm{flow}} = 26$ s, see Figure 81), the HPT NGVs never achieves true steady state, and a small correction is required. This correction is considered now.

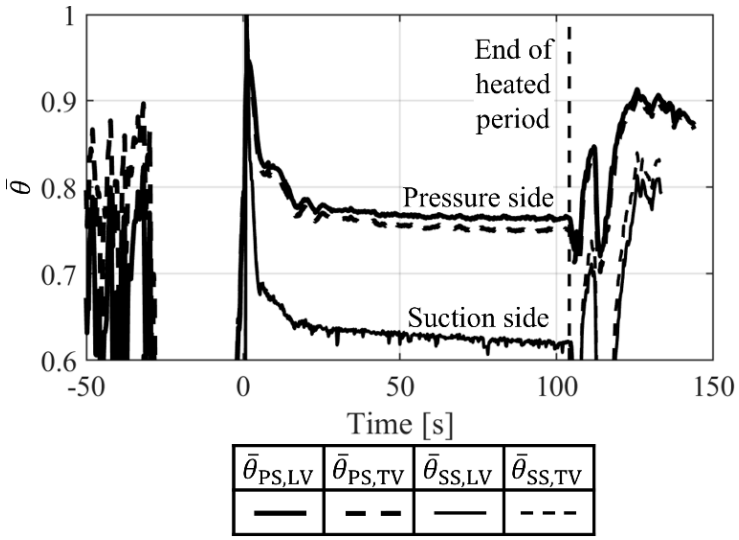

Figure 82: Overall cooling effectiveness characteristics of the leading vane and trailing vane (pressure surface and suction surface).

4.5.4 Correction for transient behaviour

In the experiment, the mainstream flow time constant (τ_{flow} = 26 s) was measured to be 11 times the HPT NGV time constant (τ_{model} = 2.3 s), and the overall test time (105 s) was greater than the flow time constant by a factor of approximately 4.0. The HPT NGVs almost reach a quasi-steady-state condition, but a small correction is implemented to determine the exact *inferred instantaneously steady state* (IISS) values of overall cooling effectiveness from the measured (transient) values. It is shown in this section that the magnitudes of correction at 50, 75 and 100 s are approximately 0.7%, 0.3% and 0.1%. These are very small corrections, but performing a time-dependent correction facilitates the use of a larger set of data in the final result. A similar approach to that outlined in chapter 3 is used for evaluating corrections for transient effects.

To perform this small correction for unsteady behaviour, a simple 1D low-order unsteady network model was used. The model consists of a single external mixing layer; a thermal mass representing the vane wall, with constant thickness t_w = 1 mm; and an internal cooling channel, fully mixed at the coolant inlet temperature. A schematic of the 1D network model is shown in Figure 83.

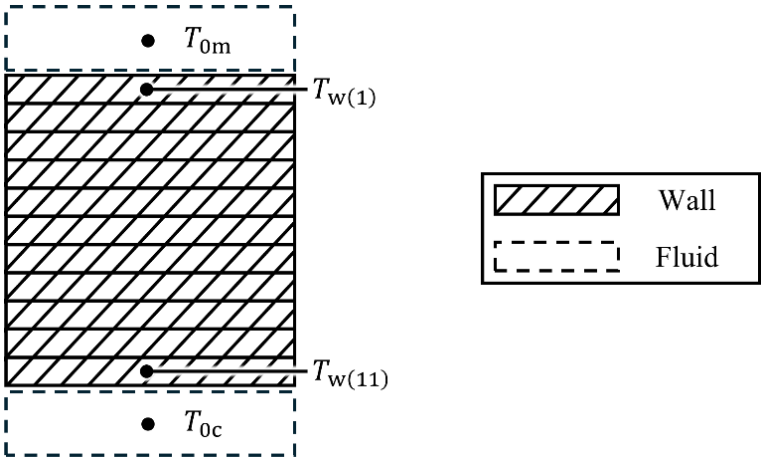

Figure 83: Schematic of the 1D low-order unsteady network model.

Conduction in the through-wall direction is considered and lateral conduction terms are excluded from the analysis (by considering the relative magnitude of length scales, it can be shown that this approximation is valid for many vane geometries). Time-dependent mainstream and coolant inlet temperature boundary conditions were obtained directly from experimental measurements. Time-dependent mixing layer temperature (driving temperature for heat transfer) was obtained by combining the temperature boundary conditions with the film effectiveness of the mixing layer (η_{ML}). Wall thermal conductivity was modelled using a best fit to experimental data of the form $k_w = 0.017T_w + 5.480$, which is typical of nickel alloys (see, e.g., Zielińska et al. [26]). All recovery ratios (c_c, c_h and c_m) are fixed with constant value 0.99—a typical value of surface-averaged recovery ratios for HPT NGVs.

The initial wall temperature distributions are uniform with value equal to the coolant inlet temperature at $t = 0$ s (isothermal initial condition). The network model was calibrated on a per-run basis by tuning three local surface BCs (η_{ML}, h_m and h_c) with the objective of minimising the mean difference between model-predicted and experimentally-measured surface-averaged overall cooling effectiveness trends over the entire time series (calibration is discussed further in a moment). The network model was calibrated and run separately for each of the four surface temperature characteristics of interest (PS and SS for both LV and TV; corresponding experimentally measured surface-averaged temperature characteristics shown in Figure 81). The

network model consists of one node in the streamwise direction and 13 nodes in the through-wall direction (one node for each of the mixing layer and internal coolant and 11 nodes for the wall).

The predicted temporal temperature characteristics from the transient low-order network model are shown in Figure 84 (leading vane only).

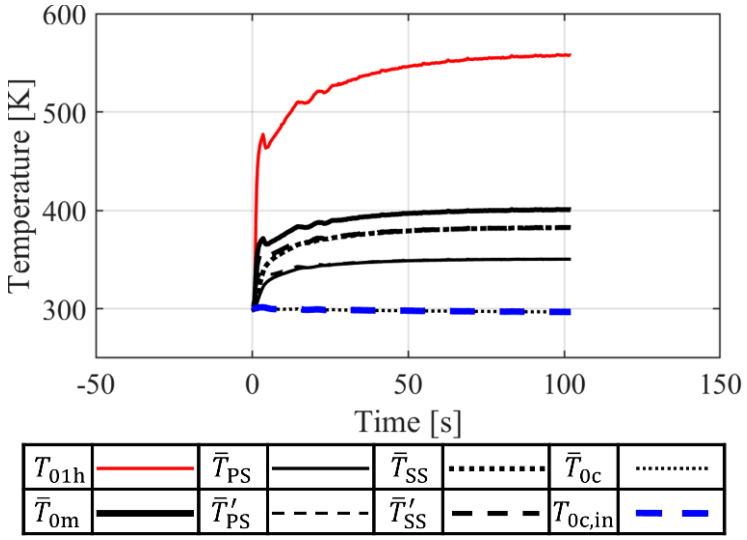

Figure 84: Temperature characteristics from the 1D transient thermal network model (leading vane).

The mainstream temperature, $T_{01h}(t)$, and coolant inlet temperature, $T_{0c,in}(t)$, are from an experimental run (same data as Figure 81), and are the temporal boundary conditions on the network model. The coolant duct temperature, $\overline{T}_{0c}(t)$, the mixing layer temperature, $\overline{T}_{0m}(t)$, and the PS and SS wall temperatures, $\overline{T}_{PS}(t)$ and $\overline{T}_{SS}(t)$ respectively, are the network model outputs. They are of similar form to the measured external and internal wall temperature trends shown in Figure 81. Corresponding IISS values (prime notation is used to distinguish them) $\overline{T}'_{PS}(t)$ and $\overline{T}'_{SS}(t)$ are also shown. The transient network model was run for a time period corresponding to that of the heated period (from $t = 0$ s to approximately $t = 105$ s). The IISS values are slightly higher than the uncorrected values in the initial period of the run ($0 < t < 30$ s) but in the latter period of the run ($t > 30$ s) the two characteristics quickly converge.

Overall cooling effectiveness characteristics corresponding to $\overline{T}_{PS}(t)$, $\overline{T}_{SS}(t)$, $\overline{T}'_{PS}(t)$ and $\overline{T}'_{SS}(t)$ (these are referred to as $\overline{\theta}_{PS}(t)$, $\overline{\theta}_{SS}(t)$, $\overline{\theta}'_{PS}(t)$ and $\overline{\theta}'_{SS}(t)$) are shown in Figure 85.

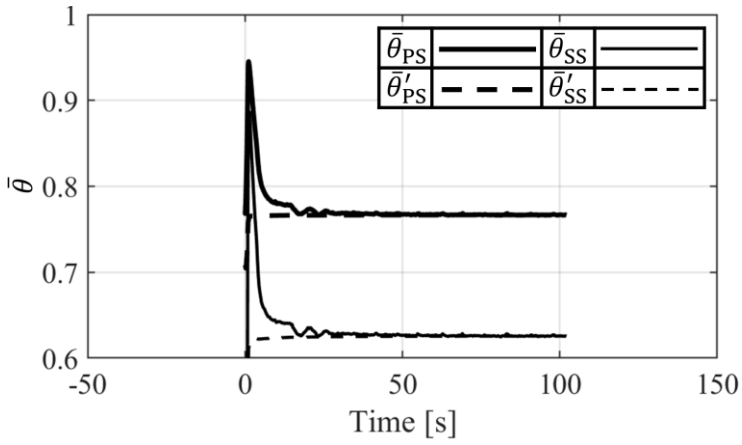

Figure 85: Transient ($\theta_{PS}(t)$ and $\theta_{SS}(t)$) and inferred instantaneously steady state ($\theta'_{PS}(t)$ and $\theta'_{SS}(t)$) overall cooling effectiveness characteristics from the 1D transient thermal network model (leading vane).

As expected (on the basis of simple time-constant arguments), the pairs of data (IISS trend and corresponding unsteady trend) are strongly converging, the difference corresponding to approximately 0.7%, 0.3% and 0.1% of the maximum value of θ (i.e. unity) at 50, 75 and 100 s. This is most clearly seen by looking at the residuals $\bar{\theta}'_{PS}(t) - \bar{\theta}_{PS}(t)$ and $\bar{\theta}'_{SS}(t) - \bar{\theta}_{SS}(t)$. These are shown in Figure 86.

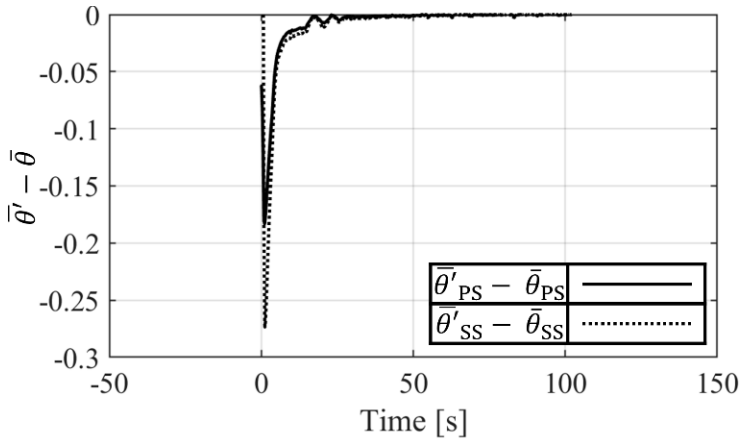

Figure 86: Residuals $\bar{\theta}'_{PS}(t) - \bar{\theta}_{PS}(t)$ and $\bar{\theta}'_{SS}(t) - \bar{\theta}_{SS}(t)$.

In addition to evaluating the magnitudes of the residuals, the residuals are used to transform the experimentally measured uncorrected laterally-averaged data $\bar{\theta}(x,t)$ to equivalent IISS values $\bar{\theta}'(x,t)$. This correction is performed on a per-run basis; the particular residual functions arising from the particular (run-specific) mainstream and coolant inlet temperature characteristics, $T_{01h}(t)$

and $T_{0c,in}(t)$, respectively. This allows one to use entire time-series data in the analysis presented in this chapter. In section 4.5.5 the calibration of the network model against experimental data is discussed.

4.5.5 Calibration of transient solver and application for determining spatial distributions $\bar{\theta}'(x,t)$ from $\bar{\theta}(x,t)$

In section 4.5.4 results from a 1D network model (through-wall temperature variation only) were discussed to demonstrate the typical magnitude of the correction to IISS values. In this section the calibration of the transient solver, and the application of the correction to IISS values as a function of both time and streamwise position, x, are discussed. This is the approach of chapter 3 for correcting overall cooling effectiveness measurements for transient effects.

The transient solver uses fixed values (i.e. not time-varying) for each of three local surface BCs (η_{ML}, h_m and h_c) for each surface (PS or SS) of each vane (LV or TV) for each particular run. Film effectiveness of the mixing layer is initially set to 0.40—a common value of *adiabatic film effectiveness* for flat-plate test articles (see, for example, Vinton et al. [24])—and heat transfer coefficients h_m and h_c are initially set to approximately 1500 $Wm^{-2}K^{-1}$ and 500 $Wm^{-2}K^{-1}$, respectively. The latter two values are typical surface-averaged (over PS and SS) values of h_m and h_c at conventional laboratory conditions of absolute temperature (i.e. low absolute temperature) and engine operating conditions of temperature ratio (TR = 2.0) for HPT NGVs. To tune the network model against the experimental data calibration coefficients (C_1 to C_3) are used for each of the three local surface BCs. They are introduced as multipliers. The nominal value of these multipliers is unity, but optimum values are found that minimise the mean deviation of the low-order-model data and experimental data. The correction is performed separately for the four surface temperature characteristics of interest on a per-run basis, using laterally-averaged time-based data for the PS and SS (i.e. $\bar{\theta}_{PS}(x,t)$ and $\bar{\theta}_{SS}(x,t)$).

The maximum and minimum values that multipliers C_1 to C_3 take across all the data (all experimental runs in chapter 4) are summarised in Table 8. It is observed that for the pressure surface and late suction surface, the maximum deviations from unity are 0.57 and 0.46,

respectively. The deviation from unity is significant and it is noted that the deviation is in the direction of increasing η_{ML} and h_c and decreasing h_m, which demonstrates that the initial values of local surface BCs used in the network model combine to underpredict the true cooling performance of the HPT NGVs. This is likely because the initial estimate of film effectiveness of the mixing layer—based on distributions of *adiabatic film effectiveness* for *flat-plate* test articles from the literature—is significantly lower than the true value for the geometry used in this chapter. Looking at the maximum-to-minimum value ratio for individual coefficients (last two rows of table) it is observed that values lie in the range 1.05 to 1.44. The wide extent of this range shows that the boundary conditions vary significantly with temperature ratio, as expected.

Once the calibration coefficients (C_1 to C_3) are determined for a particular run, the (corrected) laterally-averaged IISS overall cooling effectiveness characteristics, $\overline{\theta}'_{PS}(x,t)$ and $\overline{\theta}'_{SS}(x,t)$, can be evaluated from the uncorrected characteristics, $\overline{\theta}_{PS}(x,t)$ and $\overline{\theta}_{SS}(x,t)$. The process for this is as follows.

Table 8: Values of the calibration coefficients C_1 to C_3 for each correlation.

		Calibration coefficient		
		C1 (η_{ML})	C2 (h_m)	C3 (h_c)
Min. value	PS	1.50	0.43	1.50
	SS	1.22	0.54	1.22
Max. value	PS	1.57	0.50	1.57
	SS	1.46	0.78	1.46
Max-to-min ratio	PS	1.05	1.16	1.05
	SS	1.20	1.44	1.20

The starting point is a converged calibrated 1D *transient solution* which has experimentally-measured mainstream and coolant inlet temperatures as inputs, $T_{0h}(t)$ and $T_{0c,in}(t)$, and which has three calibrated correlations (for η_{ML}, h_m and h_c) with calibration coefficients (C_1 to C_3) particular to the individual run. For each timestep of the converged transient network model solution the IISS surface temperature, $T'_S(t)$, is evaluated using Eq. (81)

$$\overline{T}'_{\mathrm{S}}(t) = c_{\mathrm{m}}\overline{T}_{0\mathrm{m}}(t) - \left(1 + \frac{h_{\mathrm{m}}}{h_{\mathrm{c}}} + \frac{h_{\mathrm{m}}t_{\mathrm{w}}}{\overline{k}_{\mathrm{w}}}\right)^{-1} \times \left(c_{\mathrm{m}}\overline{T}_{0\mathrm{m}}(t) - \overline{T}_{0\mathrm{c}}(t)\right) \tag{81}$$

where c_{m} is mixing layer recovery ratio, $T_{0\mathrm{m}}$ is mixing layer total temperature and t_{w} is wall thickness.

Eq. (81) is derived by considering an energy balance between external heat transfer rate (external mixing layer to external surface) and overall heat transfer rate (external mixing layer to internal coolant) for a 1D system (i.e. no lateral conduction). The corresponding surface-averaged IISS overall cooling effectiveness, $\overline{\theta}'(t)$, is evaluated by combining $\overline{T}'_{\mathrm{S}}(t)$ with Eq. (80). By taking the difference between the two solutions the residuals $\overline{\theta}'_{\mathrm{PS}}(t) - \overline{\theta}_{\mathrm{PS}}(t)$ and $\overline{\theta}'_{\mathrm{SS}}(t) - \overline{\theta}_{\mathrm{SS}}(t)$ are evaluated at each timestep. The residuals are evaluated using only information from the calibrated transient 1D network model. Once the residuals are determined, the experimentally-measured laterally-averaged effectiveness characteristics, $\overline{\theta}_{\mathrm{PS}}(x,t)$ and $\overline{\theta}_{\mathrm{SS}}(x,t)$, are corrected to get the corresponding corrected-IISS characteristics $\theta'_{\mathrm{PS}}(x,t)$ and $\theta'_{\mathrm{SS}}(x,t)$. It is noted that the residual is evaluated using a 1D network model and therefore has no spatial variation. The one-dimensional value is applied uniformly over the surface when correction overall cooling effectiveness measurements. The reader is referred to chapter 3 for an example of a more sophisticated transient correction approach that makes use of a 2D low-order unsteady network model with more comprehensive treatment of the boundary conditions.

A somewhat arbitrary decision needs to be made about which (time-series) data to correct, and data is chosen for which the mainstream and coolant control systems were settled (such that oscillatory 'tails' for $\overline{\theta}$ trends associated with the startup period of each individual run are removed, leading to cleaner plots of $\overline{\theta}$ vs TR). It is complex to ascribe a meaningful additional uncertainty due to the process of correcting to IISS values, but—using the same reasoning as in chapter 3 (extremely well-behaved data)—it is assumed the arising additional uncertainty is at least an order of magnitude smaller than the value of the correction itself, i.e. extremely small (of order 0.01% of the surface-averaged value of θ).

4.5.6 Correction for off-target conditions of PR and CMPR

During experiments, PR and CMPR were held close to their target values (PR = 1.73 and CMPR = 1.020) but there was uncontrolled variation (sympathetic with changes in temperature ratio) in the ranges: $1.63617 \leq \text{PR} \leq 1.80136$; and $1.01405 \leq \text{CMPR} \leq 1.02580$. All data are corrected back to the target point by performing simulations to assess the sensitivity to off-target conditions of PR and CMPR. This is the method of chapter 3 for evaluating corrections for off-target operating conditions. The required simulations were performed using the 2D low-order conjugate aerothermal network model described in chapter 2. Whilst the system described in chapter 2 has different geometry and—slightly—different target BCs (PR = 1.75 and CMPR = 1.025) to those of the experiment, it is assumed that it can be used to predict the correction offsets for the HPT NGVs considered in this chapter with sufficient accuracy. This is justified on the grounds that the 2D network model in chapter 2 was carefully designed so as to accurately capture the physics of a typical HPT NGV cooling system.

For all simulations the entrainment-rate distribution, $\dot{m}_{\text{e}}(x)$, is scaled by assuming that the ratio of entrainment-rate to mainstream inlet mass flow rate remains unchanged from the baseline point (i.e. the point with reference conditions of temperature ratio and target conditions of PR and CMPR i.e. TR = 2.0; PR = 1.75; and CMPR = 1.025). This constraint, expressed mathematically by Eq. (25) in chapter 2, ensures geometric similarity of the cooling film as one moves away from the baseline point. This is justified on the grounds that, when CMPR and therefore momentum flux ratio are matched, it is expected that the mixing-determining structures remain largely unchanged as one moves away from the reference point. When CMPR is varied (as is the case for evaluating correction offsets for off-target conditions of CMPR), it is unclear whether this assumption remains valid and—if the assumption is no longer valid—to what extent the final results are impacted by failing to relax this geometric similarity constraint. In these simulations, because the sensitivity to each variable is very low, the variables were studied independently of

each other (assumed linear superposition). The low-order-model-estimated impacts on overall cooling effectiveness arising from off-target conditions of PR and CMPR are shown in Figure 87.

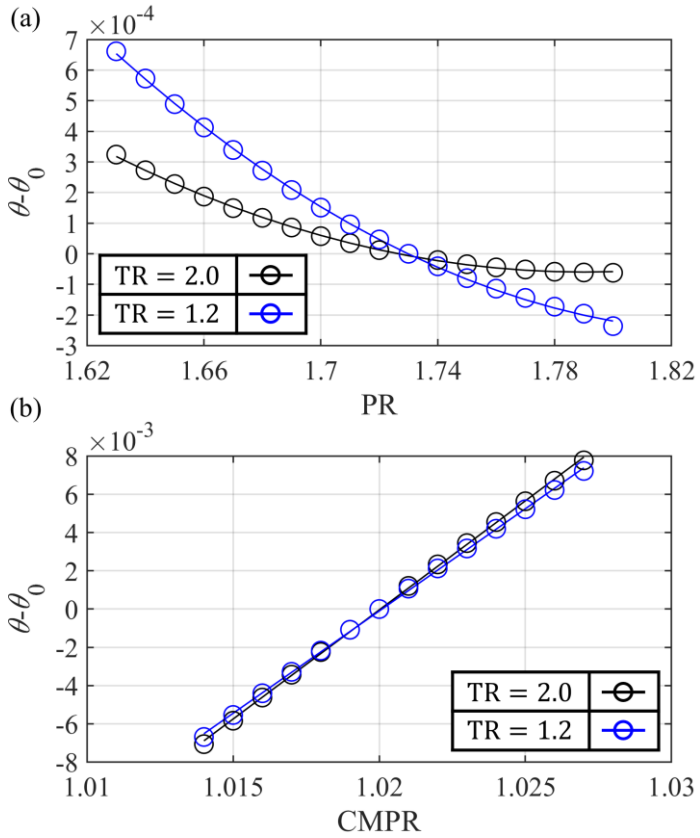

Figure 87: Low-order-model-estimated differences in overall cooling effectiveness from the design condition arising from uncontrolled variations in: (a) PR; and (b) CMPR.

Results are shown for engine conditions (TR = 2.0) and conventional lab conditions (TR = 1.2) of temperature ratio. Individual data points (converged network model simulations) and best-fit curves are presented. The data are presented as correction offsets for off-design PR and CMPR: frame a and b, respectively.

The following observations are made:

i) The change due to uncontrolled variation in CMPR is greater than that due to uncontrolled variation in PR. This is primarily via the impact of CMPR on η_{ML} and h_c.

ii) The sensitivity of corrections to TR for off-target CMPR is small but the sensitivity to TR for off-target PR is significant.

The data in Figure 87 for TR = 2.0 is used to correct all of the experimental data at off-target conditions of PR and CMPR back to the nominal operating point. As mentioned above, the sensitivity of corrections to TR for off-target PR is significant however these corrections are an order of magnitude smaller than those for off-target CMPR, so it is assumed that it is acceptable to use the corrections for TR = 2.0 only. Taking all data used in this study, the average correction was -0.10%. The corrections are small in magnitude, and it is believed they can be accurately performed.

Trends of overall cooling effectiveness with temperature ratio have been corrected for these effects. Double prime symbols are used to indicate overall cooling effectiveness measurements that have been corrected for both transient effects and off-target conditions of PR and CMPR: for example, θ''_{PS} and θ''_{SS}. The reader is referred to chapter 3 for a more sophisticated approach to determining the correction offsets for off-target operating conditions. In chapter 3, a 2D low-order conjugate aerothermal network model with geometry and boundary conditions *precisely* matched to the particular test article and experiment was used. The entrainment rate distribution was obtained from adiabatic CFD simulations at engine conditions of temperature ratio (TR = 2.0) for various combinations of off-target Re, M and CMPR. This ensured that there was no need to impose the geometric similarity constraint discussed in this section when evaluating correction offsets *at the reference TR* (of course, once the entrainment rate distribution at the reference TR is established, it is scaled to non-engine temperature ratios by imposing the geometric similarity constraint, as discussed in chapter 2). It is believed that the approach considered here is robust and the corrections have been carefully performed, however further discussion of robust correction methodology in the community would be welcomed.

4.6 Impact of temperature ratio on overall cooling effectiveness

The key result of this chapter, which is the impact of temperature ratio on overall cooling effectiveness, is now considered. The streamwise distribution for the HPT NGVs is considered first, followed by surface-averaged results.

4.6.1 Overall cooling effectiveness distribution

The experimentally measured distributions (with streamwise position) of overall cooling effectiveness are shown in Figure 88 for TR = 1.26, 1.45 and 1.84.

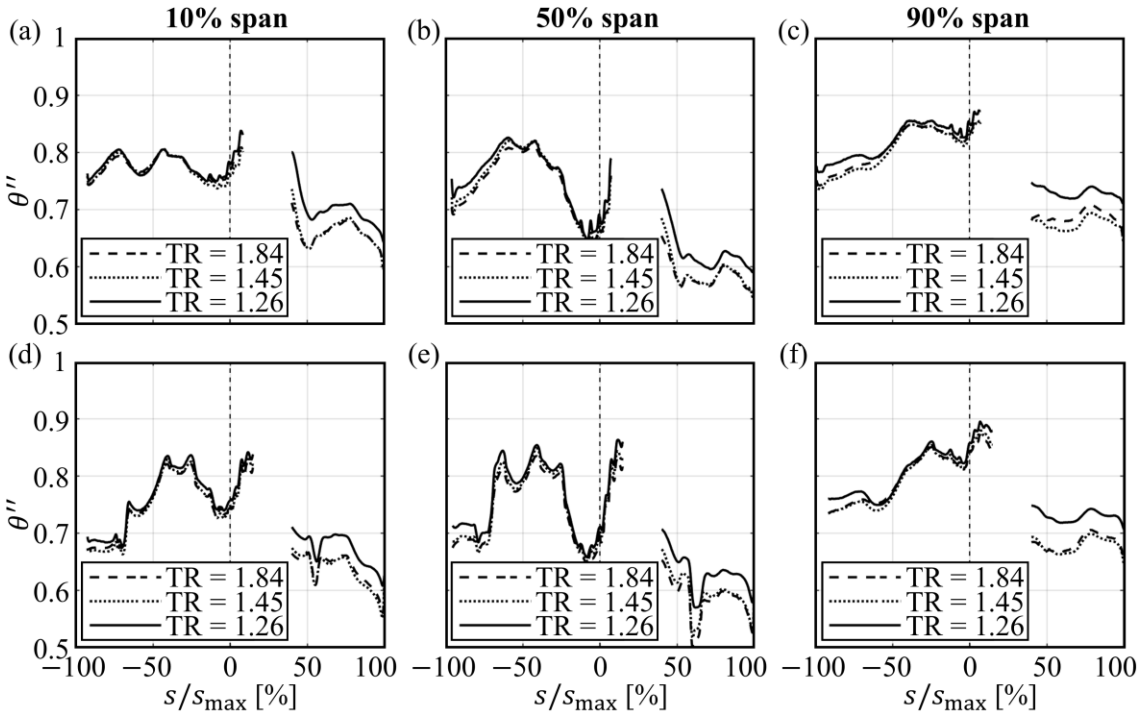

Figure 88: Streamwise distributions of overall cooling effectiveness at 10%, 50%, and 90% span for (a)–(c) leading vane; and (d)–(f) trailing vane.

The data in the figure have been averaged over the time period corresponding to the period in which the mainstream and coolant control systems were settled. The data have been corrected for both transient effects and off-target conditions of PR and CMPR. The distributions $\theta''(x)$, at three span fractions (S = 10%, 50%, and 90%), are shown in Figure 88. Data for the leading vane (LV) are shown in the top row (frames a–c, respectively) and data for the trailing vane (TV) are shown in the bottom row (frames d–f, respectively). At a given spanwise location the streamwise position, s, is normalised by the surface length, $s_{\max}$. The PS takes negative values, and the SS positive values.

The trends of overall cooling effectiveness with streamwise position are described first, with reference to experimental and simulated trends of adiabatic film effectiveness (η) and external heat transfer coefficient (h_{m}) for simplified HPT NGVs from the literature. The reason for

discussing streamwise trends of $\theta''(x)$ in terms of $\eta(x)$ and $h_m(x)$ is as follows. The low-order network model results of chapter 2 demonstrated that the trend for overall cooling effectiveness with streamwise position is primarily driven by the variation of film effectiveness of the mixing layer and external heat transfer coefficient with streamwise position. It was also demonstrated that distributions of local through-wall average wall thermal conductivity, internal heat transfer coefficient and internal cooling effectiveness are approximately constant and their contributions to the trends of $\theta''(x)$ with streamwise position are second order. The trend for film effectiveness of the mixing layer (η_{ML}) with streamwise position is of similar form to the trend for adiabatic film effectiveness (η) (see, for example, the CFD and low-order network model results of Naidu and Povey [17]) and so experimentally-measured flat-plate distributions of $\eta(x)$ from the literature (see, for example, the experimental results of Natsui et al. [54]) are referred to when discussing the trends for $\eta_{ML}(x)$. For experimentally-measured representative distributions of external heat transfer coefficient (h_m) with streamwise position for HPGNVs, see—for example—the experimental results of Zhang and Glezer [55].

Consider first the results for the PS ($s/s_{max} < 0\%$) of the LV and the TV. Pressure surface distributions of $\theta''(x)$ at 10%, 50% and 90% were broadly similar for both vanes. There is a local minimum in overall cooling effectiveness in the vicinity of the LE ($s/s_{max} \cong 0$); here, the external heat transfer coefficient is very high because the boundary layer is extremely thin. As one moves from the LE to the TE, it is observed that overall cooling effectiveness increases to a maximum value (which is positioned within the streamwise region $-0.43 \leq s/s_{max} \leq -0.24$, where the exact location depends on the particular span fraction) and decreases as one moves beyond this point. There are two primary factors driving this trend. Firstly, external heat transfer coefficient initially decreases—which acts to increase $\theta''(x)$—with streamwise position, as the boundary layer thickens. There is a point at which $h_m(x)$ takes a minimum value, beyond which it increases—which acts to reduce $\theta''(x)$—with streamwise position, due to an increase in external Reynolds number, $Re_m(x)$, as the flow accelerates through the vane passage. Secondly, film effectiveness

of the mixing layer initially increases—which acts to increase $\theta''(x)$—with streamwise position, due to superposition of cooling films. There is a point at which $\eta_{\mathrm{ML}}(x)$ takes a maximum value, beyond which it decreases with streamwise position, due to entrainment of hot gas in the mixing layer. There are local flow disturbances in the vicinity of cooling holes, which result in local maxima and minima in the overall cooling effectiveness distributions. Looking at the results for 10% and 50% span for the PS of the TV (Figure 88 d–e, respectively), it is observed that there is a distinct local minimum in $\theta''(x)$ distributed in the approximate streamwise region $-80\% \leq s/s_{\max} \leq -70\%$ (the exact position of the minimum depends on the particular span fraction). This is the result of a local flow disturbance caused by the presence of the calibration patch. The mean surface-average effectiveness (across all data) was 0.78 for the LV and 0.77 for the TV.

Now consider the results for the SS ($s/s_{\max} > 0\%$) of the LV and the TV. Suction surface distributions of $\theta''(x)$ at 10%, 50% and 90% were broadly similar for both vanes. Firstly, there is a sharp increase in overall cooling effectiveness due to an increase in film effectiveness of the mixing layer in the showerhead region (high density of film-cooling rows) and a reduction in external heat transfer coefficient as the boundary layer thickens. The white space in the regions $8\% \leq s/s_{\max} \leq 40\%$ (LV) and $15\% \leq s/s_{\max} \leq 40\%$ (TV) corresponds to the section of the SS that could not be observed by the downstream IR camera (view of this region is blocked by the adjacent vane). One can, however, infer that there is a sudden reduction in overall cooling effectiveness in the blank region, which is caused by an increase in $h_{\mathrm{m}}(x)$ due to an increase in $\mathrm{Re}_{\mathrm{m}}(x)$, which is caused by rapid acceleration of the external flow in this region (see, for example, the experimental results for Mach number presented in Zhang and Glezer [55]). As one moves from $s/s_{\max} = 40\%$ to the TE there is a reduction in $\theta''(x)$, which is driven by a reduction in $\eta_{\mathrm{ML}}(x)$ caused by entrainment of hot gas in the mixing layer, whilst there is a negative contribution caused by a reduction in $h_{\mathrm{m}}(x)$ as the flow—slightly—decelerates in this region. Looking at the results for 10% and 50% span for the SS of the TV (Figure 88 d–e, respectively), it is observed that there

is a distinct local minimum in $\theta''(x)$ distributed in the approximate streamwise region $50\% \leq s/s_{max} \leq 70\%$ (the exact position of the minimum depends on the particular span fraction). This is the result of a local flow disturbance caused by the presence of the in-situ calibration assembly. The mean surface-average value of overall cooling effectiveness for the late suction surface is 0.64 for the LV and 0.65 for the TV.

Now consider the trend with TR. For three very different temperature ratios (TR = 1.26, 1.45 and 1.84) the data are extremely similar for the PS, showing low sensitivity of this result to TR for this surface, whilst there is a more significant spread of data for the SS, showing higher sensitivity of this result to TR for this surface. This result is analysed in much more detail later in section 4.6.2, where a significantly larger data set is considered and results are discussed in the context of experimental uncertainty.

4.6.2 Surface-averaged experimental results

Experimental measurements of surface-averaged overall cooling effectiveness as a function of TR are presented in Figure 89.

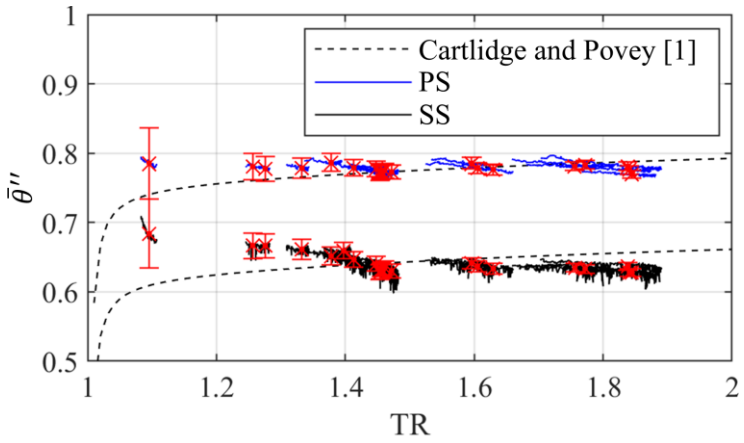

Figure 89: Corrected ($\bar{\theta}''_{PS}$ and $\bar{\theta}''_{SS}$) surface-averaged overall cooling effectiveness.

Data are presented for the PS and SS of the LV. Data corrected for both transient effects and off-target conditions of PR and CMPR ($\bar{\theta}''_{PS}$ and $\bar{\theta}''_{SS}$) are both presented. Error bars, which were derived from uncertainty limits evaluated using the method of chapter 3 and the data for Surface 1 (see Figure 59), but with U_T = 1.1 K for all temperature measurements (so-called special limits

of error for thermocouples; when IR temperatures are calibrated using Calibration Method 2, uncertainty in these measurements is dominated by uncertainty in the temperature measurements (via thermocouple) at the location of the calibration patch), are also presented. For best-fitting, the low-order network model of chapter 2 (system 1 in chapter 2) is used. In order to use these trends as best-fit curves for the experimental data, offsets are applied (uniformly over all temperature ratios) to the low-order-model-predicted $\bar{\theta}$ values (Figure 36 in chapter 2). The offsets are calculated by minimising the RMS deviation of the time-averaged experimental $\bar{\theta}$ values (for the 20 runs with TR in the range TR > 1.1) from the offset low-order network model trends. This process is repeated for both the PS and SS. When performing this RMS minimisation, the run with time-averaged temperature ratio of TR = 1.09 is omitted, as the experimental uncertainty in these data points explode, such that they could have a detrimental impact on the quality of the best fits. It is noted that the offset low-order network model predictions of chapter 2 are crude approximations to the true underlying trends of $\bar{\theta}$ with TR for the HPT NGV geometry considered in chapter 4. It is believed that the network model of chapter 2 accurately captures the physics relevant to changes in $\bar{\theta}$ with TR and that the low-order-model trend (Figure 36 in chapter 2) is sufficient for applying crude best fits to the experimental data in chapter 4. It is recommended that this analysis is improved in future studies by performing simulations for the real-engine HPT NGV geometry considered here. Simulations can be performed with a proprietary in-house conjugate heat-transfer tool. The steps for this process are outlined in section 4.6.3. Best fit curves are presented in Figure 89 (marked as Cartlidge and Povey [1]).

In all, there are 21 experimental runs covering the TR range $1.08 \leq \text{TR} \leq 1.89$. The time-series of data that has been selected corresponds to the time period in which the mainstream and coolant control systems were settled. Over the entire data series of 21 runs, the time-averaged corrections for transient effects for the PS and SS were $\Delta\bar{\theta} = -5.0 \times 10^{-4}$ and -9.4×10^{-4}, respectively, and the time-averaged corrections for off-target conditions of PR and CMPR were $\Delta\bar{\theta} = +7.8 \times 10^{-5}$ and $+5.3 \times 10^{-5}$. The corresponding temperature-ratio-averaged corrections were $\Delta\bar{\theta} = -0.0011$

and -0.0018 (transient effects) and $\Delta\bar{\theta} = -4.6 \times 10^{-4}$ and -4.7×10^{-4} (off-target conditions of PR and CMPR). These corrections are relatively small.

Consider the trend with TR of the corrected overall cooling effectiveness ($\bar{\theta}''_{\mathrm{PS}}$ and $\bar{\theta}''_{\mathrm{SS}}$). Taking the entire data set (all runs) it is observed that overall cooling effectiveness is approximately constant with temperature ratio for the PS. For the SS, the trend is approximately flat in the range TR > 1.4 and—gradually—increasing with reducing TR in the range TR ≤ 1.4. This is the primary result of this chapter and is discussed in detail in section 4.6.3. Considering runs individually, it is observed that there is a small decrease in corrected overall cooling effectiveness with increasing TR; that is, a somewhat contradictory trend to the underlying trend for all runs.

4.6.3 Comparison of experimental results and low-order network model results of chapters 2 and 3

The trend of overall cooling effectiveness with TR is now considered: the key result of this chapter. The general trend for overall cooling effectiveness for the PS is flat. The general trend for the SS is approximately flat in the range TR > 1.4 and—gradually—increasing with reducing TR in the range TR ≤ 1.4. In order to gain physical insight, the results are compared to the modelling work of chapters 2 and 3. In chapter 2, a modelling exercise was performed for a system of the same general type. In the system of chapter 2, the inner wall was treated as adiabatic, so only the outer wall was considered. In chapter 3, a modelling exercise—with experimental validation—was performed for a heavily-cooled flat-plate test article. In the system of chapter 3, the inner wall was treated as diabatic, so both the inner and outer walls were considered. Additionally, the system considered in chapter 3 included conducting webs between inner and outer wall. The presence of these webs was shown to significantly reduce the magnitude of change in overall cooling effectiveness with TR. The experimental results may be compared to Surface 1 of the system studied in chapter 3 (Figure 65 in chapter 3). The experimentally-measured trends of overall cooling effectiveness with TR are now explored in more detail.

Reference overall cooling effectiveness values $\overline{\theta}_{PS,ref}$ and $\overline{\theta}_{SS,ref}$ are defined as the surface-averaged values of the offset (system 1) low-order network model of chapter 2 at a temperature ratio of TR = 2.0. The reference surface-averaged effectiveness values were $\overline{\theta}_{PS,ref} = 0.79$ and $\overline{\theta}_{SS,ref} = 0.66$. Differences from the reference points, i.e. values that represent the corrections from reference conditions of temperature ratio, are presented in Figure 90.

Data for the PS are presented in the top row (frame a) and data for the SS are presented in the bottom row (frame b). 95% confidence limits for the experimental data are also shown. For completeness the calibrated low-order-model predictions are included for Surface 1 of the system considered in chapter 3 (marked as Cartlidge et al. [2]). This represents a system with a high degree of coupling between external and internal walls. For the real-engine HPT NGV geometry of chapter 4, there is no wall coupling for the PS and there is a small amount of coupling for the late SS. Given the limited extent of wall coupling for the HPT NGV geometry considered here, it is unclear to what extent the comparison of the experimental results with the calibrated low-order-model predictions of the system considered in chapter 3 is relevant, however the results of chapter 3 are included as an extra point of comparison. Differences for both the experimental data and low-order-model results are taken from the same reference temperature ratio i.e. TR = 2.0. The reference overall cooling effectiveness value for the calibrated network model of chapter 3 is and $\overline{\theta} = 0.51$, respectively. It is noted that the reference effectiveness value for the calibrated low-order network model of chapter 3 is very different to the corresponding values for the experimental data, however it was demonstrated in chapter 2 that the trend for $\Delta\overline{\theta}$ with TR is insensitive to the mean effectiveness at the reference TR. Good agreement is therefore expected between the experimental and both low-order-model results for the trend of $\Delta\overline{\theta}$ with TR i.e. the rig-to-engine correction.

Looking at Figure 90a, the following observations are made: the global trend for overall cooling effectiveness for the PS is flat with TR; the trends for individual runs are—slightly—increasing with reducing TR and they collapse poorly onto a single trend; and errors increase in

magnitude with reducing TR. Now looking at Figure 90b the following points are noted: the global trend for overall cooling effectiveness for the SS is flat with TR in the range TR > 1.4; the global trend is—slightly—increasing and accelerating with reducing TR in the range TR ≤ 1.4; the trends for individual runs are relatively flat and there is reasonable collapse onto a single trend.

The general trends of Figure 90 can be regarded as the key result of this chapter. Considering the results for the PS, the experimental data is not confirmatory in itself however—given the difficulties in accurately quantifying experimental uncertainty—the results are considered to be broadly in agreement with the low-order-model predictions, in that there is no significant deviation between the trends. The effects of uncertainties in grey-body parameters (ε and ε_{CP}) and IR window transmittance (τ), and additional uncertainties inherent in Calibration Method 2 e.g. errors associated with assuming a uniform q^* correction, have not been considered. It is therefore likely that the error bars presented in Figure 90 underestimate the true uncertainties in the measurements. Consequently, it is expected that all data points for the PS would match the low-order-model predictions within the margin of error, were these additional effects to be included in the uncertainty analysis. Considering the results of the SS and following the same logic, the results are considered to be largely in agreement with the low-order-model predictions in the range TR > 1.4, however the deviation of the results in the range TR ≤ 1.4 is an unresolved question. It is believed that the origin for this discrepancy is rooted in inadequacies in the in-situ calibration technique (Calibration Method 2) for the SS in the low-TR range. Input from the community, regarding refinement of the in-situ IR calibration techniques presented in this chapter, would be welcomed.

Considering trends for individual runs, the data for the PS are marginally increasing with reducing TR, as discussed above. This phenomenon is unresolved however it is believed to arise due to inadequacies in the transient-correction methodology. The reader is referred to chapter 3 for detailed discussion of this effect for a similar experimental data set (i.e. data expressed in the form $\bar{\theta} = f(\mathrm{TR})$ for a conjugate system). Further experimental and theoretical studies of this

unresolved aspect of the data, and further discussion of robust transient-correction methodology in the community, would be welcomed. Corrections for transient effects and off-target conditions have been performed with great care and a large set of data has been presented in order to expose this phenomenon.

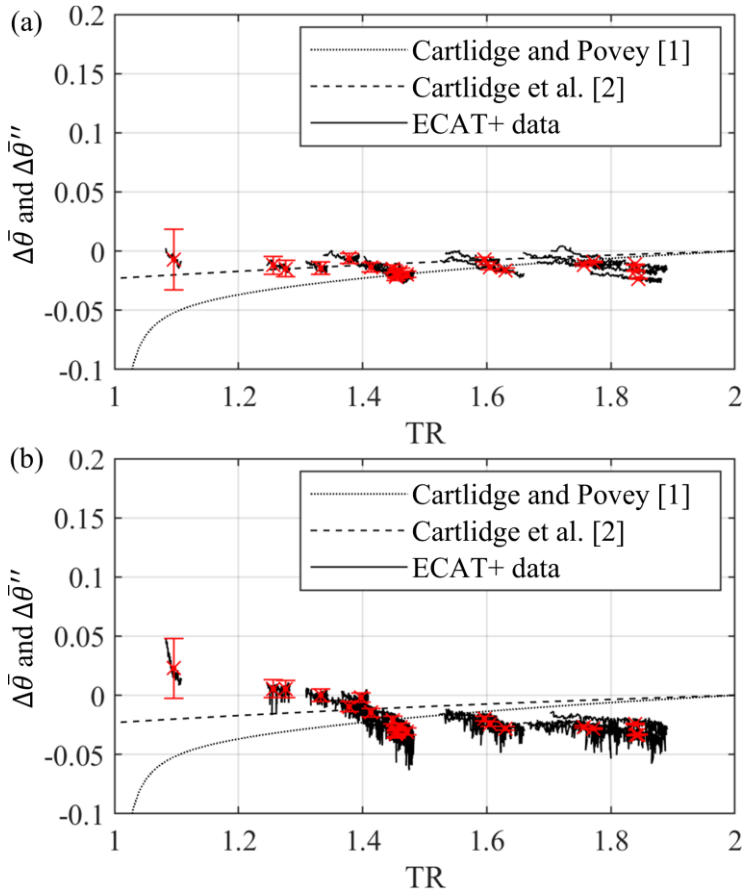

Figure 90: Magnitude of the change in surface-averaged overall cooling effectiveness as a function of TR for the leading vane for (a) PS; and (b) SS.

The corrected experimental results are compared to the low-order-model predictions of chapters 2 and 3 in Figure 90. The experimental data for the PS are in broad agreement with both network models (general trends are relatively flat), although just three data points match the low-order-model trends of chapter 2 (marked as Cartlidge and Povey [1] in Figure 90) within the margin of error. The RMS (integrated over the TR domain) difference in $\Delta\bar{\theta}$ (across all data) between experimental data and low-order-model predictions of chapters 2 and 3 was 0.016 and 0.012, respectively. As percentages of the mean absolute corrections predicted by the network

models throughout the range $1.08 \leq \mathrm{TR} \leq 1.89$ (0.021 and 0.010, respectively), these values correspond to differences of 73.6% and 119%. The experimental data for the SS are in broad agreement with both network models in the range $\mathrm{TR} > 1.4$ whilst, in the range $\mathrm{TR} \leq 1.4$, the trends diverge. Only one data point matches the low-order-model predictions of chapter 2 within the margin of error and the RMS difference between experimental data and low-order-model predictions of chapters 2 and 3 was 0.028 and 0.028, respectively. As percentages of the mean absolute corrections predicted by the network models throughout the range $1.08 \leq \mathrm{TR} \leq 1.89$ (0.021 and 0.010, respectively), these values correspond to differences of 132% and 273%. The key points here are that the experimental results of chapter 4 do not directly confirm the theoretical results of chapter 2; and the discrepancy between the two is likely not accounted for entirely by consideration of the effects of through-wall conduction because the experimental data do not collapse perfectly with the calibrated low-order-model predictions of chapter 3. As discussed above, the general trends for the PS (for all TR) and the SS (for TR in the range $\mathrm{TR} > 1.4$) are considered to be broadly in agreement with the low-order-model trends (i.e. relatively flat).

Consideration of the experimental results—and corresponding discrepancies for the SS data in the low-TR range with the low-order-model results—leads to the following question: Are the trends driven primarily by underlying physical mechanisms or errors in experimental methodology? In order to gain physical insight into the experimental data of chapter 4—and to help answer these questions—it is recommended that best-fitting to the experimental data is performed using a network model with geometry matching the HPT NGV cooling schemes used in the experiments and boundary conditions matching those of the experiments. An example procedure for performing the required simulations is proposed shortly. See chapter 3 for details of an example procedure for calibrating a low-order network model against experimental data of similar form i.e. data of the form $\overline{\theta} = f(\mathrm{TR})$.

It was demonstrated in chapter 3 that the effect of coupling (via conduction) between external and internal surfaces is to reduce the magnitude of the change in overall cooling effectiveness

with TR i.e. the rig-to-engine correction. Consequently, careful consideration must be given to the degree of coupling between external and internal walls when scaling from conventional laboratory to engine conditions. In light of this, it is unclear to what extent direct comparison between the experimental data of chapter 4 and the low-order-model predictions of chapters 2 and 3 is appropriate, until the degree of coupling has been assessed and quantified for the present cooling system. Simple observations of design drawings for the parts used in the study indicate that there is no coupling of external and internal walls for the PS and early SS, whereas there is a small degree of coupling for the late SS. This indicates that the PS trends are not affected by coupling but the SS results are affected to some degree. To summarise: There is significant variation in the magnitude of the rig-to-engine correction across four independent sources of information in the range $TR \leq 1.4$ i.e. the systems of chapters 2 and 3 (which were both representative of NGV cooling schemes) and the experimental data of chapter 4 for the PS and SS; and there is evidence that coupling between the external and internal walls significantly affects the rig-to-engine correction (see chapter 3). These observations lead to the conclusion that it is important to compare the experimental data set with an additional data set from simulations run with a bespoke network model for the NGV geometry considered in chapter 4 and identical boundary conditions to those of the experiments. This would provide a direct comparison point for the experimental data.

A procedure for performing the necessary simulations for providing a direct comparison point with the experimental data is now briefly outlined. Proprietary in-house conjugate heat-transfer tools for engine-design applications allow for simulations of real vane geometry subject to input cooling system BCs and input distributions of local surface BCs. The solver will then evaluate for the resulting overall cooling effectiveness distributions.

A proposal procedure for performing the required simulations with a bespoke conjugate-heat-transfer tool is summarised below:

i) Run bespoke network model at engine conditions i.e. reference conditions of temperature ratio (TR = 2.0) and high absolute temperature ($T_{01h} \cong 1750$ K) with combustion products for the mainstream gas. Obtain distributions of overall cooling effectiveness ($\theta(x,y)$) and corresponding local surface BCs ($\eta_{ML}(x,y)$, $\bar{k}_w(x,y)$, $h_m(x,y)$, $h_c(x,y)$ and $\lambda(x,y)$).

ii) Scale local surface BCs $\eta_{ML}(x,y)$ and $h_m(x,y)$ to low absolute temperature ($T_{01h} = 600$ K), with air for the mainstream gas, using simple scaling rules derived from a simpler network model (for example, the low-order network model of chapter 2). An example of a simple scaling procedure would be to scale the 2D full-surface distributions of local surface BCs (obtained in step 1), uniformly over the entire surface, by an amount equal to the change in each *surface-averaged* BC as one moves from high absolute temperature with combustion products for the mainstream gas (step 1) to low absolute temperature with air for the mainstream gas (step 2). Run network model at the new conditions. Obtain distributions of overall cooling effectiveness and corresponding local surface BCs.

iii) Scale local surface BCs from engine conditions of temperature ratio (TR = 2.0) to TRs in the range $1.0 < TR \leq 2.0$ using simple scaling rules derived from a simpler network model (for example, that of chapter 2). Run network model at TRs in the range $1.0 < TR \leq 2.0$ with the scaled local surface BCs. Obtain distributions of overall cooling effectiveness. Add locus of change in surface-averaged overall cooling effectiveness ($\Delta\bar{\theta}$) versus TR to Figure 90.

Some of the main results of chapter 2 are now briefly rehearsed in order to gain physical insight into the trends for the low-order-model predictions of chapters 2 and 3 (i.e. the expected trends for the experimental data). The key conclusion of chapter 2 was that overall cooling effectiveness decreases with reducing TR. To gain physical insight into results, results for the change in overall cooling effectiveness were decomposed into the isolated changes in θ caused by each individual local surface BC as TR is varied. It was demonstrated that a linear superposition of the individual change in θ caused by each local surface BC is approximately equal to the overall change in θ.

This showed that the chosen local surface BCs form a closed set and that a complete explanation for the change in θ with TR is provided by considering isolated changes in θ due to changes in each local surface BC. It was demonstrated in chapter 2 that a decrease in overall cooling effectiveness with reducing TR is caused primarily by reductions in η_{ML} and λ and an increase in h_m. There were second order contributions from changes in $\bar{k}_w$ and h_c.

The primary physical mechanisms driving changes in each local surface BC, as reported in chapter 2, are briefly rehearsed below (the reader is referred to chapter 2 for a comprehensive discussion of all physical mechanisms driving changes in each local surface BC):

i) *Effectiveness of the mixing layer* (η_{ML}): As one moves from reference conditions of TR (TR = 2.0) to lower-than-reference TR, $\eta_{ML}(x)$ decreases, mainly due to an increase in the ratio of entrained hot-gas to coolant mass flow rate.

ii) *Local through-wall average thermal conductivity* ($\bar{k}_w$): As one moves from reference conditions of TR to lower-than-reference TR, $\bar{k}_w(x)$ decreases, which is driven by a reduction in $T_w(x)$. The effect of decreasing $\bar{k}_w(x)$ is to increase Biot number, which drives a reduction in the cooling of the external surface, which results in the decoupling of the external and internal surfaces.

iii) *External heat transfer coefficient* (h_m): As one moves from the reference TR to lower-than-reference TR, external heat transfer coefficient, $h_m(x)$, increases. This effect is caused by an increase in external Nusselt number, $Nu_m(x)$, which is driven by an increase in external Reynolds number, $Re_m(x)$, caused by an increase in density of the mixing layer, $\rho_m(x)$. This is the result of lower absolute mainstream temperature, which acts to lower the average absolute temperature of the mixing layer.

iv) *Internal heat transfer coefficient* (h_c): As one moves from the reference TR to lower-than-reference TR, internal heat transfer coefficient, $h_c(x)$, increases due to an increase in coolant density, $\rho_c(x)$, as TR is reduced. This is because of lower absolute heat

transfer rate from internal wall to coolant, which leads to lower average absolute coolant temperature.

v) *Internal cooling effectiveness* (λ): As one moves from the reference TR to lower-than-reference TR, the internal cooling effectiveness, $\lambda(x)$, decreases (coolant becomes non-dimensionally warmer). This effect is mostly definitional and is caused directly by changes in TR, combined with the definitions of $\lambda(x)$ and $\theta(x)$ and distributions of recovery ratios $c_c(x)$ and $c_h(x)$.

Similar results were obtained in chapter 3, in terms of both the trend in $\Delta\bar{\theta}$ with TR and the physical mechanisms driving changes in $\bar{\theta}$ with TR. The magnitude of $\Delta\bar{\theta}$ was significantly smaller due to the presence of webs connecting the external and internal walls, which act to couple the two surfaces via conduction. It is believed that these are the physical mechanisms driving changes in overall cooling effectiveness in the ECAT+ experiments presented in this chapter (this was observed for three very different cooling systems in chapter 2 and, independently, for a fourth cooling system in chapter 3), however it is noted that the present experimental data set does not directly confirm this to be the case. Extensions to the current analysis, that will help to verify the theoretical work of chapter 2, have been suggested.

The low-order network model of chapter 2 was designed purposely to complement the experiments of chapter 4. The cooling systems considered in the low-order network model were designed specifically to both represent conventional vane cooling systems and cover an extreme range of constraints on the internal coolant flow, thus demonstrating the insensitivity of the general result to the internal cooling architecture. The physics is sophisticated and it is believed that the network model can be used to accurately predict changes in overall cooling effectiveness with varying TR for real-engine HPT NGV cooling systems. The experiments of chapter 4 were performed with well-controlled boundary conditions and in-situ calibrations have been carefully performed. Robust corrections for transient effects and off-target PR and CMPR have also been implemented. It is a surprise that the general trends of this chapter do not directly confirm the

theoretical trends presented in chapter 2. The results of the experiments and the two low-order network models are however considered to be broadly in agreement (general trends for overall cooling effectiveness with TR are relatively flat)—particularly in light of the difficulties associated with accurately quantifying all errors in the experimental processing chain. Further experimental, computational and theoretical studies on this topic in the community would be welcomed and further corroborating studies are encouraged, particularly those with well-established boundary conditions.

4.7 Sensitivity of results to grey-body parameters

In this section, the sensitivity of the results to grey-body parameters, i.e. emissivities of the vane surface and the calibration patch, and transmittance of the IR window, is considered. In order to do this, modified values of each parameter in the ranges $0.90 \leq \varepsilon' \leq 1.0$, $0.90 \leq \varepsilon'_{CP} \leq 1.00$ and $0.85 \leq \tau' \leq 0.95$ are considered. These ranges are arbitrary and represent extreme (i.e. unrealistic) deviation in each parameter from their nominal values. Changes in each parameter—in isolation of changes in the other two parameters are considered. That is, each grey-body parameter is varied individually, whilst keeping the other two terms fixed. The experimental results are re-processed with the modified grey-body parameters. Trends of changes in time-averaged surface-averaged uncorrected overall cooling effectiveness from reference conditions of temperature ratio (TR = 2.0) are presented in Figure 91–Figure 93.

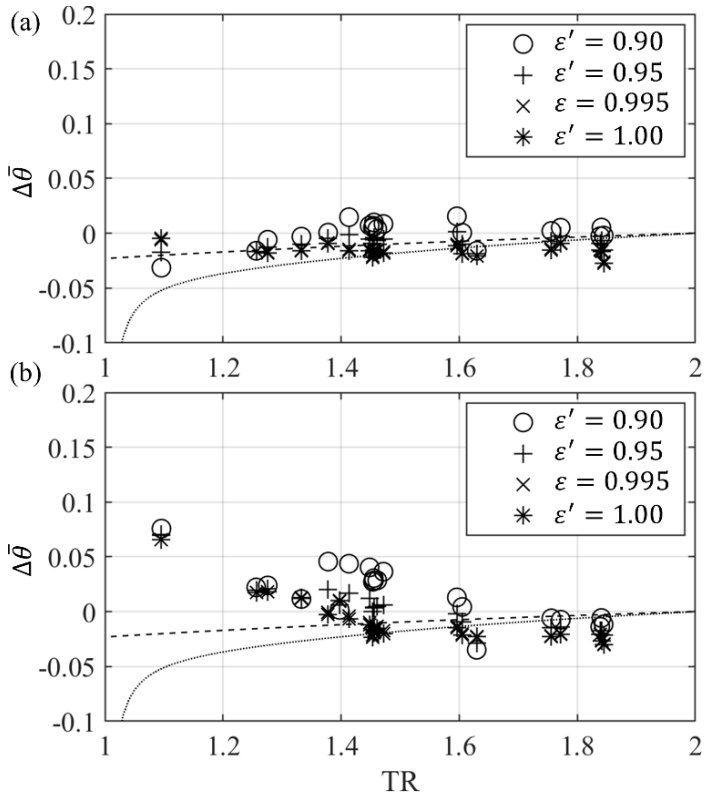

Figure 91: Sensitivity of the change in surface-averaged overall cooling effectiveness with TR to the emissivity of the vane surface for (a) PS; and (b) SS.

For each trend, the reference effectiveness is taken to be the surface-averaged effectiveness values for the low-order network model of chapter 2 (system 1 in chapter 2), offset by values that minimise the RMS deviation between network model and experimental trends for the baseline case (i.e. $\varepsilon = 0.995$, $\varepsilon_{CP} = 0.97$ and $\tau = 0.91$), as discussed in section 4.6.2. The reference surface-averaged effectiveness values were $\overline{\theta}''_{PS,ref} = 0.79$ and $\overline{\theta}''_{SS,ref} = 0.66$. For each figure, data for the PS (leading vane) are presented in the top row (frame a) and data for the SS (leading vane) are presented in the bottom row (frame b). Uncertainties in ε and τ have been estimated in the literature (see, for example, Michaud et al. [30]) to be around ±1% and ±3%, respectively (i.e. they are very low). The purpose of this section is to gauge the relative sensitivity of the results to each parameter and to understand if the experimental results and low-order-model predictions of chapters 2 and 3 could be reconciled entirely by adjusting one of these parameters. If this were the case, this could be indicative of errors in the quoted grey-body parameters or flawed

assumptions in chapter 4 (for example, assumptions of uniform emissivity with surface position and viewing angle).

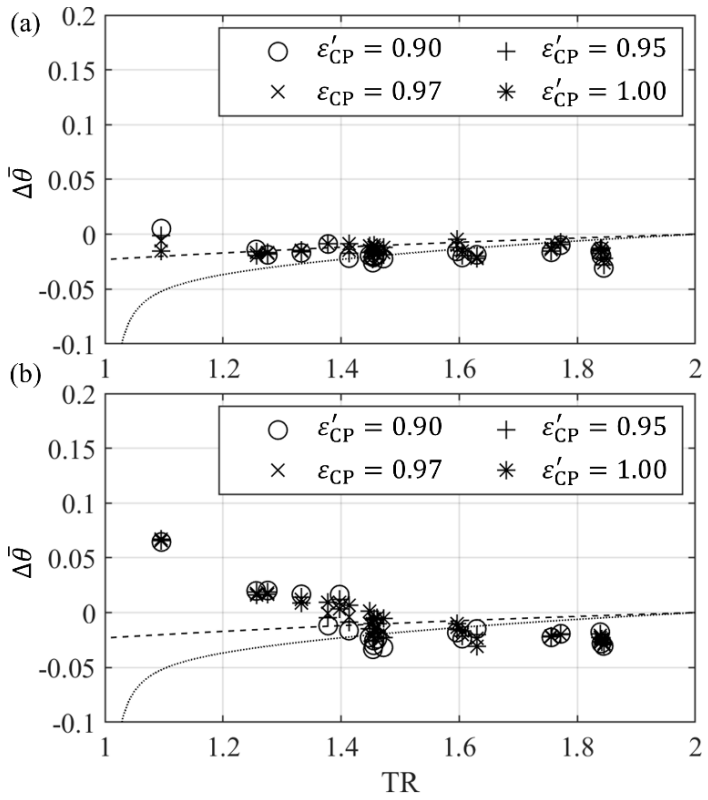

Figure 92: Sensitivity of the change in surface-averaged overall cooling effectiveness with TR to the emissivity of the calibration patch for (a) PS; and (b) SS.

Looking first at Figure 91 it is observed that the data are fairly sensitive to changes in ε'. The mean (across TR conditions) of the local RMS difference between trends (for the three trends corresponding to $\varepsilon' = 0.90$, 0.95 and 1.0) normalised by the local nominal (i.e. the case with $\varepsilon = 0.995$) value of $\Delta\bar{\theta}$ was 1.1 and 1.7 for the PS and SS, respectively (i.e. 110% and 170% of the local values). It is concluded that the discrepancy between the experimental and low-order-model data is likely not reconciled exclusively by changing the value of ε.

Looking now at Figure 92 it is observed that the data are somewhat sensitive to changes in ε'_{CP}, but less sensitive than they are to changes in ε'. The mean (across TR conditions) of the local RMS difference between trends (for the three trends corresponding to $\varepsilon'_{CP} = 0.90$, 0.95 and 1.0) normalised by the local nominal (i.e. the case with $\varepsilon = 0.97$) value of $\Delta\bar{\theta}$ was 0.65 and 1.1 for the

PS and SS, respectively (i.e. 65% and 110% of the local values). It is concluded that the discrepancy between the experimental and low-order-model data is likely not reconciled exclusively by changing the value of ε_{CP}.

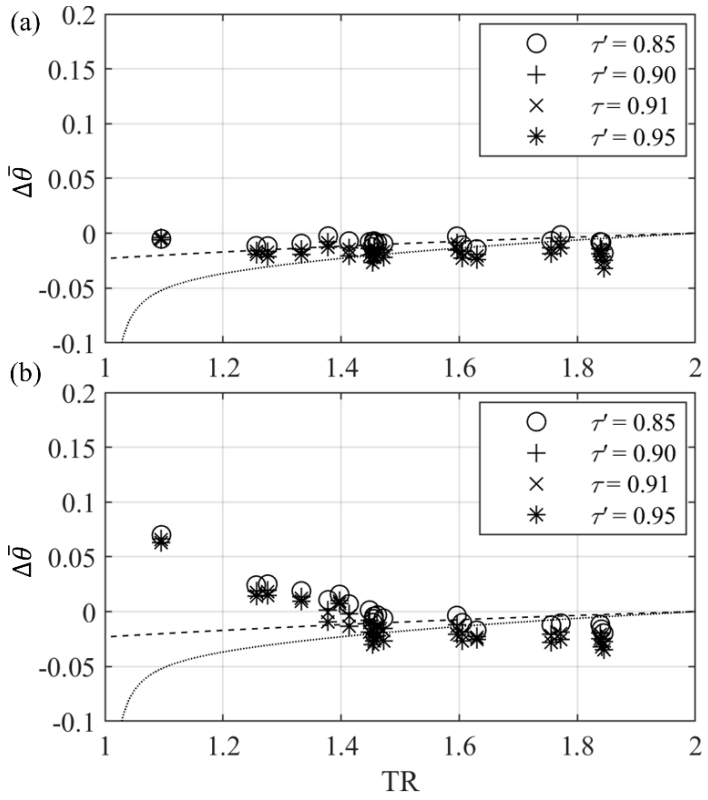

Figure 93: Sensitivity of the change in surface-averaged overall cooling effectiveness with TR to the transmittance of the IR window for (a) PS; and (b) SS.

Looking finally at Figure 93, it is observed that the data are relatively insensitive to changes in τ'. The mean (across TR conditions) of the local RMS difference between trends (for the three trends corresponding to $\tau = 0.85$, 0.90 and 0.95) normalised by the local nominal (i.e. the case with $\tau = 0.91$) value of $\Delta\bar{\theta}$ was 0.31 and 0.33 for the PS and SS, respectively (i.e. 31% and 33% of the local values). It is concluded that the discrepancy between the experimental and low-order-model data is likely not reconciled exclusively by changing the value of τ.

In summary, the experimental results of chapter 4 are fairly sensitive to the grey-body parameters. The results are most sensitive to ε, followed (in order of decreasing sensitivity) by ε_{CP} and τ. It is not believed that the difference between experimental and low-order-model data is

explained by inaccuracies in the values of grey-body parameters and window transmittance used in this chapter. It is, however, recommended that a directional in-house emissivity calibration is performed for TBC and black paint to sanity check the emissivity values used in this chapter and the assumptions of uniform emissivity with surface position and viewing angle.

4.8 Impact of in-situ calibration for IR measurements on final results

In this section the final overall cooling effectiveness results (see Figure 90) based on IR temperature measurements using Calibration Methods 1, 3 and 4 are considered. The purpose of an in-situ calibration is to correct the black-body-equivalent IR temperature measurements for the effects of stray radiation from the surroundings; grey-body phenomena associated with the target surface; and a non-transparent IR window.

4.8.1 Calibration Method 1

This technique uses the black-body calibration only i.e. raw values converted to black-body-equivalent temperatures using the conversion curve supplied by the manufacturer. This was the technique used in chapter 3. For each experimental run and for both the PS and SS IR temperature measurements are calibrated with Calibration Method 1. The corrections for transient effects and for off-target conditions of PR and CMPR are then applied as described in previous sections. This corrected data is referred to as $\theta^{*''}(x,y,t)$.

Transient overall cooling effectiveness characteristics for both the PS and SS (same run as discussed in the context of Figure 81) are shown in Figure 94. Looking at the figure it is observed that the trends are highly unsteady and significantly less steady than the corresponding trends for Calibration Method 2. The effect of moving from Calibration Method 2 to Calibration Method 1 is to reduce steadiness by a factor of 3.1 and 6.0 for the PS and the SS, respectively. The overall cooling effectiveness characteristics are expected to be relatively steady because both the existing ECAT facility and the high-temperature upgrade (ECAT+) were carefully conditioned so as to achieve quasi-steady overall cooling effectiveness trends throughout a run. This is supported by

the experimental results for ECAT presented in Kirollos et al. [9] and the low-order-transient-model-predictions for ECAT+ presented in Messenger and Povey [53].

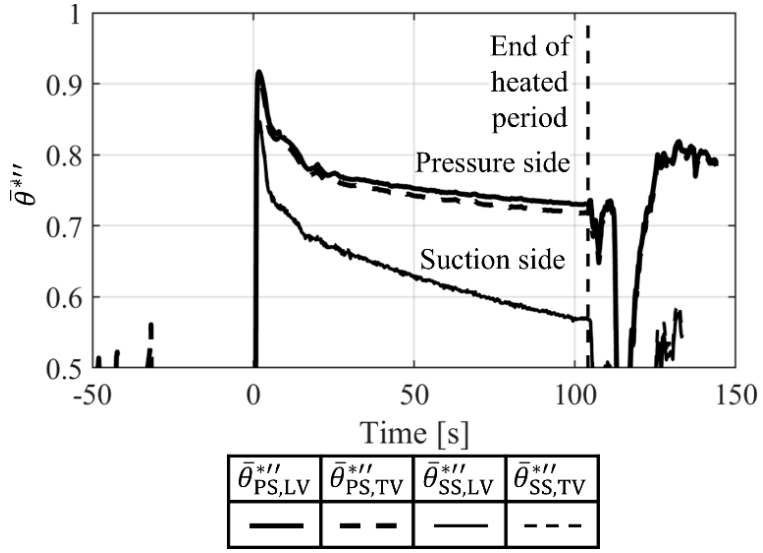

Figure 94: Transient overall cooling effectiveness characteristics for LV and TV, when IR temperature measurements are calibrated with Calibration Method 1.

It is therefore believed that Calibration Method 2 provides more accurate measurements of the true underlying overall cooling effectiveness and discussion is focused on results based on IR temperature measurements using this method in this chapter.

The final characteristics for $\theta^{*\prime\prime}$ (LV only) are shown in Figure 95, where the change in $\theta^{*\prime\prime}$ from reference conditions of TR = 2.0 (i.e. the equivalent of Figure 90, but for $\theta^{*\prime\prime}$) is plotted. For best-fitting, offsets are evaluated for the low-order-model trend of chapter 2 (system 1) that minimise the RMS deviation between experimental and low-order-model data (as discussed in section 4.6.2, but for $\theta^{*\prime\prime}$). Reference effectiveness values are taken to be the low-order-model predictions at TR = 2.0. The reference surface-averaged effectiveness values were $\bar{\theta}''_{\mathrm{PS,ref}} = 0.78$ and $\bar{\theta}''_{\mathrm{SS,ref}} = 0.64$. Data for the PS are shown in the top row (frame a) and data for the SS are shown in the bottom row (frame b). Error bars are also included for the time-series average values of $\theta^{*\prime\prime}$. In order to evaluate the error bars, the uncertainty analysis outlined earlier is repeated but, for surface temperatures, the quoted bias uncertainty for the IR camera is taken as $U_T = 2.0$ K.

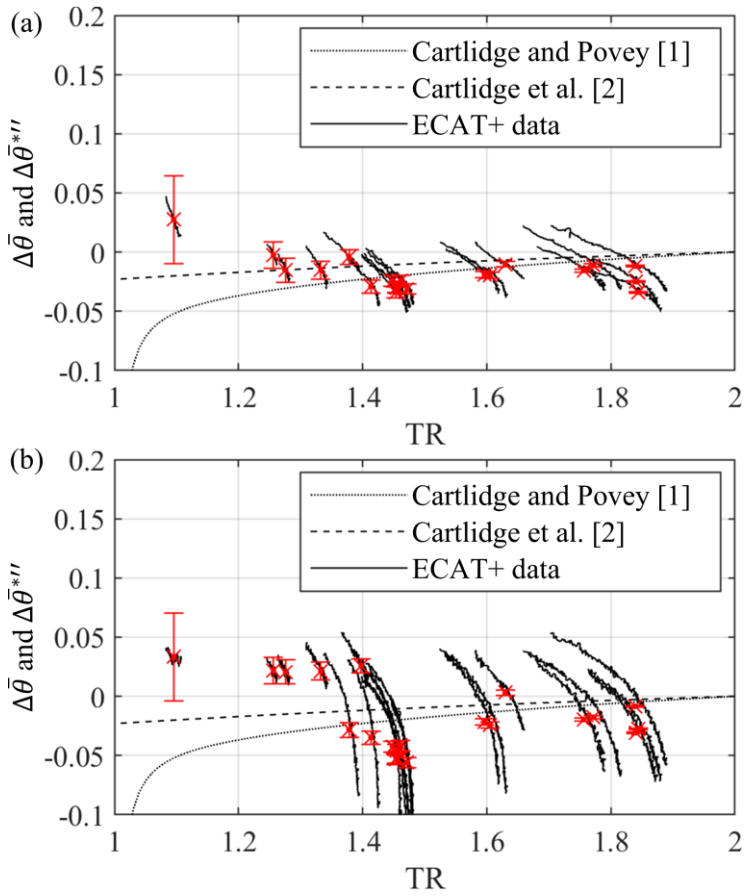

Figure 95 Magnitude of the change in surface-averaged overall cooling effectiveness as a function of TR for the leading vane, when IR temperature measurements are calibrated with Calibration Method 1, for (a) PS; and (b) SS.

Looking at the Figure 95a, it is observed that the general trend for the PS is flat and the trends for individual runs are highly unsteady; increase sharply with reducing TR; and do not collapse on to a single trend. As with Calibration Method 2, errors increase with reducing TR. Looking at Figure 95b, it is observed that the general trend is flat—with average value $\Delta\bar{\theta} \cong 0$—in the range TR > 1.4 and flat—with average value $\Delta\bar{\theta} \cong 0.05$ in the range TR ≤ 1.4. As was seen with the results of the PS, the individual-run trends are highly unsteady and do not collapse on to a single trend; and errors increase with reducing TR. It has been outlined why other calibration methods are preferred over Calibration Method 1.

4.8.2 Calibration Method 3

This technique uses an isothermal calibration patch mounted on the target surface to evaluate a correction offset, in real-time, between the black-body-equivalent temperature and the surface

temperature at the location of the calibration patch. This technique was used in chapter 3 and is based on similar techniques that have been used extensively in the literature (see, for example, [32–33], Bryant and Rutledge [16] and Michaud et al. [30]). Briefly, this correction offset is used as a correction to the black-body-equivalent IR temperature measured by the IR camera such that, at the location of the patch, the corrected IR temperature is matched to the measured (via thermocouple) copper-patch temperature. The simple assumption that the correction offset is uniform across the entire surface is made.

A correction offset is defined at the location of the calibration patch

$$\Delta T_{\mathrm{CP}}(t) = T_{\mathrm{S}}\left(x_{\mathrm{CP}},y_{\mathrm{CP}},t\right) - T_{\mathrm{bb}}\left(x_{\mathrm{CP}},y_{\mathrm{CP}},t\right) \tag{82}$$

where all symbols have been defined previously.

The *real-time-corrected* local surface temperature, $T_{\mathrm{S}}(x,y,t)$, is then defined by

$$T_{\mathrm{S}}(x,y,t) = T_{\mathrm{bb}}(x,y,t) + \Delta T_{\mathrm{CP}}(t) \tag{83}$$

Eq. (83) is substituted into Eq. (80) to evaluate the in-situ-calibrated overall cooling effectiveness, $\theta^{**}(x,y,t)$. The corrections for transient effects and for off-target conditions of PR and CMPR are then applied as described in previous sections. This corrected data is referred to as $\theta^{**\prime\prime}(x,y,t)$.

Correction offset time-series characteristics for each run are plotted in Figure 96 as a function of mainstream total temperature, $T_{01\mathrm{h}}$. Data for the PS are presented in the top row (frame a) and data for the SS are presented in the bottom row (frame b). Data is plotted for the time period in which the mainstream and coolant control systems were settled. ΔT_{CP} is expected to loosely correlate with $T_{01\mathrm{h}}$ (see, for example, the experimental results of chapter 3), however the results of chapter 4 do not collapse on to a single global trend with $T_{01\mathrm{h}}$, as they did in chapter 3. Looking at Figure 96, it is observed that the general trend for ΔT_{CP} for a particular run (for both the PS and the SS) is to move from a maximum (positive) value to a maximum (negative) value. The magnitude of the starting value is loosely correlated with $T_{01\mathrm{h}}$ for the PS and strongly correlated

with T_{01h} for the SS, whilst the magnitude of the end value is loosely correlated with T_{01h} (for both the PS and the SS). The final characteristics for $\theta^{**\prime\prime}$ (LV only) are shown in Figure 97, where the change in $\theta^{**\prime\prime}$ from reference conditions of TR = 2.0 (i.e. the equivalent of Figure 90, but for $\theta^{**\prime\prime}$) is plotted.

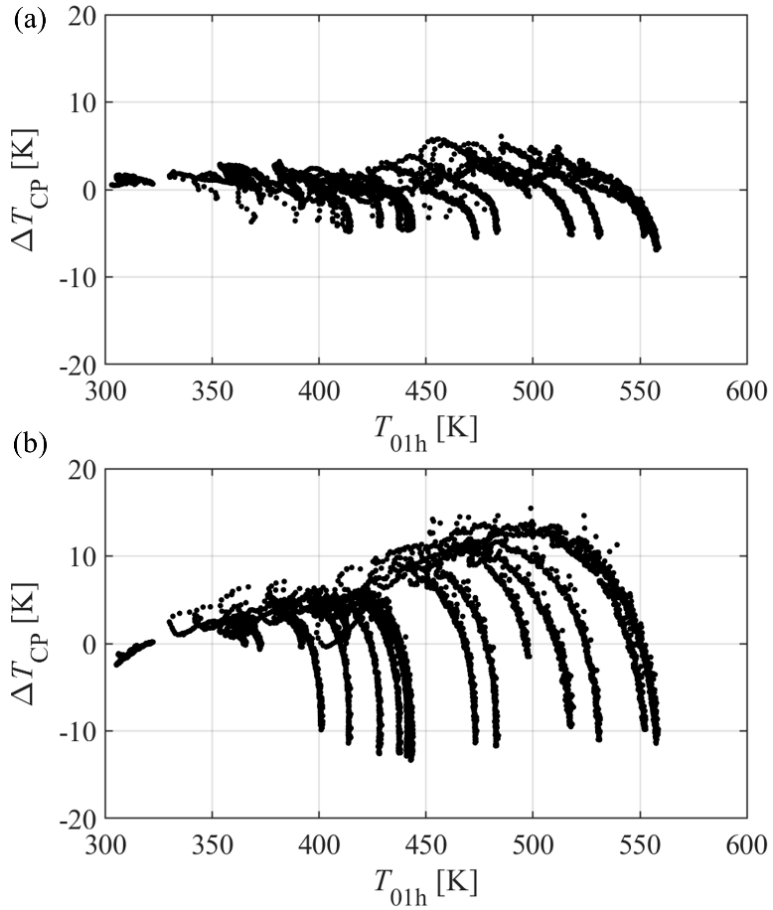

Figure 96: Correction offset as a function of T_{01h} for (a) PS; and (b) SS.

For best-fitting, offsets are evaluated for the low-order-model trend of chapter 2 (system 1) that minimise the RMS deviation between experimental and low-order-model data (as discussed in section 4.6.2, but for $\theta^{**\prime\prime}$). Reference effectiveness values are taken to be the low-order-model predictions at TR = 2.0. The reference surface-averaged effectiveness values were $\overline{\theta}''_{PS,ref} = 0.78$ and $\overline{\theta}''_{SS,ref} = 0.65$. Data for the PS are shown in the top row (frame a) and data for the SS are shown in the bottom row (frame b). Error bars are also included for the time-series average values

of $\theta^{**\prime\prime}$ (error bars are derived from the same data set used to derive error bars for results calibrated with Calibration Method 2).

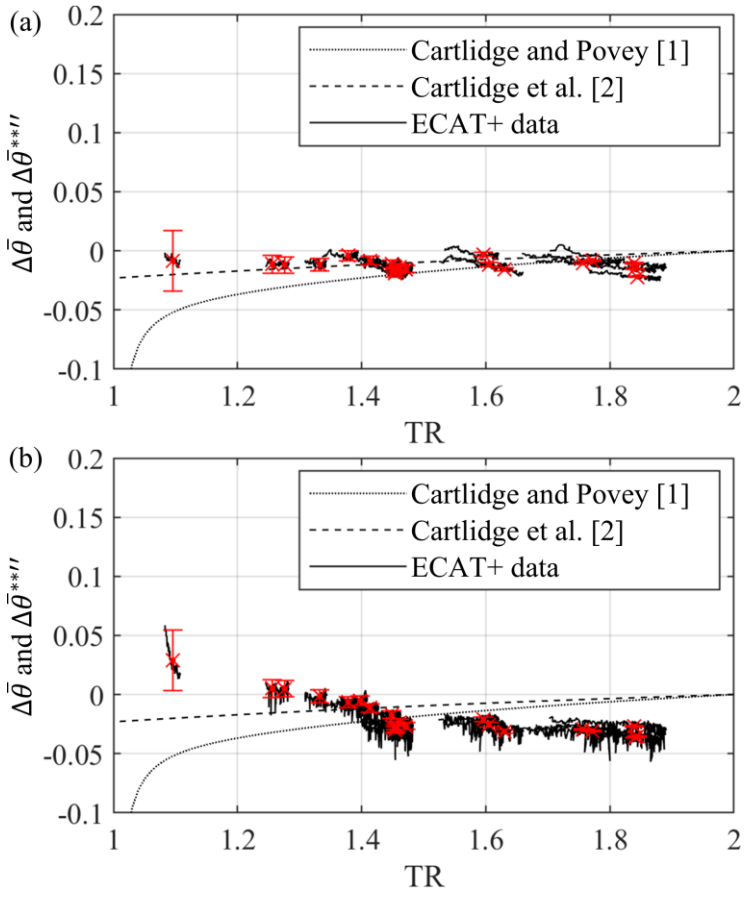

Figure 97: Magnitude of the change in surface-averaged overall cooling effectiveness as a function of TR for the leading vane, when IR temperature measurements are calibrated with Calibration Method 3, for (a) PS; and (b) SS.

The results are very similar in form to those of Calibration Method 2 i.e. the general trends are relatively flat; the individual-run trends do not collapse well onto a single trend for the PS but do collapse fairly well onto a single trend for the SS; and errors increase with reducing TR. This is not surprising because it was demonstrated in chapter 3 that Eq. (79) and Eq. (83) are equivalent when the product of transmittance and surface emissivity is non-unity but approximately unity ($\tau\varepsilon \cong 1$) and the correction offset is non-unity but sufficiently small ($\Delta T_{CP}/T_{bb} \ll 1$). This technique is not used in the main results sections of this chapter (sections 4.6.1, 4.6.2 and 4.6.3) because calibration techniques that are based on a physical model (i.e. Calibration Method 2) are preferred.

4.8.3 Calibration Method 4

This technique uses an isothermal calibration patch mounted on the target surface to derive a conversion curve (mapping raw image values to surface temperatures) for each run. The conversion curve is derived by evaluating the best-fit curve that represents the functional relationship $T_S = f(R)$ at the location of the calibration patch. The data used for best fitting were the measured (via thermocouple) calibration-patch temperature, $T_S(x_{CP},y_{CP},t)$, and the raw image value measured on the calibration patch, $R(x_{CP},y_{CP},t)$, where here the R value is averaged over all pixels containing the calibration patch. Experimental best-fit curves were derived using data for the time period in which the mainstream and coolant control systems were settled. The range of R values, measured by the IR camera *at the location of the calibration patch*, over the entire time series for a particular run, is referred to as the *best-fit region* for that run. Considering all pixels in the image, the IR camera will usually measure R values that lie significantly beyond the limits of the best-fit region for a particular run. Linear extrapolation is used to estimate surface temperatures for R values that lie outside the best-fit region. It is assumed that the derived conversion curve, which represents the functional relationship $T_S = f(R)$ at the location of the calibration patch, applies to all surface positions and the curve is therefore applied uniformly over the surface. An interesting feature of this technique is that the black-body conversion curve is not used at all i.e. the raw image values measured by the camera are converted directly to calibrated IR temperatures by using the derived conversion curve (mapping raw image values to surface temperatures) for the particular run.

Conversion curves (with linear extrapolation), along with the overlayed experimentally-measured raw data used to derive each curve, for all 21 runs are shown in Figure 98.

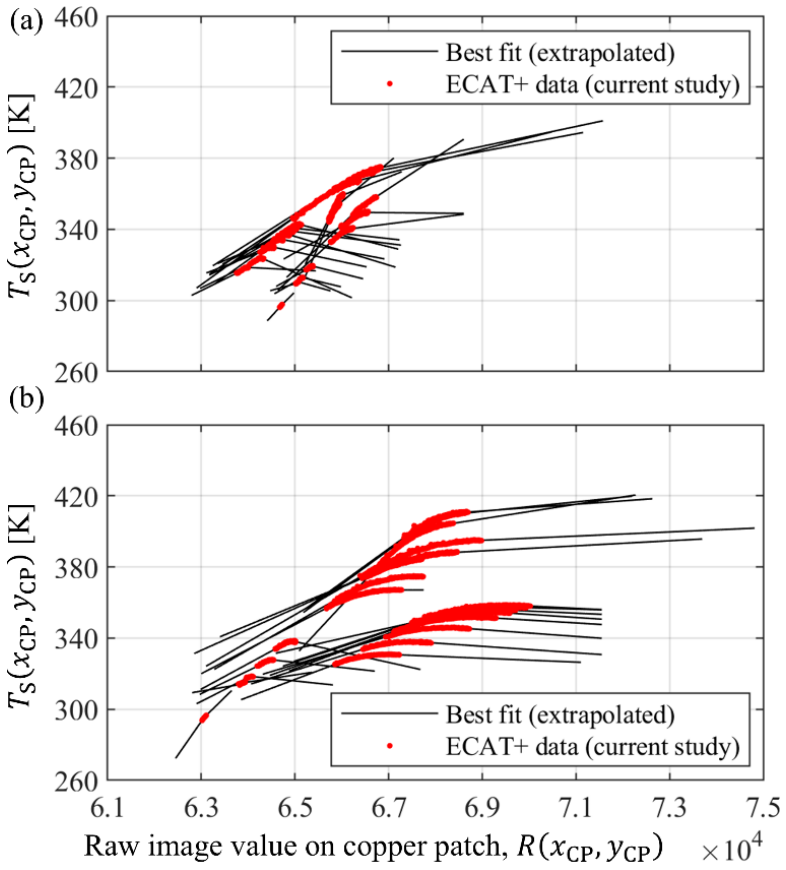

Figure 98: Conversion curves, used for calibrating IR temperature measurements with Calibration Method 4, for all 21 runs for (a) PS; and (b) SS.

Data for the PS are presented in the top row (frame a) and data for the SS are presented in the bottom row (frame b). Data are plotted for the time period in which the mainstream and coolant control systems were settled. It is noted that the raw image data are unsigned 16-bit integer values (maximum value 65535) and there is a threshold surface temperature corresponding to R = 65535. Once this temperature is exceeded, the raw image value instantaneously drops to 0 and R increases from 0 as surface temperature is further increased. For all R values corresponding to a surface temperature exceeding the threshold temperature, all R values are offset by +65535, in order to present continuous trends in the figure. The final characteristics for $\theta^{***\prime\prime}$ (LV only) are shown in Figure 99, where the change in $\theta^{***\prime\prime}$ from reference conditions of TR = 2.0 (i.e. the equivalent of Figure 90, but for $\theta^{***\prime\prime}$) are plotted.

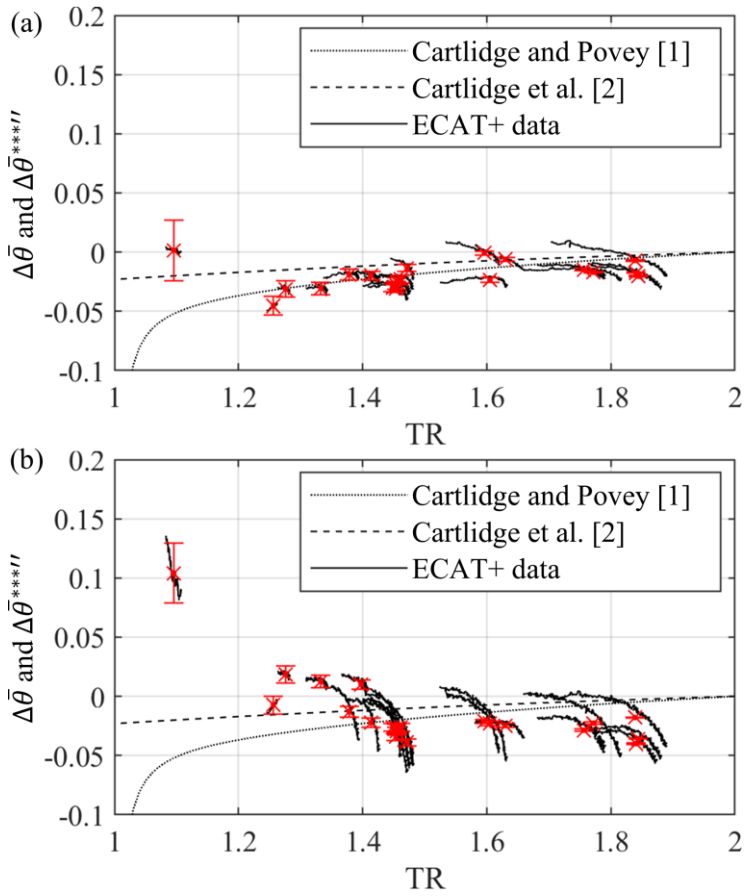

Figure 99: Magnitude of the change in surface-averaged overall cooling effectiveness as a function of TR for the leading vane, when IR temperature measurements are calibrated with Calibration Method 4, for (a) PS; and (b) SS.

For best-fitting, offsets are evaluated for the low-order-model trend of chapter 2 (system 1) that minimise the RMS deviation between experimental and low-order-model data (as discussed in section 4.6.2, but for $\theta^{***\prime\prime}$). Reference effectiveness values are taken to be the low-order-model predictions at TR = 2.0. The reference surface-averaged effectiveness values were $\bar{\theta}''_{\mathrm{PS,ref}} = 0.76$ and $\bar{\theta}''_{\mathrm{SS,ref}} = 0.60$. Data for the PS are shown in the top row (frame a) and data for the SS are shown in the bottom row (frame b). Error bars for the time-series average values of $\theta^{***\prime\prime}$ (error bars are derived from the same data set used to derive error bars for results calibrated with Calibration Method 2) are also included. Looking at Figure 99a, the following observations are made: The general trend for the PS data is to decrease with reducing TR; the agreement with the low-order-model-predicted trends is good; the trends for individual runs do not collapse well on

to a global trend (for some runs, the trend is in the opposite direction to the global trend); and errors increase with reducing TR. Now looking at Figure 99b, the following observations are made: As observed with Calibration Method 2 to 3, the general trend with TR is relatively flat in the range $TR > 1.4$ and increasing—slightly—with reducing TR in the range $TR \leq 1.4$; the individual-run trends are sharply increasing with reducing TR and they do not collapse well on to a global trend; and errors increase with reducing TR.

It is noted that the agreement between experimental data and low-order-model predictions is arguably the best when using this in-situ calibration approach; particularly so far as the general trends for the PS are concerned. Two significant downsides to this approach are identified, which make it less suitable for calibrating IR temperature measurements when compared to the other calibration methods discussed in this chapter. The key disadvantages to this approach are as follows:

i) The range of raw image values (and corresponding copper-patch temperatures) on the calibration patch is limited and—for some runs—significantly smaller than the total range of raw image values recorded for all pixels in the image (covering the entire surface). Consequently, the linear-extrapolation regions are extensive—in some cases covering a wider range of R values than the best-fit regions—which could lead to the accumulation of large errors in the calibrated IR temperatures, for measurements in which the underlying R values lie well outside the best-fit regions.

ii) The relationship between $T_{CP}(x,y,t)$ and $\overline{R}_{CP}(t)$ at a particular time instance is (amongst other factors) a function of the total surrounding radiant flux, $q^*(t)$. This implies that the true underlying calibration (mapping from $\overline{R}_{CP}(t)$ to $T_{CP}(x,y,t)$) is itself a function of time. The true underlying conversion curve at any time instance would therefore change—slightly—with time throughout a run. The assumption of a single time-invariant conversion curve for a particular run is therefore incorrect and could lead to the accumulation of significant errors in the calibrated IR temperature measurements.

Reservations with Calibration Methods 1, 3 and 4 have been expressed and analysis is focused on Calibration Method 2 in the main results sections (sections 4.6.1, 4.6.2 and 4.6.3) of this chapter.

4.9 Conclusions

In this chapter, experiments were performed in the ECAT+ facility to quantify the effect of temperature ratio on overall cooling effectiveness using real-engine high-pressure turbine nozzle guide vanes. Experiments were performed for temperature ratios in the range $1.08 \leq \mathrm{TR} \leq 1.89$ subjected to domain-global boundary conditions of fixed domain inlet-to-exit total-to-static pressure ratio with fixed atmospheric exit static pressure. The purpose of this study was to experimentally validate the theory for scaling of overall cooling effectiveness with temperature ratio, originally proposed in chapter 2. Corrections for both transient behaviour of the HPT NGVs; and off-target conditions of PR and CMPR were performed. The impact of temperature ratio on θ was studied through consideration of streamwise distributions of $\theta(x)$; and trends for surface-averaged effectiveness, $\bar{\theta}$, as a function of TR. Experimental results were compared with the low-order-model predictions of chapters 2 and 3 (two engine-representative—but very different—cooling systems). The supplementary conclusions for the PS and the SS are as follows:

i) *Pressure surface*: The general trend of $\bar{\theta}$ with TR is flat and broadly in agreement with the low-order-model-predicted trends of chapters 2 and 3.

ii) *Suction surface*: The general trend of $\bar{\theta}$ with TR is flat in the range $\mathrm{TR} > 1.4$ and—slightly—increasing with reducing TR (at a mildly accelerating rate) in the range $\mathrm{TR} \leq 1.4$. This means that the trend is broadly in agreement with the low-order-model predicted trends of chapters 2 and 3 in the range $\mathrm{TR} > 1.4$ but the trends diverge in the range $\mathrm{TR} \leq 1.4$.

The experimental data presented in this chapter do not *directly confirm* the theoretical results of chapter 2 but the general trends are considered to be broadly in agreement with the low-order-model results of chapters 2 and 3—particularly in light of the difficulties associated with

quantifying all errors in the processing chain (especially in the low-TR range). The somewhat contradictory trends for the SS in the range TR ≤ 1.4 are a matter of ongoing interest and input from the community on this matter would be welcomed. To the authors' knowledge, this is the first study attempting to experimentally validate the theoretical work of chapter 2 using real-engine HPT NGVs. Further corroborating experimental and computational studies are encouraged, particularly those with carefully considered boundary conditions..

5. Conclusions and future work

5.1 Conclusions

In this thesis, the effect of temperature ratio on overall cooling effectiveness for typical HPT NGVs, subject to two commonly-used laboratory boundary conditions, has been quantified and explained. For quantification purposes, low-order models with experimental validation were used. The results were explained by decomposing changes in overall cooling effectiveness with TR into changes associated with local surface boundary conditions. It was demonstrated that, for a system with minimal coupling between external and internal walls (typical of HPT NGV PS and early SS), moving between a typical engine temperature ratio for large civil aircraft of 2.0 to a conventional laboratory temperature ratio of 1.2 leads to a change in effectiveness of approximately -0.040 for a mean effectiveness of 0.500. This is equivalent to a -8% change. The rate of change accelerates with decreasing temperature ratio. This result was found to be insensitive to the cooling system network and the type of domain-global BCs imposed, and the mean value of overall cooling effectiveness at the reference TR.

The system studied in chapter 3 was found to have a significantly smaller magnitude of correction than the systems considered in chapter 2. It was demonstrated that this is because there is coupling between external and internal walls (due to the webs separating each module in the lateral direction) for the system considered in chapter 3. These coupling terms act to significantly reduce the magnitude of change in overall cooling effectiveness with temperature ratio. This shows that quantifying the degree of external-internal coupling is important when applying the results.

Importantly, the trends of overall cooling effectiveness with TR are supported by five corroborating sources of information (low-order-model results of chapter 2; calibrated low-order-model results of chapter 3; experimental results for the flat-plate studied in chapter 3; and experimental results for real-engine HPT NGVs presented in chapter 4). When the changes due

to both *absolute* temperature and combustion products are considered (the engine-to-rig scaling problem) the correction offset can be both positive or negative, with a sweet-spot at TR = 1.25, for which the correction offset is zero (for systems with minimal coupling between external and internal walls). It is believed that this is the first study to systematically quantify and explain from first principles the effect of TR on overall cooling effectiveness. This was done for a number of cooling system networks and for domain-global boundary conditions relevant to laboratory and engine testing. The resulting scaling charts allow scaling of overall effectiveness data between low-temperature-ratio laboratory tests and engine temperature ratios.

5.2 Future work

In this thesis, the effect of temperature ratio on overall cooling effectiveness for typical HPT NGVs, subject to two commonly-used laboratory boundary conditions, has been quantified and explained. Guidance for turbine vane designers interested in accurately predicting in-service metal temperatures, using a combination of experimental and low-order-modelling techniques, has been outlined.

The main weaknesses associated with the general approach for scaling overall cooling effectiveness outlined in this thesis are now briefly summarised:

i) The overall engine-to-rig correction, $\overline{\Delta\theta}_{\text{E-R}}$, derived in chapter 2 is not independent of system geometry and applied domain-global BCs (although it was demonstrated in chapter 2 that the sensitivity is low). It is estimated that, when θ is measured in ECAT operating at TR = 1.25 and the engine value of overall cooling effectiveness is predicted by applying a correction, $\overline{\Delta\theta}_{\text{E-R}} = 0$ (this is the method of Scaling Procedure 1; see section 1.3.1), the (small) residual in the scaling chain (i.e. the difference between the predicted and actual surface-averaged effectiveness at engine conditions) is likely to take a value up to about 0.01 for a conventional cooling system cooling design. For more accurate predictions for a particular geometry, the calibrated low-order model technique outlined in chapter 3 is

recommended (this is the method of Scaling Procedure 2; see section 1.3.2). Scaling Procedure 2 is less simple, and it is unclear what (small) residual (i.e. the difference between the predicted and actual surface-averaged effectiveness at engine conditions) is associated with this process using the techniques presented in this thesis (consider that the experimental and low-order-model results of chapter 3 are in broad agreement but are not directly confirmatory). Future work should focus on deriving simple robust scaling rules that are truly independent of geometry and boundary conditions and can be used to make rapid, accurate predictions of engine metal temperatures based on an experimentally-measured value of θ.

ii) Experimental validation is incomplete. The experimental and low-order-model results of chapters 3 and 4 are in broad agreement but are not directly confirmatory. The reasons for this are twofold: There are inadequacies in the physics of the low-order models (for example, the correlation for external heat transfer coefficients is for a flat plate rather than a HPT NGV with pressure gradient); and there are unresolved aspects of the experimental methods (for example, questions surrounding in-situ calibration techniques). Addressing both aspects of the problem will help to close the gap between low-order-model predictions and experimental results. Perhaps low-order models intrinsically fail to capture all of the physics relevant to the problem and, moving forward, higher-fidelity methods must be employed in order to bridge the remaining gap between model and experiment.

iii) It is unclear how to evaluate overall cooling effectiveness in practice. A preferred definition of overall cooling effectiveness for highly-compressible flow domains has been specified (see Eq. (2)), based on constraining this parameter between 0 and 1. It is possible to evaluate θ in the context of virtual experiments (see chapters 2 and 3) because additional simulations can be performed to evaluate the recovery ratio associated with the coolant total temperature (c_c), by imposing a boundary condition of a perfect cooling film (no entrainment). It is, however, unclear how to evaluate c_c (and c_h) accurately on a per-run

basis using an experimental data set from an engine-realistic test vehicle such as ECAT. In chapter 4, an approximation to c_c was evaluated using a CFD-based approach with associated assumptions (see section 4.4.1). Future work should focus on experimental methods for evaluating both c_c and c_h (consider, as a starting point, the regression-based technique outlined in Luque et al. [8] for systems in which all non-dimensional groups are fixed as TR is varied), and comparison with the CFD-based approach outlined in chapter 4.

To summarise, future work in this field should focus primarily on improving the physics of the low-order network models, mainly through modifying the correlations used throughout this thesis where appropriate. This may result in more accurate scaling predictions and provide more robust validation of the scaling theory. Additional attention should be given to refining the experimental methods discussed in chapters 3 and 4, in order to improve experimental validation of the theory of scaling of overall cooling effectiveness with TR. A framework for addressing some of these points is provided below. The recommendations for future work are divided into four categories corresponding to theoretical/numerical studies; modifications to conjugate low-order-network-model correlations; future flat-plate experiments; and future ECAT+ experiments. Note: several additional recommendations to the analysis presented in this thesis (not included here) are provided in earlier chapters.

5.2.1 Future theoretical/numerical studies

Recommendation for future theoretical/numerical studies is summarised below:

i) Perform simulations with a proprietary in-house conjugate heat-transfer tool, for the specific HPT NGV model used in the ECAT+ experiments (chapter 4). This will provide a further corroborating source of information for validating the theory of scaling of overall cooling effectiveness with temperature ratio; it can be used to perform experimental best-fitting for the experimental data; and can provide physical insight into the ECAT+ experimental results.

5.2.2 Modifications to conjugate low-order-network-model correlations

The bespoke conjugate low-order network models developed using MATLAB (see chapters 2 and 3) are useful tools for predicting the change in overall cooling effectiveness with TR for a wide range of HPT NGV cooling systems. These models make use of conventional correlations to evaluate various parameters, including cooling channel pressure loss and heat transfer coefficients. For several of these parameters, for example the external heat transfer coefficient, common flat-plate correlations are used. The justification here is that primary interest is in *changes* in *surface-averaged* overall cooling effectiveness with TR and any sensible correlation that captures the physics relevant to these changes is sufficient for this purpose. Considering the good match between the calibrated low-order network model and the experimental data of chapter 3, at least so far as the general trend of surface-averaged overall cooling effectiveness with TR is concerned (see Figure 66), it is believed that the applicability of the correlations is generally high. Despite the good agreement between the existing low-order network models and experimental data (see also Figure 90), there is scope for improving the physics of the models. This might lead to a better match between model and experiment and improve the quality of the model calibration. This would have the effect of moving calibration multipliers β_1–β_6 in chapter 3 (see section 3.8.4) closer to unity. One approach for improving the physics of the models it to review all correlations and, where appropriate, replace them with more suitable alternatives for the particular system under consideration. Several considerations for modifications to the existing correlations are outlined below:

i) *Recovery factor,* $r(x)$. In chapters 2 and 4, the commonly-used turbulent flow correlation for recovery factor, $r(x) = \mathrm{Pr}(x)^{1/3}$, is used. The validity of this correlation outside the conventional laboratory range ($T(x) > 600$ K) is unknown. It is recommended that an extensive review of the available literature is conducted to identify all correlations in general use. The sensitivity of the general result to this parameter should then be tested by

running the model of chapter 2 (or a similar low-order network model) with the different correlations identified.

ii) *Friction coefficient,* $f_c(x)$. In chapters 2 and 3, this was evaluated from the smooth-pipe Moody chart correlations. In chapter 3, $f_c(x)$ was enhanced by a factor of 7.00 (experimentally determined in Han and Zhang [40]). The validity of the assumption of smooth internal cooling channels is unknown. Additionally, the applicability of Eq. (59), with K_{2i}, in chapter 3 appears to be poor given the significant deviation from unity for the calibration multipliers $\beta_4-\beta_6$. It is very difficult to measure friction coefficient for the geometries considered in this thesis however one possible empirical approach for the model discussed in chapter 3 (and other arbitrary low-order network models) is to use a range of correlations in place of Eq. (59) for different values of relative roughness (see, for example, Bergman et al. [22]), re-calibrate the model against the experimental data (the procedure for this is outlined in section 3.8.4) for each relative roughness value, and choose the relative roughness (and corresponding correlation) which provides the lowest deviations of $\beta_4-\beta_6$ from unity. The exact form of friction coefficient is not considered to be of primary importance, provided that a sensible correlation is chosen, as the model is calibrated against experimental data and it is believed that the calibration procedure is robust.

iii) *External heat transfer coefficient,* $h_m(x)$. A flat-plate correlation, Eq. (21), is used in both chapters 2 and 3. This correlation is of similar form to typical external heat transfer coefficient distributions for HPT NGV pressure sides and suction sides, however it is recommended that the sensitivity of the general result to this correlation is tested. This could be performed by exploring alternative correlations with sound physical bases, for example those that account for pressure gradients, heat transfer from fluid to wall, and local flow disturbances caused by ejection from film cooling holes.

iv) *Effectiveness of the mixing layer,* $\eta_{ML}(x)$. For the cooling systems in chapter 2, an incompressible adiabatic film effectiveness corelation (Vinton et al. [24]), for a flat plate

with a single row of cooling holes, is used. Eq. (23) is of similar form to typical HPT NGV film effectiveness distributions and is therefore believed to be sufficient for the primary purpose of this thesis i.e. predicting the *change* in *surface-averaged* overall cooling effectiveness with TR. It is recommended that the sensitivity of the general result to this correlation is tested, by exploring alternatives with sound physical bases, for example those that account for pressure gradients and local flow disturbances caused by ejection from film cooling holes.

v) *Internal heat transfer coefficient,* $h_c(x)$. It was demonstrated in chapter 3 that the applicability of the underlying correlations, defined by Eq. (59), for internal Nusselt number for Surface 3 and 4 is poor. This is unsurprising given that experimentally-determined (see Han and Zhang [40]) multipliers K_{23} and K_{24} are used. This is not a concern given that the form of the correlations is sensible and the absolute values are determined by a calibration procedure (see section 3.8.4), which is considered to be robust. Nevertheless, one approach to improving the applicability of the correlations might be to experimentally measure the enhancement factors (K_{23} and K_{24}) for internal heat transfer coefficient for the particular geometry and boundary conditions considered, using techniques developed by Han and Zhang [40].

5.2.3 Future flat-plate experiments

Recommendations for future flat-plate experiments are summarised below:

i) Perform several additional experiments with the test article, domain-global BCs and range of temperature ratios considered in chapter 3. Data is currently available for only 9 runs. Obtaining a larger data set would allow more robust validation of the low-order-model results and would help to address concerns surrounding the repeatability of the data (for example, can identical trends for surrounding radiance, q^*, be obtained?)

ii) Install vortex tube in the coolant supply system of the flat-plate test facility (discussed in chapter 3) and increase mainstream heater settings. This will allow testing over the

approximate range $1.0 \leq \mathrm{TR} \leq 2.0$. Then perform at least 100 runs over the range $1.0 \leq \mathrm{TR} \leq 2.0$ in order to obtain a large set of data. This will facilitate more robust validation of the scaling theory.

iii) Manufacture a new test piece with geometry identical to system 1 studied in chapter 2 i.e. one of the original geometries used to develop the scaling theory proposed in chapter 2. One key consideration is how to eliminate the coupling effect introduced by the webs that connect the external and internal wall of the test article considered in chapter 2 (the webs are required in order to straighten the flow, so cannot be removed entirely). One option is to reduce the number of webs, and another option is to use plastic webs (low thermal conductivity). Perform at least 100 tests for the new test article over the range $1.0 \leq \mathrm{TR} \leq 2.0$ in order to obtain a large data set. This will allow robust validation of the theory for scaling of θ with TR (large range of experimental data points for a different geometry) and will allow direct validation of the low-order-model predicted results for system 1 in chapter 2.

iv) Improve the transient-correction methodology. It was shown in chapter 2 that this approach closes the gap significantly between the transient experimental characteristic and the steady-state aerothermal network model predictions but that the corrected data consists of local contradictory trends, associated with each run, of decreasing θ with increasing TR. It is possible that the optimisation algorithm used for calibration of the transient aerothermal low-order network model is inadequate and it is also possible that the model does not sufficiently capture the relevant physics. It is recommended that both of these points are investigated.

5.2.4 Future ECAT+ experiments

Recommendations for future ECAT+ experiments are summarised below:

i) Improve rigidity of mounting assembly for downstream infrared (IR) camera. The purpose of this step is to eliminate the vibrations induced in the camera throughout a run and obtain a higher-quality data set.

ii) Run the PLC in active control mode. When operated in this mode, the PLC updates the values of the target control pressures in real-time, in order to maintain fixed PR and coolant-to-mainstream pressure ratio (CMPR) throughout a run (instead of setting a fixed total pressure upstream of both the mainstream and coolant CFVNs, as in this thesis). This will improve the steadiness of the pressure ratios throughout a run, thus reducing the need for corrections for off-design pressure ratios. This will help to eliminate sources of uncertainty in the data processing chain.

iii) Perform at least 100 experiments in the range $1.0 \leq TR \leq 2.0$ (the existing data set of 21 runs is quite small). This will provide further corroborating information for the validation of the scaling theory and will address concerns surrounding repeatability of the experimental results.

iv) Conduct experimental, theoretical and numerical studies to validate the isothermal-patch methods used to correct ECAT/ECAT+ data for the effects of surrounding radiance, non-unity vane surface emissivity and non-unity IR window transmittance. Proposals for this work are outlined extensively in chapter 4.

6. References

[1] Cartlidge, J., and Povey, T., 2024, "Fundamentals of Scaling of Overall Cooling Effectiveness with Temperature Ratio," *ASME J Turbomach*, 146(1), p. 011008. DOI: 10.1115/1.4063730.

[2] Cartlidge, J., Naidu, A. D., Chowdhury, N. H. K., and Povey, T., 2024, "Impact of Temperature Ratio on Overall Cooling Effectiveness: Experimental Validation of a Scaling Theory," under review.

[3] Cartlidge, J., Messenger, A., Chowdhury, N. H. K., Goenaga, F., and Povey, T., 2024, "Experimental Study of the Impact of Temperature Ratio on Overall Cooling Effectiveness of High-Pressure Nozzle Guide Vanes," complete draft.

[4] Ornano, F., and Povey, T., 2020, "Theory of Non-Dimensional Groups in Film Effectiveness Studies," *ASME J Turbomach*, 142(4), p. 041002. DOI: 10.1115/1.4046277.

[5] Eckert, E. R. G., 1992, "Similarity Analysis of Model Experiments for Film Cooling in Gas Turbines," *Wärme- und Stoffübertragung*, 27(4), pp. 217-223. DOI: 10.1007/BF01589919.

[6] Baldauf, S., and Scheurlen, M., 1996, "CFD Based Sensitivity Study of Flow Parameters for Engine Like Film Cooling Conditions," *Proceedings of the ASME 1996 International Gas Turbine and Aeroengine Congress and Exhibition*, Birmingham, UK, June 10-13, 1996, ASME Paper No. 96-GT-310. DOI: 10.1115/96-GT-310.

[7] Greiner, N. J., Polanka, M. D., and Rutledge, J. L., 2015, "Scaling of Film Cooling Performance From Ambient to Engine Temperatures," *ASME J Turbomach*, 137(7), p. 071007. DOI: 10.1115/1.4029197.

[8] Luque, S., Jones, T. V., and Povey, T., 2016, "Theory for the Scaling of Metal Temperatures in Cooled Compressible Flows," *International Journal of Heat and Mass Transfer*, 102, pp. 331-340. DOI: 10.1016/j.ijheatmasstransfer.2016.06.025.

[9] Kirollos, B., Lubbock, R., Beard, P., Goenaga, F., Rawlinson, A., Janke, E., and Povey, T., 2017, "ECAT: An Engine Componenet Aerothermal Facility at the University of Oxford," *Proceedings of the ASME Turbo Expo 2017: Turbomachinery Technical Conference and Exposition*, Charlotte, North Carolina, USA, June 26-30, 2017, ASME Paper No. GT2017-64736. DOI: 10.1115/GT2017-64736.

[10] Luque, S., Jones, T. V., and Povey, T., 2017, "Scaling of Turbine Metal Temperatures in Cooled Compressible Flows - Experimental Demonstration of a New Theory," *ASME J Turbomach*, 139(8), p. 081001. DOI: 10.1115/1.4035831.

[11] Sweeney, P. C., and Rhodes, J. F., 2000, "An Infrared Technique for Evaluating Turbine Airfoil Cooling Designs," *ASME J Turbomach*, 122(1), pp. 170-177. DOI: 10.1115/1.555438.

[12] Albert, J. E., and Bogard, D. G., 2013, "Measurements of Adiabatic Film and Overall Cooling Effectiveness on a Turbine Vane Pressure Side With a Trench," *ASME J Turbomach*, 135(5), p. 051007. DOI: 10.1115/1.4007820.

[13] Rutledge, J. L., Polanka, M. D., and Greiner, N. J., 2017, "Computational Fluid Dynamics Evaluations of Film Cooling Flow Scaling Between Engine and Experimental Conditions," *ASME J Turbomach*, 139(2), p. 021004. DOI: 10.1115/1.4034557.

[14] Fischer, J. P., McNamara, L. J., Rutledge, J. L., and Polanka, M. D., 2020, "Scaling Flat-Plate, Low-Temperature Adiabatic Effectiveness Results Using the Advective Capacity Ratio," *ASME J Turbomach*, 142(8), p. 081010. DOI: 10.1115/1.4046544.

[15] McNamara, L. J., Fischer, J. P., Rutledge, J. L., and Polanka, M. D., 2021, "Scaling Considerations for Thermal and Pressure-Sensitive Paint Methods Used to Determine Adiabatic Effectiveness," *ASME J Turbomach*, 143(1), p. 011004. DOI: 10.1115/1.4049102.

[16] Bryant, C. E., and Rutledge, J. L., 2023, "Theoretical Considerations for Scaling Convection in Overall Effectiveness Experiments," *ASME J Turbomach*, 145(1), p. 011007. DOI: 10.1115/1.4055446.

[17] Naidu, A. D., and Povey, T., 2023, "Impact of Temperature Ratio on Overall Cooling Performance: Low-Order-Model-Based Analysis of Experiment Design," *ASME J Turbomach*, 145(9), p. 091006. DOI: 10.1115/1.4062279.

[18] Messenger, A., Cartlidge, J., Chowdhury, N. H. K., Goenaga, F., and Povey, T., 2023, "ECAT+: A Second-Generation High-Temperature Engine Component Aerothermal Facility at the University of Oxford," *Proceedings of the ASME 2023: Turbomachinery Technical Conference and Exposition*, Boston, Massachusetts, USA, June 26–30, 2023, ASME Paper No. GT2023-102935. DOI: 10.1115/GT2023-102935.

[19] Michaud, M., Ornano, F., and Povey, T., 2023, "Annular Dump Diffuser and Deswirl System for Back-Pressure Control in Engine-Scale Transonic Annular Cascade," *ASME J Turbomach*, 145(4), p. 041006. DOI: 10.1115/1.4055863.

[20] Kirollos, B., and Povey, T., 2014, "Reverse-Pass Cooling Systems for Improved Performance," *ASME J Turbomach*, 136(11), p. 111004. DOI: 10.1115/1.4028161.

[21] McAdams, W. H., *Heat Transmission*, second ed., New York and London: McGraw-Hill Book Company, Inc., ISBN 978-0070-85483-3, 1942.

[22] Bergman, T. L., Lavine, A. S., Incropera, F. P., and Dewitt, D. P., *Fundamentals of Heat and Mass Transfer*, seventh ed., United States of America: John Wiley & Sons, Inc., ISBN 978-0470-50197-9, 2011.

[23] Kirollos, B., and Povey, T., 2015, "An Energy-Based Method for Predicting the Additive Effect of Multiple Film Cooling Rows," *ASME J Turbomach*, 137(12), p. 122607. DOI: 10.1115/1.4030907.

[24] Vinton, K. R., Watson, T. B., Wright, L. M., Crites, D. C., Morris, M. C., and Ardeshir, R., 2017, "Combined Effects of Freestream Pressure Gradient and Density Ratio on the Film Cooling Effectiveness of Round and Shaped Holes on a Flat Plate," *ASME J Turbomach*, 139(4), p. 041003. DOI: 10.1115/1.4035044.

[25] Cumpsty, N. A., and Heyes, A. L., *A Simple Guide to the Aerodynamics and Thermodynamic Design and Performance of Jet Engines*, third ed., United States of America: Cambridge University Press, ISBN 978-1-107-51122-4, 2015.

[26] Zielińska, M., Yavorska, M., Poręba, M., and Sieniawski, J., 2010, "Thermal Properties of Cast Nickel Based Superalloys," *Archives of Materials Science and Engineering*, 44(1), pp. 35-38.

[27] Rhee, D., Kang, Y. S., Cha, B. J., and Lee, S., 2017, "Overall Cooling Effectiveness Measurements on Pressure Side Surface of the Nozzle Guide Vane With Optimized Film Cooling Hole Arrangements," *Proceedings of the ASME 2017: Turbomachinery Technical*

Conference and Exposition, Charlotte, North Carolina, USA, June 26-30, 2017, ASME Paper No. GT2017-63421. DOI: 10.1115/GT2017-63421.

[28] Poferl, D. J., Svehla, R. A., and Lewandowski, K., 1969, "Thermodynamic and Transport Properties of Air and the Combustion Products of Natural Gas and of ASTM-A-1 Fuel with Air," NASA Report No. NASA TN D-5452.

[29] Oldfield, M. L. G., and Guo, S. M., 1997, "Aero-thermal Properties of Foreign Gas (SF_6/AR) and Air: Recommended Formulae from 160–1000 K," OUEL Report No. 2141/97. Department of Engineering Science, University of Oxford, Oxford, UK.

[30] Michaud, M., Chowdhury, N. H. K., and Povey, T., 2023, "Experimental Study of Impact of In-Service Deterioration on Thermal Performance of High-Pressure Nozzle Guide Vanes," *ASME J Turbomach*, 145(2), p. 021014. DOI: 10.1115/1.4055864.

[31] Michaud, M., Ornano, F., Chowdhury, N. H. K., and Povey, T., 2020, "Methodology for High-Accuracy Infrared Calibration Environments with Through-Wall Heat Flux," *J. Glob. Power Propuls. Soc.*, 4, pp. 1-13. DOI: 10.33737/jgpps/118091.

[32] Williams, R. P., Dyson, T. E., Bogard, D. G., and Bradshaw, S. D., 2014, "Sensitivity of the Overall Cooling Effectiveness to Film Cooling and Internal Cooling on a Turbine Vane Suction Side," *ASME J Turbomach,* 136(3), p. 031006. DOI: 10.1115/1.4024681.

[33] Nathan, M. L., Dyson, T. E., Bogard, D. G., and Bradshaw, S. D., 2014, "Adiabatic and Overall Effectiveness for the Showerhead Film Cooling of a Turbine Vane," *ASME J Turbomach*, 136(3), p. 031005. DOI: 10.1115/1.4024680.

[34] Dyson, T. E., Bogard, D. G., Piggush, J. D., and Kohli, A., 2013, "Overall Effectiveness for a Film Cooled Turbine Blade Leading Edge With Varying Hole Pitch," *ASME J Turbomach*, 135(3), p. 031011. DOI: 10.1115/1.4006872.

[35] Michaud, M., and Povey, T., 2021, "Methods to Extract Underlying Boundary Conditions from Transient Metal Effectiveness Measurements," *Journal of Thermophysics and Heat Transfer*, 35(4), pp. 657–668. DOI: 10.2514/1.T6137.

[36] Kirollos, B., and Povey, T., 2017, "Laboratory Infrared Thermal Assessment of Laser-Sintered High-Pressure Nozzle Guide Vanes to Derisk Engine Design Programs," *ASME J Turbomach*, 139(4), p. 041009. DOI: 10.1115/1.4035074.

[37] Kirollos, B., and Povey, T., 2016, "Cooling Optimization Theory—Part I: Optimum Wall Temperature, Coolant Exit Temperature, and the Effect of Wall/Film Properties on Performance," *ASME J Turbomach*, 138(8), p. 081002. DOI: 10.1115/1.4032612.

[38] Kirollos, B., and Povey, T., 2016, "Cooling Optimization Theory—Part II: Optimum Internal Heat Transfer Coefficient Distribution," *ASME J Turbomach*, 138(8), p. 081003. DOI: 10.1115/1.4032613.

[39] Thomas, M., and Povey, T., 2015, "A Novel Scalar Tracking Method For Optimising Film Cooling Systems," *Proceedings of the Institution of Mechanical Engineers, Part A: Journal of Power and Energy*, 230(1), pp. 3−15. DOI: 10.1177/0957650915605944.

[40] Han, J. C., and Zhang, Y. M., 1992, "High Performance Heat Transfer Ducts with Parallel Broken and V-shaped Broken Ribs," *International Journal of Heat and Mass Transfer*, 35(2), pp. 513−523. DOI: 10.1016/0017-9310(92)90286-2.

[41] Mehendale, A. B., and Han, J., C., 1993, "Reynolds Number Effect on Leading Edge Film Effectiveness and Heat Transfer Coefficient," *International Journal of Heat and Mass Transfer*, 36(15), pp. 3723–3730. DOI: 10.1016/0017-9310(93)90052-8.

[42] McNamara, L., Fischer, J., Kernan, M., and Rutledge, J., 2023, "Scaling Flat Plate Overall Effectiveness Measurements," *ASME J Turbomach*, 145(3), p. 031003. DOI: 10.1115/1.4055614.

[43] Dyson, T., Bogard, D., McClintic, J., and Bradshaw, S., 2013, "Adiabatic and Overall Effectiveness for a Fully Cooled Turbine Vane," *Proceedings of the ASME 2013: Turbomachinery Technical Conference and Exposition*, San Antonio, Texas, USA, June 3–7, 2013, ASME Paper No. GT2013-94928. DOI: 10.1115/GT2013-94928.

[44] Shi, B., Li, J., Li, M., Ren, J., and Jiang, H., 2016, "Overall Cooling Effectiveness on a Flat Plate With Both Film Cooling and Impingement Cooling in Hot Gas Condition," *Proceedings of the ASME 2016: Turbomachinery Tenchnical Conference and Exposition*, Seoul, South Korea, June 13–17, 2016, ASME Paper No. GT2016-57224. DOI: 10.1115/GT2016-57224.

[45] Hossain, M. A., Ameri, A., Gregory, J. W., and Bons, J. P., 2021, "Experimental Investigation of Innovative Cooling Schemes on an Additively Manufactured Engine Scale Turbine Nozzle Guide Vane," *ASME J Turbomach*, 143(5), p. 051004. DOI: 10.1115/1.4049618.

[46] An, B., Hu, J., and Liu, J., 2023, "Experimental Investigation on Overall Effectiveness of Flat Plate Combined Impingement Cooling With Film-Cooling of Diffusion Slot Holes," *Proceedings of the ASME 2023: Turbomachinery Technical Conference and Exposition*, Boston, Massachusetts, USA, June 26–30, 2023, ASME Paper No. GT2023-104261. DOI: 10.1115/GT2023-104261.

[47] Luque, S., and Povey, T., 2010, "A Novel Technique for Assessing Turbine Cooling System Performance," *ASME J Turbomach*, 133(3), p. 031013. DOI: 10.1115/1.4001232.

[48] Luque, S., Batstone, J., Gillespie, D. R. H., Povey, T., and Romero, E., 2014, "Full Thermal Experimental Assessment of a Dendritic Turbine Vane Cooling Scheme," *ASME J Turbomach*, 136(2), p. 021011. DOI: 10.1115/1.4023940.

[49] Luque, A., Jones, T. V., and Povey, T., 2017, "Effects of Coolant Density, Specific Heat Capacity, and Biot Number on Turbine Vane Cooling Effectiveness," *ASME J Turbomach*, 139(11), p. 111005. DOI: 10.1115/1.4037029.

[50] Parker, J., and Povey, T., 2022, "Method for Determining Adiabatic Film Effectiveness in Presence of Thermal Boundary Layer," *ASME J Turbomach*, 144(5), p. 051010. DOI: 10.1115/1.4053021.

[51] Amend, J., Lubbock, R., Ornano, F., Chowdhury, N. H. K., and Povey, T., 2024, "Aerodynamic and Thermal Field Development of Cooled Transonic HP NGV," *ASME J Turbomach*, 146(2), p. 021010. DOI: 10.1115/1.4063879.

[52] Warren, T. J., Bowles, N. E., Donaldson Hanna, K., and Thomas, I. R., 2017, "The Oxford Space Environment Goniometer: A New Experimental Setup for Making Directional Emissivity Measurements Under a Simulated Space Environment," *Rev. Sci. Instrum.*, 88(12), 124502. DOI: 10.1063/1.4986657.

[53] Messenger, A., and Povey, T., 2020, "Calibrated Low-Order Transient Thermal and Flow Models for Robust Test Facility Design," *J. Glob. Power Propuls. Soc.*, 4, pp. 94–113. DOI: 10.33737/jgpps/122270.

[54] Natsui, G., Little, Z., Kapat, J. S., and Dees, J. E., 2017, "Adiabatic Film Cooling Effectiveness Measurements Throughout Multirow Film Cooling Arrays," *ASME J Turbomach*, 139(10), p. 101008. DOI: 10.1115/1.4035520.

[55] Zhang, L. J., and Glezer, B., 1997, "Turbine Airfoil External Heat Transfer Measurement in a Hot-Cascade," *Proceedings of the ASME 1997: International Gas Turbine and Aeroengine Congress and Exhibition*, Orlando, Florida, USA, June 2–5, 1997, ASME Paper No. 97-GT-327. DOI: 10.1115/97-GT-327.